



HAL
open science

Modelling damage and dilatant two-phase flow at pore scale using Smoothed Particle Hydrodynamics (SPH) method

Rafael C. Deptulski

► **To cite this version:**

Rafael C. Deptulski. Modelling damage and dilatant two-phase flow at pore scale using Smoothed Particle Hydrodynamics (SPH) method. Fluid mechanics [physics.class-ph]. Sorbonne Université, 2021. English. NNT: 2021SORUS214 . tel-03481975

HAL Id: tel-03481975

<https://theses.hal.science/tel-03481975>

Submitted on 15 Dec 2021

HAL is a multi-disciplinary open access archive for the deposit and dissemination of scientific research documents, whether they are published or not. The documents may come from teaching and research institutions in France or abroad, or from public or private research centers.

L'archive ouverte pluridisciplinaire **HAL**, est destinée au dépôt et à la diffusion de documents scientifiques de niveau recherche, publiés ou non, émanant des établissements d'enseignement et de recherche français ou étrangers, des laboratoires publics ou privés.



Thesis manuscript
Modelling damage and dilatant two-phase flow at
pore scale using Smoothed Particle
Hydrodynamics (SPH) method

Rafael C. Deptulski

Pôle Environnement / Laboratoire d'étude et de recherche sur les transferts et les interactions
dans les sols (LETIS)

Ecole doctorale Sciences Mécaniques Acoustique Electronique Robotique (SMAER) - ED 391 /
Institut Jean le Rond d'Alembert - UMR 7190

Modelling damage and dilatant two-phase flow at pore scale using Smoothed Particle Hydrodynamics (SPH) method

Rafael C. Deptulski

Director **Djimédo Kondo**
Sorbonne Université

Supervisor **Magdalena Dymitrowska**
Institut de Radioprotection et de Sûreté Nucléaire

Rafael C. Deptulski

Thesis manuscript

Modelling damage and dilatant two-phase flow at pore scale using Smoothed Particle Hydrodynamics (SPH) method

Director: Djimédo Kondo

Sorbonne Université

Ecole doctorale Sciences Mécaniques Acoustique Electronique Robotique (SMAER) - ED 391

Institut Jean le Rond d'Alembert - UMR 7190

4 Place Jussieu

75005 Paris

Supervisor: Magdalena Dymitrowska

Institut de Radioprotection et de Sûreté Nucléaire (IRSN)

Pôle Environnement

Laboratoire d'étude et de recherche sur les transferts et les interactions dans les sols (LETIS)

31 Avenue de la Division Leclerc

92260 Fontenay-aux-Roses

Contents

Introduction	1
1 Geological disposal of radioactive waste: managing risks from nano to macroscale	5
Overview	5
1.1 Deep geological disposal of radioactive waste: state of the art	6
1.1.1 The French case: Cigéo project	7
1.1.2 Callovo-Oxfordian host rock	8
1.2 Two-phase flow coupled with mechanical load at pore scale: experimental and numerical reviews	12
1.3 Hydro-mechanical pore-scale model	18
1.3.1 Fluid phases	19
1.3.2 Elastic solid phase	21
1.3.2.1 Large deformations in continuum mechanics	21
1.3.2.2 Governing equations and Saint Venant-Kirchhoff constitutive model	22
1.3.2.3 Governing equations and linear elastic law	24
1.3.3 Interface conditions	25
Concluding remarks	25
2 Numerical modelling: Smoothed Particle Hydrodynamics	27
Overview	27
2.1 Mathematical formulation: smoothed functions and derivatives	28
2.1.1 Types of smoothing functions	30
2.1.2 Kernel interpolation	31
2.1.3 Kernel derivatives continuous approximation	33
2.1.3.1 First derivatives approximation	34
2.1.3.2 Second order derivatives approximation	35
2.1.4 SPH discrete approximation	37
2.2 Time integration	41
2.2.1 Verlet integration scheme	41
2.2.2 Leapfrog integration scheme	41
2.2.3 Maximal time-step: CFL stability conditions	42

2.3	Improvements of numerical modelling	42
2.3.1	Mixed kernel function and gradient correction	44
2.3.2	Artificial viscosity	46
2.3.3	XSPH velocities correction	47
2.3.4	SPH in GPU parallel computing	47
2.4	Elastic body dynamics	47
2.4.1	SPH discrete governing equations and Saint Venant-Kirchhoff constitutive model	47
2.4.2	SPH discrete governing equations and linear elastic law	49
2.4.3	SPH algorithm	51
2.5	Validation and analysis: mixed kernel and gradient correction	55
2.5.1	Computing SPH divergence with or without symmetry terms and gradient corrections	57
2.5.2	Influence of particles density	60
2.5.3	Influence of particles disorder	60
2.5.4	From 1D to 3D validation	64
2.6	SPH as a local EDP solver for elastic media	67
2.6.1	Stress and displacement-based momentum equations for small deformations	68
2.6.2	Small and large deformations	70
2.6.3	XSPH and artificial viscosity	70
	Concluding remarks	70
3	Non-local elasticity by SPH	75
	Overview	75
	Modelling non-local elasticity in 1D vibrating rods using Smoothed Particle Hydrodynamics method	77
	Concluding remarks	110
4	SPH modelling of local elasto-damage	111
	Overview	111
4.1	Thermodynamics-based formulation of damage models	113
4.1.1	Free energy and dissipation potential	113
4.1.2	Dissipation pseudo-potential and evolution laws	114
4.1.3	Account of unilateral effects (microcracks closure)	116
4.1.4	Examples of degradation functions and of critical energy release	118
4.1.5	SPH-based algorithm implementation of the damage models	119
4.2	Application to 1D dynamic softening bar	121
4.2.1	Material point densities independence validation	123

4.2.2	Non-local characterisation by means of the numerical parameter $2h$ -length	127
4.2.3	Comparison between different SPH formulations	127
4.3	Application to 2D fiber reinforced plate	131
4.3.1	Introduction	131
4.3.2	Quasi-static response of fiber reinforced plate	133
4.3.2.1	Tensile loading	134
4.3.2.2	Compressive loading	139
4.3.2.3	Analysis of SPH discretization independence and limit values for SPH support-length	143
4.3.3	Dynamic response of fiber reinforced plate	146
4.3.3.1	Tensile loading	146
4.3.3.2	Compressive loading	150
4.3.3.3	Analysis of limit values for SPH support-length	153
	Concluding remarks	156
5	Simulations of drainage coupled with damage in a sample of clay rock	157
	Overview	157
5.1	SPH fluid phases: pore-water and hydrogen	157
5.2	Numerical sample and parameters for drainage simulations	160
5.3	Drainage with purely elastic clay matrix	166
5.4	Drainage with elasto-damage clay matrix	168
5.4.1	Confining stress of $\sigma_{conf}=8$ MPa	169
5.4.2	Confining stress of $\sigma_{conf}=6$ MPa	171
5.5	Drainage of a sample with disconnected pores	174
	Concluding remarks	177
	Conclusion and Outlooks	179
A	Appendix: Rigid bodies (mineral inclusions)	183
A.1	Continua equations	183
A.2	Discrete equations	184
A.3	Interface conditions	185
B	Appendix: Complements of simulation results with PCW-based elastic-damage model	187
B.1	Quasi-static conditions	187
B.2	Dynamic conditions	190
	Bibliography	201

Nomenclature

Greek symbols

α, γ	Arbitrary spatial dimensions
$\check{\alpha}, \check{\beta}$	Arbitrary constant parameters for artificial viscosity
$\check{\nu}$	Artificial viscosity auxiliary function
$\check{\gamma}$	Coefficient of surface tension
$\check{\kappa}$	Local interface curvature
$\check{\sigma}_{rel}$	Relative error
ΔP	Pressure drop
Δt	Time step
δx	Spatial step
δ	Dirac's delta function
ϵ_{GL}	Green-Lagrange deformation tensor
Γ	Boundary domain
$\hat{\alpha}, \hat{\beta}$	Arbitrary constant parameters for PCW damage function
$\hat{\epsilon}$	Arbitrary constant parameter for XSPH
$\hat{\kappa}$	Multiplier factor
Λ	Damage scalar
λ	SPH kernel support-length
λ, μ	Lamé coefficients (solid material)
μ	Dynamic viscosity (fluid material)
μ	Shear modulus (solid material)
ν	Poisson's ratio (solid material)

Ω	Domain
ω	Angular velocity
$\bar{\rho}$	Arithmetic mean of density
∂	Partial differential operator
Φ	Arbitrary function
ϕ	Relative angle with respect to the reference axes
Π	Artificial viscosity term
ρ	Density
Σ	Sum
σ	Cauchy stress tensor
σ_{conf}	Confining stress
θ	Contact angle
ε	Small deformations strain tensor
φ	Dissipation pseudo-potential
φ^*	Dual potential

Other variables

\check{c}	Color function
\check{d}	Pore diameter
\check{F}	Volumetric surface tension
\check{N}	Number of material points inside the smoothing function domain
\hat{d}	Spatial dimension
\hat{F}	Force density
\hat{v}	Corrected velocity after XSPH
\mathcal{D}	Intrinsic dissipation
\mathcal{E}	Energy functional
\mathcal{F}	Scalar function
\mathcal{J}	Derivative integrals
\mathcal{O}	Error order
\mathcal{Y}	Damage energy release

\mathcal{Y}_c	Critical damage energy release
w	Arbitrary continuous monotonic function
\bar{c}	Arithmetic mean of sound velocity
\vec{n}	Unit normal
$\widetilde{\nabla}, \widetilde{\widetilde{\nabla}}$	Corrected forms of the gradient of the kernel function
$\widetilde{W}, \widetilde{\widetilde{W}}$	Normalized form of kernel function
a	Acceleration
B	Symmetric function
c, c_e, c_s	Sound velocity
c_w	Normalisation parameter
d	Rate of deformation tensor
E	Young Modulus
$E^{\hat{D}}$	Global dissipated energy
$E^{\hat{T}}$	Global kinetic energy
$E^{\hat{W}}$	Global elastic energy
E^{TOT}	Global total energy
err	Approximation error
F	Deformation gradient tensor
f	Arbitrary function
f_c	Uniaxial compressive strength
f_t	Tensile strength
g	Gravity acceleration
G_c	Fracture toughness
h	Smoothing scale
H_r	Height of a reservoir
I	Moment of inertia
J	Jacobian operator
K	Corrective matrix
k	Bulk modulus (solid material)

L	Bar half-length or plate side length
l	Velocity gradient tensor
l_c	Material internal length
M	Multiplier factor
m	Mass
P	First Piola-Kirchhoff stress tensor
p	Pressure
q	Norm of the position differences
R	Root mean square deviation
r, r'	Material point spatial coordinates
$R_{<.>}$	Radii of curvature
S	Second Piola-Kirchhoff stress tensor
s_l	Damage limit bound
T	Torque
t	Time
u	Displacement
V	Volume
v	Velocity
W	Smoothing function
w	Thermodynamics potential / Strain energy density
w	Thermodynamics potential
X	Initial position
x	Current position
x, y, z	Cartesian coordinates
a	Surface of a domain

Indices

0	Initial value or reference configuration
a	Studied material point
ab	Difference between the studied material point and its neighbour

B	Rigid body
b	Any material point neighbour
c	Compressive state
c_0	Initial compressive failure
c_u	Ultimate compressive failure
CM	Center of mass
e	Elastic phase
f	Fluid phases
g	Gas phase
irr	Irreversible state
l	Liquid phase
max	Maxima
min	Minima
rev	Reversible state
S	Smoothed approximation form
s	Solid phase
t	Tensile state
t_0	Initial tensile failure
t_u	Ultimate tensile failure
u	Ultimate failure
x, y, z	First spatial derivatives
$xx, yy, zz, xy, xz, yz, etc$	Second spatial derivatives

Tensor notations

$:$	Double dot product
\cdot	Dot product
δ^{ij}	Kronecker delta
\mathbb{C}	Stiffness fourth order tensor
\mathbb{I}	Fourth order unity tensor
\mathbb{J}	Spherical projection of fourth order tensor

\mathbb{K} Deviatoric projection of fourth order tensor

\mathbb{T} Fourth order tensor

$\nabla \cdot \underline{\underline{T}}$ Divergence of a second order tensor

$\nabla \underline{T}$ Gradient of a first order tensor

\otimes Kronecker product

$\text{tr}(\underline{\underline{T}})$ Trace of a second order tensor

$\underline{\underline{1}}$ Second order unity tensor

\underline{T} Second order tensor

$\underline{\underline{T}}^T$ Transpose of a second order tensor

$\underline{\underline{T}}^d$ Deviatoric part of a second order tensor

\underline{T} First order tensor

Dimensionless numbers

Bo Bound number

Ca Capillary number

M Mobility ratio

Re Reynolds number

Introduction

Within the ongoing debate on the pros and cons of using nuclear technologies, a major issue in this domain concerns the management of their sub-products and wastes that are being or already have been produced. This is particularly challenging for the high-level and long-lived intermediate-level radioactive waste, notably resulting from the production of electricity, which can reach a lifetime of the order of hundreds of thousands of years. Some technologies for their partial treatment are already known and new solutions are under active development.

However, so far, no definitive solution has been able to neutralise the radioactivity of these wastes. Currently, several projects seek to dispose of radioactive waste in a facility located in "deep geological formations" that can assess some conditions: very low permeability, low seismic activity and no important fault [70], [104]. The host rock considered for such a disposal facility in France is a Callovo-Oxfordian (COx) age rock, composed of about a half of clays, about a quarter of carbonates and another quarter of quartz [37], [143]. This argillaceous formation has been strongly compacted during its geological history. A significant threat to safety in such facilities is the large production of dihydrogen, a gas mainly due to the anaerobic corrosion of metal elements (waste containers, liners and supporting structures) and the water radiolysis. It highlights the necessity to preserve the favourable containment properties of the host rock and engineered seals for a very long time [88]. The first experimental results have shown that the gas percolation through the water-saturated COx pore-space may trigger degradation of its clay matrix [48], [106], [165]. Indeed, more detailed studies about the coupling between gas invasion and the mechanical response of the clay matrix need to be carried out. For the time being, the first theoretical/numerical models are based on the opening of a network of predefined fractures simplified in terms of shape, size, density and orientation (see [106], [144]). One of the difficulties related to the representation of pore-scales phenomena in clay rock is the multi-modal pore size distribution with a substantial amount of nano-metric pores invisible in the most up-to-date 3D imaging techniques [154]. Thus, the pore-scale studies need to compensate for the absence of the smallest pores and the lack of connectivity.

This thesis aims at improving the understanding of such gas transfer phenomena and its relation with the surrounding geological environment. In order to describe with confidence the gas migration inside and around the disposal facility over a very long time, it is crucial to use relevant transfer laws at the macroscopic scale (that would be at the same time consistent with gas transfer mechanisms at the pore-scale). Many aspects are present in a pore-scale gas migration problem. In this context, the deformation mechanisms, including damage of the clay matrix, play an essential role in interaction with the pore pressure. Indeed, a detailed study of the mechanical behaviour of the clay matrix needs to take place. So far, in the available SPH model, a simple macroscopic damage model, based on Rankine and Mohr-Coulomb criteria, has been applied to simulate both phenomena mentioned above [126]. Nevertheless, further investigations in terms of damage laws are necessary for effective implementation at the pore scale.

Although important progress achieved in the characterisation of this host rock and the coupled phenomena expected to take place therein, the response of the clay matrix is still the subject of many research. In particular, it is crucial to focus on the degradation process (in terms of damage initiation and fracture propagation) that may play an important role during the coupled phenomena. Fracture and damage constitute historically two different fields of study in solid mechanics. Fracture mechanics¹, as introduced by Griffith [71] and enhanced by Irwin [78] and Rice [142] will not be directly investigated here, but will be suitably addressed through localisation of damage. Such approach originated from the seminal work of Francfort and Marigo [65] devoted to a variational formulation of fracture mechanics. An approximation of this variational approach has been proposed by Bourdin *et al.* [30] based on Ambrosio and Tortorelli [1], [2]. Later, this approximation, known as phase-field approach, has been interpreted as the variational formulation of a class of gradient damage models [105], [128] which introduces a characteristic length in the description of the dissipation². This allows avoiding pathological mesh dependency, which occurs when local damage models are considered. Recently, extensions to dynamic conditions have been proposed in literature (see for instance [22], [28], [93]). Concerning non-local damage models, mention has to be also made of integral methods in which the local damage variable (or its conjugated force) is replaced by its non-local version (through a convolution procedure) [18], [129].

In this context, this study seeks to propose an alternative approach to damage and fracture phenomena based on non-local modelling of damage and to be able to describe the transition from damage to fracture nucleation and growth. The proposed model will mainly maintain the local formulation of the damage model, while the non-local

¹See for instance the textbook by Leblond [87].

²An alternative to this class of gradient damage model consists in introducing the characteristic length in a gradient term occurring in the stored energy as proposed by Lorentz and Andrieux [101][102].

regularisation will be made numerically through the Smoothed Particle Hydrodynamics (SPH) framework. The later is a meshless method capable of providing non-local versions to any variable, generating a non-local system. The thesis is organised as follows:

Chapter 1 will first present a literature review of the radioactive waste management context, including the most recent studies about the safety issues related to the long-term host rock evolution. The French project to dispose of radioactive waste will be introduced, focusing on the clayey rock Callovo Oxfordian (COx) expected to host this disposal facility. We will also recall the gas generation issue expected to take place therein and the gas migration through saturated pore-space of the COx. Besides, a brief overview of the numerical models most often used to simulate such coupled problems will be presented. Moreover, we will provide the previous use of the SPH method for multiphase-flow and pore-network computing. In a second part of the chapter, we will present, for each phase identified in the coupled phenomenon, the continua governing equations focusing on fluid phases and the elasticity of the clayey rock for which small and a large deformations approaches will be considered.

Chapter 2 will treat first the mathematical approaches used in the SPH method. Then, we will present an extended description of the numerical model and the main algorithms that will be used therein. The time integration schemes and the numerical improvements adopted to solve some SPH inconveniences will also be introduced. A particular emphasis will be placed on the discrete governing equations and the constitutive model of an elastic material through small and large deformation approaches. The last part of the chapter will be devoted to validation tests of the improved numerical SPH model. In particular, a vibration problem will be used to validate SPH as a local EDP solver. Our results will be additionally compared to other SPH models available in the literature.

In Chapter 3, we will explore the interpolated nature of SPH to represent higher-order interaction effects (reputed as non-local effects) that can be achieved through finite support domains of the SPH kernel function in elastic materials. In a 1D vibration problem, the numerical results will be compared to analytical lattice discrete and continua solutions: stress gradient and continualized models for different order approximations. We will investigate the capability of our numerical method to capture non-local elastic effects independently of the discretisation. Finally, we will investigate the SPH invariance using finite or infinite domain kernel functions or using stress-based and strain-based gradient formulations.

The capability of the SPH to solve coupled elasto-damage response accounting for the non-local effects due to damage will be investigated in Chapter 4. This chapter will start with a brief theoretical recall of the thermodynamics-based framework used

to model the elasto-damage response, emphasising the dissipative aspects. Moreover, particular attention will be placed on the unilateral effect of damage, allowing for the treatment of asymmetric responses between tensile and compressive loadings (as often observed for geomaterials). A 1D benchmark problem of a softening bar will be presented, providing a first characterisation of non-local responses of a damaged material. In order to investigate a 2D configuration, we will consider a simple structure consisting of a square plate containing a rigid inclusion. Quasi-static and dynamic loading conditions will be considered. For these cases, a full description of the transition from damage to fracture will be presented. Asymmetric tensile-compressive responses in the presence of non-local damage will also be discussed. Finally, an in-depth investigation of the role of the numerical parameter (the support length of the SPH kernel function) as a potential characteristic length of the material will also be presented.

In Chapter 5, we will propose a practical numerical application consisting of simulating the drainage in clayey rock. The SPH form of the fluid governing equations will be first recalled. Then, we will describe the numerical implementation used to reproduce a multiphase flow at the pore-space of a clay matrix. In the following, different cases will be considered: a purely elastic solid medium (in order to obtain the reference stress field) and an elasto-damage solid under two different confining stresses. Particular attention will be given to the damage nucleation and its transition to fracture occurrence and growth. Lastly, a two isolated pores configuration will be investigated to verify if the model can predict a percolation flow path through the numerical sample. In all clay sample applications, we will provide various analyses of damage, stress and displacement fields. The evolution of porosity, water and gas saturation in the clay sample will also be analysed.

Geological disposal of radioactive waste: managing risks from nano to macroscale

Overview: The safety assessment of a deep geological disposal facility of radioactive waste located in very low permeable clay is the global issue to which this work aims to contribute. The first chapter of this thesis is organised in two main parts: a literature review and a theoretical resume of the considered phenomena. In section 1.1, we introduce a brief context of the radioactive waste management with respect to its disposal in deep geological formations. In the following, the French project to dispose of radioactive waste is recalled, focusing on the Callovo-Oxfordian clayey rock expected to host the disposal facility. The coupled hydromechanical properties of the host rock are of high interest here. Given a substantial amount of gases generated within such disposal, a gas migration is expected to produce a multiphase flow through the water-saturated pore-space of the COx (leading to high mechanical loads on the porous matrix). In section 1.2, brief overview of experimental, theoretical and numerical studies used most often to describe phenomena related to drainage in COx samples is presented, focusing on previous use of the SPH method for multiphase-flow and pore-network computing. The section 1.3 presents the continua governing equations of fluid dynamics. Besides, we focus on the elasticity of the clayey rock for which small and a large deformations approaches are considered.

Studies in radioprotection and nuclear safety became increasingly important for spreading nuclear technologies, in particular with respect to the management of radioactive wastes. A general review of the different types of radioactive waste is presented by Ewing *et al.* [61] where the classification of different types of waste is explained taking into account their radioactivity level and lifetime (which may vary by different countries). In France, radioactive waste is classified as either Very Low-Level (VLLW), Low-Level (LLW) Intermediate-Level (ILW) or High-Level (HLW). For wastes that contain radionuclides with a half-life of fewer than 100 days, it is said to be "Very Short-Lived". It is considered "Short-Lived" with a half-life of fewer than 31 years and "Long-Lived" with a half-life of more than 31 years. Fig. 1.1 present the general management strategy of the French government to dispose of radioactive waste (see [77])

for more details) depending on its type.

Half-life	Very short-lived (less than 100 days)	Short-lived (less than 31 years)	Long-lived (more than 31 years)
Very low-level waste	Managed by radioactive decay	Dedicated surface disposal Recycling solutions (activity < 100 Bq/g)	
Low-level waste		Surface disposal	Dedicated subsurface disposal (under consideration)
Intermediate-level waste			
High-level waste		Solutions under consideration *possibly deep geological disposal	

Fig. 1.1.: Strategies of the French government for management of disposal of radioactive waste (from [77], modified).

The continuous research for alternatives for managing long-lived intermediate-level and high-level waste is at the forefront of research worldwide. In recent decades, one of the main options attracting the most nuclear power countries is the concept of deep geological disposal of radioactive waste. The present work aims at improving the understanding of phenomenological issues related to the safety of such a facility.

1.1 Deep geological disposal of radioactive waste: state of the art

Over more than sixty years, several concepts for the long term management of long-lived intermediate-level and high-level radioactive waste have been proposed. Nevertheless, the deep geological disposal is still today, the solution that presents an important degree of safety thanks to the multi-barrier concept where a part of containment strategy is based on the properties of a geological layer. Several studies suggest that low-permeability clayey formation enhanced by appropriate human-made engineering barriers (waste containers, liners, bentonite plugs and seals, ...) form a coherent multi-layer barrier system, resulting in suitable concepts for safer disposal of radioactive waste. Bernd Grambow [70] presents an analysis on the use of clay geological formations as a

host-rock for the disposal of radioactive waste based on experiences acquired in three different research sites: the Hades, Mol in Belgium (created in 1980); the Mont Terri rock laboratory in Switzerland (since 1987); and the Centre of Meuse-Haute-Marne in Bure, France (since 2004). He argues that theoretical and practical data suggest strong retention properties in clayey rocks, low water permeability and a very high retention rate for radionuclides under reducing geochemical conditions.

1.1.1 The French case: Cigéo project

In the early 90s, the French government has created the independent public agency Andra (French National Radioactive Waste Management Agency), a WMO under supervision of governmental control bodies. Andra is in charge of implementing solutions for managing radioactive waste, notably the development the French project of deep geological disposal for radioactive waste, called as Cigéo. In its present concept (see the conceptual plan in Fig. 1.2 [10]), it is planned to dispose of about 10.000 m³ of HLW and 75.000 m³ of ILW-LL. The underground facility is expected to reach about 15 km² at a depth of 500 metres and to be operated for more than 100 years (in reversible operational conditions) before being definitively closed.

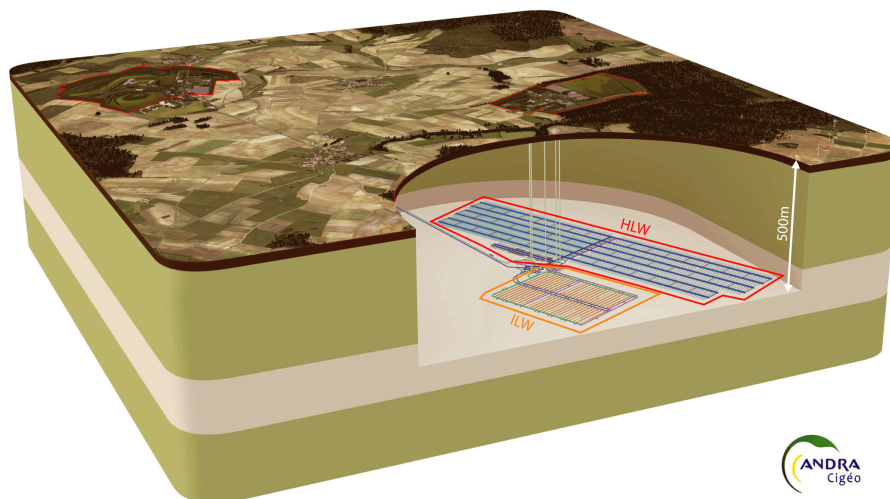


Fig. 1.2.: Cigéo deep geological facility for disposal of radioactive waste (from [10], modified) at the stage of the Safety Option Dossier, 2016.

In order to clarify the phenomenological evolution of Cigéo, the transitory processes expected inside the facility and its geological environment have been classified into six groups [9], [10], [104]:

1. Temperature increase due to exothermic waste.
2. Desaturation and resaturation cycles of the host rock due to the excavation and exploitation phases of the facility.
3. Mechanical evolution of the facility and the host rock related to the excavation, operating and post-closure phases.
4. Chemical degradation of disposal components with and without pore-water contact.
5. Chemical degradation of EDZ in contact with disposal components.
6. Production of dihydrogen due to the corrosion of metallic elements of the disposal.

The present study focuses on the coupling between topics 3 and 6. The production of dihydrogen results from the water's hydrolysis but especially from the anaerobic corrosion of metal elements placed in the disposal facility (waste containers, liners, support structures, ...) [9]. In order to better understand these issues, the host rock and its overall characteristics are presented in the following sections as well as the hydromechanical phenomena that are expected to take place therein.

1.1.2 Callovo-Oxfordian host rock

The choice of a site for geological disposal is conditioned by the fulfilment of several predefined criteria ensuring the necessary safety of such a facility. The Callovo-Oxfordian formation is currently being studied for the Cigéo project (to be located at the eastern side of the Paris basin, between the French departments of Meuse and Haute-Marne). It originates from the Jurassic period (dated from more than 150 million years ago). In the area chosen by Andra for the disposal siting, it presents an average thickness of 150 meters and can be found at a depth of about 500m [9], [10]. Fig. 1.3 illustrates the geological log of the studied site.

Regarding its sedimentary origin, the Callovo-Oxfordian is a deep indurated clayey formation mainly made up of carbonates, clay minerals and tectosilicates [37]. This composition can vary according to the sub-layers but very little laterally. The microstructure of the COx is illustrated in Fig. 1.4 by a Scanning Electron Microscopy (SEM) acquisition as well as a segmented version of each component present therein.

Carbonates (mainly calcite) vary between 22% and 37% of total volume and are responsible for the **chemical stability** of the medium, due to its condition of being in constant chemical equilibrium with carbon dioxide dissolved in water while regulating the pH of the medium [37]. The clay minerals are between 20% and 50% of the total volume

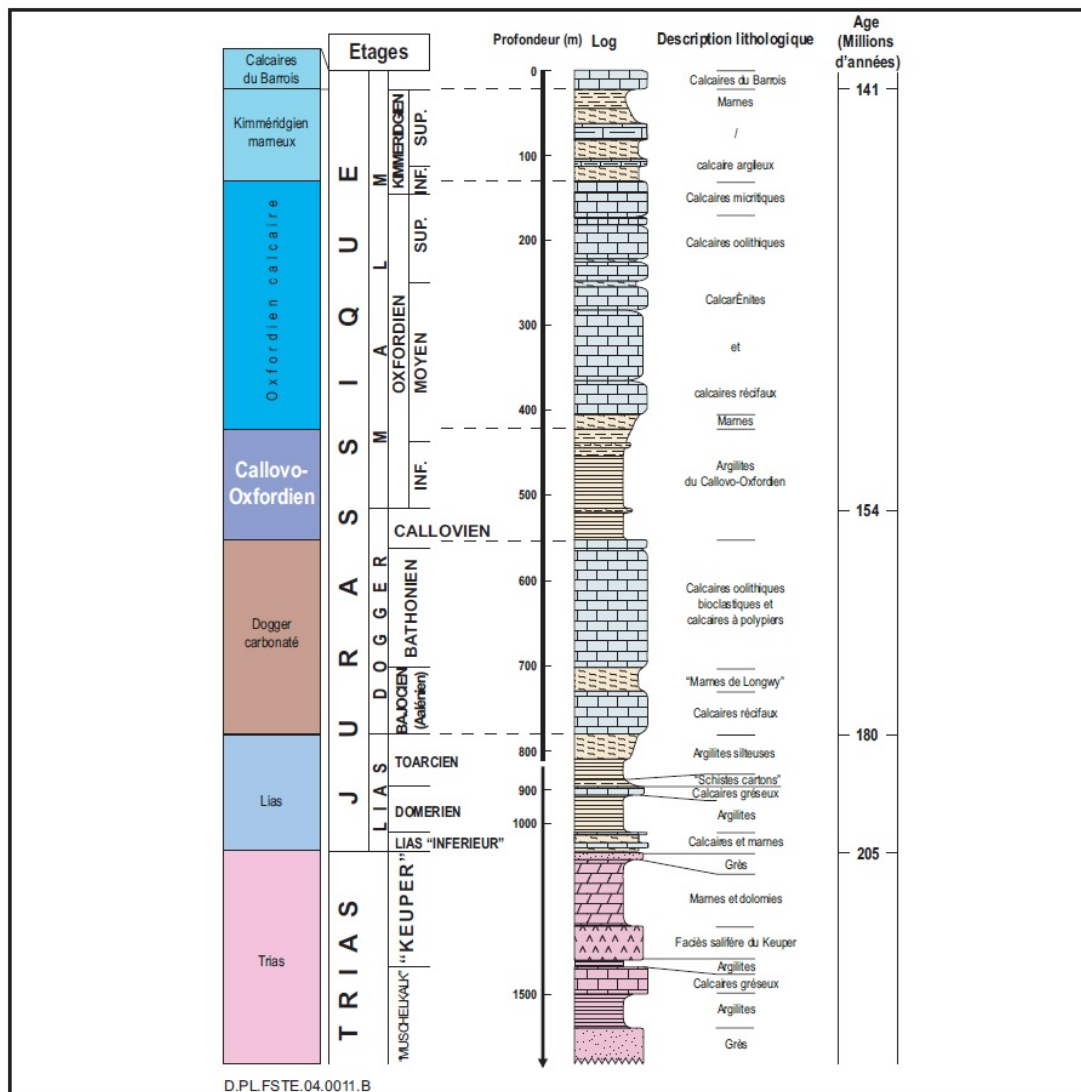


Fig. 1.3.: Geological log of the Cigéo site (from [7]).

and are mainly composed by aluminium and silica (but also K, O, Ca, Fe, Mg). Other components may be present in the COx argillite, such as organic matter (2 to 3%) or pyrite for instance. A clay matrix has the form of an assembly of platelets that have negative surface charges and can retain some important radioelements present in radioactive waste such as calcium, caesium, magnesium, sodium and strontium [37]. It is also between these sheets where H₂O molecules may be captured.

Tectosilicates, consisting mainly of feldspar and quartz, have a volume content between 10% and 40% of the total volume and have good properties for heat conduction, which is necessary for **evacuating the heat** emitted by the waste. Also, they provide good mechanical strength (stiffness) to the COx and are inert to water [37]. Otherwise, Montes *et al.* [118] and Bauer-Plaindoux *et al.* [14] observed experimentally that the presence of these mineral particles (those larger than 50µm) could favour the material cracking during drying, due to their non-deformable nature.

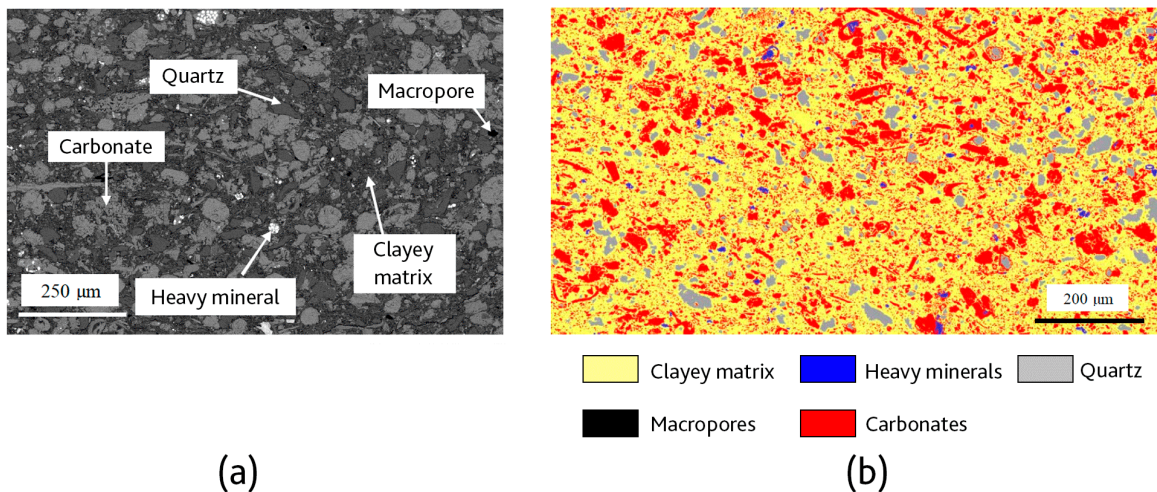


Fig. 1.4.: SEM image of COx microstructure (a) and segmented image presenting each component (b) (from [143], modified).

The current literature provides vast data describing the porous network of the COx from Meuse/Haute-Marne, its intrinsic characteristics such as its porosity or its transfer properties such as permeability [37] [8]. Mohajerani [109] shows that at least three types of porosity can be described: physical porosity, transport-related porosity and that associated with chemical interactions.

Following Andra in [7], the average porosity in COx argillite is of the order of 18%. Three classes of pores are present therein: macro-pores ($\check{d} > 100\text{nm}$), mesopores ($4\text{nm} < \check{d} < 100\text{nm}$) and micro-pores ($\check{d} < 4\text{nm}$). The materials having very few macro-pores are said to be hygroscopic, they show significant capillary forces, which result in difficult desaturation. Fig. 1.5 provides the pore size distribution obtained by a mercury intrusion test supplemented with nitrogen adsorption. The porosity consists of approximately 10% macro-pores, 86% mesopores and 4% micro-pores.

It is arranged in a network of mesopores and micropores (> 80 % of total pores), allowing water to move in response to the pressure gradients enforced by the neighbouring aquifer formations. On the other hand, these exchanges are limited by a very restrictive permeability of the clay material [7], [10]. In its natural state, due to the depth of the site (of about $\sim 500\text{m}$), the host rock is water-saturated. However, following the Cigéo concept [10], the saturated conditions will be modified during the operation phase, of about 100 years, when the whole facility and a part of its surroundings will be partially desaturated by ventilation. After this period, a process of resaturation is expected. The estimated duration of the facility's transitional period (about 100.000 years) shall depend on various factors beyond the intrinsic properties of the host rock and especially on the effect of gases, generated within the disposal (mainly dihydrogen from anoxic corrosion).

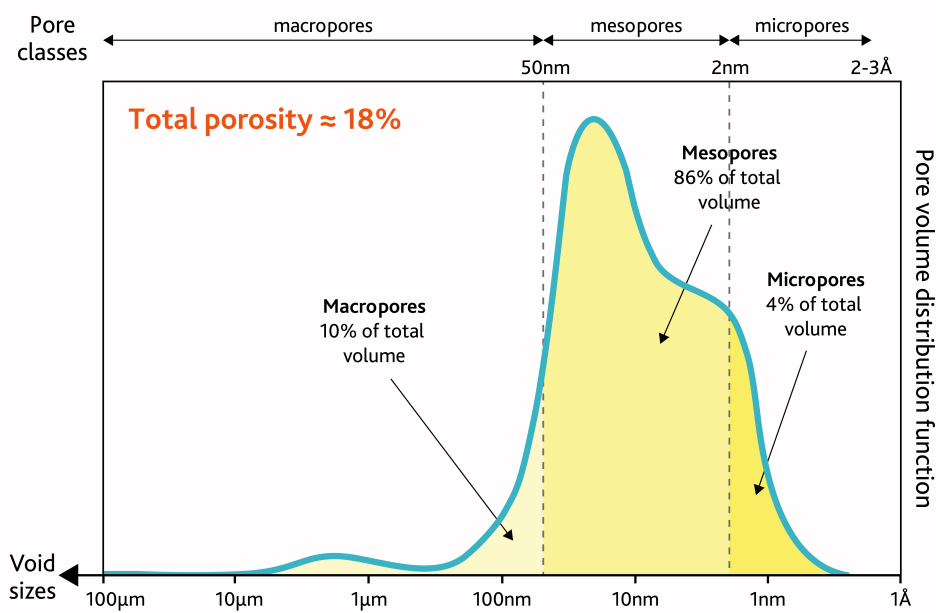


Fig. 1.5.: Pore size distribution by a mercury intrusion test supplemented with nitrogen intrusion test (from [8], modified).

In order to describe these effects, several coupled phenomena need to be taken into account.

In particular, the hydromechanical coupling has a particular interest in our work. Concerning the poroelastic properties of the COx, experimental evidences show that its compressibility parameter increases with water saturation [21], [76]. This is explained by the mineralogical analyses which show that illite-smectite inter-stratified are the most abundant minerals. Smectite, in particular, has satisfying swelling and deformability properties. Indeed, the presence of very thin smectite sheets, filling the voids between the larger aggregates, ensures that the water content variation results in modifying the thickness of the counter-ion hydration layers. It results that the clay matrix remains saturated even during global drying-resaturation cycles. Moreover, in the long term, this behaviour can ensure a degree of self-scaling of such a medium [64], [163]. Besides, Zhang *et al.* [174] carried out experiments which highlight the influence of the saturation degree on the mechanical properties of the COx argillite. They also presented the Young modulus' evolution, the maximum deformations and the maximum stresses for different values of relative humidity.

The dihydrogen generation is expected to last for about 100.000 years with the amounts produced depending on chemical conditions prevailing in different disposal parts and on the disposal concept. Fig. 1.6 shows the dihydrogen gas production over 100.000 years (see more details in [8], [88]).

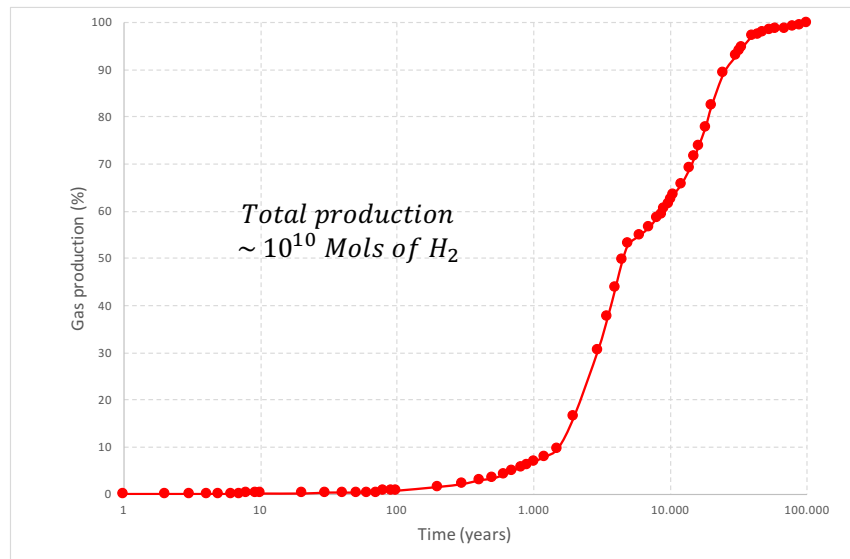


Fig. 1.6.: Dihydrogen gas production over 100.000 years (from [8], modified).

1.2 Two-phase flow coupled with mechanical load at pore scale: experimental and numerical reviews

Many research (for instance Marschall *et al.* [106]), have considered the phenomenological transport mechanisms in the low-permeability clayey formation (Opalynus clay in this case). Small differences in transport and retention properties between this rock and the Callovo-Oxfordian allow their phenomenological considerations to be almost fully transferable. Following them, the transport of gas through a very low-permeability clayey rock is controlled by its hydromechanical properties and state (*i.e.* water saturation, pore-water pressure, stress state) as well as by the gas pressure, as resumed in Fig. 1.7. It is noteworthy that Marschall *et al.* [106] introduced the idea that the transport phenomenon can be governed by the expansion of the existing pore space, generating a new flow domain and enhancing the apparent gas permeability of the host rock significantly.

Also, experimental evidence indicates that the gas percolation through saturated COx may occur by preferential pathways (which are highly unstable and partially reversible) accompanied by a local dilation of the pore space [48]. Thus, in a water-saturated host rock, the classical visco-capillary flow (usually considered and well understood) may not happen (Fig. 1.7). Many other works have presented various evidences of

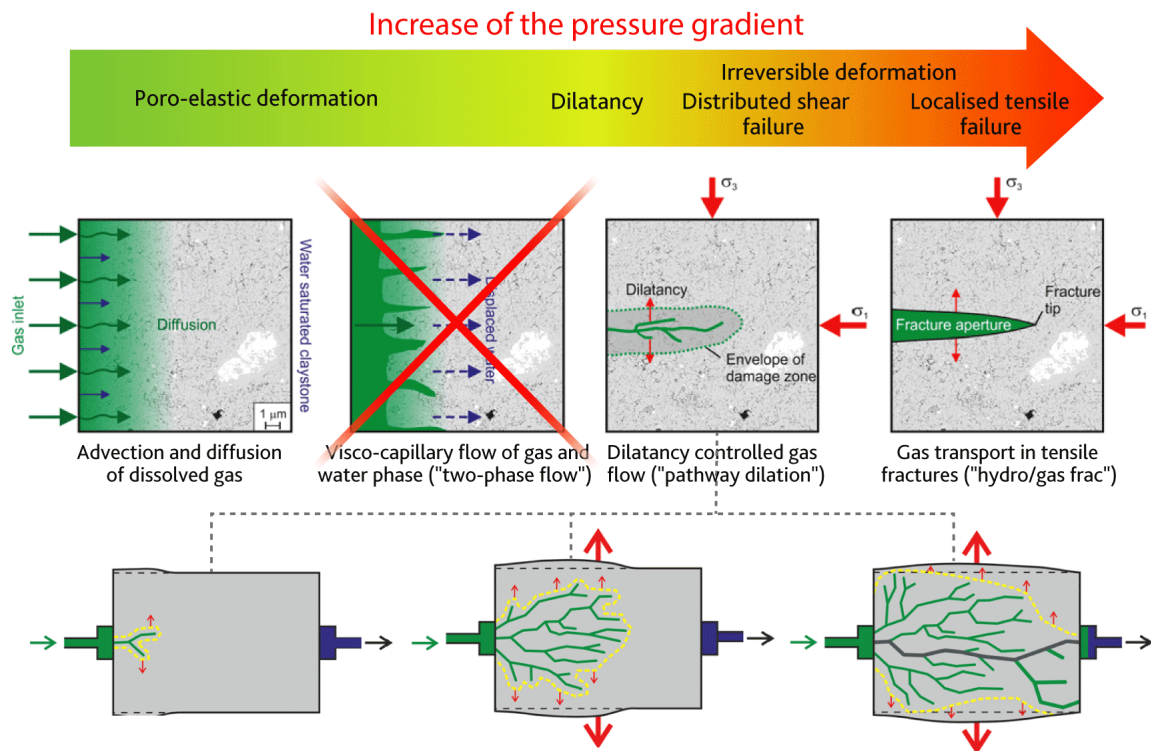


Fig. 1.7.: Gas transport processes in clayey rock: phenomenological description based on the micro-structural concept, geomechanical regime and preferential pathways evolution framework (from [106] and [48], modified).

the presence of dilatant pathways in pore-scale clay rocks [11], [13], [49], [50], [73], [153], [165]. In Fig. 1.8, we see a real-time observation of this phenomenon acquired in an experimental framework developed by Wiseall *et al.* [165]. Following these studies, once the gas pressure increases, the dilation of the pore space is observed due to gas invasion in water-saturated micro-pores, which cannot be avoided on the percolation path.

The experimental studies conducted by Marschall *et al.* [106] indicated that the pore-space dilatancy could govern the gas transport mechanism at elevated gas pressures. Besides, they highlight that the gas transport accompanied by pore-water displacement (immiscible flow) leads to a very low degree of desaturation. In the pore-scale characterisation domain, Song *et al.* [154] have carried out several experimental measures on Focused Ion Beam and Scanning Electron Microscopy imagery of the clayey matrix identifying down to 17-22 nm pore size. However, its experimental results to the Gas Breakthrough Pressure variable (1.45 – 5.3MPa) is much smaller than those obtained on intact claystone using the Peak Pore Size given by MIP simulations (7 – 14MPa). The micro-cracks generation can explain such a gap in the medium during the sample preparation. Furthermore, they conclude that the most probable gas pathways are the micro-cracks, which the breakthrough occurs by capillary digitation and the

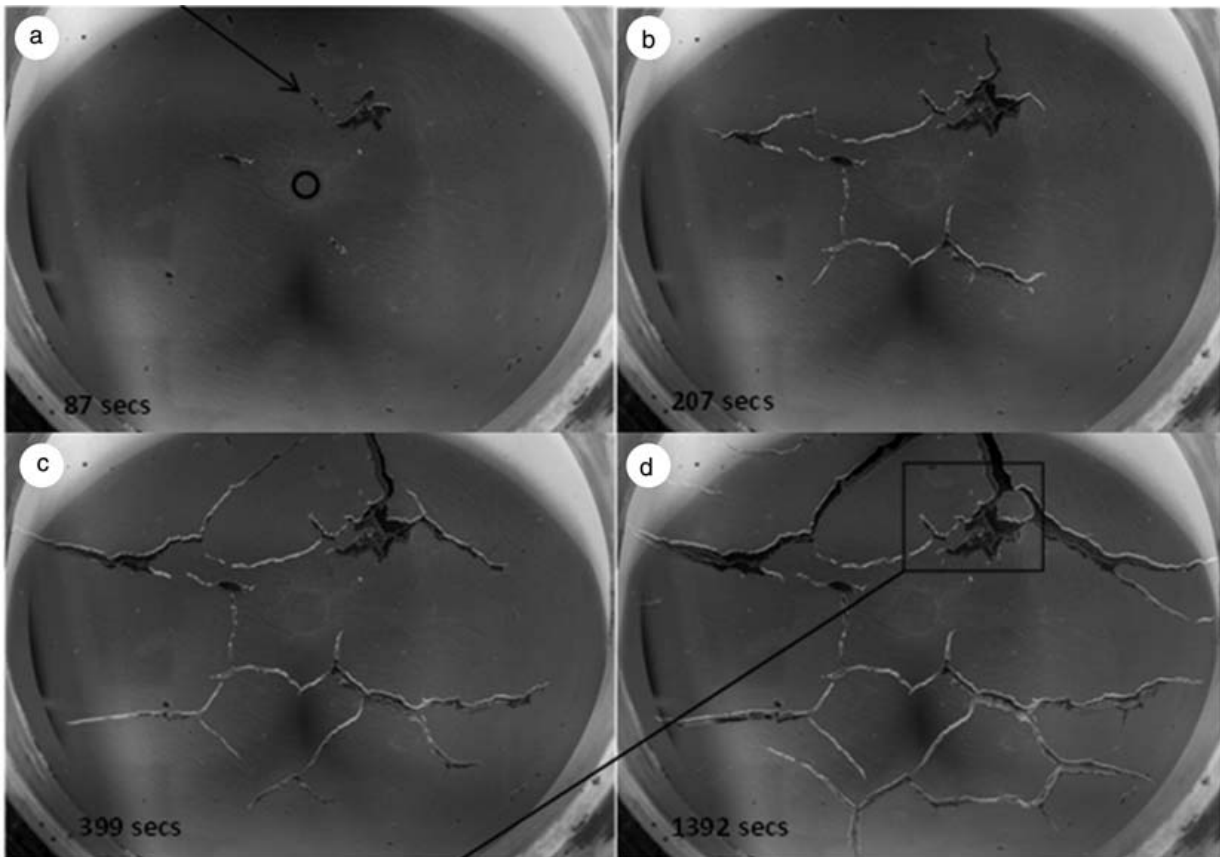


Fig. 1.8.: Adapted from Wiseall *et al.* [165] images of the evolution of dilatant pathways, chronologically, from a to d.

gas percolation does not progress homogeneously through the clayey domain. Their conclusions are on the same way to the others presented here [29], [48], [88], [104], [106].

Still another aspect of gas migration from radioactive waste disposal into an argillaceous host rock was given by Lefort [88], who investigated the hyper-slow drainage problem over thousands or even hundreds of thousands of years. [88] work postulates that such drainage problem can be governed by the generalised two-phase flow model of Darcy's law. At this point, it is quite clear that the scale size of its research does not take into account the interactions between the components at micro-scale. The quantities obtained by [88] indicate that the hyper-slow drainage operates in the vicinity of breakthrough pressure, despite the gas production rate, which is very low. His study also characterises a critical sensitivity of the model parameters due to high wetting fluid saturation which also influences the local deformation of the clayey matrix at the pore network scale caused by the gas percolating flow.

Furthermore, Lefort [88] highlights that it is widely accepted that nanoporous flow study can be done only through deformation effects of the microstructure. The experimental studies conducted by Marschall *et al.* [106] indicate the same behaviour

even on a macroscopic scale. However, the complete understanding of this coupled phenomenon in pore-scale is only a prediction carried by the set of evidence brought by several research studies so far. Lefort [88] complement that the fact that the fracturing regime becomes more or less identical with the one called as reversible dilation, as presented by Marschall *et al.* [106].

Considering the major issues to experimentally access and analyse the hydromechanical behaviour of a clayey rock at pore-scale, different numerical models were adopted to understand such coupled phenomena. For a multiphase flow occurring in a porous medium domain, the Navier-Stokes governing equations can be discretized and solved through diverse methods such as: Lattice Boltzmann [147], pore-network [86], volume-of-fluid [62], [134], finite element-finite volume [172], level-set [130] or phase-field [146].

Since the late 80s, numerical models have been used to simulate the hydrogen gas percolation through an interconnected pore network. Neimark [121] introduced a Multiscale Percolation System (MPS) model of a poly-dispersed structure with arbitrary volumetric densities and fractal properties. This model was designed to model the percolation-type transport of a fluid in a complex pore network taking into account properties such as porosity, specific surfaces, pore size distribution and fractal sizing.

Boulin [29] modelled the percolation of hydrogen gas through an interconnected pore network model. Indeed, its simulation parameters were obtained from mercury porosimetry type tests and sorption isotherms, which ultimately resulted in the characterisation of pore networks and its inter-connectivities. His research used the XDQ method to model the phenomena of percolation of hydrogen gas in a network of pores saturated with water, a phenomenon expected in deep disposal. XDQ is a tool created by Xu *et al.* [166], [167] in order to take advantage of the experimental mercury intrusion data to form a pore network with statistically equivalent transfer properties.

Carrillo *et al.* [38] recently introduced a hybrid micro-continuum approach funded in volume average principles that can be used simultaneously at two scale sizes. They treat macroscale by Darcy's Law and microscale by Navier-Stokes' equations. Zhao *et al.* [175] presented an extensive comparison of pore-scale models (Lattice Boltzmann, pore-network models, phase-field, volume-of-fluid, level-set and stochastic rotation dynamics) in order to predict the macroscopic features of unstable two-phase flows in the presence of solid inclusions. They note that although no single model can fulfil all conditions, pore-network models present the shorter computation times, and only 3D particle-based can simulate wetting films. Mehmani and Tchelepi [108] developed a pore-level multiscale method (PLMM) that successively improve the approximations of Direct Numerical Simulation (DNS) of multiphase flow. Their method split the entire

domain into sub-domains representing physical pores; in the following, they select the domains containing multiphase flow to optimise the computing. The sub-domains can be parallelised improving the computation efficiency.

Lefort [88] has attempted to explore the coupling between local mechanical flow and deformation in order to investigate the impact of porous space dilation on the gas invasion pattern and to better understand a possible dependence between breakthrough pressure and deformation. For this, a consideration of micro-mechanical effects in a pore network system consisting of solid particles linked by springs as presented in Fig. 1.9 (a) is taken into account.

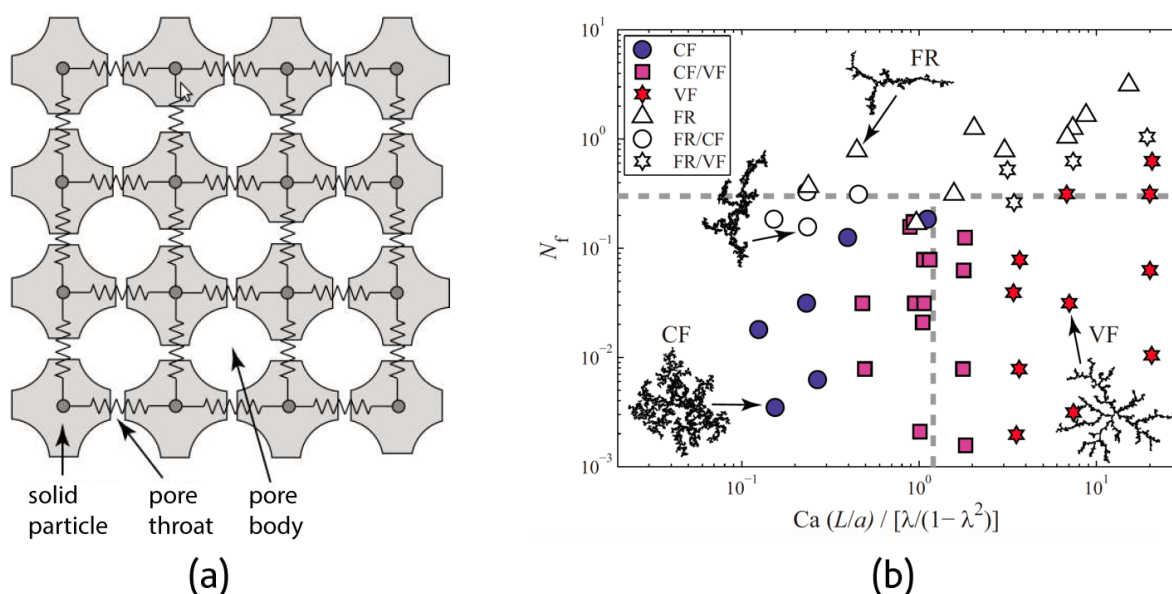


Fig. 1.9.: (a) Regular pore network system and (b) phase diagram of drainage of different invasion patterns by pore network system results (from Holtzman and Juanes [75], adapted).

The adoption of this method for the simulation of deformations in elastic media dates from the 1990s [124] when solid fracturing has also been investigated [24]. More recently, the phenomenon of drainage coupled with solid deformations has been discussed by Holtzman and Juanes [75], they proposed to characterise the drainage by a network pore system through different conditions leading to different invasion patterns (as illustrated in Fig. 1.9).

In order to numerically solve such coupled hydromechanical phenomena, this work uses a simulation code based on the Smoothed Particles Hydrodynamics (SPH) method that has been recently developed by IRSN (see [126] for more details). In the SPH domain, Xu and Fish [168] introduced an up-scaling approach for multi-porosity

media in a one-phase flow. They performed it in order to compute the local variables and integrate them at coarser scales. In a recent study, Yang *et al.* [170] used a Pairwise Force Smoothed Particle Hydrodynamics (PF-SPH) model to investigate the effect of wettability, surface tension and flow rate in a disordered and irregular shaped porous media. Sivanapillai *et al.* [151] performed SPH simulations of multiphase flow in porous network adopting a large set flow configurations. Using direct pore-scale models, they tested immiscible fluids and partial wettability configurations for large density and viscosity ratios. The continuum surface forces (CSF) provided the capillarity effects for drainage and imbibition. The influence of these phenomena on the macrostructure hydraulic properties was discussed.

In the same way, Kunz *et al.* [83] simulated, comparing with experimental data, drainage phenomena in a micro-model in dynamic and quasi-static conditions. Moreover, Tartakovsky *et al.* [157] have modelled multiphase flow, reactive transport porous media and fractured channel at pore-scale. In recent years, we observe that SPH has known essential improvements in the treatment of flow in porous media with diverse applications to simple and complex phenomena. Nevertheless, most parts of these works focus their investigations on the fluid phases and do not treat in details the response of the solid matrix or inclusions.

Over the years, the effects of cracks in porous media were a source of several studies. In a micromechanical approach of permeability-damage coupling, Dormieux and Kondo [57] presented a study on the influence of the different parameters of a fractured porous medium in the quantification of its equivalent properties from a self-consistent scheme. Their results relate the dependence of the crack opening over the equivalent macroscopic permeability. What is more, it highlights two origins of coupling between mechanical loading and effective permeability, by presenting formulations that bind Terzaghi's effective stress to crack opening and crack propagation. In mesoscale analyses of cracked porous volumes through a direct numerical approach (finite difference method), Rastiello *et al.* [137] have demonstrated the influence on the growth of mass flow and energy exchanges due to the density of a crack. For different macro and microporosity configurations, orientation and crack aperture, the interaction between the crack and the equivalent transfer properties showed nonlinear behaviours of some orders of magnitude of increase according to the crack threshold.

Pazdniakou and Dymitrowska [126] work has crucial importance in the present thesis. They seek at simulating drainage within a numerical reconstructed pore space of CO_x. In their paper, a four-phase phenomenon was simulated by an SPH approach to reproduce the drained pathways predicted in experimental studies discussed previously. All the fluid formulations, fluid-fluid and fluid-solid interactions proposed therein are adopted in this thesis. We present in the next sections several aspects of each model. Although

an extensive range of studies on macro and mesoscale coupled transfer-mechanical phenomena, a lack of studies that evaluates the damage and fracturing phenomena coupled to a multiphase flow at the microscale is observed. In the next section, we present the physical model representing such a coupled system on the pore-scale level.

1.3 Hydro-mechanical pore-scale model

This section aims at describing a physical model of the hydromechanical phenomena. Such model will be based on a 3D reconstruction of a porous media from imaging data like CT-scans, FIB-SEM, ... This is a very active research field with a significant amount of work devoted to image analysis for the extraction of poral space [80] and simulations of flow within such reconstructed structures [23], [68], [126]. Gastelum *et al.* [68] have also performed SPH simulations of a volcanic core sample after reconstructing a 3D porous space based on CT scan image data. According to the previous sections, most of the pores in COx clay have diameter of a few nanometers, nevertheless, the methods employed to obtain 3D samples are not yet capable to capture voxel smaller than about $10nm$.

In this work, we will develop our model based on FIB imaging of a COx sample of $6.545 \times 7.966 \times 1.03\mu m$ with a porosity of $3.07\% \pm 0.39\%$ and voxel size resolution of $8.49 \times 10.78 \times 10nm$ obtained from Song, Yang *et al.* [154]. Fig. 1.10a shows a 2D part of this sample followed by a conceptual version highlighting the different phases therein in Fig. 1.10b. This numerical sample was also used in [126].

Talking about the clay rocks (in the micro-scale), mineral inclusions, pores and clay matrix are well-defined and form an inhomogeneous domain, which results in the assumption of a homogeneous domain represented by a VER is only valid on a macroscopic scale. Thus, regarding at micro-scale, we consider the clay as a continuous matrix phase surrounding the pores and inclusions. Some studies showed that this medium exhibits an elastic behaviour [7], [46]. Cariou *et al.* [36] noted that such material exhibits a transversely isotropic mechanical property; however, for the sake of simplicity, the present thesis treats it as an isotropic material. Mineral inclusions are considered rigid bodies due to their low elastic properties (for instance, the Young modulus $E \sim 72GPa$ for quartz and calcite). We devote the Appendix A to resume the governing equations that treat rigid bodies.

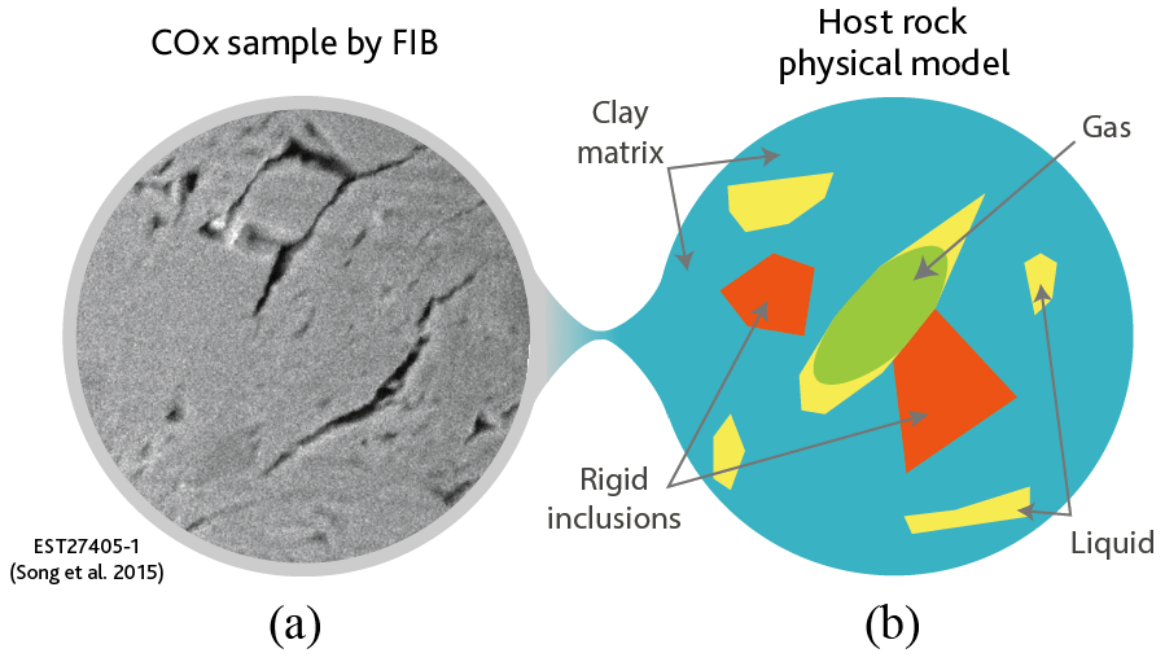


Fig. 1.10.: COx sample by FIB and physical model of the host rock.

1.3.1 Fluid phases

The scale of a domain of flow is a key variable to choose the right physical phenomena and the most adapted equations. For instance, within a few nanometers, intramolecular interactions must be taken into account, consequently, the most predictive methods are stochastic and molecular dynamics. At larger scale (from tens of nanometer to tens of micrometers), interactions between individual molecules can be neglected and the equations of Navier-Stokes for continuous fluid can be used. Finally, on macro scale, Darcy's law, with its variants, is widely used to describe a homogeneous porous media without distinction between solid and fluid parts. In this work, we are interested in at the intermediate scale. Thus, following Navier-Stokes formulations in a Lagrangian description, the conservation of mass is written as:

$$\dot{\rho} = -\rho \nabla \cdot \underline{v} \quad (1.1)$$

where ρ is the volumetric mass or density, the over-text $(\dot{\cdot})$ denotes a time derivative operator D/Dt and \underline{v} is the velocity. The momentum conservation equation in material coordinates is the following:

$$\rho \dot{\underline{v}} = -\nabla p + \nabla \cdot \left[\mu (\nabla \underline{v} + (\nabla \underline{v})^T) - \frac{2}{3} (\nabla \cdot \underline{v}) \underline{\underline{1}} \right] + \rho \underline{g} \quad (1.2)$$

with p the pressure, μ the fluid dynamic viscosity and g the gravitational acceleration. For an incompressible Newtonian fluid, the momentum equation can be simplified to:

$$\rho \dot{\underline{v}} = -\nabla p + \mu \nabla^2 \underline{v} + \rho g \quad (1.3)$$

If the thermodynamics effects can be neglected, the ideal gas equation of state, which relates pressure to density, can be written in the following form:

$$p = c^2(\rho - \rho_0) \quad (1.4)$$

where c is the sound velocity in a fluid and the subscript 0 denotes some initial value of ρ . In addition, seeking to describe the interface dynamic behaviour of a non-miscible 2-phase flow in porous media, Young-Laplace law states the pressure drop Δp for a curved interface between two fluids:

$$\Delta p = \check{\gamma} \left(\frac{1}{R_1} + \frac{1}{R_2} \right) = \check{\gamma} \nabla \cdot \underline{\vec{n}} \quad (1.5)$$

where R_1 and R_2 are the radii of curvature, $\check{\gamma}$ is the coefficient of surface tension and $\underline{\vec{n}}$ is the unit normal to the fluids interface. This phenomenon is due to the surface tension generated by the difference between the fluid properties. In order to assure the continuity of viscous stress tensor at the fluid-fluid interface, this work uses the Brackbill model [31] for calculating surface forces in a continuum approach (see for instance [96], [119]). As a first step to obtain the volumetric surface tension \check{F} , the local interface curvature $\check{\kappa}$ is defined as:

$$\check{\kappa} = -\nabla \cdot \underline{\vec{n}} = \frac{\underline{n} \cdot \nabla \|\underline{n}\|}{\|\underline{n}\|^2} - \frac{\nabla \cdot \underline{n}}{\|\underline{n}\|} \quad (1.6)$$

where the unit normal $\underline{\vec{n}}$ is expressed by the color function $\check{c}(\underline{r})$, so that:

$$\underline{\vec{n}} = \frac{\nabla \check{c}(\underline{r})}{\|\nabla \check{c}(\underline{r})\|} \quad (1.7)$$

with

$$\check{c}(\underline{r}) = \frac{\rho_l(\underline{r}) - \rho_g(\underline{r})}{\rho_l(\underline{r}) + \rho_g(\underline{r})} \quad (1.8)$$

with the subscripts l and g related, respectively, to liquid and gas phases. Hence, from (Eqs. 1.5, 1.6 and 1.7) we obtain the volumetric surface tension force $\check{F}(\underline{r})$, such as:

$$\check{F}(\underline{r}) = \frac{1}{2} \check{\gamma} \check{\kappa} \underline{\vec{n}} \quad (1.9)$$

and by assigning a color function value to the solid phase, the contact angle θ can be obtained as:

$$\theta = \arccos(\check{c}(\underline{r})) \quad (1.10)$$

Near the solid contact interface, these values are employed to compute the local unit normal.

1.3.2 Elastic solid phase

In continuum mechanics, the initial ($t = 0$) and the current ($t > 0$) configurations of a defined domain can be significantly different when the deformations and/or rotations are not infinitesimally smaller than the dimension of that domain (Fig. 1.11 presents a mixed deformation and rotation transformation). The finite strain theory is able to describe such phenomenon [145]. Otherwise, when this transformation is small to keep the constitutive properties of the material close enough to a constant value, the equations that reproduce this phenomenon can be simplified, resulting in the infinitesimal strain theory or small deformations theory. The present section recalls the elastic equations for both approaches in addition to mass and energy conservation in Eulerian and Lagrangian descriptions.

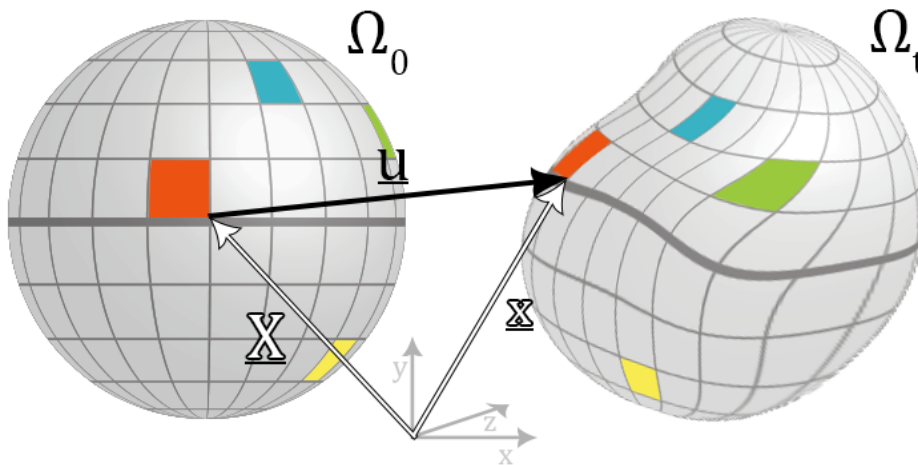


Fig. 1.11.: General 3D rotation and deformation of a domain from an initial to a current state.

1.3.2.1 Large deformations in continuum mechanics

Let us first consider a domain with initial state Ω_0 (particle initial position \underline{X}) and current state Ω_t (current position \underline{x}). In the Lagrangian description, the displacement field at time t is defined as $\underline{u}(\underline{X}, t) = \underline{x} - \underline{X}$. The deformation gradient tensor $\underline{\underline{F}}(\underline{X}, t)$ reads:

$$\underline{\underline{F}} = \frac{\partial \underline{x}}{\partial \underline{X}} = \mathbb{1} + \nabla_0 \underline{u} \quad (1.11)$$

Here, the subscript 0 denotes the reference configuration. The volumetric change between an initial infinitesimal volume $d\Omega_0$ and the corresponding volume in the current state $d\Omega_t$ is calculated using the Jacobian of $\underline{\underline{F}}$, such as:

$$d\Omega_t = J d\Omega_0 = \det(\underline{\underline{F}}) d\Omega_0 \quad (1.12)$$

Thus, considering a 3D large deformations framework in Lagrangian description, we write the Green-Lagrange strain tensor $\underline{\underline{\epsilon}}_{GL}$ which is defined, respectively, as a function of the deformation gradient or of the gradient of the displacement field, such as [145]:

$$\underline{\underline{\epsilon}}_{GL}(\underline{\underline{F}}) = \frac{1}{2}(\underline{\underline{F}}^T \cdot \underline{\underline{F}} - \mathbb{1}) \quad (1.13)$$

$$\underline{\underline{\epsilon}}_{GL}(\underline{u}) = \frac{1}{2}((\nabla \underline{u})^T + \nabla \underline{u} + (\nabla \underline{u})^T \nabla \underline{u}) \quad (1.14)$$

Considering now motion in spatial coordinates, described by means of the Eulerian velocity field $\underline{v}(\underline{x}, t)$, one gets:

$$\underline{\underline{d}} = \frac{1}{2}(\nabla \underline{v}^T + \nabla \underline{v}) \quad (1.15)$$

Note that the transpose of the gradient of the Eulerian velocity, $\underline{\underline{l}}(\underline{x}, t) = (\nabla \underline{v}(\underline{x}, t))^T$, is such that:

$$\underline{\underline{l}} = \dot{\underline{\underline{F}}} \cdot \underline{\underline{F}}^{-1} \quad (1.16)$$

Note also that the rate of the Green-Lagrange deformation tensor is related to the Eulerian rate of deformation by:

$$\dot{\underline{\underline{\epsilon}}}_{GL} = \underline{\underline{F}}^T \cdot \underline{\underline{d}} \cdot \underline{\underline{F}} \quad (1.17)$$

Let's recall the mass conservation law:

$$\rho = J^{-1} \rho_0 \quad (1.18)$$

where ρ is the material density in the current state. Besides, the mass conservation equation in spatial coordinates is given by:

$$\dot{\rho} + \nabla \cdot (\rho \underline{v}) = 0 \quad (1.19)$$

1.3.2.2 Governing equations and Saint Venant-Kirchhoff constitutive model

We remain in a Lagrangian description in order to resume an approach that results in a simple way to obtain a linear law which relates the strain and the stress tensors

in large deformations. We introduce the initial configuration of the thermodynamics potential (or strain energy density). For a material with elastic response without thermal effects, we present such potential in the case of Saint Venant-Kirchhoff constitutive model:

$$\rho_0 w = \frac{1}{2} \underline{\underline{\epsilon}}_{GL} : \mathbb{C}_0 : \underline{\underline{\epsilon}}_{GL} \quad (1.20)$$

with $(:)$ the double dot product. In next chapters the role of the tensor \mathbb{C} will be discussed. Here, the large deformations Saint Venant-Kirchhoff state law can be obtained by the second Piola-Kirchhoff stress tensor $\underline{\underline{S}}$ by means of the partial derivative of (Eq. 1.20) with respect of its state variable $\underline{\underline{\epsilon}}_{GL}$.

$$\underline{\underline{S}} = \rho_0 \frac{\partial w}{\partial \underline{\underline{\epsilon}}_{GL}} = \mathbb{C}_0 : \underline{\underline{\epsilon}}_{GL} \quad (1.21)$$

In the following, the time derivative of the thermodynamics potential reads:

$$\rho_0 \dot{w} = \rho_0 \frac{\partial w}{\partial t} = \rho_0 \frac{\partial w}{\partial \underline{\underline{\epsilon}}_{GL}} : \dot{\underline{\underline{\epsilon}}}_{GL} \quad (1.22)$$

In order to obtain the internal energy conservation, we can introduce (Eq. 1.21) into (Eq. 1.22) or obtain an alternative form in function of the first Piola-Kirchhoff stress tensor $\underline{\underline{P}}$ from the identity $\underline{\underline{S}} = \underline{\underline{F}}^{-1} \cdot \underline{\underline{P}}$ [45], such as:

$$\rho_0 \dot{w} = \underline{\underline{S}} : \dot{\underline{\underline{\epsilon}}}_{GL} = \underline{\underline{P}} : \dot{\underline{\underline{F}}} \quad (1.23)$$

Moreover, the momentum conservation in a Lagrangian description is given through the 1st Piola-Kirchhoff stress tensor:

$$\rho_0 \ddot{\underline{\underline{u}}} = -\nabla_0 \cdot \underline{\underline{P}} \quad (1.24)$$

We resume the governing equations obtained in a Lagrangian description as:

$$\begin{cases} \rho = J^{-1} \rho_0 & (1.25) \\ \ddot{\underline{\underline{u}}} = -\frac{1}{\rho_0} (\nabla_0 \cdot \underline{\underline{P}}) & (1.26) \\ \dot{w} = \frac{1}{\rho_0} (\underline{\underline{P}} : \dot{\underline{\underline{F}}}) & (1.27) \end{cases}$$

This section showed the pertinence of the Piola-Kirchhoff stress tensors in such a large deformation model. The linear constitutive model St. Venant-Kirchhoff (SVK) is easy to compute and it leads to the resolution of the governing equations after the transformation from $\underline{\underline{S}}$ to $\underline{\underline{P}}$.

1.3.2.3 Governing equations and linear elastic law

In the hypothesis of small perturbations, the second order term of the displacement gradient (*i.e.* $(\nabla \underline{u})^T \nabla \underline{u}$) is significantly smaller compared to first order terms and are neglected. The differences between material coordinates (*i.e.* Lagrangian description) or spatial coordinates (*i.e.* Eulerian description) are close enough to be neglected (*i.e.* $\det \underline{F} \approx 1$), it results in the adoption of the spatial coordinates. We consider the mechanical behaviour by neglecting the high order gradient terms in the Green-Lagrange strain tensor (Eq. 1.14), which results in the strain tensor $\underline{\underline{\varepsilon}}$ that is given as a function of the displacement vector field \underline{u} following spatial coordinates:

$$\underline{\underline{\varepsilon}} \simeq \frac{1}{2} \left((\nabla \underline{u})^T + \nabla \underline{u} \right) \quad (1.28)$$

The rate of the deformation tensor $\underline{\underline{\dot{\varepsilon}}}$ is revisited from (Eq. 1.15):

$$\underline{\underline{\dot{\varepsilon}}} = \frac{1}{2} \left((\nabla \underline{v})^T + \nabla \underline{v} \right) \quad (1.29)$$

We resume now a small deformations counterpart of finite strain theory procedure where the thermodynamics potential in current configuration reads:

$$\rho w(\underline{\underline{\varepsilon}}) = \frac{1}{2} \underline{\underline{\varepsilon}} : \mathbb{C} : \underline{\underline{\varepsilon}} \quad (1.30)$$

Here, the state law can be obtained by means of the partial derivative of (Eq. 1.30), such that:

$$\underline{\underline{\sigma}} = \rho \frac{\partial w}{\partial \underline{\underline{\varepsilon}}} = \mathbb{C} : \underline{\underline{\varepsilon}} \quad (1.31)$$

The time derivative of the thermodynamics potential is given by:

$$\rho \dot{w} = \rho \frac{\partial w}{\partial t} = \rho \frac{\partial w}{\partial \underline{\underline{\varepsilon}}} : \underline{\underline{\dot{\varepsilon}}} \quad (1.32)$$

Thus, the internal energy conservation can be obtained also in a similar way and reads:

$$\rho \dot{w} = \underline{\underline{\sigma}} : \underline{\underline{\dot{\varepsilon}}} \quad (1.33)$$

Finally, the governing equations accounting for infinitesimal deformation hypothesis can be resumed as:

$$\left\{ \begin{array}{l} \dot{\rho} = -\nabla \cdot (\rho \underline{v}) \end{array} \right. \quad (1.34)$$

$$\left\{ \begin{array}{l} \underline{\underline{\dot{u}}} = \frac{1}{\rho} (\nabla \cdot \underline{\underline{\sigma}}) \end{array} \right. \quad (1.35)$$

$$\left\{ \begin{array}{l} \dot{w} = \frac{1}{\rho} (\underline{\underline{\sigma}} : \underline{\underline{\dot{\varepsilon}}}) \end{array} \right. \quad (1.36)$$

1.3.3 Interface conditions

The boundary conditions imposed between different phases must assure the correct behaviour at the interfaces. As a general rule, the velocity of the two different phases at the contact point \underline{r} will be supposed to be the same.

$$\underline{v}_a(\underline{r}_i) = \underline{v}_b(\underline{r}_i) \quad (1.37)$$

where the subscripts a and b designate different phases. Such condition provides both no-slip boundary condition and non penetration of the phases, that must be reinforced by the continuity of normal stresses at the interface solid-fluid.

$$\underline{\underline{\sigma}}_s \cdot \underline{\vec{n}}_s = -\underline{\underline{\sigma}}_f \cdot \underline{\vec{n}}_f \quad (1.38)$$

where the subscripts s and f indicate solid and fluid phases, respectively. Therefore, the continuity of normal stresses is also imposed between the solid rigid-elastic phases.

Concluding remarks

This chapter has provided a brief overall context of radioactive waste disposal in a deep geological layer, focusing on the French project Cigéo. The transport phenomena at the pore-scale of the clayey Callovo-Oxfordian formation was introduced as a major aspect due mainly to a significant expected gas generation within such disposal facility over hundreds of thousands years. This literature review has highlighted theoretical, experimental and numerical research in the domain mainly in macro and mesoscale. A lack of studies about the characterisation of the gas preferential pathway at pore-scale was identified. To contribute to this point, we have presented a physical model treating a few main phases present in this medium.

Numerical modelling: Smoothed Particle Hydrodynamics

Overview: This chapter summarises the use of the Smoothed Particle Hydrodynamics method to simulate the hydromechanical phenomena introduced previously. We present the mathematical formulation of the numerical method (section 2.1), followed by the time integration schemes (2.2) and the numerical improvements adopted to solve some well-known SPH drawbacks (2.3). In the following, we focus on the elastic body dynamics in small and large deformation approaches (2.4). Two tests are performed: a validation of the SPH improvements (2.5) and a vibration problem used to validate SPH as a local EDP solver (2.6).

This thesis uses a simulation code based on the Smoothed Particles Hydrodynamics (SPH) method that has been recently developed by IRSN [126]. In a 3D porous medium sample (Fig. 2.1), this code can solve in the same formalism the solid elastic deformation (clayey matrix), the rigid bodies movement (carbonate or silicate inclusions), the two-phase flow (water and hydrogen) taking into account the surface tension and the capillary forces as well as interactions between all phases. SPH was firstly introduced independently by Gingold and Monaghan [69] and Lucy [103] for treatment of astrophysical problems. Nowadays, it is widely applied to simulate, with good accuracy, transient dynamics with important deformation of studied domains. Many different applications for fluid flow [35], [96], [97], [161] and multiphase flows [42], [112], [157] were made. The implementations for applications in solid dynamics have been explored since the 1990s after the structural mechanics framework introduced by Libersky and Petscheck [94], [95]. Applications in the field of heat transfer [41], [42], mass transport [84] and reactive transport [157] have also been already published. The SPH method can be described as a Lagrangian particle method that does not use a fixed mesh and where a local behaviour results from an interpolation over all particles present in an elementary area. The interpolation weights are calculated using a smoothing function (also called kernel function), defined as non-zero in a zone of radius defined by the so-called smoothing length $\hat{\kappa}h$ (Fig. 2.2 - a). Thus, a weighted sum of values of a variable at the neighbouring points results in the approximation of this variable at a central point (Fig. 2.2 - b). The mesh-free character of the SPH method can provide an important advantage in treating pore-space dilation resulting from multiphase flow related to gas percolation. Moreover, SPH structure can easily profit from CUDA technology for massively parallel computations on GPU to improve its computational efficiency.

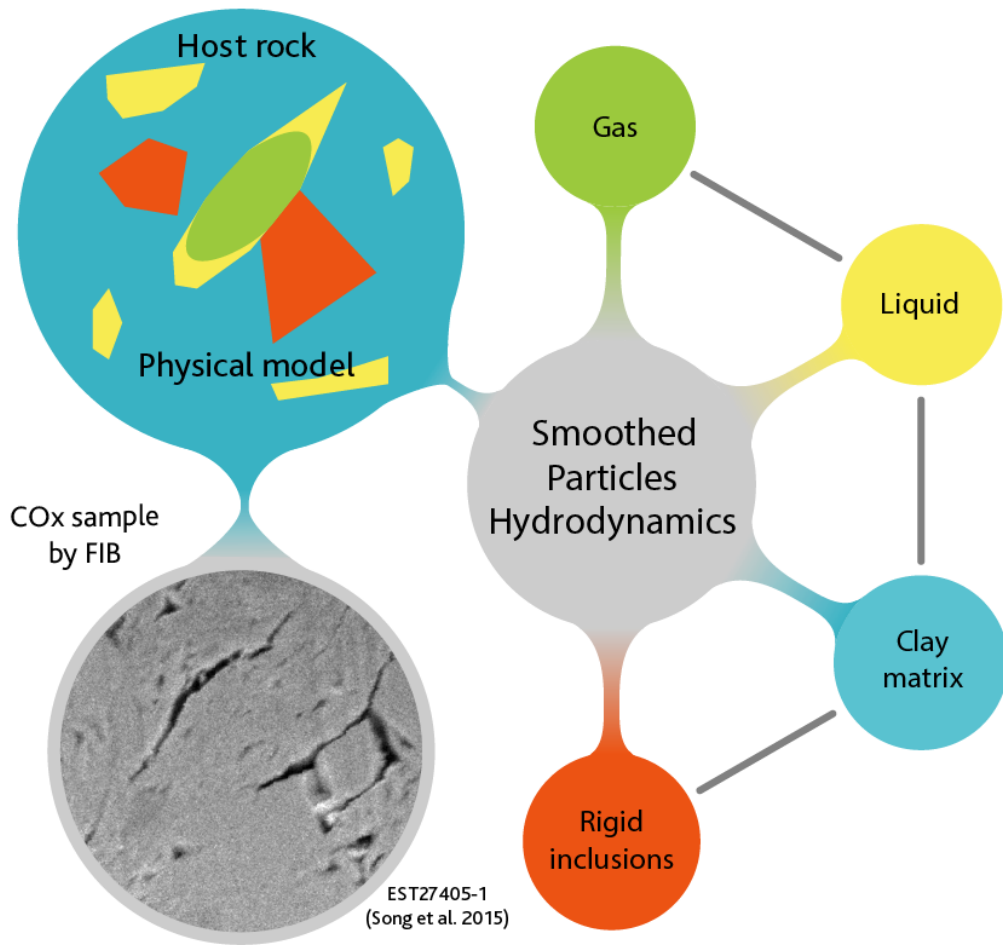


Fig. 2.1.: Physical configuration and SPH numerical model

2.1 Mathematical formulation: smoothed functions and derivatives

The SPH method is based on approximation of a given function f by means of a continuous integral in the spirit of what is possible with the Dirac's delta function δ .

$$f(\underline{r}) = \int_{\Omega} f(\underline{r}') \delta(\underline{r} - \underline{r}') d\underline{r}' \quad (2.1)$$

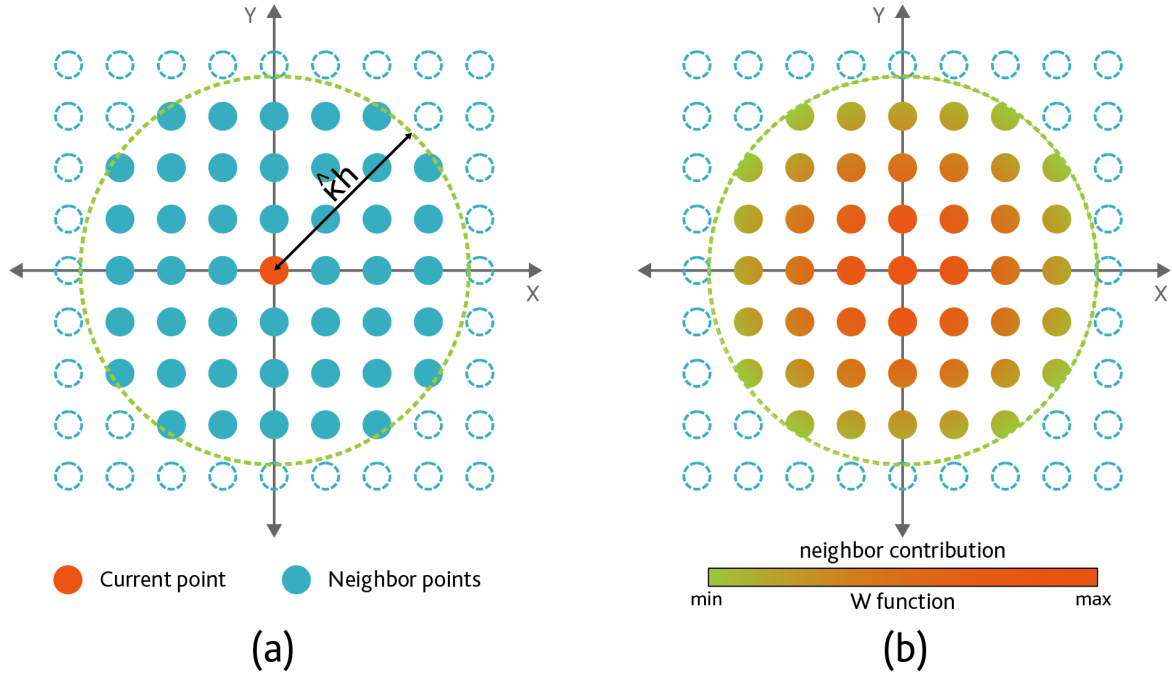


Fig. 2.2.: An conceptual example of 2D SPH ordered material points with the smoothing length \hat{h} around a central point (a) and the neighbour contribution weights following a smoothing function W (b)

where \underline{r} and \underline{r}' are the spatial coordinate vectors within the integral domain Ω . Dirac [56] introduced the delta function in his quantum mechanics work considering the following properties:

$$\delta(\underline{r} - \underline{r}') = \begin{cases} \infty, & \underline{r} = \underline{r}' \\ 0, & \underline{r} \neq \underline{r}' \end{cases} \quad (2.2a)$$

$$\int_{-\infty}^{\infty} \delta(\underline{r}) d\underline{r} = 1 \quad (2.2b)$$

Because of the singular shape of δ , it cannot be used in discrete numerical models. For such applications, this function should be replaced by an appropriate smoothing or kernel function $W(\underline{r} - \underline{r}', h)$. Thus, the kernel approximation of $f(\underline{r})$ reads:

$$\langle f(\underline{r}) \rangle = \int_{\Omega} f(\underline{r}') W(\underline{r} - \underline{r}', h) d\underline{r}' + err_{smoothing} \quad (2.3)$$

where the angle brackets $\langle \cdot \rangle$ denote a kernel approximation, h is called a smoothing scale (or smoothing length) that is related to the support-length of the function W by a multiplier \hat{k} and $err_{smoothing} = \mathcal{O}(h^2)$ is the approximation error [97] generated by this

convolution procedure. W function has unit of inverse of volume. Thus, the smoothed form of function (2.3) can be defined as:

$$\langle f_S(\underline{r}) \rangle = \int_{\Omega} f(\underline{r}') W(\underline{r} - \underline{r}', h) d\underline{r}' \quad (2.4)$$

For the sake of convenience, in later sections we omit the angle brackets $\langle \cdot \rangle$ operator and the subscript S and note the smoothed value of $f(\underline{r})$ by:

$$f(\underline{r}) \doteq \int_{\Omega} f(\underline{r}') W(\underline{r} - \underline{r}', h) d\underline{r}' \quad (2.5)$$

To ensure the method consistency, kernel functions must fulfil several conditions. In particular, it must converge to the Dirac function when h tends to zero:

$$\lim_{h \rightarrow 0} W(\underline{r} - \underline{r}', h) = \delta(\underline{r} - \underline{r}') \quad (2.6)$$

and be normalised:

$$\int_{\Omega} W(\underline{r} - \underline{r}', h) d\underline{r}' = 1 \quad (2.7)$$

Additionally, W must be positively defined and even in order to give the same weights for all points located at the same distance. Usually, functions with a compact support are used, such that:

$$W(\underline{r} - \underline{r}', h) = 0 \quad \text{when } |\underline{r} - \underline{r}'| > \hat{\kappa}h \quad (2.8)$$

where $\hat{\kappa}$ is a multiplier related to the smoothing function and $\hat{\kappa}h$ gives the support length. Furthermore, the choice of W should allow the conservation of angular and linear momentum, which is ensured by the following condition:

$$\int_{\Omega} (\underline{r} - \underline{r}') W(\underline{r} - \underline{r}', h) d\underline{r}' = 0 \quad (2.9)$$

2.1.1 Types of smoothing functions

In order to achieve accuracy and numerical stability in different applications, several smoothing functions are proposed following different needs. Two most frequent smoothing functions are recalled here: the Gaussian function introduced by Gingold [69] is an excellent option to obtain accuracy and stability, but has a high computation cost given its infinite support form, which requires the adoption of periodic boundary conditions.

$$W(q, h) = \left(\frac{1}{h\sqrt{\pi}} \right)^d \exp \left[- \left(\frac{q}{h} \right)^2 \right] \quad (2.10)$$

where $q = \|\underline{x} - \underline{x}'\|$ and \hat{d} represents the spatial dimension. For computational convenience, smoothing functions are often represented by polynomial forms. Among the most common formulations are the quadratic and cubic spline functions [97] which are frequently employed in hydrodynamics (see more in [117]). The following cubic B-spline smoothing function first introduced by Monaghan and Lattanzio [113] is used in most cases in the present work.

$$W(q, h) = \frac{M}{h^{\hat{d}}} \begin{cases} \frac{2}{3} - (\frac{q}{h})^2 + \frac{1}{2}(\frac{q}{h})^3 & \text{if } 0 \leq q < h \\ \frac{1}{6}(2 - \frac{q}{h})^3 & \text{if } h \leq q < 2h \\ 0 & \text{if } q \geq 2h \end{cases} \quad (2.11)$$

where M is a factor equal to 1, $15/7\pi$ and $3/2\pi$ for 1D, 2D and 3D respectively. For convenience, we will call this function just "spline function". The size of the support is $\lambda = \hat{\kappa}h = 2h$ for spline function and for Gaussian function, it is defined arbitrary as $\lambda = \hat{\kappa}h = 2\sqrt{2}h$ (see [51], [162] for more details).

2.1.2 Kernel interpolation

In order to exemplify the theoretical base of the SPH method, a simple case of spatial regression is presented in Fig 2.3. A data set composed of 200 points is randomly generated following $f(x) = \tan(x)$ shape with a standard deviation of $1/4$.

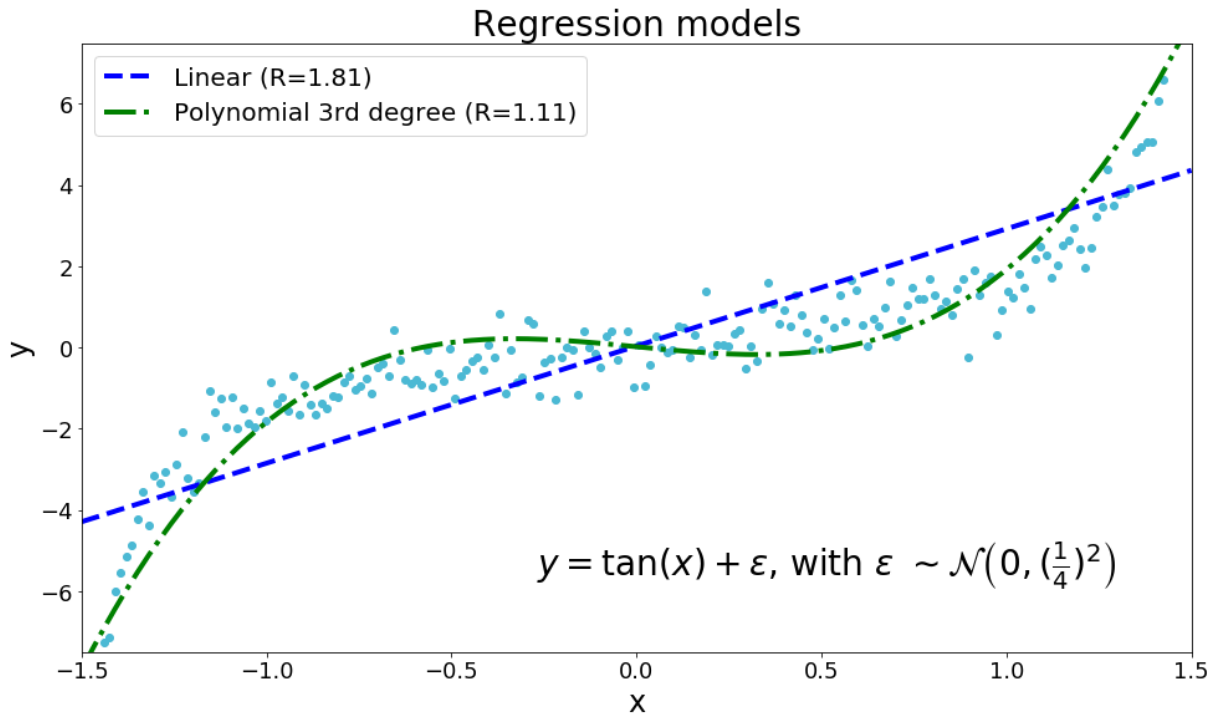


Fig. 2.3.: Randomly generated data following $f(x) = \tan(x)$ with a standard deviation of $1/4$ and its linear and polynomial regressions.

Here, R is the root-mean-square deviation of each regression form. Two well known regression methods (linear and polynomial) are showed, but following the root-mean-square deviation (R) they do not give an optimal fit on this data set. Another method is the regression by a cubic spline kernel function (Eq. 2.11), where a support domain ($\hat{\kappa}h$) determines the size of the area of influence used to compute an average point by a weighted sum. In this exercise, we adopt $\hat{\kappa} = 1$. Fig. 2.4 shows that such method with a too small scale length ($h = 0.05$) leads to an over-fitted regression, represented by an important variation of the fit derivative.

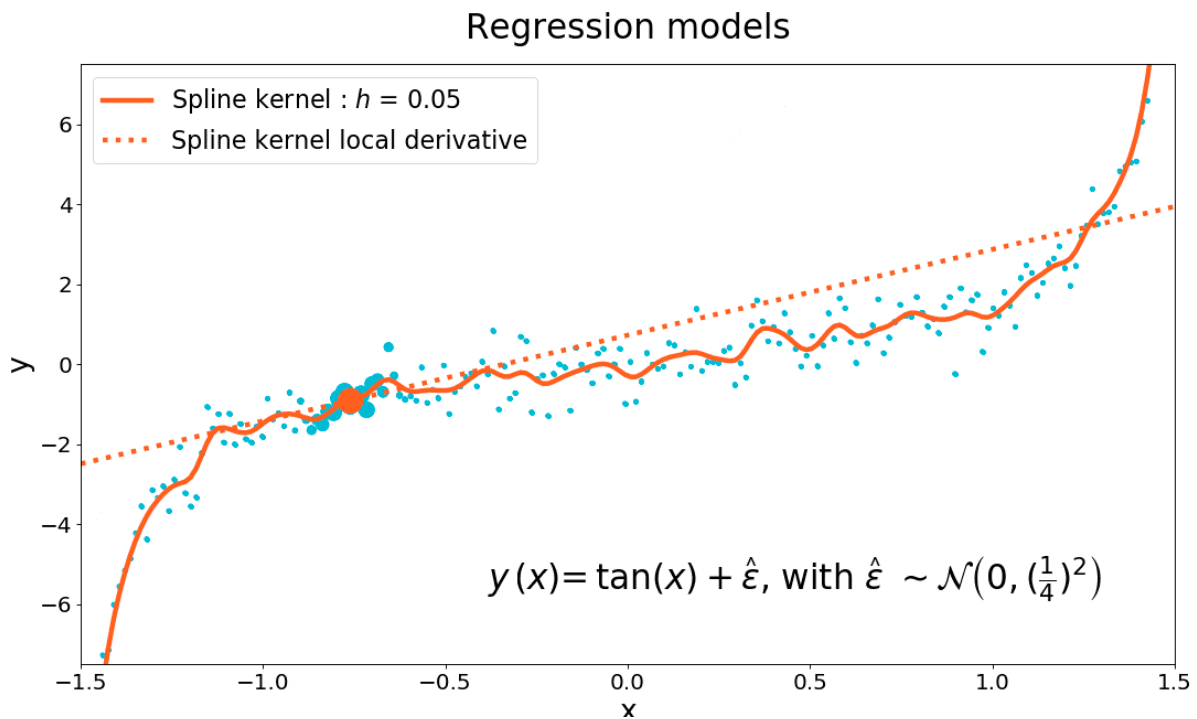


Fig. 2.4.: Randomly generated data following $f(x) = \tan(x)$ with a standard deviation of $1/4$ and its cubic spline kernel regression with $h = 0.05$.

Otherwise, when we adopt an over sized kernel scale length ($h = 2$) in Fig. 2.5, this regression tends to a linear regression. Thus, seeking to optimally fit ($R \sim 1.00$) the data set through the cubic spline kernel regression, we choose by calibration an "optimal" value of $h = 0.46$. We present in Fig. 2.6 the set of linear, polynomial and the "optimal" cubic spline kernel regressions. Although the regression by kernel interpolation has higher computational cost, it presents an interesting property linking two different scales, which is called a non-local effect. This capability of SPH has a key role in its use as a PDE solver.

Regression models

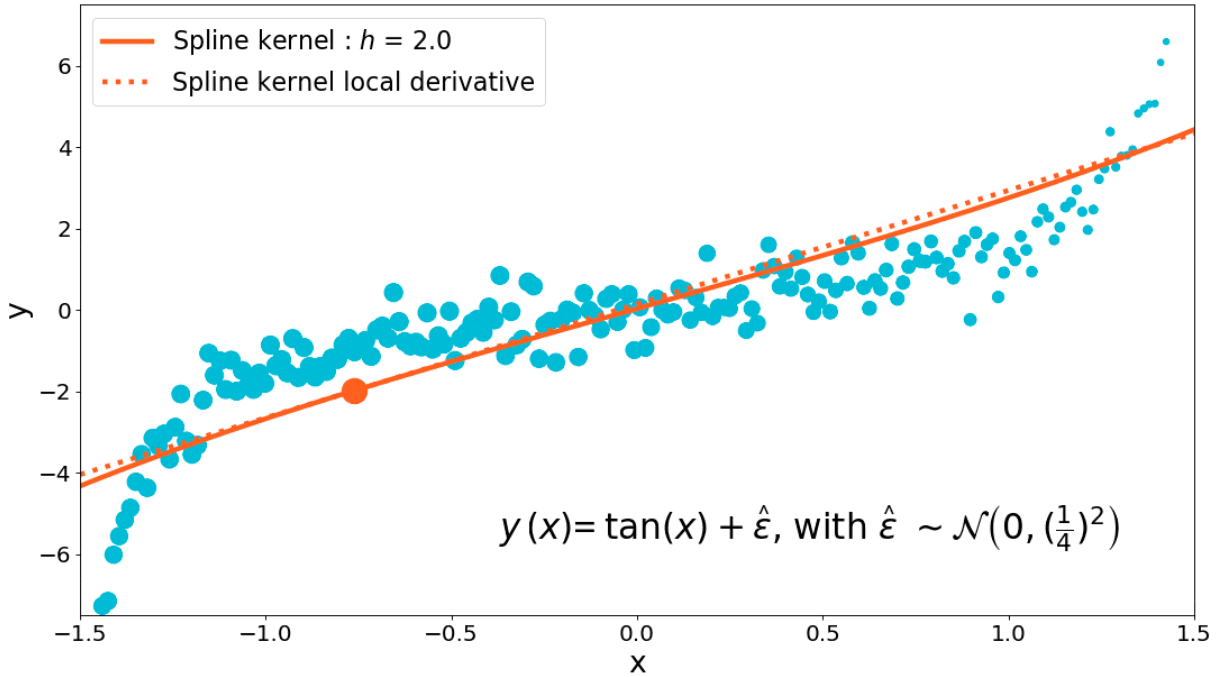


Fig. 2.5.: Randomly generated data following $f(x) = \tan(x)$ with a standard deviation of $1/4$ and its cubic spline kernel size of $h = 2$.

Regression models

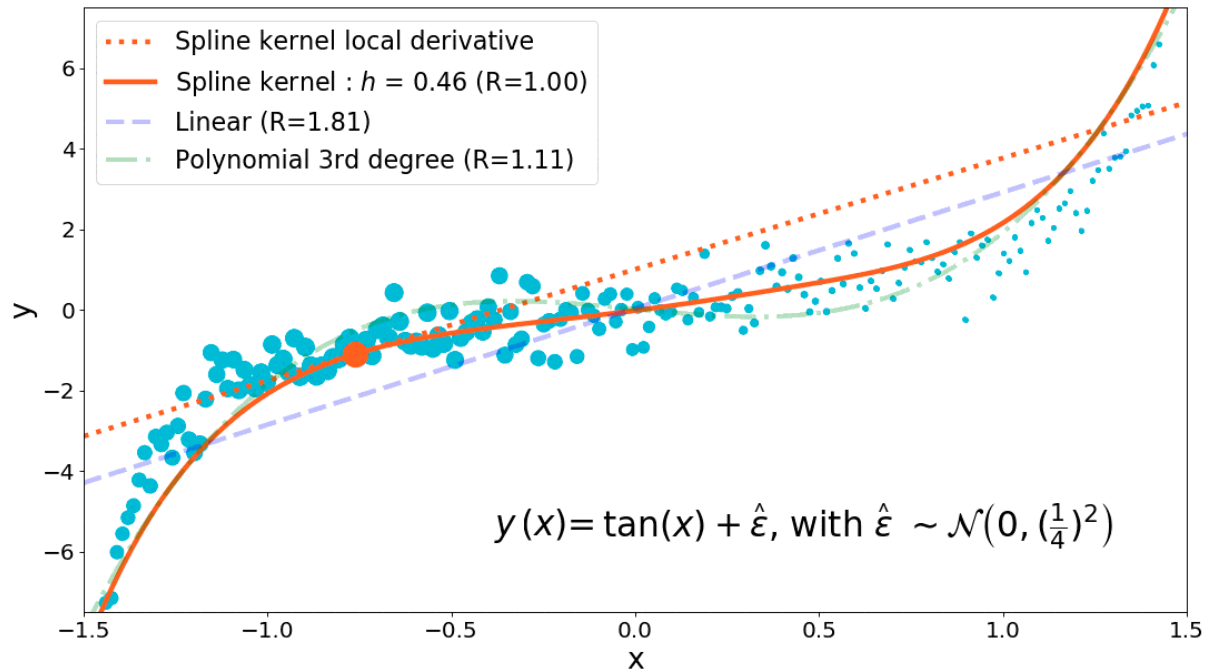


Fig. 2.6.: Randomly generated data following $f(x) = \tan(x)$ with a standard deviation of $1/4$ and its linear and polynomial and optimal cubic spline kernel ($h = 0.46$) regressions.

2.1.3 Kernel derivatives continuous approximation

This subsection presents some different ways to construct derivatives in SPH method. The approach to be adopted will depend on what is the most suitable for a problem that we are seeking to solve.

2.1.3.1 First derivatives approximation

The approximation of the gradient of a vector function can be obtained by replacing $f(\underline{r})$ by $\nabla f(\underline{r})$ in (Eq. 2.5):

$$\nabla f(\underline{r}) = \int_{\Omega} [\nabla f(\underline{r}')] W(\underline{r} - \underline{r}', h) d\underline{r}' \quad (2.12)$$

Consider f as a vector field and Φ as a scalar field, we apply the following gradient product identity:

$$\nabla (\Phi f) = \Phi (\nabla f) + f \otimes \nabla (\Phi) \quad (2.13)$$

with \otimes the outer product between two vector fields. Hence, introducing (Eq. 2.13) into (Eq. 2.12), where $f = f(\underline{r}')$ and $\Phi = W(\underline{r} - \underline{r}', h)$:

$$\nabla f(\underline{r}) = \int_{\Omega} \nabla \cdot [f(\underline{r}') W(\underline{r} - \underline{r}', h)] d\underline{r}' - \int_{\Omega} f(\underline{r}') \otimes \nabla [W(\underline{r} - \underline{r}', h)] d\underline{r}' \quad (2.14)$$

We apply the generalised Stokes theorem [39] in order to solve the first integral term in the right-hand side of (Eq. 2.14). It relates the volume Ω integral to its surface a integral, in a way that:

$$\int_{\Omega} \nabla \cdot [f(\underline{r}') W(\underline{r} - \underline{r}', h)] d\underline{r}' = \int_{\partial\Omega} f(\underline{r}') W(\underline{r} - \underline{r}', h) da \quad (2.15)$$

Considering the compact support condition presented in (Eq. 2.8), W is equal to zero on the surface of the support and outside. Although Gaussian kernel function has no compact support, W tends to zero when $\underline{r} - \underline{r}'$ tends to infinity and in SPH configuration (Eq. 2.15) vanishes. As a result, the gradient approximation (Eq. 2.14) becomes:

$$\nabla f(\underline{r}) = - \int_{\Omega} f(\underline{r}') \otimes \nabla W(\underline{r} - \underline{r}', h) d\underline{r}' \quad (2.16)$$

The previous procedure to obtain the SPH gradient is similar to the development proposed by Liu and Liu [97] in order to obtain the approximation of the divergence of a vector field. We recall it by introducing $\nabla \cdot f(\underline{r})$ into (Eq. 2.5):

$$\nabla \cdot f(\underline{r}) = \int_{\Omega} [\nabla \cdot f(\underline{r}')] W(\underline{r} - \underline{r}', h) d\underline{r}' \quad (2.17)$$

Consider the following identity of the divergence of the product of a vector field f and a scalar field Φ :

$$\nabla \cdot (\Phi f) = \Phi (\nabla \cdot f) + f \cdot \nabla (\Phi) \quad (2.18)$$

we use the Gauss theorem to obtain the divergence approximation:

$$\nabla \cdot f(\underline{r}) = - \int_{\Omega} f(\underline{r}') \cdot \nabla W(\underline{r} - \underline{r}', h) d\underline{r}' \quad (2.19)$$

Thus, based on these approximations of gradient and divergence, in the following sections we present different ways to compute higher order derivatives.

2.1.3.2 Second order derivatives approximation

We obtain directly a second order derivative in SPH form by applying twice the gradient procedure in (Eq. 2.5) as recalled in last subsection:

$$\frac{\partial^2 f(\underline{r})}{\partial x^2} = \int_{\Omega} f(\underline{r}') \cdot \nabla^2 W(\underline{r} - \underline{r}', h) d\underline{r}' \quad (2.20)$$

where $\nabla^2 W(\underline{r} - \underline{r}', h)$ is the Laplacian of the kernel function. This direct form presents some drawbacks as stated by Monaghan *et al.* [117]: the Laplacian value depends on the second derivative sign, which may generate non-physical phenomena such as heat transfer from cold to hot domain. This form is also very sensitive to material point disorder.

Thus, we recall here the integral approximation of the second derivative by using Taylor series expansion as proposed by [33], [34]. In a general divergence form considering two vector fields $\Phi(\underline{r})$ and $f(\underline{r})$:

$$\nabla \cdot (\Phi(\underline{r}) \nabla f(\underline{r})) + \mathcal{O}(h^2) = \int_{\Omega} [\Phi(\underline{r}) + \Phi(\underline{r}')] [f(\underline{r}) - f(\underline{r}')] \frac{\nabla W(\underline{r} - \underline{r}', h)}{(\underline{r} - \underline{r}')} d\underline{r}' \quad (2.21)$$

where the gradient of the kernel function will be rewritten as proposed by Monaghan *et al.* [117]:

$$\nabla W(\underline{r} - \underline{r}', h) = (\underline{r} - \underline{r}') \cdot \mathcal{F}(|\underline{r} - \underline{r}'|) \quad (2.22)$$

Thus, introducing (Eq. 2.22) into (Eq. 2.21) we obtain a new $\nabla W(\underline{r} - \underline{r}', h)$ form:

$$\nabla \cdot (\Phi(\underline{r}) \nabla f(\underline{r})) = \int_{\Omega} [\Phi(\underline{r}) + \Phi(\underline{r}')] [f(\underline{r}) - f(\underline{r}')] \mathcal{F}(|\underline{r} - \underline{r}'|) d\underline{r}' \quad (2.23)$$

For a 1D configuration, if we consider a second derivative of a field vector f and a constant field $\Phi = 1$, (Eq. 2.23) becomes:

$$\frac{\partial^2 f(r)}{\partial x^2} = \int_{\Omega} 2[f(r) - f(r')] \mathcal{F}(|r - r'|) dr' \quad (2.24)$$

Since \mathcal{F} is a scalar function with $\mathcal{F} \leq 0$, it implies that if $f(r) < f(r')$, then $\partial f(r)/\partial r > 0$ and inversely, if $f(r) > f(r') \implies \partial f(r)/\partial r < 0$ [117]. This construction corrects the second derivative sign issue.

Bi-dimensional configuration:

By using the same procedure with two vector fields $\Phi(\underline{r})$ and $f(\underline{r})$, Monaghan *et al.* [117] obtained the following 2D second order derivative form:

$$\nabla \cdot (\Phi(\underline{r})\nabla f(\underline{r})) + \mathcal{O}(h^2) = \mathcal{J}_{xx} + \mathcal{J}_{yy} \quad (2.25)$$

where \mathcal{J} are second derivative integrals and their subscripts denote spatial derivatives, such that:

$$\frac{\partial^2 \mathcal{J}}{\partial \alpha \partial \gamma} = \int_{\Omega} \frac{\Delta \alpha \Delta \gamma}{(\Delta r)^2} [\Phi(\underline{r}) + \Phi(\underline{r}')][f(\underline{r}) - f(\underline{r}')] \mathcal{F}(|\underline{r} - \underline{r}'|) d\underline{r}' \quad (2.26)$$

where Δ indicates the distance between points following the spatial dimensions α and γ and Δr is the norm of the vector \underline{r} . Expanding $\Phi(\underline{r})$ and $f(\underline{r})$ to a second order Taylor series, (Eq. 2.26) becomes:

$$\mathcal{J}_{xx} = \Phi \left(\frac{3}{4} f_{xx} + \frac{1}{4} f_{yy} \right) + \frac{3}{4} \Phi_x f_x + \frac{1}{4} \Phi_y f_y \quad (2.27a)$$

$$\mathcal{J}_{yy} = \Phi \left(\frac{1}{4} f_{xx} + \frac{3}{4} f_{yy} \right) + \frac{1}{4} \Phi_x f_x + \frac{3}{4} \Phi_y f_y \quad (2.27b)$$

$$\mathcal{J}_{xy} = \mathcal{J}_{yx} = \frac{1}{4} (2\Phi f_{xy} + \Phi_y f_x + \Phi_x f_y) \quad (2.27c)$$

By adopting a constant field $\Phi = 1$ the second derivative of a field vector f in (Eq. 2.25) simplifies to:

$$\frac{\partial^2 f(\underline{r})}{\partial \alpha \partial \gamma} = \int_{\Omega} \left[4 \frac{\Delta \alpha \Delta \gamma}{(\Delta r)^2} - \delta^{\alpha \gamma} \right] [f(\underline{r}) - f(\underline{r}')] \mathcal{F}(|\underline{r} - \underline{r}'|) d\underline{r}' \quad (2.28)$$

Three-dimensional configuration:

A similar procedure in 3D configuration requires adding a term \mathcal{J}_{zz} into (Eq. 2.25) (see Espanol and Revenga [60] for more details). The second derivative integrals $\mathcal{J}_{\alpha\gamma}$ can be obtained from (Eq. 2.26). Hence, expanding $\Phi(\underline{r})$ and $f(\underline{r})$ in the second

order Taylor series, the second partial derivatives (\mathcal{J}_{xx} , \mathcal{J}_{yy} and \mathcal{J}_{zz}) have similar forms and all mixed derivatives (e.g. \mathcal{J}_{xy}) have also similar expressions:

$$\mathcal{J}_{xx} = \Phi \left(\frac{3}{5} f_{xx} + \frac{1}{5} f_{yy} + \frac{1}{5} f_{zz} \right) + \frac{3}{5} \Phi_x f_x + \frac{1}{5} \Phi_y f_y + \frac{1}{5} \Phi_z f_z \quad (2.29a)$$

$$\mathcal{J}_{xy} = \frac{2}{5} \Phi_x f_{xy} + \frac{1}{5} \Phi_x f_y + \frac{1}{5} \Phi_y f_x \quad (2.29b)$$

In a 3D configuration the general form of second derivative (obtained with $\Phi = 1$) is given by:

$$\frac{\partial^2 f(\underline{r})}{\partial \alpha \partial \gamma} = \int_{\Omega} \left[5 \frac{\Delta \alpha \Delta \gamma}{(\Delta r)^2} - \delta^{\alpha \gamma} \right] [f(\underline{r}) - f(\underline{r}')] \mathcal{F}(|\underline{r} - \underline{r}'|) d\underline{r}' \quad (2.30)$$

2.1.4 SPH discrete approximation

We note that most of SPH literature adopts the nomenclature "particle" instead of "material points" when talking about the spatial discretisation, which is evident given the fact that the term "particle" is part of the name of this numerical method. Although this nomenclature is more appropriate for fluid mechanics, where the Lagrangian unit of small volume of fluids is represented by the evolution of a SPH "particle", the same is not true in solid mechanics where SPH points are simply the initially selected locations within a continuous medium. The notation of "material points" also stresses the mathematical character of SPH method, which can be seen as a mere solver of any PDE where no "particles" are meant to be present.

In the following, our numerical method seeks to discretise a continuum domain by a set of material points that can be ordered (Fig. 2.2) or not (Fig. 2.7). The properties of a given material point (subscript a) are computed by means of a weighted sum over its neighbourhood points (denoted by the subscript b). The points do not have fixed or determined shape, however they are associated with volumes that determined from the density and mass of a point:

$$V_a = \frac{m_a}{\rho_a} \quad (2.31)$$

where V , m and ρ are, respectively, the volume, the mass and the density at the material point a . Any continuous integral can be approximated by a summation from 1 to \hat{N} , where \hat{N} is the number of material points inside the domain determined by support length of the kernel function W . The approximation at a material point of the $f(\underline{r})$ function as presented in (2.5) is thus given by:

$$f(\underline{r}_a) = \sum_{b=1}^{\hat{N}} f(\underline{r}_b) W(\underline{r}_a - \underline{r}_b, h) V_b = \sum_{b=1}^{\hat{N}} \frac{m_b}{\rho_b} f(\underline{r}_b) W(\underline{r}_a - \underline{r}_b, h) \quad (2.32)$$

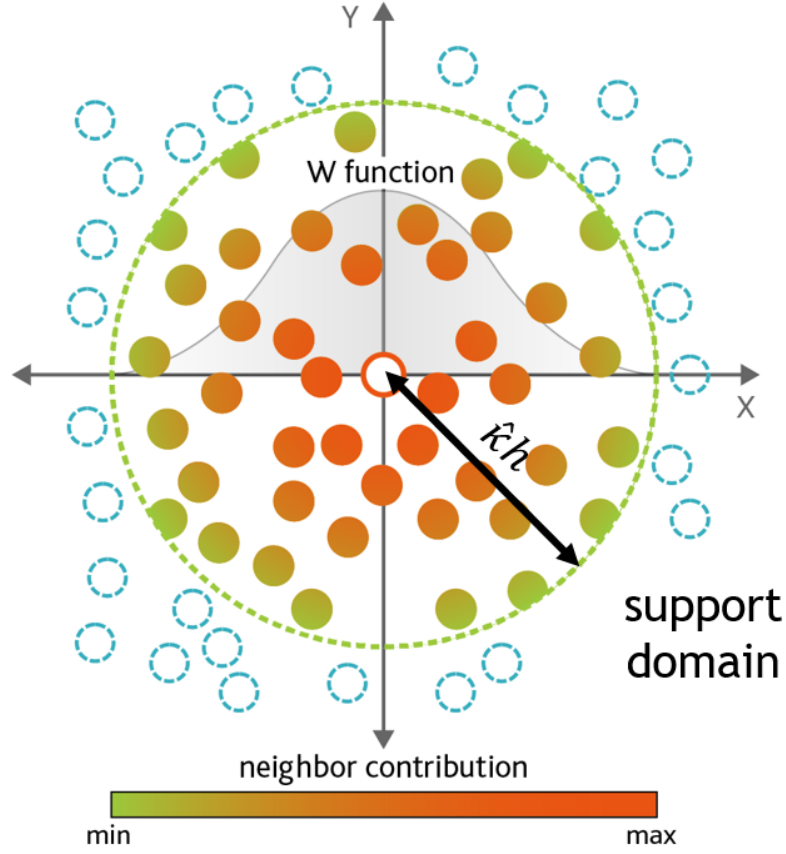


Fig. 2.7.: 2D SPH disordered material points, the smoothing scale h and the neighbour contribution weight following a smoothing function W

The sum approximation of continuous integrals presented above generates an estimation error $err_{integral} = \mathcal{O}(\frac{\Delta}{h})$, with Δ the length scale characterising the average distance between the particles [157]. For the sake of simplicity, the kernel function W will be denoted as W_{ab} for $W(\underline{r}_a - \underline{r}_b, h)$. Since W is an even function, it is evident that $W_{ab} = W_{ba}$. Thus, the SPH approximation of a function f now reads:

$$f(\underline{r}_a) = \sum_{b=1}^{\hat{N}} \frac{m_b}{\rho_b} f(\underline{r}_b) W_{ab} \quad (2.33)$$

First derivative approximations

A similar procedure adopted to approximate a continuous $f(\underline{r})$ function by its discrete version $f(\underline{r}_a)$ is used here to obtain the SPH form of the gradient of a function f presented in (Eq. 2.16):

$$\nabla f(\underline{r}_a) = - \sum_{b=1}^{\hat{N}} \frac{m_b}{\rho_b} f(\underline{r}_b) \otimes \nabla_b W_{ab} = \sum_{b=1}^{\hat{N}} \frac{m_b}{\rho_b} f(\underline{r}_b) \otimes \nabla_a W_{ab} \quad (2.34)$$

Similarly, the SPH divergence operator of a function f reads:

$$\nabla \cdot f(\underline{r}_a) = - \sum_{b=1}^{\hat{N}} \frac{m_b}{\rho_b} f(\underline{r}_b) \cdot \nabla_b W_{ab} = \sum_{b=1}^{\hat{N}} \frac{m_b}{\rho_b} f(\underline{r}_b) \cdot \nabla_a W_{ab} \quad (2.35)$$

The change of signs in (Eqs. 2.34 and 2.35) is explained since W is an even function $\nabla_a W_{ab} = -\nabla_b W_{ab}$ and $\nabla_b W_{ba} = -\nabla_a W_{ba}$. In addition, the identity between $\nabla_a W_{ab}$ and \mathcal{F}_{ab} based in (Eq. 2.22) was detailed by Monaghan *et al.* [117] as follows:

$$\nabla_a W_{ab} = \frac{(\underline{r}_a - \underline{r}_b)}{r_{ab}} \frac{\partial W(r_{ab}, h)}{\partial r_{ab}} = \underline{r}_{ab} \mathcal{F}_{ab} \quad (2.36)$$

with

$$r_{ab} = |\underline{r}_a - \underline{r}_b| \quad (2.37)$$

and

$$\mathcal{F}(r_{ab}) = \frac{1}{r_{ab}} \frac{\partial W(r_{ab}, h)}{\partial r_{ab}} \quad (2.38)$$

Monaghan *et al.* [117] recalled that the exact derivatives found by SPH does not vanish if f is a constant function. In order to fix this issue and to increase the accuracy of gradient calculations we can reuse (Eq. 2.13) in the following form:

$$\nabla f = \frac{1}{\Phi} [\nabla (\Phi f) - f \otimes \nabla \Phi] \quad (2.39)$$

Using (Eq. 2.39), various gradient expressions can be proposed by introducing (Eq. 2.39) into (Eq. 2.34) for different functions Φ (see [117], [157]), for instance:

$$\nabla f(\underline{r}_a) = \sum_{b=1}^{\hat{N}} \frac{m_b}{\rho_b} [f(\underline{r}_b) - f(\underline{r}_a)] \otimes \nabla_a W_{ab} \quad \text{with} \quad \Phi = 1 \quad (2.40a)$$

$$\nabla f(\underline{r}_a) = \frac{1}{\rho_a} \sum_{b=1}^{\hat{N}} m_b [f(\underline{r}_b) - f(\underline{r}_a)] \otimes \nabla_a W_{ab} \quad \text{with} \quad \Phi = \rho \quad (2.40b)$$

$$\nabla f(\underline{r}_a) = \rho_a \sum_{b=1}^{\hat{N}} m_b \left[\frac{f(\underline{r}_b)}{\rho_b^2} + \frac{f(\underline{r}_a)}{\rho_a^2} \right] \otimes \nabla_a W_{ab} \quad \text{with} \quad \Phi = \frac{1}{\rho} \quad (2.40c)$$

For the divergence operator, after (Eq. 2.18), we can similarly use:

$$\nabla \cdot f = \frac{1}{\Phi} [\nabla \cdot (\Phi f) - f \cdot \nabla \Phi] \quad (2.41)$$

Several divergence operator forms are also found after introducing (Eq. 2.41) into (Eq. 2.35) for different values of Φ :

$$\nabla \cdot f(\underline{r}_a) = \sum_{b=1}^{\hat{N}} \frac{m_b}{\rho_b} [f(\underline{r}_b) - f(\underline{r}_a)] \cdot \nabla_a W_{ab} \quad \text{with } \Phi = 1 \quad (2.42a)$$

$$\nabla \cdot f(\underline{r}_a) = \frac{1}{\rho_a} \sum_{b=1}^{\hat{N}} m_b [f(\underline{r}_b) - f(\underline{r}_a)] \cdot \nabla_a W_{ab} \quad \text{with } \Phi = \rho \quad (2.42b)$$

$$\nabla \cdot f(\underline{r}_a) = \rho_a \sum_{b=1}^{\hat{N}} m_b \left[\frac{f(\underline{r}_b)}{\rho_b^2} + \frac{f(\underline{r}_a)}{\rho_a^2} \right] \cdot \nabla_a W_{ab} \quad \text{with } \Phi = \frac{1}{\rho} \quad (2.42c)$$

The forms in Eqs. 2.40c and 2.42c are called as symmetrical formulations [171].

Second derivative approximations

Since the first and second derivatives have similar continuous forms, their approximations in a SPH discrete forms follow exactly the same procedure. The second order derivative (Eq. 2.17) in discrete SPH form reads:

$$\nabla^2 f(\underline{r}_a) = \sum_{b=1}^{\hat{N}} \frac{m_b}{\rho_b} f(\underline{r}_b) \cdot \nabla_b^2 W_{ab} \quad (2.43)$$

Because of increased complexity, we present here the SPH forms based on the integral approximation of the second derivative through Taylor series expansion. Consider two functions f and Φ , the SPH expression for (Eq. 2.23) becomes:

$$\nabla \cdot (\Phi(\underline{r}_a) \nabla f(\underline{r}_a)) = \sum_{b=1}^{\hat{N}} \frac{m_b}{\rho_b} [\Phi(\underline{r}_a) + \Phi(\underline{r}_b)] [f(\underline{r}_a) - f(\underline{r}_b)] \mathcal{F}_{ab} \quad (2.44)$$

Such expression presents better accuracy under ideal conditions (e.g. ordered material points, homogeneous properties and continuous fields). However, Cleary and Monaghan [43] have noted that in case of discontinuity between $\Phi(\underline{r}_a)$ and $\Phi(\underline{r}_b)$ this expression lead to inaccurate results. Thus, based on a finite difference analysis using a harmonic mean, they proposed to replace the term $[\Phi(\underline{r}_a) + \Phi(\underline{r}_b)]$ by $4 \frac{\Phi(\underline{r}_a)\Phi(\underline{r}_b)}{(\Phi(\underline{r}_a) + \Phi(\underline{r}_b))}$. It results in a new form of (Eq. 2.44):

$$\nabla \cdot (\Phi(\underline{r}_a) \nabla f(\underline{r}_a)) = \sum_{b=1}^{\hat{N}} \frac{m_b}{\rho_b} \left[4 \frac{\Phi(\underline{r}_a)\Phi(\underline{r}_b)}{(\Phi(\underline{r}_a) + \Phi(\underline{r}_b))} \right] [f(\underline{r}_a) - f(\underline{r}_b)] \mathcal{F}_{ab} \quad (2.45)$$

By adopting this formulation, [43] showed good accuracy for calculations for jumps in Φ of a factor of 10^3 . Parshikov and Medin [125] have also proposed another expression to fix the discontinuities issues by multiplying the harmonic mean term in (Eq. 2.45) by a

factor taking into account the average distance between material points. Following this form, they showed good accuracy for jumps in Φ by a factor of 10^9 .

Furthermore, in the special case of $\Phi = 1$, we have the discrete general forms for 1D (Eq. 2.24), 2D (Eq. 2.27) and 3D (Eq. 2.29) respectively:

$$(1D) \implies \frac{\partial^2 f(\underline{r}_a)}{\partial \alpha^2} = \sum_{b=1}^{\hat{N}} \frac{m_b}{\rho_b} 2 [f(\underline{r}_a) - f(\underline{r}_b)] \mathcal{F}_{ab} \quad (2.46a)$$

$$(2D) \implies \frac{\partial^2 f(\underline{r}_a)}{\partial \alpha \gamma} = \sum_{b=1}^{\hat{N}} \frac{m_b}{\rho_b} \left[4 \frac{r_{\alpha,ab} r_{\gamma,ab}}{\|\underline{r}_{ab}\|^2} - \delta^{\alpha\gamma} \right] [f(\underline{r}_a) - f(\underline{r}_b)] \mathcal{F}_{ab} \quad (2.46b)$$

$$(3D) \implies \frac{\partial^2 f(\underline{r}_a)}{\partial \alpha \gamma} = \sum_{b=1}^{\hat{N}} \frac{m_b}{\rho_b} \left[5 \frac{r_{\alpha,ab} r_{\gamma,ab}}{\|\underline{r}_{ab}\|^2} - \delta^{\alpha\gamma} \right] [f(\underline{r}_a) - f(\underline{r}_b)] \mathcal{F}_{ab} \quad (2.46c)$$

recalling that α and γ are spatial dimensions and a and b are material point identifiers.

2.2 Time integration

In order to integrate the movement equations presented in Sec. 1.3, two explicit time schema are introduced here.

2.2.1 Verlet integration scheme

This 2^{nd} -order method presents good numerical stability as well as time reversibility.

$$\underline{r}_a^{t+\Delta t} = \underline{r}_a^t + \underline{v}_a^t \Delta t + \underline{a}_a^t \frac{\Delta t^2}{2} \quad (2.47a)$$

$$\underline{v}_a^{t+\Delta t} = \underline{v}_a^t + \left(\underline{a}_a^t + \underline{a}_a^{t+\Delta t} \right) \frac{\Delta t}{2} \quad (2.47b)$$

2.2.2 Leapfrog integration scheme

Leapfrog is a 2^{nd} -order approach, which presents more stability for constant time-step. This method updates the positions and velocities at shifted time moments. [157].

$$\underline{r}_a^{t+\Delta t} = \underline{r}_a^t + \underline{v}_a^{t+\frac{\Delta t}{2}} \Delta t \quad (2.48a)$$

$$\underline{v}_a^{t+\frac{\Delta t}{2}} = \underline{v}_a^{t-\frac{\Delta t}{2}} + \underline{a}_a^t \Delta t \quad (2.48b)$$

2.2.3 Maximal time-step: CFL stability conditions

The explicit time scheme are much simpler to implement and to parallelize. However, their time step Δt must respect the Courant-Friedrich-Levy (CFL) conditions in order to ensure the numerical stability of the system (see [119] for more details).

$$\Delta t \leq \begin{cases} 0.25 \frac{h}{\|v_{max}\|} \\ 0.25 \sqrt{\frac{h}{\|a_{max}\|}} \end{cases} \quad (2.49)$$

We add that, for an elastic material, the following CFL condition is also requested:

$$\Delta t \leq h \sqrt{\frac{\rho_e}{\lambda_e + 2\mu_e}} \quad (2.50)$$

where λ and μ are the *Lamé coefficients* and the subscript e relates to the elastic phase.

2.3 Improvements of numerical modelling

Despite its several advantages, SPH also presents a few well-known drawbacks: non-physical noisy fluctuations, free boundary inconsistencies, tensile instability and zero-energy modes. Thus, various research works have been carried out in order to treat such issues. Namely, corrections of the kernel function and its derivatives are widely used to improve the accuracy on material properties calculations at boundary material points [117]. XSPH was introduced to improve the stability of simulations by correcting the non-physical noisy fluctuations of velocities [100], [117]. In addition, some formulations such as Total Lagrangian [132], [159], [160] allow to correct the tensile instability issues [58], [67], [135]. The Moving Least Squares functions (MLS) [54], [55] can treat the tensile instability as well as the zero-energy modes problems [67], [132]. Some of these improvements are integrated into our code and will be presented in this chapter.

Sigalotti *et al.* [149] have recently discussed the consistency issues in SPH given the particle disorder or if a boundary truncates the support domain. They observed that a loss of SPH accuracy is mainly due to a loss of consistency, where the accuracy depends only on the number of particles within the smoothing h -length and does not depend on the smoothing length itself. The consistency may be enhanced by constructing a smoothing function from Taylor series expansions of kernel function W and its derivatives. The ensured order of consistency m leads to the $m + 1$ order of accuracy. The first condition

that ensure the 0^{th} order consistency on a kernel function is its normalisation as showed in continuous Eq. (2.51a) and discrete form Eq. (2.51b).

$$\int W(|\underline{x} - \underline{r}'|, h) d\underline{r}' = 1 \quad (2.51a)$$

$$\sum_{b=1}^{\hat{N}} \frac{m_b}{\rho_b} W_{ab} = 1 \quad (2.51b)$$

As showed in Fig. 2.8, this condition is not true for boundary particles, due to truncated support domain, where no contributions come from the outside. Quinlan *et al.* [131]

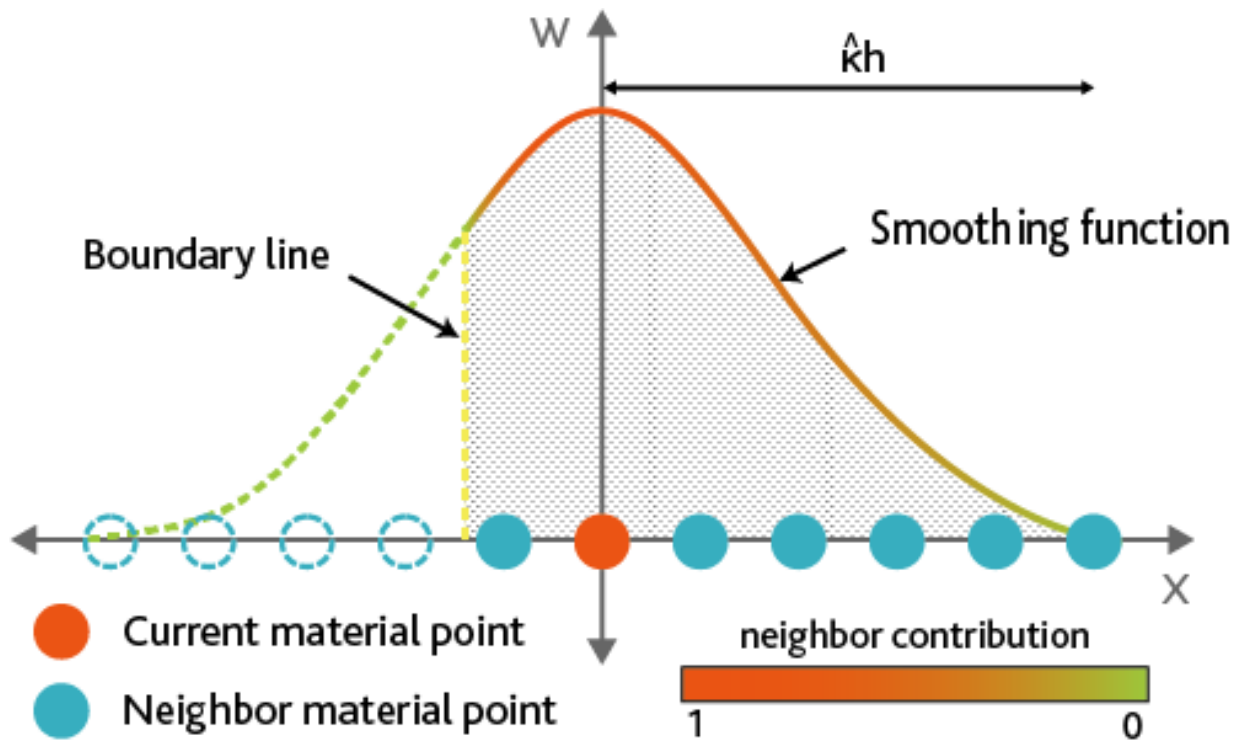


Fig. 2.8.: SPH boundary particle particles for the one-dimensional case

developed a truncation error analysis to study the influence of the smoothing length h and the ratio of particle spacing to the smoothing length $\frac{\Delta r}{h}$ on consistency order. They observed that the non-uniform distribution of particles increases the discretization error in SPH. Liu and Liu [98] stated that the particle disorder issue can be treated by the use of an even and non-negative smoothing function, which leads a 1^{st} order consistency and 2^{nd} order accuracy. Furthermore, they showed that the 1^{st} order consistency can be ensured if the following condition is respected:

$$\int (\underline{x} - \underline{r}') W(|\underline{x} - \underline{r}'|, h) d\underline{r}' = \underline{0} \quad (2.52a)$$

$$\sum_{b=1}^{\hat{N}} \frac{m_b}{\rho_b} \underline{r}_{ab} W_{ab} = \underline{0} \quad (2.52b)$$

2.3.1 Mixed kernel function and gradient correction

In the cases where support domains are underpopulated or truncated, the 1st order consistency can be guaranteed by assuring the conditions in (Eqs. 2.51 and 2.52). This is what Liu *et al.* [99] followed by Bonet and Lok [25] have proposed by introducing a corrected kernel form (here denoted by a over-text $\widetilde{}$) fulfilling the follow conditions:

$$\sum_{b=1}^{\hat{N}} \frac{m_b}{\rho_b} \widetilde{W}_{ab} = 1 \quad (2.53a) \quad \sum_{b=1}^{\hat{N}} \frac{m_b}{\rho_b} r_{ab} \widetilde{W}_{ab} = \underline{0} \quad (2.53b)$$

Aiming to ensure the 1st order consistency, \widetilde{W} is redefined in the following general form dependent on functions $\underline{f}(r)$ and $\underline{\Phi}(r)$:

$$\widetilde{W}_{ab} = W_{ab} \underline{f}(r_a) \left[1 + \underline{\Phi}(r_a) \cdot r_{ab} \right] \quad (2.54)$$

Introducing the corrected kernel presented above into Eq. (2.53b) leads to:

$$\sum_{b=1}^{\hat{N}} \frac{m_b}{\rho_b} r_{ab} W_{ab} \underline{f}(r_a) \left[1 + \underline{\Phi}(r_a) \cdot r_{ab} \right] = \underline{0} \quad (2.55)$$

$\underline{\Phi}(r)$ and $\underline{f}(r)$ are obtained, respectively, by rearranging Eq. (2.55) and replacing it into Eq. (2.53a), such that:

$$\underline{\Phi}(r_a) = - \left(\sum_{b=1}^{\hat{N}} \frac{m_b}{\rho_b} r_{ab} \otimes r_{ab} W_{ab} \right)^{-1} \sum_{b=1}^{\hat{N}} \frac{m_b}{\rho_b} r_{ab} W_{ab} \quad (2.56a)$$

$$\underline{f}(r_a) = \left[\sum_{b=1}^{\hat{N}} \frac{m_b}{\rho_b} W_{ab} \left(1 + \underline{\Phi}(r_a) \cdot r_{ab} \right) \right]^{-1} \quad (2.56b)$$

This new interpolation function can ensure the angular momentum conservation since respecting the follow condition:

$$\sum_{b=1}^{\hat{N}} \frac{m_b}{\rho_b} \nabla_a W_{ab} \otimes r_{ba} = \underline{1} \quad (2.57)$$

However, given the dependency of \underline{f} and $\underline{\Phi}$ on r , this form is computationally expensive to calculate. Thus, a simpler formulation, so-called Shepard's interpolation [25], that considers $\underline{\Phi}(r) = \underline{0}$ is adopted as following:

$$\widetilde{W}_{ab} = \frac{W_{ab}}{\sum_{b=1}^{\hat{N}} \frac{m_b}{\rho_b} W_{ab}} \quad (2.58)$$

Although this correction can ensure a 0^{th} order consistency without an expensive computations, it cannot ensure the angular momentum conservation. This issue will be treated through a kernel gradient correction. Thus, seeking to restore the first order consistency and to ensure the angular momentum conservation of the kernel derivatives, we recall the correction procedure presented by Randles and Libersky [136], that uses a matrix function of the gradient of the kernel function $\underline{\underline{K}}(W)$, applied to the original gradient, such as:

$$\widetilde{\nabla}_a W_{ab} = \underline{\underline{K}}_a \nabla_a W_{ab} \quad (2.59)$$

where the correction matrix $\underline{\underline{K}}$ is computed as:

$$\underline{\underline{K}}(\nabla_a W_{ab})_a = \left(\sum_{b=1}^{\hat{N}} \frac{m_b}{\rho_b} \nabla_a W_{ab} \otimes \underline{r}_{ba} \right)^{-1} \quad (2.60)$$

This correction is then able to ensure the necessary condition presented in Eq. (2.57). In order to correct drawbacks due to underpopulated or truncated support domains in gradient calculations, two corrections to the kernel gradient are present in literature. The gradient of the corrected kernel form calculated by applying the quotient rule to the Shepard's interpolation (Eq. 2.61a - as presented by Bonet and Lok [25]) and a corrected gradient form based on the Shepard's interpolation itself (Eq. 2.61b). Although the last approach is not mathematically consistent, it is adopted in different studies (see for instance [141]).

$$\nabla_a \widetilde{W}_{ab} = \frac{\nabla_a W_{ab} \left(\sum_{b=1}^{\hat{N}} \frac{m_b}{\rho_b} W_{ab} \right) - \left(\sum_{b=1}^{\hat{N}} \frac{m_b}{\rho_b} \nabla_a W_{ab} \right) W_{ab}}{\left(\sum_{b=1}^{\hat{N}} \frac{m_b}{\rho_b} W_{ab} \right)^2} \quad (2.61a)$$

$$\nabla_a \widetilde{\widetilde{W}}_{ab} = \frac{\nabla_a W_{ab}}{\sum_{b=1}^{\hat{N}} \frac{m_b}{\rho_b} \nabla_a W_{ab}} \quad (2.61b)$$

As showed in Eq. (2.60), the corrected matrix $\underline{\underline{K}}$ depends on the kernel gradient function ∇W , thus, for each respective correction presented in (Eqs. 2.61) a new matrix correction will be necessary.

$$\underline{\underline{K}}(\nabla_a \widetilde{W}_{ab})_a = \left(\sum_{b=1}^{\hat{N}} \frac{m_b}{\rho_b} \nabla_a \widetilde{W}_{ab} \otimes \underline{r}_{ba} \right)^{-1} \quad (2.62a)$$

$$\underline{\underline{K}}(\nabla_a \widetilde{\widetilde{W}}_{ab})_a = \left(\sum_{b=1}^{\hat{N}} \frac{m_b}{\rho_b} \nabla_a \widetilde{\widetilde{W}}_{ab} \otimes \underline{r}_{ba} \right)^{-1} \quad (2.62b)$$

From that, we find the following possible mixed kernel and gradient correction forms:

$$\widetilde{\nabla}_a W_{ab} = \underline{\underline{K}}(\nabla_a W_{ab})_a \nabla_a W_{ab} \quad (2.63a)$$

$$\widetilde{\nabla}_a \widetilde{W}_{ab} = \underline{\underline{K}} (\nabla_a \widetilde{W}_{ab})_a \nabla_a \widetilde{W}_{ab} \quad (2.63b)$$

$$\widetilde{\nabla}_a \widetilde{\widetilde{W}}_{ab} = \underline{\underline{K}} (\nabla_a \widetilde{\widetilde{W}}_{ab})_a \nabla_a \widetilde{\widetilde{W}}_{ab} \quad (2.63c)$$

Finally, by replacing W and ∇W by, respectively, its mixed kernel and gradient corrected forms \widetilde{W} and $\widetilde{\nabla} \widetilde{W}$ we can ensure the angular momentum conservation and restore the 1st order consistency. A validation test and additional discussions about this corrections are performed at the end of this chapter.

2.3.2 Artificial viscosity

Neumann and Richtmyer [122] first introduced the artificial viscosity seeking to stabilise numerical solutions by smoothing shock phenomena. It was introduced to SPH by Monaghan and Gingold [114] to simulate discontinuities, shocks or stabilise SPH algorithms numerically. After them, many researchers adopted the artificial viscosity to treat fluid [44], [136] or elastic dynamics [141], [171]. Libersky *et al.* [95] stated that the significant increase of oscillations in unstable conditions (for instance disordered material points or shock phenomena) results from the omission of the dissipative terms in governing equations. The artificial viscosity acts on the relative motion of material points by adding a Π_{ab} term into the momentum equation interpolation between material points a and b . We adopt here the version proposed by Monaghan [110], [115] that depends on the divergence of \underline{v}_{ab} :

$$\Pi_{ab} = \begin{cases} -\frac{\check{\alpha} \bar{c}_{ab} \check{\nu}_{ab} + \check{\beta} \check{\nu}_{ab}^2}{\bar{\rho}_{ab}} & \text{if } (\underline{v}_{ab} \cdot \underline{r}_{ab}) < 0 \\ 0 & \text{if } (\underline{v}_{ab} \cdot \underline{r}_{ab}) \geq 0 \end{cases} \quad (2.64)$$

where $\check{\alpha}$ and $\check{\beta}$ are arbitrary constant parameters and the over-line on the sound speed c and on the density ρ denote their arithmetic mean with respect to a and b . In addition $\check{\nu}_{ab}$ is defined such as:

$$\check{\nu}_{ab} = -\frac{h(\underline{v}_{ab} \cdot \underline{r}_{ab})}{r_{ab}^2 + 0.01h^2} \quad (2.65)$$

with the denominator term 0.01 introduced to prevent singularities and h the smoothing length of SPH kernels. Some desirable features can be noted about the viscosity: it is Galilean invariant, it conserves linear and angular momenta and vanishes for rigid body rotations [110]. We observe from (Eq. 2.64) that the artificial viscosity vanishes when $\nabla \cdot v$ is greater or equal to zero. Inversely, when two material points are moving towards each other ($\nabla \cdot v < 0$) it produces a repulsive force that depends on two constants: $\check{\alpha}$ which is linear with the velocity difference and dominant when it is small (this term is equivalent to a bulk viscosity [111]) and $\check{\beta}$ which is dominant when the velocity difference is large (it is a Von Neumann-Richtmyer [122] like viscosity).

2.3.3 XSPH velocities correction

The XSPH approach seeks to improve the numerical stability by correcting non-physical noisy fluctuations [4], [85], [100], [117]. Such correction ensure that, when the momenta are constant, the velocities in a close neighbourhood are not too distinct. Thus, the method updates the calculated velocities by using a corrected velocity:

$$\hat{v}_a = v_a + \hat{\epsilon} \sum_b m_b \frac{2(v_b - v_a)}{\rho_a + \rho_b} \quad (2.66)$$

where $\hat{\epsilon}$ is an arbitrary constant parameter that may vary from 0 to 1 for different applications.

2.3.4 SPH in GPU parallel computing

The increasing performance of GPUs has led to their increased usage for numerical modelling. Their performance is given mainly by the parallel nature of the graphical processing units, which is well-suited for intensive methods like the Smoothed Particle Hydrodynamics with almost local nature. The code used in this thesis is written in C++ to ease the separation the computing components and in CUDA for GPU parallelisation.

2.4 Elastic body dynamics

In this section, we present the SPH form of equations describing the solid phase. We seek to evaluate the numerical stability of approaches based on finite and infinitesimal formulations. In addition, the rigid body dynamics equations are recalled in Appendix A.

2.4.1 SPH discrete governing equations and Saint Venant-Kirchhoff constitutive model

As presented in Sec. 1.3.2.2, the deformation gradient $\underline{\underline{F}}$ and its time derivative $\dot{\underline{\underline{F}}}$ are key variables in our Saint Venant-Kirchhoff (SVK) constitutive model. Based on the continuum (Eq. 1.11), their discrete SPH forms with mixed normalisation and correction of kernels are given by:

$$\underline{\underline{F}}_a = \left[\sum_{b=1}^{\hat{N}} \frac{m_b}{\rho_{b,0}} (r_b - r_a) \otimes \widetilde{\nabla}_{a,0} \widetilde{W}_{ab,0} \right] + \mathbb{1} \quad (2.67)$$

$$\dot{\underline{\underline{F}}}_a = \left[\sum_{b=1}^{\hat{N}} \frac{m_b}{\rho_{b,0}} (\underline{v}_b - \underline{v}_a) \otimes \widetilde{\nabla}_{a,0} \widetilde{W}_{ab,0} \right] \quad (2.68)$$

In addition, aiming to obtain the SVK constitutive model, by simple matrix operations of $\underline{\underline{F}}_a$ and $\dot{\underline{\underline{F}}}_a$ we calculate the following intermediary variables:

$$\underline{\underline{1}}_a = \dot{\underline{\underline{F}}}_a \cdot \underline{\underline{F}}_a^{-1} \quad (2.69)$$

$$\underline{\underline{d}}_a = \frac{1}{2} (\underline{\underline{1}}_a^T + \underline{\underline{1}}_a) \quad (2.70)$$

We are also able to construct the Green-Lagrange deformation tensor as well as its incremental form by:

$$\underline{\underline{\epsilon}}_{GLa} = \frac{1}{2} (\underline{\underline{F}}_a^T \cdot \underline{\underline{F}}_a - \mathbb{1}) \quad (2.71)$$

$$\dot{\underline{\underline{\epsilon}}}_{GLa} = \underline{\underline{F}}_a^T \cdot \underline{\underline{d}}_a \cdot \underline{\underline{F}}_a \quad (2.72)$$

The Saint Venant-Kirchhoff state law for a material point is then given by:

$$\underline{\underline{S}}_a = \rho \frac{\partial \psi}{\partial \underline{\underline{\epsilon}}_{GL}} = \mathbb{C}_0 : \underline{\underline{\epsilon}}_{GLa} \quad (2.73)$$

In terms of local material properties (for an isotropic case), it reads:

$$\underline{\underline{S}}_a = \underbrace{k \operatorname{tr} \underline{\underline{\epsilon}}_{GLa}}_{\text{volumetric stress}} \underline{\underline{1}} + \underbrace{2\mu \underline{\underline{\epsilon}}_{GLa}^d}_{\text{deviatoric stress}} \quad (2.74)$$

where k is the bulk modulus, μ the shear modulus and the superscript d relates to the deviatoric part of the tensor $\underline{\underline{\epsilon}}_{GLa}^d = \underline{\underline{\epsilon}}_{GLa} - \frac{1}{3} \operatorname{tr}(\underline{\underline{\epsilon}}_{GL})_a \underline{\underline{1}}$. We can obtain the discrete momentum conservation equation by transforming the continuum (Eq. 1.26) in an equivalent form of (Eq. 2.42a) with $\Phi = 1$ and $f = \underline{\underline{P}}$:

$$\ddot{\underline{u}}_a = -\frac{1}{m_a} \sum_{b=1}^{\hat{N}} \frac{m_a}{\rho_{a,0}} \frac{m_b}{\rho_{b,0}} (\underline{\underline{P}}_b - \underline{\underline{P}}_a) \cdot \nabla_{a,0} W_{ab,0} \quad (2.75)$$

We recall for a mixed corrected kernel and gradient obtained after (Eq. 2.63b) that $\widetilde{\nabla}_{a,0} \widetilde{W}_{ab,0} \neq -\widetilde{\nabla}_{b,0} \widetilde{W}_{ba,0}$. This condition leads to the following interpolated form of the momentum conservation equation adopted in our work:

$$\ddot{\underline{u}}_a = -\frac{1}{m_a} \sum_{b=1}^{\hat{N}} \frac{m_a}{\rho_{a,0}} \frac{m_b}{\rho_{b,0}} (\underline{\underline{P}}_b \widetilde{\nabla}_{b,0} \widetilde{W}_{ba,0} - \underline{\underline{P}}_a \widetilde{\nabla}_{a,0} \widetilde{W}_{ab,0}) \quad (2.76)$$

In the same way, we obtain the discrete rate of the internal energy by introducing (Eq. 2.68) into (Eq. 1.27). Thus, by applying the identity $\underline{\underline{P}} : (\underline{v}_{ba} \otimes \widetilde{\nabla}_{a,0} \widetilde{W}_{ab,0}) =$

$\underline{v}_{ba} \cdot \underline{P} \widetilde{\nabla}_{a,0} \widetilde{W}_{ab,0}$ (as shown in [27]), we obtain the interpolated form of the energy conservation equation:

$$\dot{w}_a = \sum_{b=1}^{\hat{N}} \frac{m_a}{\rho_{a,0}} \frac{m_b}{\rho_{b,0}} (\underline{v}_b - \underline{v}_a) \cdot \underline{P}_a \widetilde{\nabla}_{a,0} \widetilde{W}_{ab,0} \quad (2.77)$$

The Jacobian J used in the mass conservation equation is written as:

$$J_a = \det(\underline{F}_a) \quad (2.78)$$

It results in the SVK-SPH discrete form of the governing equations:

$$\left\{ \begin{array}{l} \rho_a = J^{-1} \rho_{a,0} \\ \ddot{\underline{u}}_a = -\frac{1}{m_a} \sum_{b=1}^{\hat{N}} \frac{m_a}{\rho_{a,0}} \frac{m_b}{\rho_{b,0}} (\underline{P}_b \widetilde{\nabla}_{b,0} \widetilde{W}_{ba,0} - \underline{P}_a \widetilde{\nabla}_{a,0} \widetilde{W}_{ab,0}) \\ \dot{w}_a = \sum_{b=1}^{\hat{N}} \frac{m_a}{\rho_{a,0}} \frac{m_b}{\rho_{b,0}} (\underline{v}_b - \underline{v}_a) \cdot \underline{P}_a \widetilde{\nabla}_{a,0} \widetilde{W}_{ab,0} \end{array} \right. \quad (2.79)$$

$$\left. \begin{array}{l} \ddot{\underline{u}}_a = -\frac{1}{m_a} \sum_{b=1}^{\hat{N}} \frac{m_a}{\rho_{a,0}} \frac{m_b}{\rho_{b,0}} (\underline{P}_b \widetilde{\nabla}_{b,0} \widetilde{W}_{ba,0} - \underline{P}_a \widetilde{\nabla}_{a,0} \widetilde{W}_{ab,0}) \end{array} \right\} \quad (2.80)$$

$$\left. \begin{array}{l} \dot{w}_a = \sum_{b=1}^{\hat{N}} \frac{m_a}{\rho_{a,0}} \frac{m_b}{\rho_{b,0}} (\underline{v}_b - \underline{v}_a) \cdot \underline{P}_a \widetilde{\nabla}_{a,0} \widetilde{W}_{ab,0} \end{array} \right\} \quad (2.81)$$

We highlight that in this section the only variables computed through a weighted average are the deformation gradient and its time derivative. In addition, only a few matrix operations are necessary to obtain the linear elastic part of the Saint Venant-Kirchhoff constitutive model.

2.4.2 SPH discrete governing equations and linear elastic law

A much simpler approach is used for infinitesimal strain theory, given the fact that we can neglect the second order terms. Consider SPH form with mixed normalisation and correction of kernels. The infinitesimal strain $\underline{\underline{\varepsilon}}$ and the rate of the deformation tensor $\underline{\underline{\dot{\varepsilon}}}$ are given by:

$$\underline{\underline{\varepsilon}}_a = \left[\sum_{b=1}^{\hat{N}} \frac{m_b}{\rho_b} (\underline{r}_b - \underline{r}_a) \otimes \widetilde{\nabla}_a \widetilde{W}_{ab} \right] \quad (2.82)$$

$$\underline{\underline{\dot{\varepsilon}}}_a = \left[\sum_{b=1}^{\hat{N}} \frac{m_b}{\rho_b} (\underline{v}_b - \underline{v}_a) \otimes \widetilde{\nabla}_a \widetilde{W}_{ab} \right] \quad (2.83)$$

We write the infinitesimal state law such as:

$$\underline{\underline{\sigma}}_a = \mathbb{C} : \underline{\underline{\varepsilon}}_a \quad (1.31 \text{ Revisited})$$

In local material properties (for an isotropic case), it reads:

$$\underline{\underline{\sigma}}_a = \underbrace{k \operatorname{tr} \underline{\underline{\varepsilon}}_a}_{\text{volumetric stress}} \underline{\underline{1}} + \underbrace{2\mu \underline{\underline{\varepsilon}}_a^d}_{\text{deviatoric stress}} \quad (2.84)$$

Hence, by reproducing a similar procedure from the previous section, we obtain the following discrete forms of the infinitesimal governing equations:

$$\left\{ \begin{array}{l} \dot{\rho}_a = -\rho_a \sum_{b=1}^{\hat{N}} \frac{m_b}{\rho_b} (\underline{v}_b - \underline{v}_a) \cdot \widetilde{\nabla}_a \widetilde{W}_{ab} \\ \ddot{u}_a = -\frac{1}{m_a} \sum_{b=1}^{\hat{N}} \frac{m_a m_b}{\rho_a \rho_b} (\underline{\sigma}_b \widetilde{\nabla}_b \widetilde{W}_{ba} - \underline{\sigma}_a \widetilde{\nabla}_a \widetilde{W}_{ab}) \\ \underline{w}_a = \sum_{b=1}^{\hat{N}} \frac{m_a m_b}{\rho_a \rho_b} (\underline{v}_b - \underline{v}_a) \underline{\sigma}_a \widetilde{\nabla}_a \widetilde{W}_{ab} \end{array} \right. \quad (2.85)$$

$$\left. \begin{array}{l} \ddot{u}_a = -\frac{1}{m_a} \sum_{b=1}^{\hat{N}} \frac{m_a m_b}{\rho_a \rho_b} (\underline{\sigma}_b \widetilde{\nabla}_b \widetilde{W}_{ba} - \underline{\sigma}_a \widetilde{\nabla}_a \widetilde{W}_{ab}) \end{array} \right\} \quad (2.86)$$

$$\left. \begin{array}{l} \underline{w}_a = \sum_{b=1}^{\hat{N}} \frac{m_a m_b}{\rho_a \rho_b} (\underline{v}_b - \underline{v}_a) \underline{\sigma}_a \widetilde{\nabla}_a \widetilde{W}_{ab} \end{array} \right\} \quad (2.87)$$

We note that following this approach, the only interpolated variables are $\underline{\underline{\varepsilon}}$ and $\underline{\underline{\dot{\varepsilon}}}$. The advantage of this infinitesimal approach is a much lower computation cost than for the large deformations model.

Displacement-based momentum equation

Here we present a second formulation for computing the momentum equation in small deformation formulation. From (Eq. 1.35), we can rewrite a volumetric elastic force density components $\nabla \cdot \underline{\underline{\sigma}}$ of an isotropic medium in terms of partial derivatives of the local displacement field, such as:

$$\left. \begin{array}{l} \left(\frac{\partial^2 u_x}{\partial t^2} \right) = \frac{1}{\rho} \left[\left(\frac{4}{3}\mu + k \right) \frac{\partial^2 u_x}{\partial x^2} + \mu \left(\frac{\partial^2 u_x}{\partial y^2} + \frac{\partial^2 u_x}{\partial z^2} \right) + \left(\frac{1}{3}\mu + k \right) \left(\frac{\partial^2 u_y}{\partial x \partial y} + \frac{\partial^2 u_z}{\partial x \partial z} \right) \right] \\ \left(\frac{\partial^2 u_y}{\partial t^2} \right) = \frac{1}{\rho} \left[\left(\frac{4}{3}\mu + k \right) \frac{\partial^2 u_y}{\partial y^2} + \mu \left(\frac{\partial^2 u_y}{\partial x^2} + \frac{\partial^2 u_y}{\partial z^2} \right) + \left(\frac{1}{3}\mu + k \right) \left(\frac{\partial^2 u_x}{\partial x \partial y} + \frac{\partial^2 u_z}{\partial y \partial z} \right) \right] \\ \left(\frac{\partial^2 u_z}{\partial t^2} \right) = \frac{1}{\rho} \left[\left(\frac{4}{3}\mu + k \right) \frac{\partial^2 u_z}{\partial z^2} + \mu \left(\frac{\partial^2 u_z}{\partial x^2} + \frac{\partial^2 u_z}{\partial y^2} \right) + \left(\frac{1}{3}\mu + k \right) \left(\frac{\partial^2 u_x}{\partial x \partial z} + \frac{\partial^2 u_y}{\partial y \partial z} \right) \right] \end{array} \right\} \quad (2.88)$$

In the following, these continuous components can be converted into their discrete form by following the steps presented in Sec. 2.1.4, starting by the second order spatial derivatives $\frac{\partial^2 u_a}{\partial x^2}$ and $\frac{\partial^2 u_a}{\partial x \partial y}$ after (Eq. 2.46c):

$$\left(\frac{\partial^2 u_x}{\partial x^2} \right)_a = \sum_{b=1}^{\hat{N}} \frac{m_b}{\rho_b} \left[5 \frac{r_{x,ab} r_{x,ab}}{\|r_{ab}\|^2} - \delta^{xx} \right] [u_a - u_b] \mathcal{F}_{ab} \quad (2.89a)$$

$$\left(\frac{\partial^2 u_x}{\partial x \partial y} \right)_a = \sum_{b=1}^{\hat{N}} \frac{m_b}{\rho_b} \left[5 \frac{r_{x,ab} r_{y,ab}}{\|r_{ab}\|^2} - \delta^{xy} \right] [u_a - u_b] \mathcal{F}_{ab} \quad (2.89b)$$

The other differential components can be obtained in a similar way. Thus, the components of the acceleration \underline{u}_a in a discrete form are:

$$\ddot{u}_{x,a} = -\frac{1}{m_a} \sum_{b=1}^{\hat{N}} \frac{m_a}{\rho_a} \frac{m_b}{\rho_b} \left[\left(\frac{4}{3}\mu + k \right) \left(5 \frac{r_{x,ab}^2}{\|r_{ab}\|^2} - 1 \right) + \mu \left(5 \frac{r_{y,ab}^2 + r_{z,ab}^2}{\|r_{ab}\|^2} - 2 \right) + \left(\frac{1}{3}\mu + k \right) \left(5 \frac{r_{x,ab} (r_{y,ab} + r_{z,ab})}{\|r_{ab}\|^2} \right) \right] \underline{u}_{x,ab} \mathcal{F}_{ab} \quad (2.90a)$$

$$\ddot{u}_{y,a} = -\frac{1}{m_a} \sum_{b=1}^{\hat{N}} \frac{m_a}{\rho_a} \frac{m_b}{\rho_b} \left[\left(\frac{4}{3}\mu + k \right) \left(5 \frac{r_{y,ab}^2}{\|r_{ab}\|^2} - 1 \right) + \mu \left(5 \frac{r_{x,ab}^2 + r_{z,ab}^2}{\|r_{ab}\|^2} - 2 \right) + \left(\frac{1}{3}\mu + k \right) \left(5 \frac{r_{y,ab} (r_{x,ab} + r_{z,ab})}{\|r_{ab}\|^2} \right) \right] \underline{u}_{y,ab} \mathcal{F}_{ab} \quad (2.90b)$$

$$\ddot{u}_{z,a} = -\frac{1}{m_a} \sum_{b=1}^{\hat{N}} \frac{m_a}{\rho_a} \frac{m_b}{\rho_b} \left[\left(\frac{4}{3}\mu + k \right) \left(5 \frac{r_{z,ab}^2}{\|r_{ab}\|^2} - 1 \right) + \mu \left(5 \frac{r_{x,ab}^2 + r_{y,ab}^2}{\|r_{ab}\|^2} - 2 \right) + \left(\frac{1}{3}\mu + k \right) \left(5 \frac{r_{z,ab} (r_{x,ab} + r_{y,ab})}{\|r_{ab}\|^2} \right) \right] \underline{u}_{z,ab} \mathcal{F}_{ab} \quad (2.90c)$$

For the sake of clearness, in next parts of this study we note this formulation as $f(\underline{u})$ or "displacement-based" and the classical "stress-based" as $f(\underline{\sigma})$.

2.4.3 SPH algorithm

We present in Fig. 2.9 the algorithm flow chart used to compute the response of a solid material point taking into account the GPU parallelization. We exemplify here the numerical implementation of an infinitesimal deformation approach.

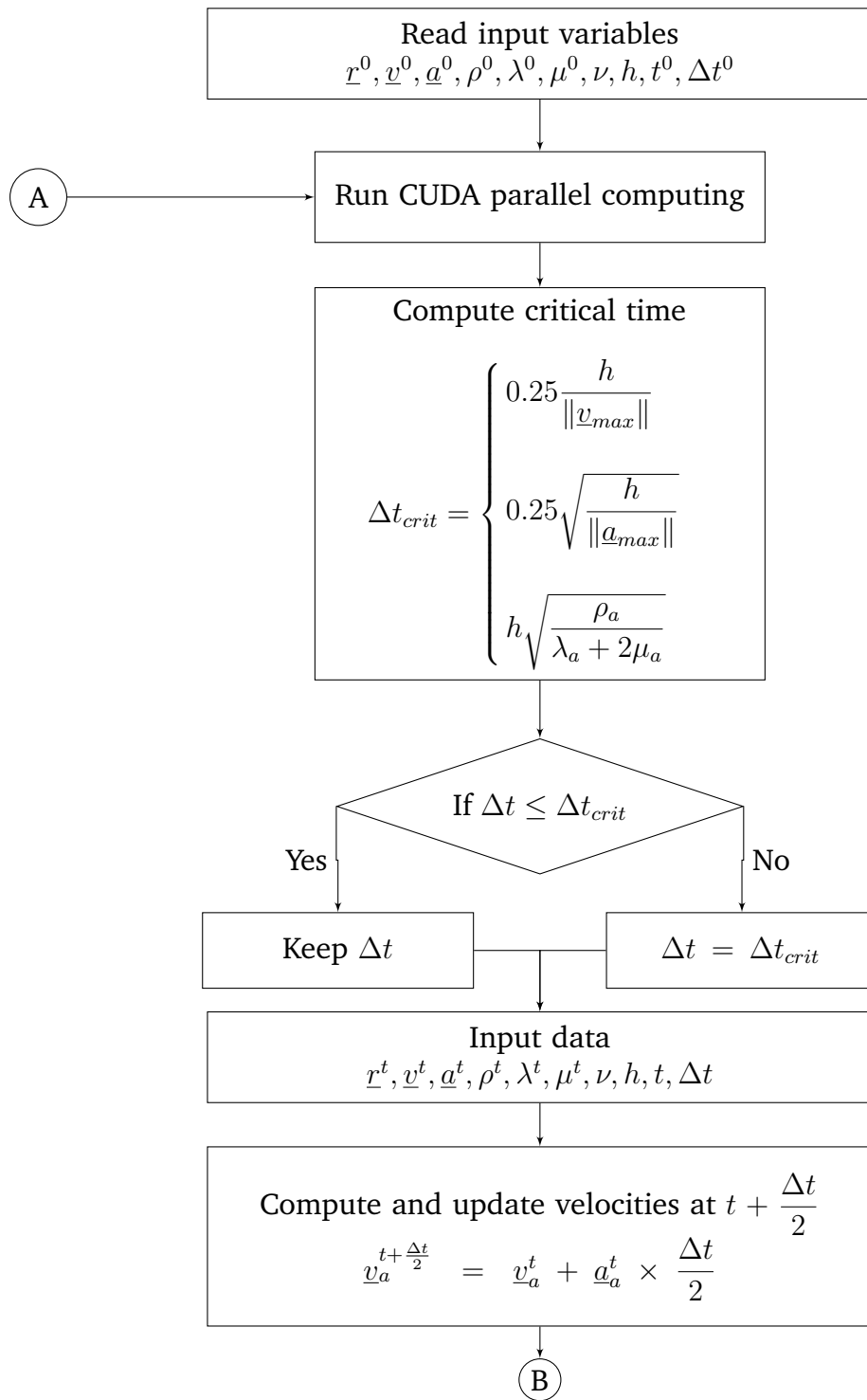


Fig. 2.9.: SPH computing flow chart for solid particles

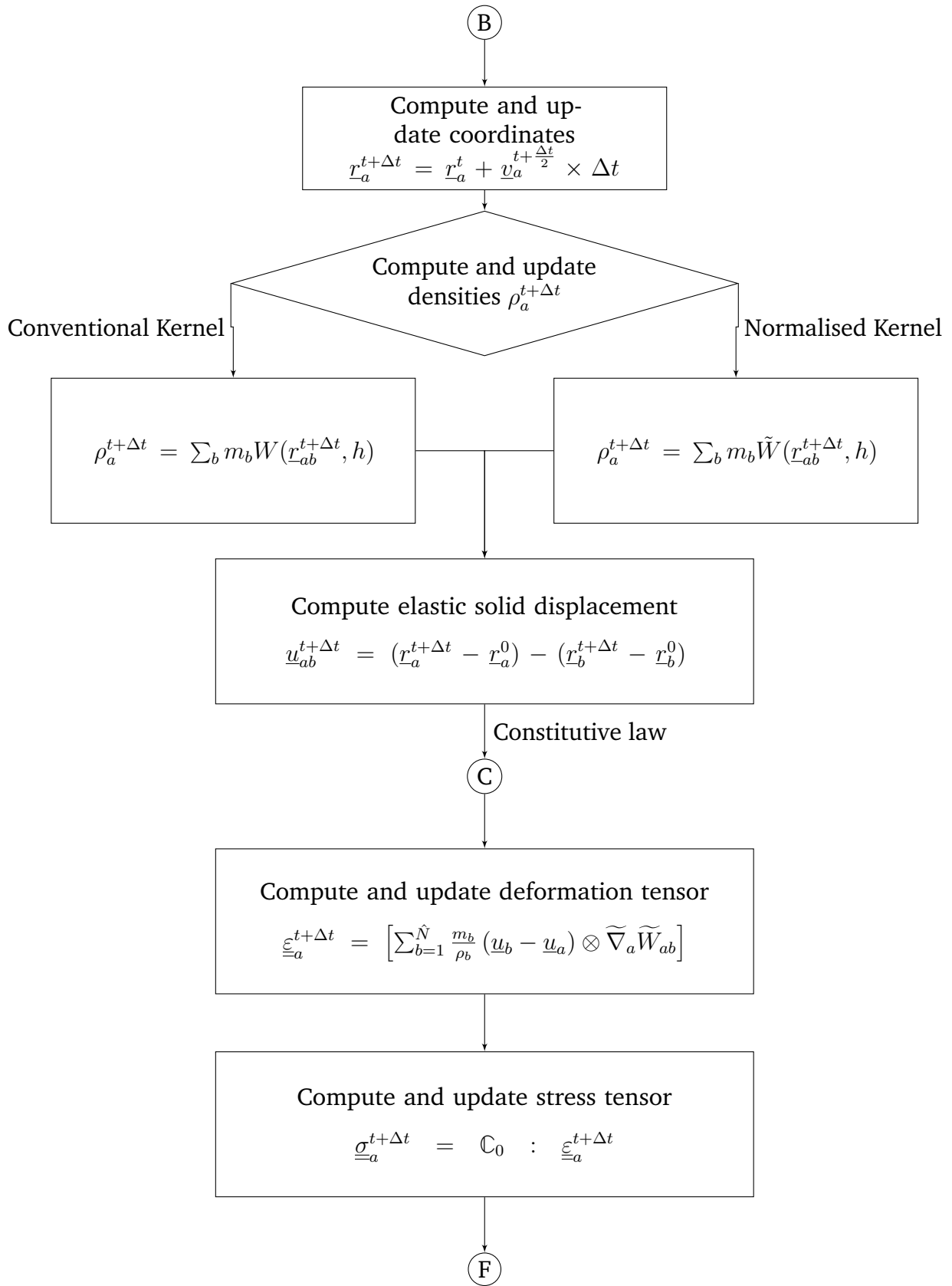


Fig. 2.9.: SPH computing flow chart for solid particles

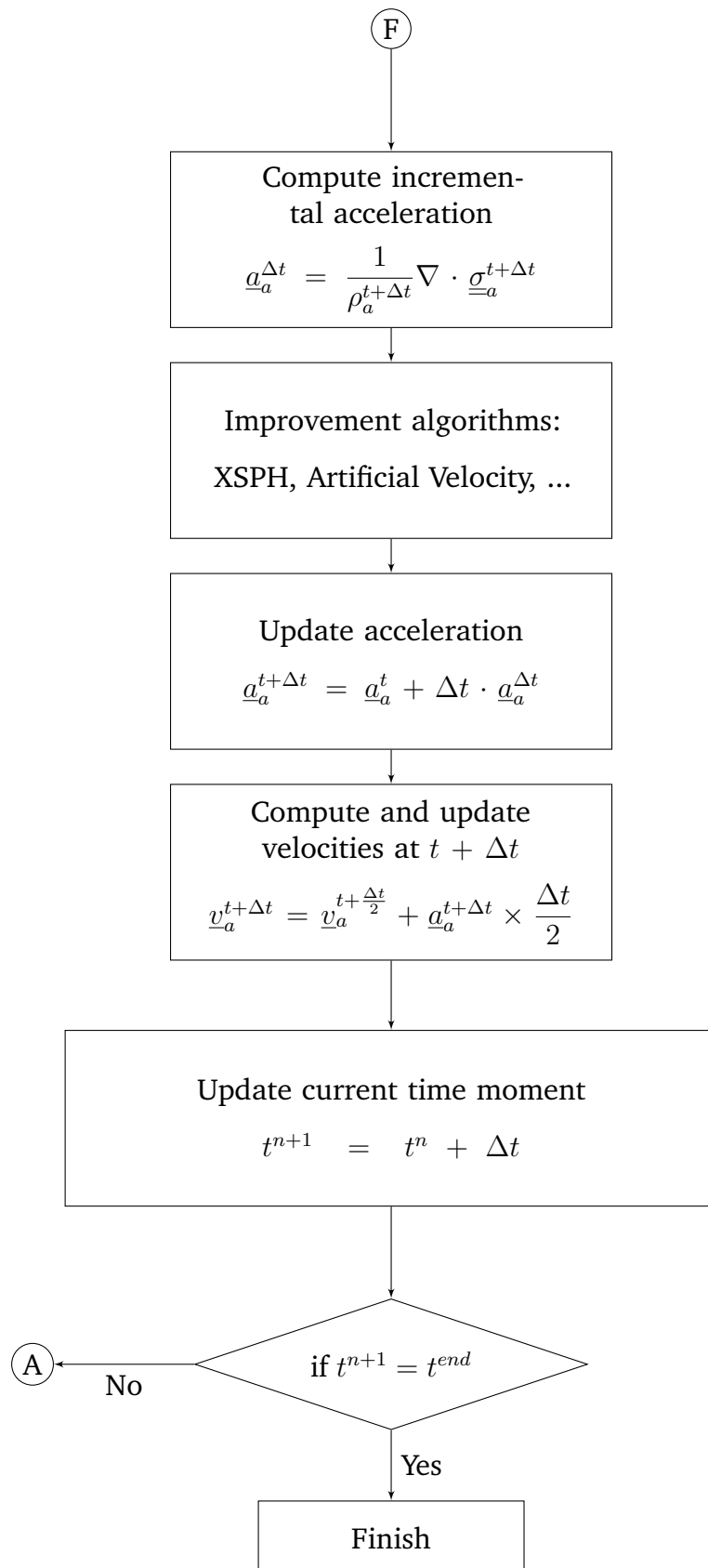


Fig. 2.9.: SPH computing flow chart for solid particles

2.5 Validation and analysis: mixed kernel and gradient correction

In this section, the most common features presented in the literature to correct the SPH first-order variables will be tested and discussed to validate our algorithm and to better understand how each addition can influence the solutions in one simple and one more complex cases.

The validation test for mixed kernel and gradient correction proposed here was based on Young [171]. We apply different velocity fields in a 1D rod Fig. 2.10. Here, the size of the bar is $L = 1\text{m}$ and it is discretised with $N = 5$ equally spaced material points of $\delta x = \frac{L}{N}$, starting and ending respectively at $x = 50.1\text{m}$ and $x = 50.9\text{m}$. We recall that the material points in SPH represent a center of a small zone. For the case $N = 5$, the domain is divided in 5 equal parts and each material point is located at the centre of each part. It explains why the distance between the first and the last material points is lower than L .

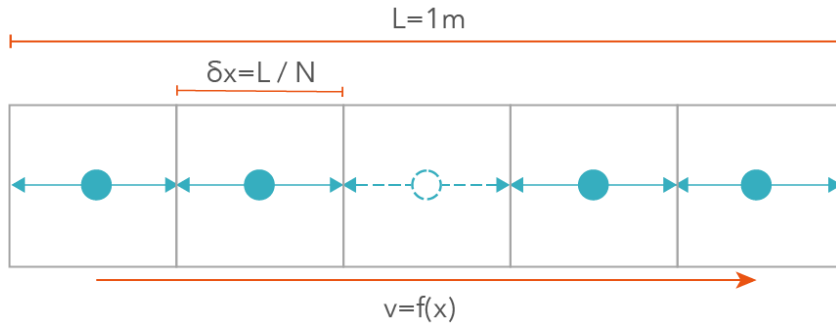


Fig. 2.10.: 1D bar of length 1m discretized into $N = 5$ equally spaced of δx material points [171]

In this problem, the smoothing length h is equal to $2.8\delta x$ and $\hat{\kappa} = 1$, a velocity field $v(x)$ is applied in each material point in order to calculate SPH velocity divergence, which can be obtained from (Eq. 2.35) or (Eq. 2.42a).

$$\nabla \cdot \underline{v} = \sum_{b=1}^{\hat{N}} \frac{m_b}{\rho_b} (\underline{v}_b) \cdot \nabla_a W_{ab} \quad (2.91a)$$

$$\nabla \cdot \underline{v} = \sum_{b=1}^{\hat{N}} \frac{m_b}{\rho_b} (\underline{v}_b - \underline{v}_a) \cdot \nabla_a W_{ab} \quad (2.91b)$$

In conventional SPH, the kernel interpolation computing is strongly influenced by truncated domains. In this section, we seek to validate our algorithm and to compare the efficiency of non-symmetric and symmetric formulations. In addition, we compare the

three different formulations of mixed kernel-and-gradient corrections presented in (Eqs. 2.63). We also explore various scenarios using the following constant, linear and a quartic velocity fields:

$$\underline{v}_1(x) = 20 \quad (2.92a)$$

$$\underline{v}_2(x) = 20x \quad (2.92b)$$

$$\underline{v}_3(x) = -4x^4 + 3x^3 + 15x^2 - x + 15 \quad (2.92c)$$

We investigate the influence of the particle density and their distribution along the domain. Results for 2D and 3D configurations are also given in this validation section. Based on the scheme proposed in Fig. 2.10, we reproduce with some adaptations the problem [171] which $N = 5$ and the velocities v_2 or v_3 are applied. Table 2.1 and Table 2.2 present the velocity divergence of the fourth material point following, respectively, (Eq. 2.92b) and (Eq. 2.92c) and adopting the correction of the kernel gradient after (Eq. 2.63b).

Pairs i-j	$V_b(\underline{v}_b - \underline{v}_a) \cdot \widetilde{\nabla}_a \widetilde{W}_{ij}$	$V_b(\underline{v}_b) \cdot \widetilde{\nabla}_a \widetilde{W}_{ij}$
4 - 2	3.879	-5.333
4 - 3	7.572	-28.395
4 - 4	0.000	4.569
4 - 5	8.549	49.159
$\nabla \cdot \underline{v}$	$\sum_b = 20.0$	$\sum_b = 20.0$
Analytical $\nabla \cdot \underline{v} = 20.0$		$\check{\sigma}_{rel} = 1.10^{-14}\%$

Tab. 2.1.: Velocity divergence of the pair contributions for a linear velocity (Eq. 2.92b).

Pairs i-j	$V_b(\underline{v}_b - \underline{v}_a) \cdot \widetilde{\nabla}_a \widetilde{W}_{ij}$	$V_b(\underline{v}_b) \cdot \widetilde{\nabla}_a \widetilde{W}_{ij}$
4 - 2	-95159.963	2900053.551
4 - 3	-186899.604	11507941.882
4 - 4	0.000	-1485695.206
4 - 5	-213580.328	-13417940.121
$\nabla \cdot \underline{v}$	$\sum = -495639.894$	$\sum = -495639.894$
Analytical $\nabla \cdot \underline{v} = -496640.962$		$\check{\sigma}_{rel} = 0.202\%$

Tab. 2.2.: Velocity divergence of the pair contributions for a quartic velocity (Eq. 2.92c).

where $\check{\sigma}_{rel}$ is relative error for each data point x compared to the analytical solution, such that:

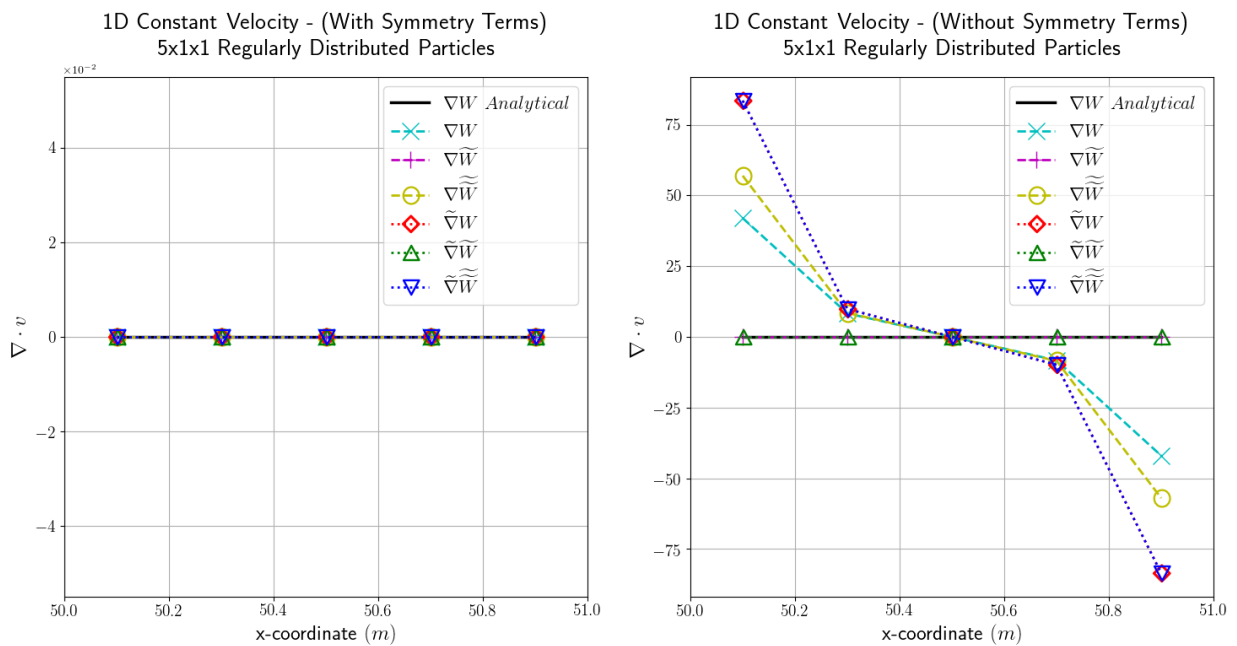
$$\check{\sigma}_{rel} = 100 \times \frac{|x_{analyt.} - x|}{|x_{analyt.}|} \quad (2.93)$$

With Tables 2.1 and 2.2, we validate the implemented mixed correction algorithm for a linear and a quartic velocity field (in order to account for a higher level of complexity). Following Monaghan *et al.* [117], the adoption of the symmetric formulation can fix the issue of not vanishing solution for constant fields. In the same way, Young [171] has

recently proposed an analysis of pros a cons of symmetric and not-symmetric formulations. The next section discusses this issue.

2.5.1 Computing SPH divergence with or without symmetry terms and gradient corrections

In order to better understand the pros and cons of the use of a formulation with or without symmetry terms, the bar configuration of $N = 5$ is studied again following three velocities fields v_1 , v_2 and v_3 (Eqs. 2.92). The six formulations of kernel gradients (Eqs. 2.61 and 2.63) are used here. First Fig. 2.11a shows as required that the SPH

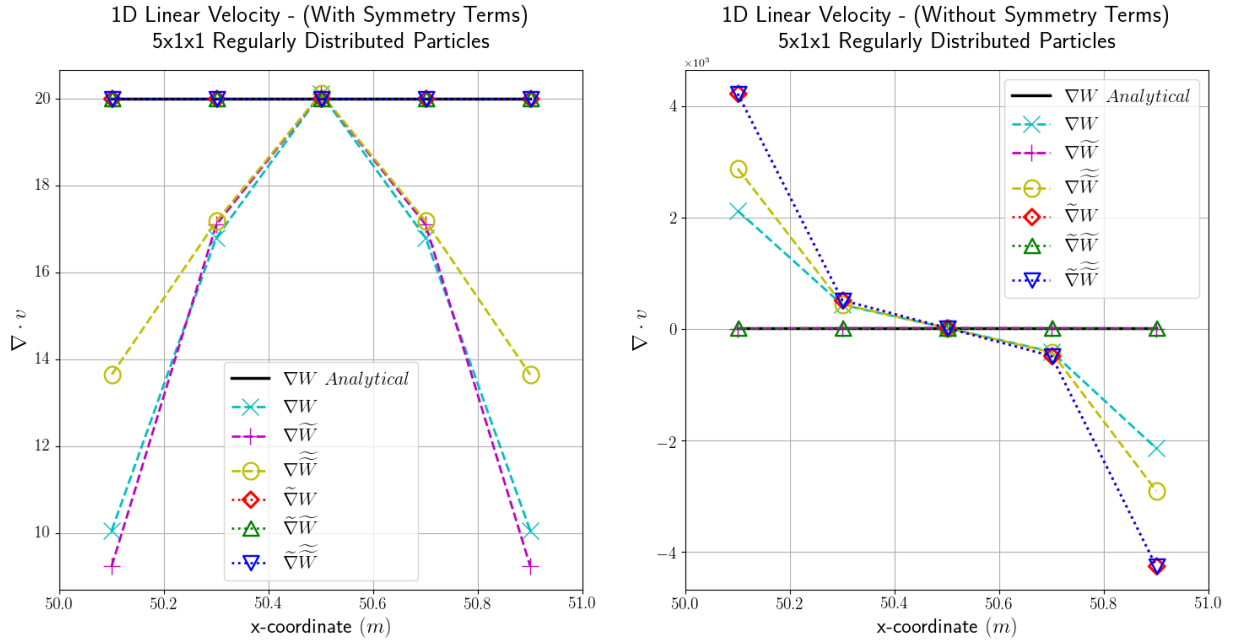


(a) With symmetry terms (Eq. 2.91b).

(b) Without symmetry terms (Eq. 2.91a).

Fig. 2.11.: Velocity divergence of a 5-points bar under a constant velocity field.

divergence vanishes when using a symmetrical formulation with a constant field. In this case, no corrections at the boundary points are necessary, it can be explained by the fact that the internal contributions within each pair are equal and opposite. On the other side, for non-symmetrical formulations (Fig. 2.11b), among the forms of mixed kernel and gradient corrections (Eqs. 2.62 and 2.63), only the versions derived from (Eq. 2.61a and 2.63b) ensure values of null divergence of the velocity field. If the computation cost must be taken into account, for a non-complex problem like this one, the choice of a formulation without symmetry terms seems to be inefficient and all the correction procedures can just be replaced by a formulation with symmetry terms.



(a) With symmetry terms (Eq. 2.91b).

(b) Without symmetry terms (Eq. 2.91a).

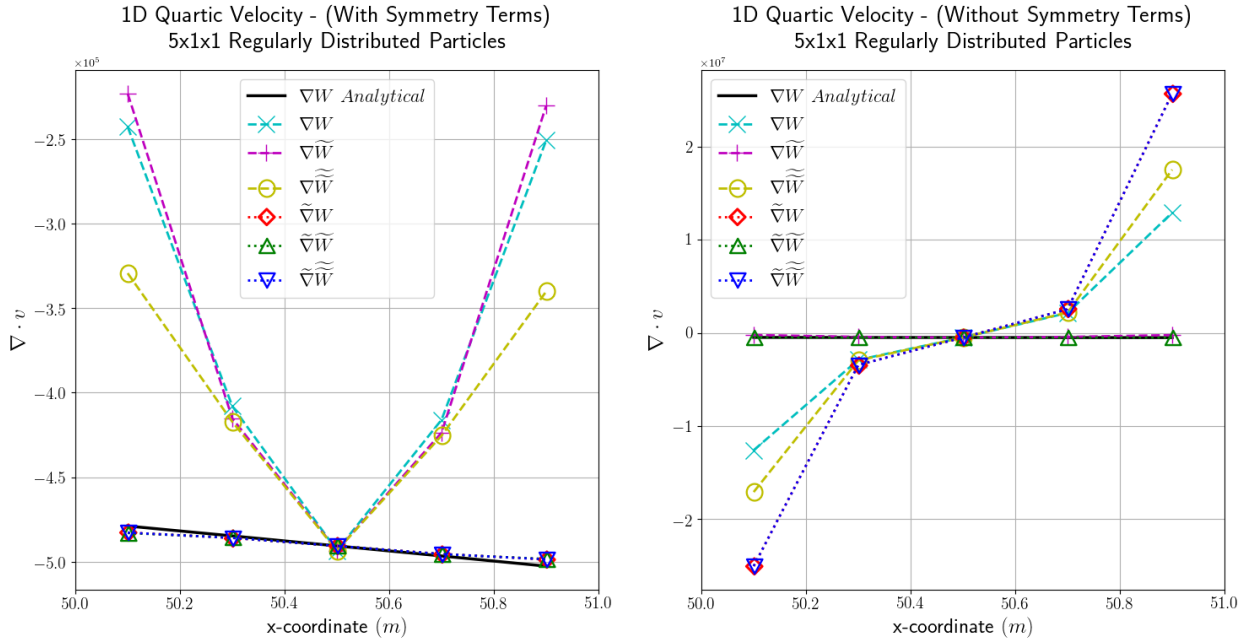
Fig. 2.12.: Velocity divergence of a 5-points bar under a linear velocity field.

In the next test a linear velocity field (Eq. 2.92b) is applied to all material points. The expected constant value of the velocity divergence along the bar is no longer obtained by the formulation with symmetry terms Fig. 2.12a. Only the use of the corrected gradient forms from (Eqs. 2.63) is able to recover accurate solutions. Fig. 2.12b shows that the mixed kernel and gradient corrections given by (Eqs. 2.61a and 2.63b) are the only ways to ensure a constant velocity divergence.

Finally, we observe from Fig. 2.13a where the velocity field is given by a quartic function (Eq. 2.92c), that symmetrical and non-symmetrical formulations present an quite similar behaviour compared to the linear velocity field, with inverse sign and even larger magnitude difference. This time, the mixed kernel and gradient corrections given from Eq. (2.63c) are not as close to the analytical solution as before.

We see that the deviation of the formulation without symmetric terms in the previous results is much more important than the one with symmetric terms, which justifies the adoption of the symmetrical terms formulation in next sections. In addition, in Fig. 2.15 only three formulations with symmetry terms of mixed correction of gradient of kernel (Eqs. 2.63) are presented.

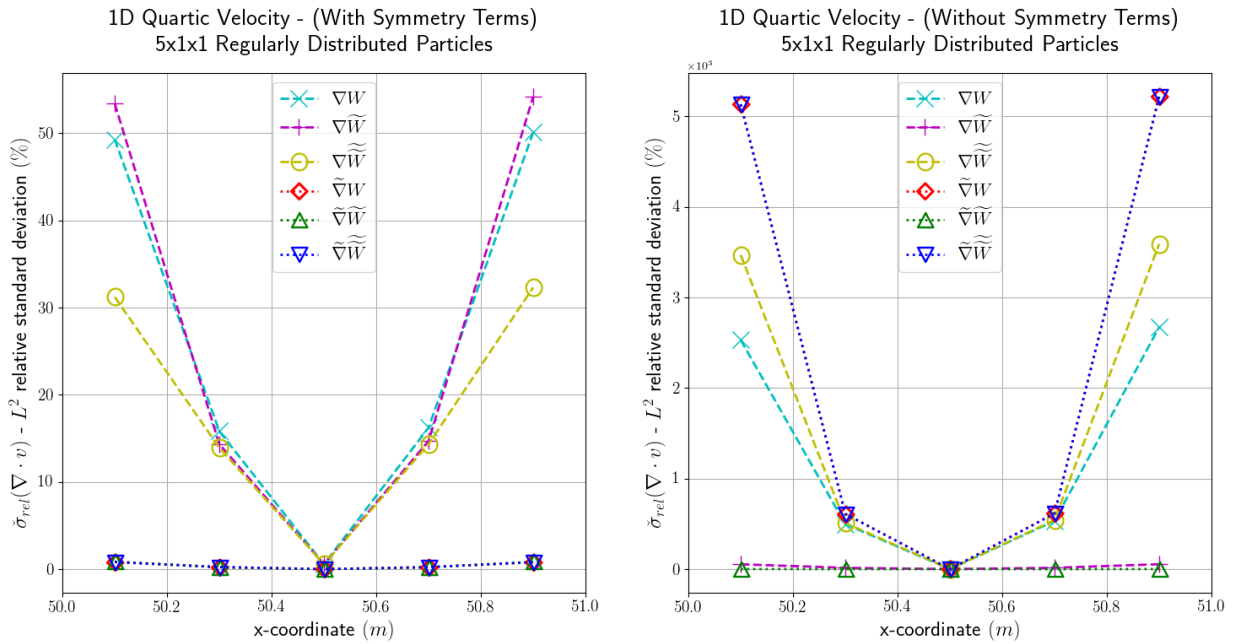
The maximal relative errors presented in Fig. 2.14 are close to 0.8% for all mixed correction forms, which is low enough to ensure accurate solutions. We observe from Fig. 2.15 that the mixed corrections given by (Eqs. 2.63) present similar results. In



(a) With symmetry terms (Eq. 2.91b).

(b) Without symmetry terms (Eq. 2.91a).

Fig. 2.13.: Velocity divergence of a 5-points bar under a quartic velocity field.

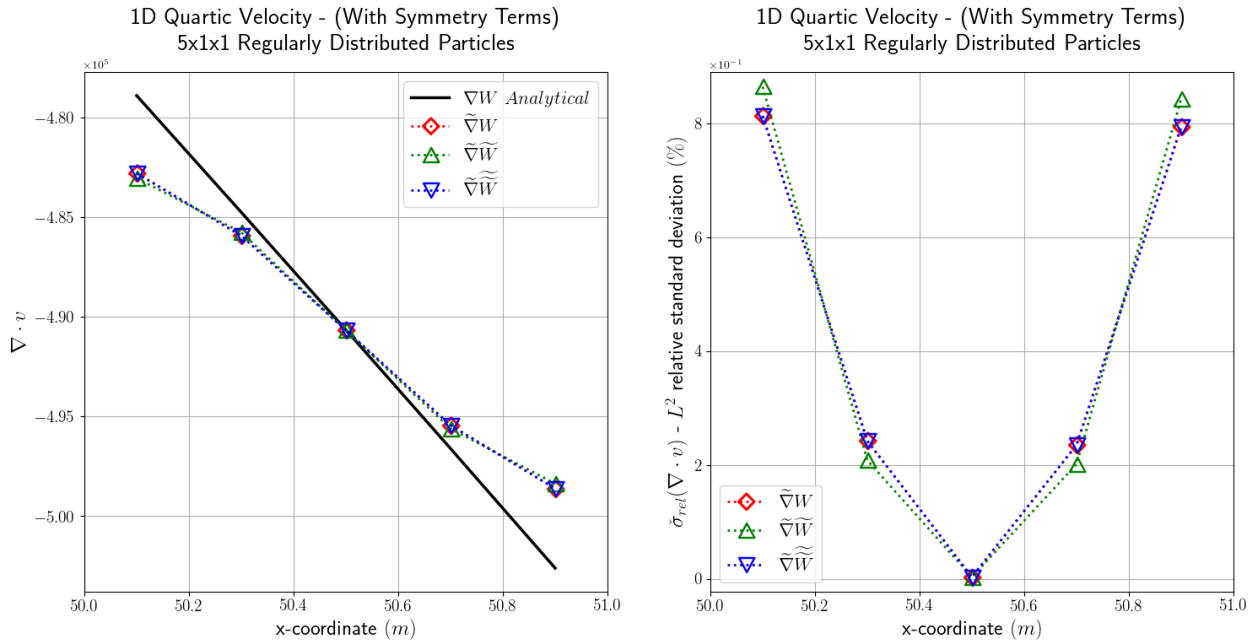


(a) With symmetry terms (Eqs. 2.91b and 2.93).

(b) Without symmetry terms (Eqs. 2.91a and 2.93).

Fig. 2.14.: Relative error (Eq. 2.93) of velocity divergence of a 5-points bar under a quartic velocity field.

addition, the mixed gradient and kernel correction (Eqs. 2.63b - as presented by gives slightly better results for internal points and worse results for boundary points.



(a) Velocity divergence (Eq. 2.91b).

(b) Relative error (Eq. 2.93).

Fig. 2.15.: Velocity divergence computed by mixed correction kernel gradient of a 5-points bar under a quartic velocity field.

2.5.2 Influence of particles density

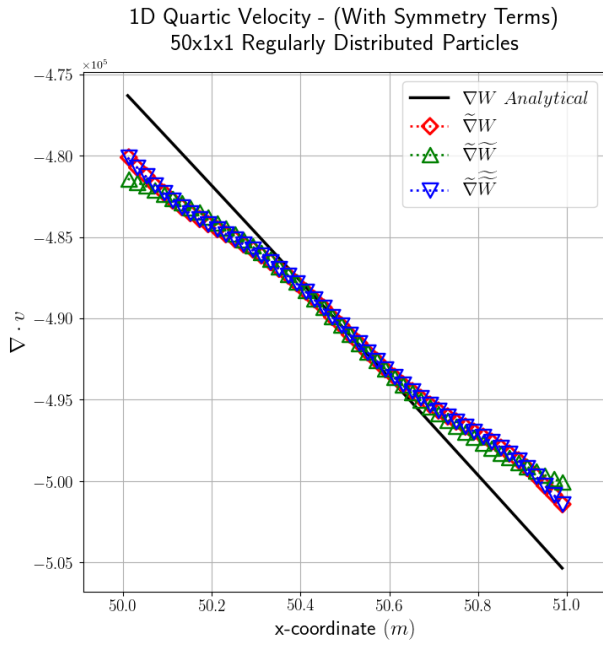
In this section we analyse the influence of the density of discretisation points along the bar. By keeping exactly the same configuration, we increase the quantity of material points without changing the size of the bar or the smoothing length h .

We observe that the two configurations with 50 (Fig. 2.16a) and with 500 (Fig. 2.17a) points present a quite similar behaviour with the 5-points case. In all cases, the relative error is smaller than 1.2%.

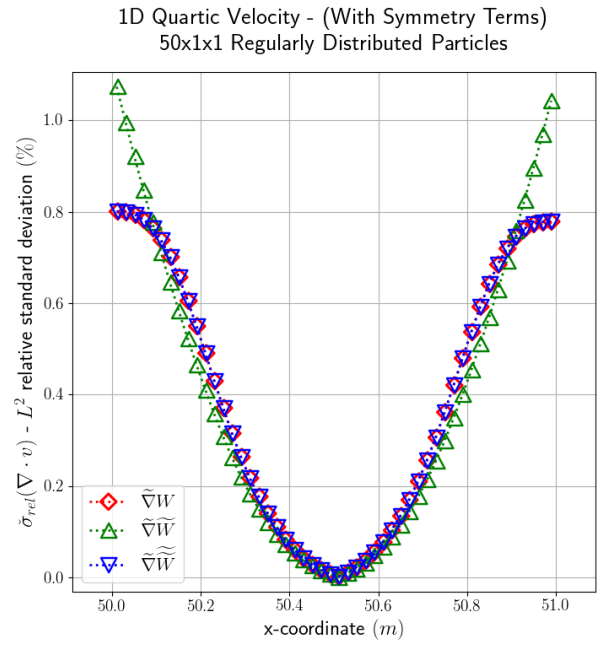
2.5.3 Influence of particles disorder

Finally, we test a disordered distribution of material points along the bar. We maintain the same simulation conditions as before.

From Fig. 2.18, Fig. 2.19 and Fig. 2.20, the influence of the particle distribution is the most important for the 5-points bar, but even in this case, the relative error is of around 1%. Therefore, the higher the number of material points, the more the result is independent of on the point disorder.

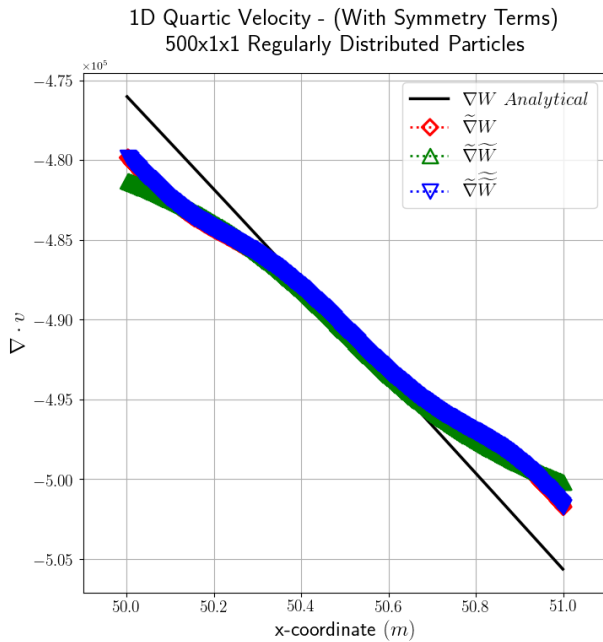


(a) Velocity divergence (Eq. 2.91b).

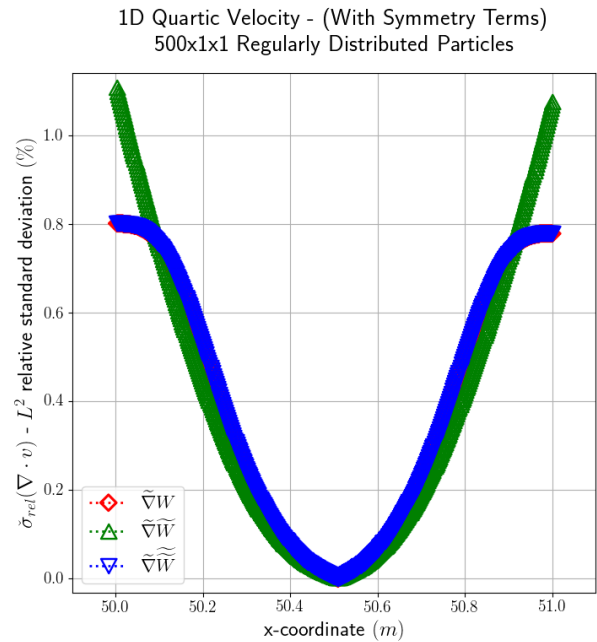


(b) Relative error (Eqs. 2.93) and (2.93).

Fig. 2.16.: Velocity divergence computed by mixed correction kernel gradient of a 50-points bar under a quartic velocity field.

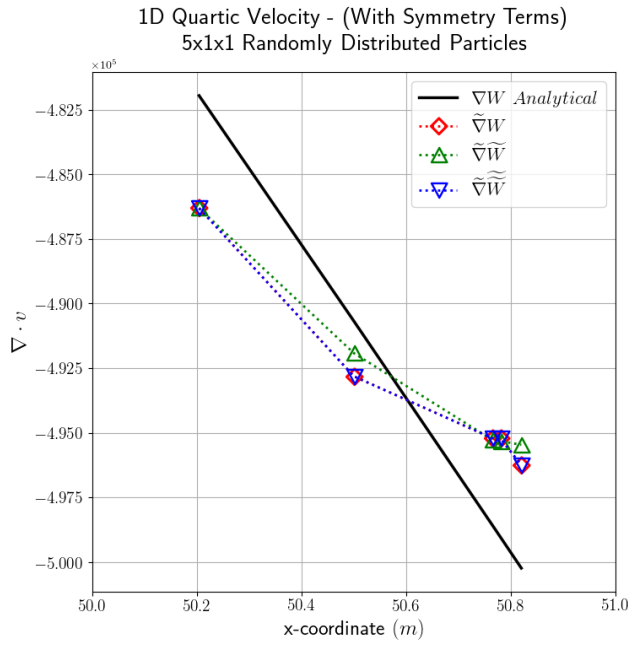


(a) Velocity divergence (Eq. 2.91b).

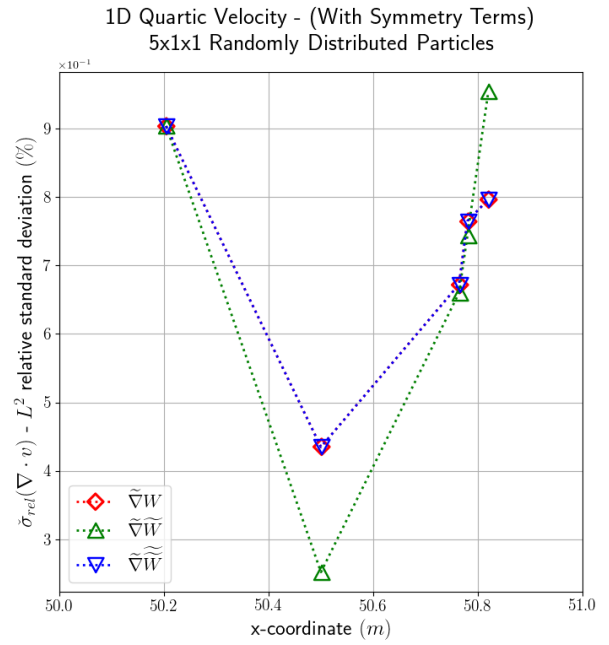


(b) Relative error (Eq. 2.93).

Fig. 2.17.: Velocity divergence computed by mixed correction kernel gradient of a 500-points bar under a quartic velocity field.

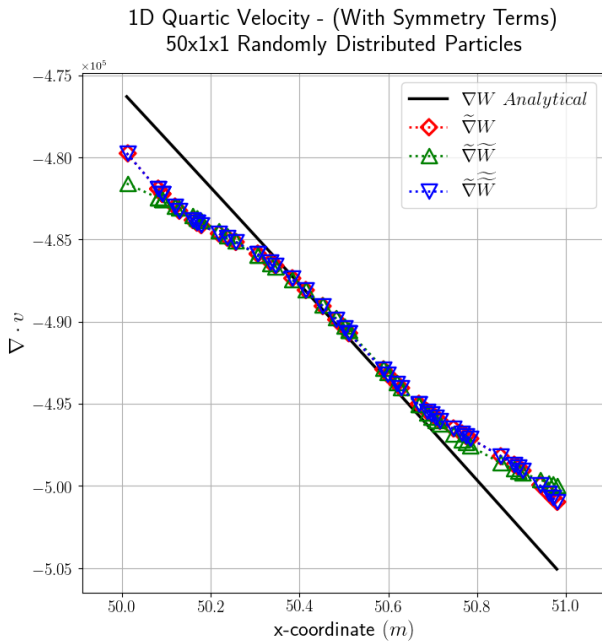


(a) Velocity divergence (Eq. 2.91b).

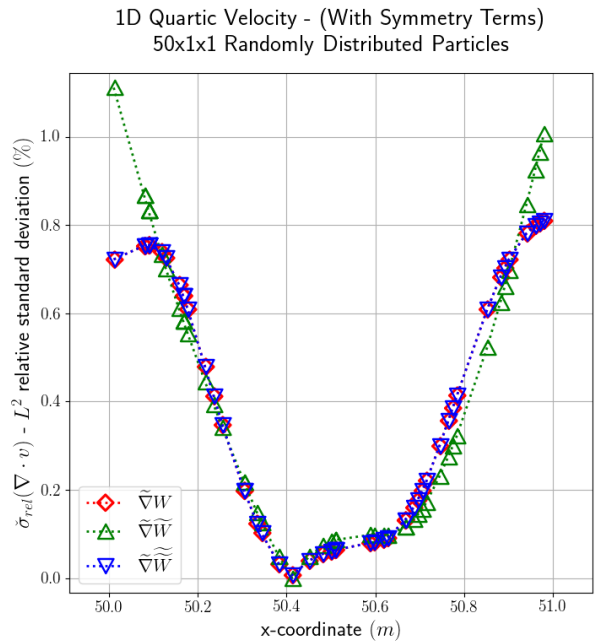


(b) Relative error (Eq. 2.93).

Fig. 2.18.: Velocity divergence computed by mixed correction kernel gradient of a 5 randomly distributed particles bar under a quartic velocity field.

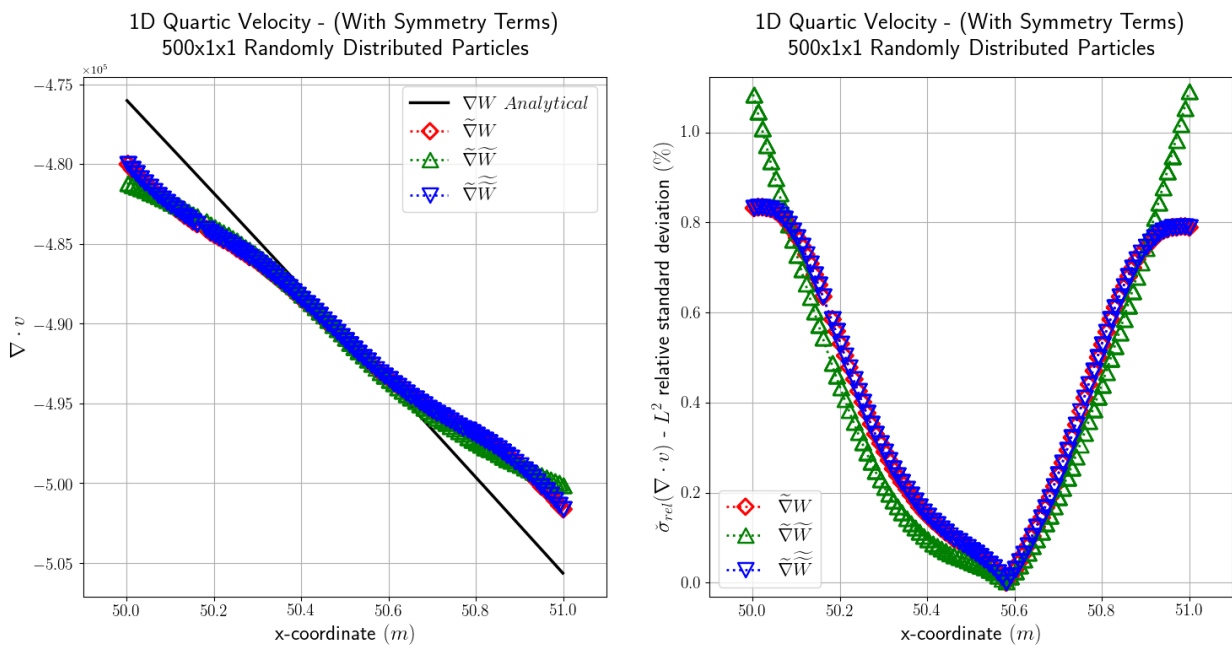


(a) Velocity divergence (Eq. 2.91b)



(b) Relative error (Eq. 2.93)

Fig. 2.19.: Velocity divergence computed by mixed correction kernel gradient of a 50 randomly distributed particles bar under a quartic velocity field



(a) Velocity divergence (Eq. 2.91b)

(b) Relative error (Eq. 2.93)

Fig. 2.20.: Velocity divergence computed by mixed correction kernel gradient of a 500 randomly distributed particles bar under a quartic velocity field

2.5.4 From 1D to 3D validation

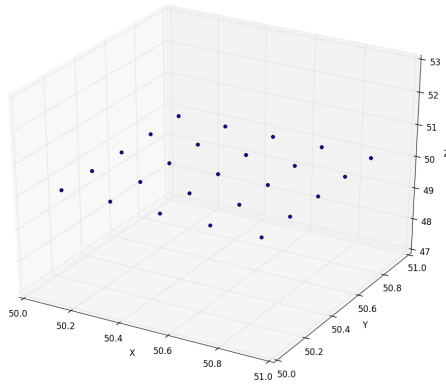
Given the detailed discussion presented previously about the 1D configuration, this section proposes to extend this analysis to 2D (Fig. 2.21a) and 3D (Fig. 2.21b) cases. The new configurations take into account 5 particle per axis following linear (Eqs. 2.94) or quartic (Eqs. 2.95) velocity fields:

$$\underline{v}_2^{2D}(x, y) = 20x \hat{e}_x + 20y \hat{e}_y \quad (2.94a)$$

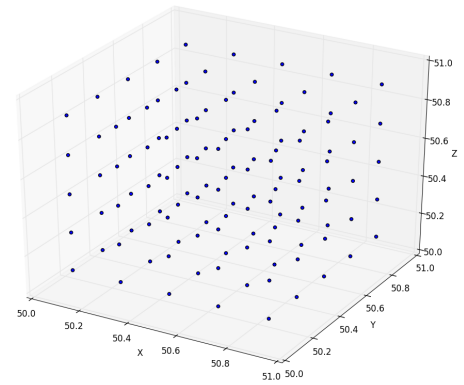
$$\underline{v}_2^{3D}(x, y, z) = 20x \hat{e}_x + 20y \hat{e}_y + 20z \hat{e}_z \quad (2.94b)$$

$$\begin{aligned} \underline{v}_3^{2D}(x, y) = & (-4x^4 + 3x^3 + 15x^2 - x + 15) \hat{e}_x + \\ & (-4y^4 + 3y^3 + 15y^2 - y + 15) \hat{e}_y \end{aligned} \quad (2.95a)$$

$$\begin{aligned} \underline{v}_3^{3D}(x, y, z) = & (-4x^4 + 3x^3 + 15x^2 - x + 15) \hat{e}_x + \\ & (-4y^4 + 3y^3 + 15y^2 - y + 15) \hat{e}_y + \\ & (-4z^4 + 3z^3 + 15z^2 - z + 15) \hat{e}_z \end{aligned} \quad (2.95b)$$



(a) 2D

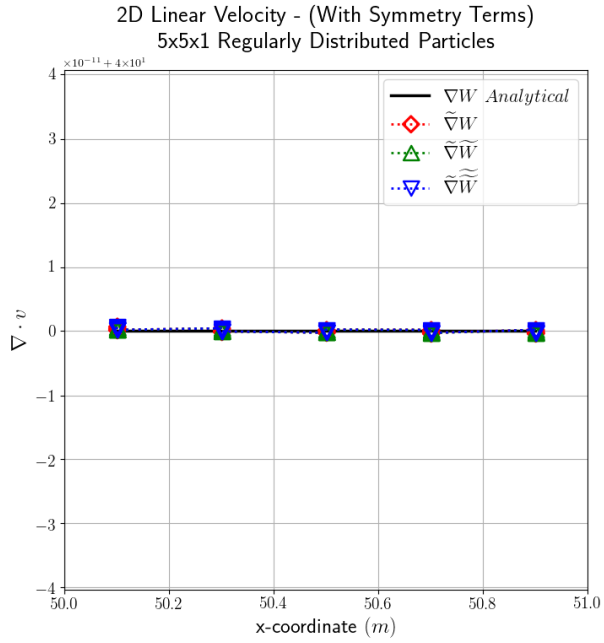


(b) 3D

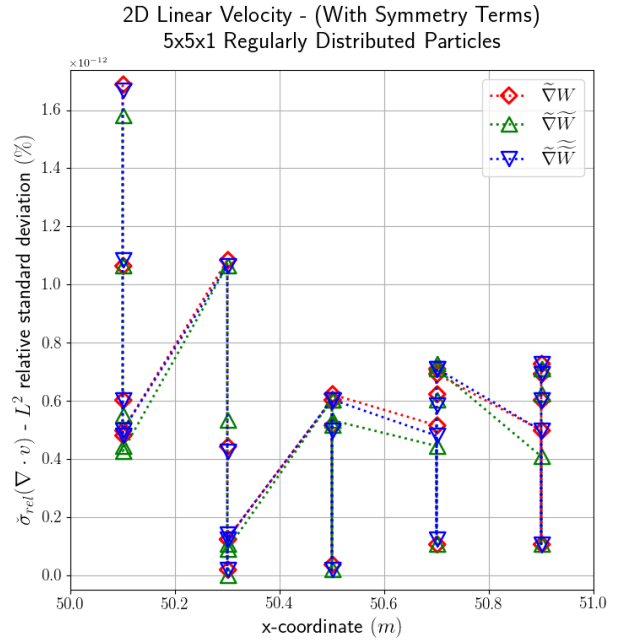
Fig. 2.21.: 2D and 3D particles distribution

Three formulations of mixed kernel-and-gradient corrections (Eqs. 2.63) are tested. The calculation results are shown on graphs with all particles present in the system following their x-coordinate.

We observe for the linear velocity field (2D - Fig. 2.22 and 3D - Fig. 2.23), that the computed variables present an error of about $\sim 10^{-14}$. For quartic velocity fields (2D - Fig. 2.24 and 3D - Fig. 2.25), the error is of about $\sim 1\%$, which is the same relative error as in the 1D configuration. This validates our calculation method also in 2D and 3D.

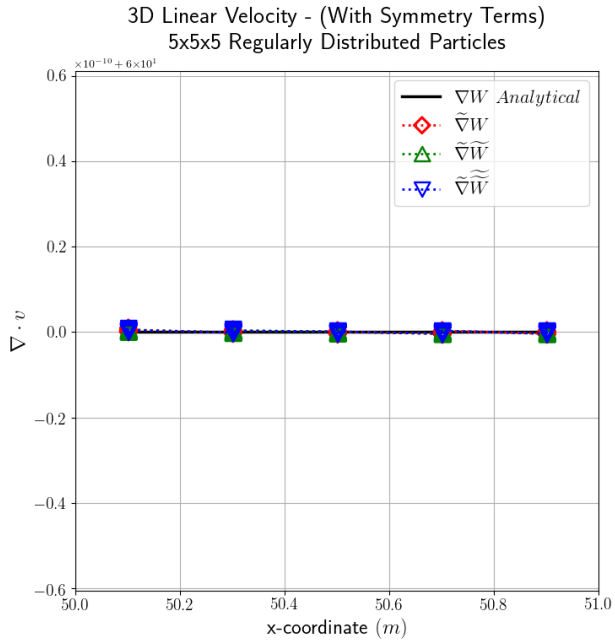


(a) 2D velocity divergence (Eq. 2.91b)

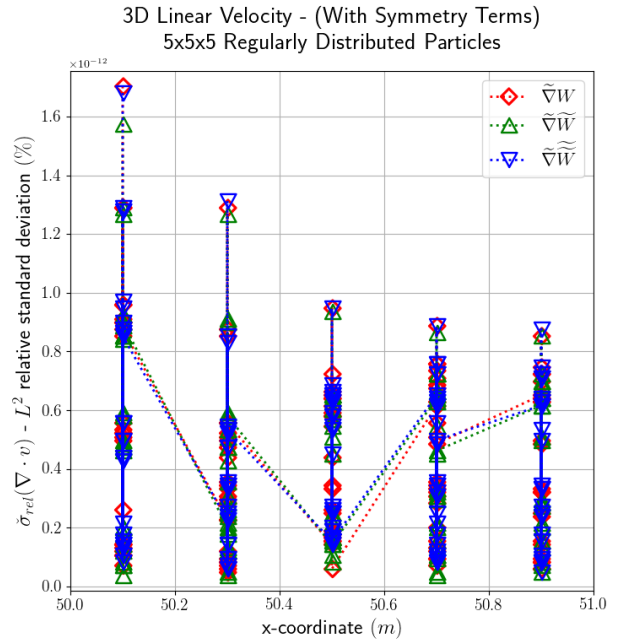


(b) Relative error (Eq. 2.93)

Fig. 2.22.: 2D Velocity divergence computed by mixed correction kernel gradient of a 25 particles discretized plan under a linear velocity field

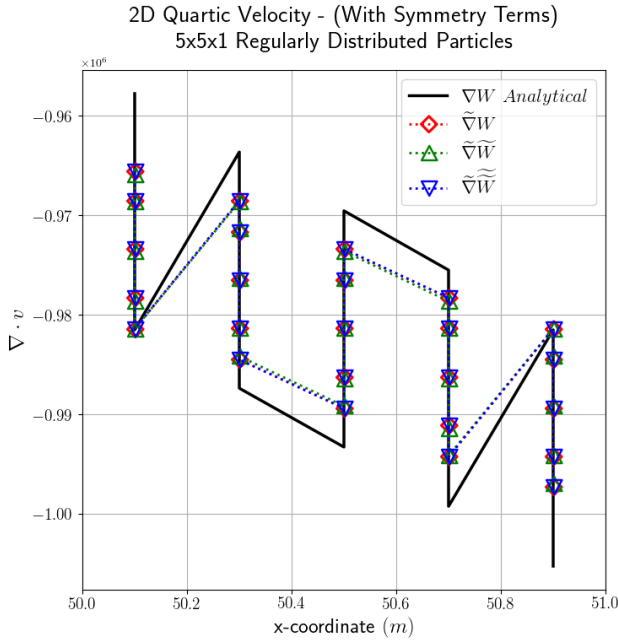


(a) 3D velocity divergence (Eq. 2.91b)

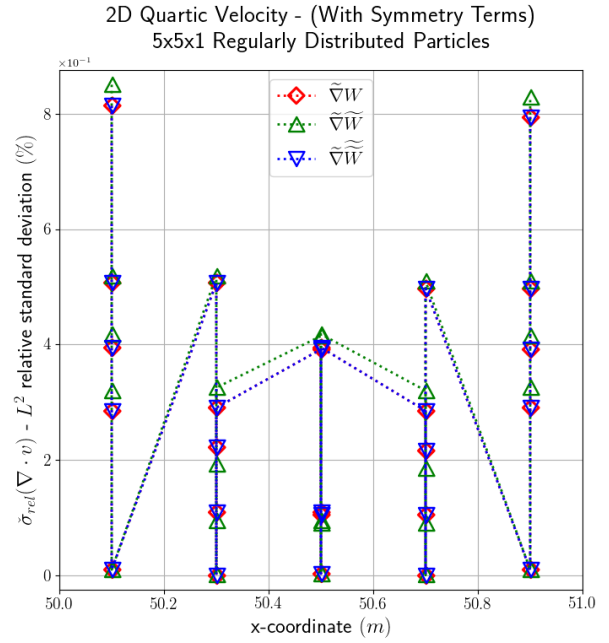


(b) Relative error (Eq. 2.93)

Fig. 2.23.: 3D Velocity divergence computed by mixed correction kernel gradient of a 125 particles discretized volume under a linear velocity field

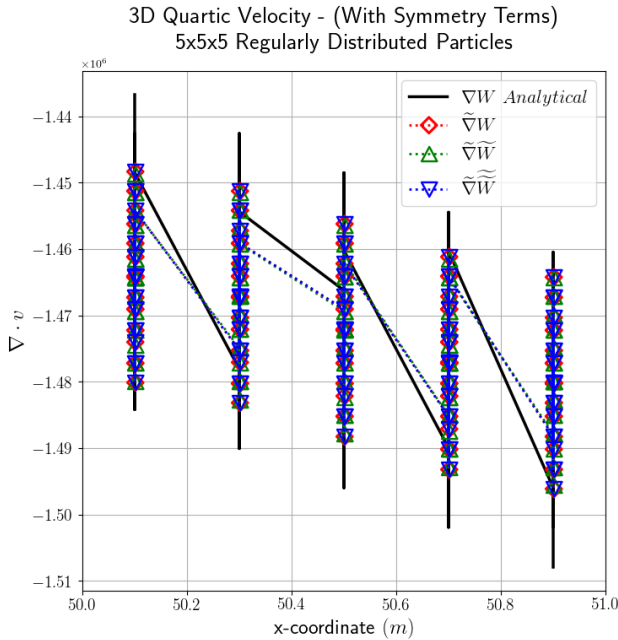


(a) 2D velocity divergence (Eq. 2.91b)

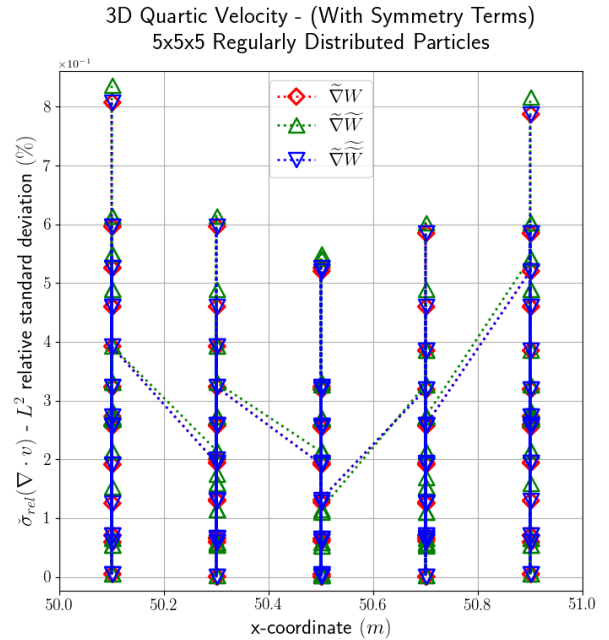


(b) Relative error (Eq. 2.93)

Fig. 2.24.: 2D Velocity divergence computed by mixed correction kernel gradient of a 25 particles discretized plan under a quartic velocity field



(a) 3D velocity divergence (Eq. 2.91b)



(b) Relative error (Eq. 2.93)

Fig. 2.25.: 3D Velocity divergence computed by mixed correction kernel gradient of a 125 particles discretized volume under a quartic velocity field

2.6 SPH as a local EDP solver for elastic media

This section discusses and validates the capability of the SPH solver to describe the evolution of an elastic solid material. Different applications may require specific corrections to simulate them regularly and stably for this kind of materials, and there are no general optimal solutions. Here, we evaluate the most pertinent approaches and improvements to treat elastic dynamics problems. To this purpose, we simulate a classical validation case of a 1D bar with an initial constant velocity applied in its first quarter (as presented in Fig. 2.26). This initial condition results in significant velocity jumps, which also mean important gradient values along the bar. Besides, we work here with an SPH code version based on the finite deformation approach (SVK-SPH - Eqs. 2.81) with some additives like XSPH and artificial viscosity.

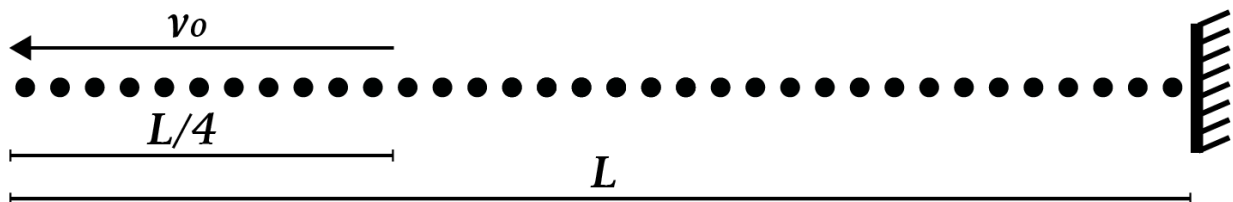


Fig. 2.26.: Clamped-free boundary conditions of a 40 material points bar for SPH validation as EDP solver.

This test is often used as a test-case for tensile instability solutions, as introduced for SPH by Dyka and Ingel [59]. Bonet and Kulasegaram [26] have used this test to validate a hypoelastic large deformation SPH version, Their study adopted the mixed normalisation and correction of the kernel function $\widetilde{\nabla}\widetilde{W}$. This formulation is quite close to the one presented in this work since a mixed normalised and corrected version of the SPH and Saint Venant-Kirchhoff SPH (SVK-SPH) approaches are used here.

Parameter	Sign	Value
Young modulus	E	200 [GPa]
Linear mass density	ρ	7833 [kg/m]
Bar length	L	0.1333 [m]
Number of material points	N	40 [-]
Time step	Δt	10^{-7} [s]
Initial velocity	v_0	-5 [m/s]

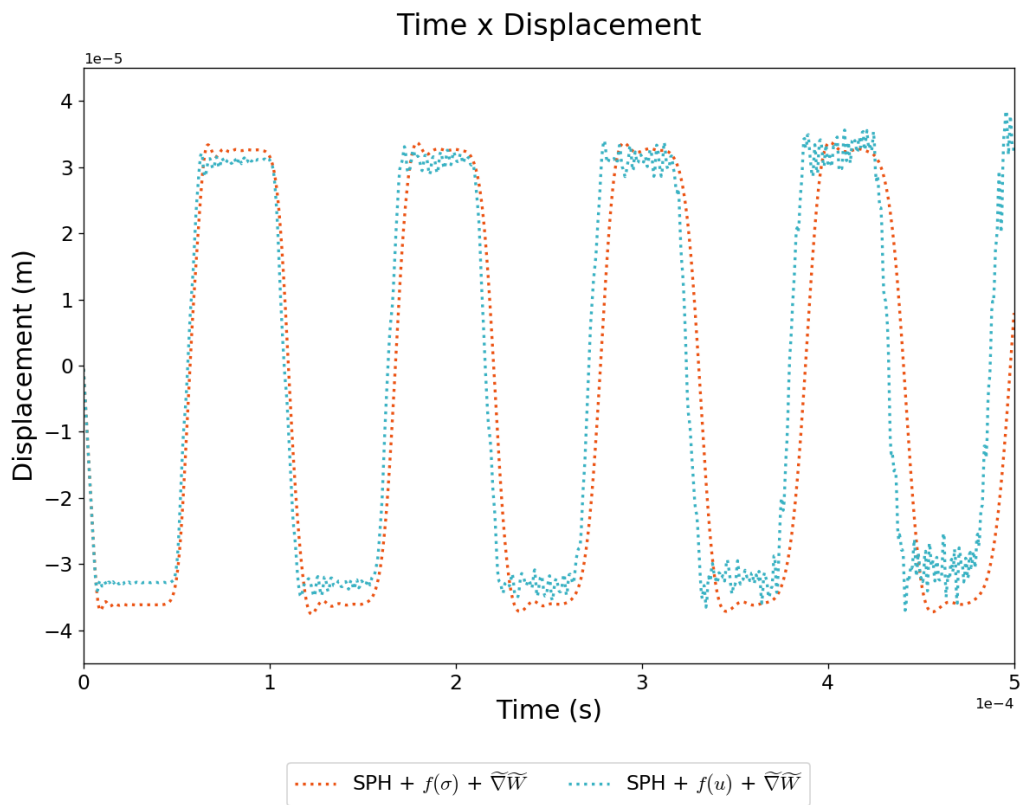
Tab. 2.3.: Input data for a 1D bar problem for SPH validation as a local EDP solver.

The bar is discretised with 40 uniformly distributed material points, it is free at the left-end and clamped at the right-end. Ghost particles algorithm is adopted at the fixed-side in order to ensure the appropriate boundary conditions. Also, velocity v_0 is imposed as an initial condition in the left quarter of the bar. The input data with material properties and simulation parameters are presented in Tab. 2.3.

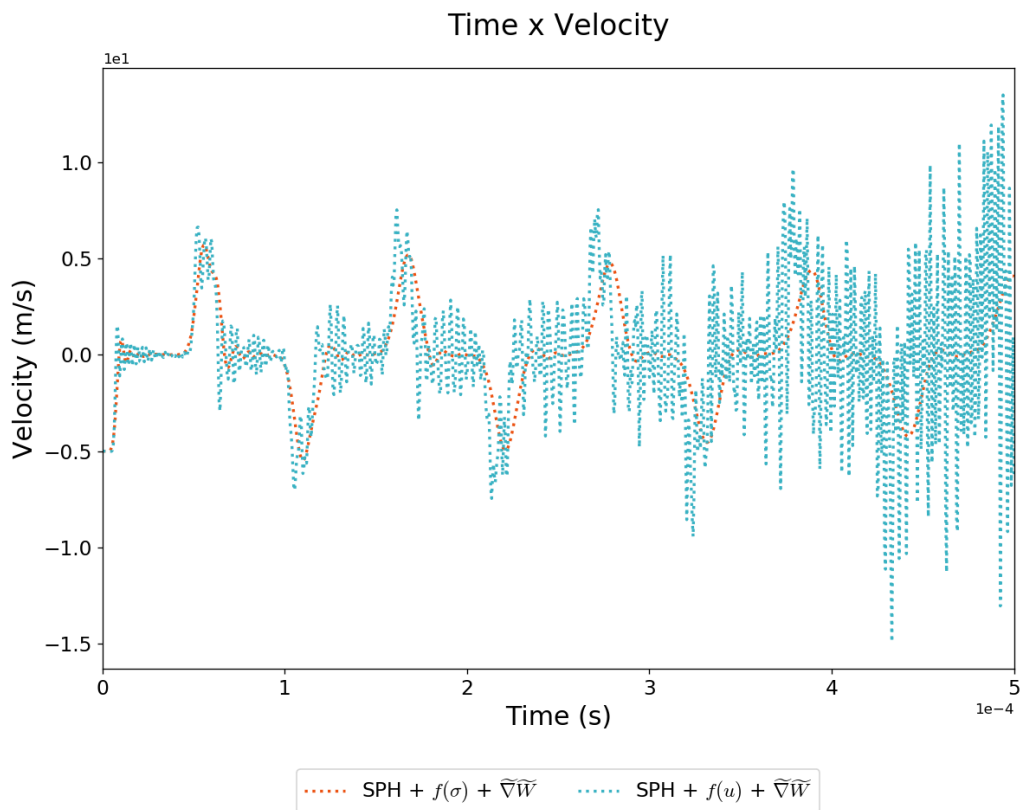
In Fig. 2.27a the early time evolution of displacement of the first left-side material point is presented. It compares our SVK-SPH to a SPH version enhanced with stress points as proposed by Dyka and Ingel [59], a Finite Element Method and the mixed and corrected Total Lagrangian (TLSPH) with $\widetilde{\nabla}\widetilde{W}$ as proposed by Bonet and Kulasegaram [26]. As expected, the two large deformation models present a quasi-similar time evolution, with the exception of a shorter period of vibration for the SVK-SPH. Both large deformation formulations present better stability than the stress points SPH. The velocity of the first material point is presented in Fig. 2.27b. Similarly to the displacement evolution, the mixed corrected large deformation formulations are more stable with small differences of period and amplitude.

2.6.1 Stress and displacement-based momentum equations for small deformations

In this part, we compare the displacement-based and the stress-based formulations (in a small deformations description) of the momentum equation presented in Sec. 2.4.2. This simple application is also used to validate the SPH approaches based on small and large deformations (Sec. 2.4). Lastly, beyond the validation of our large deformation framework, this section shows also the results of the numerical improvements presented in Sec. 2.3 such as XSPH and artificial viscosity. The displacement and velocity evolution (Fig. 2.28) show that the $f(\sigma)$ version present a less noisy maxima and minima amplitudes. Nevertheless, both formulations are used for investigations of optimisation approaches.



(a) Displacement evolution of the last free material point.



(b) Velocity evolution of the last free material point.

Fig. 2.28.: Mixed normalised and corrected versions of the small deformations SPH models: stress-based and displacement-based

2.6.2 Small and large deformations

Dyka and Ingel [59] noted that due to the appearance of tensile instability, this problem could not be solved by the classical version of SPH (small deformations). We observe that this assumption is not valid for our version of mixed normalised and corrected kernel SPH (Fig. 2.29a), despite its slightly more extended period oscillations. From the velocity evolution shown in Fig. 2.29b, such instability becomes more critical in large deformations SPH version. The displacement evolution of the 1st material point shows little difference between SPH and SVK-SPH models, which does not seem to invalidate these formulations.

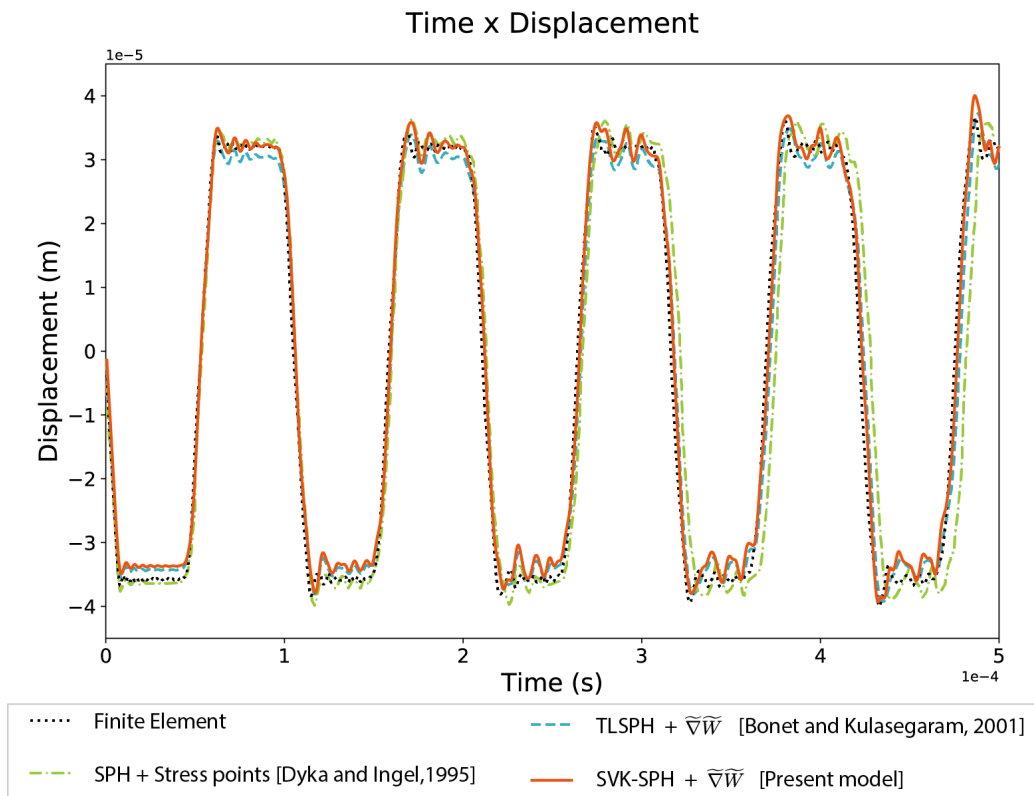
2.6.3 XSPH and artificial viscosity

The previous results can be improved by correcting the velocity noise with XSPH (which acts in all load conditions) and by adding the artificial viscosity acting in tensile loading. Fig. 2.30 shows for an $\hat{\epsilon} = 0.5$ in (Eq. 2.66) a slight reduction of oscillations for both formulations. In addition, the artificial viscosity with parameters $\check{\alpha} = 0.2$ and $\check{\beta} = 0.4$ in (Eq. 2.64) results in a significant noise reduction for the same formulations.

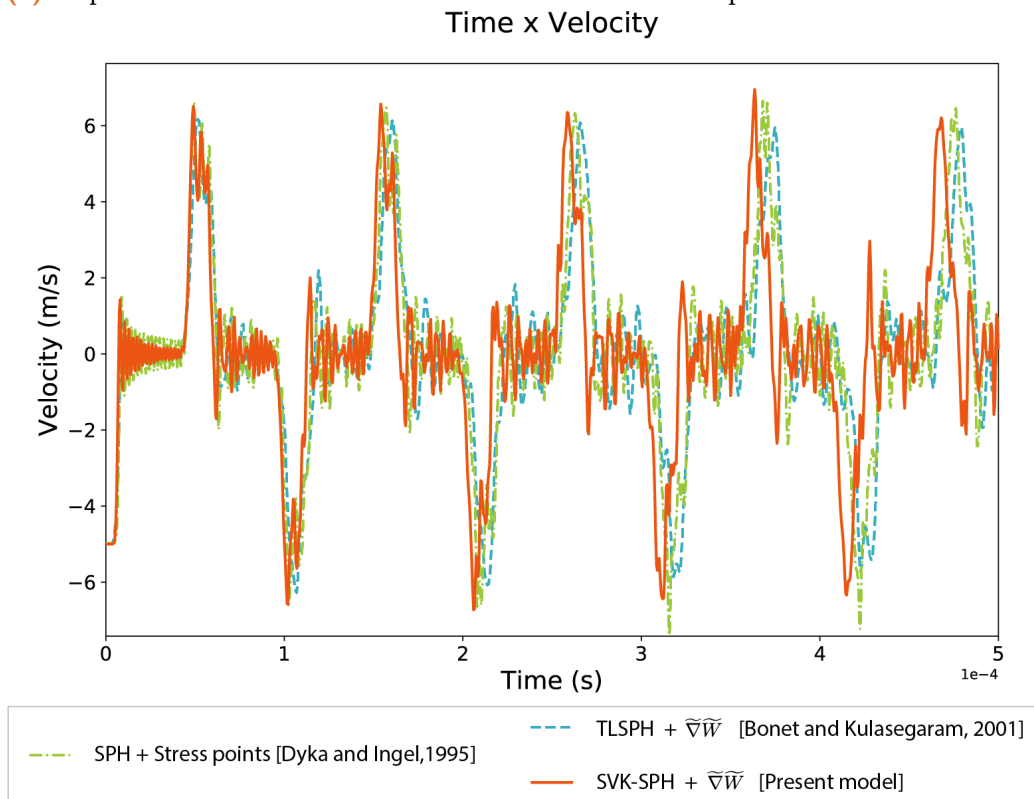
Based on these results, the numerical improvements (artificial viscosity and XSPH) will be incorporated in the SPH method to be used in the following chapters.

Concluding remarks

In this chapter, we have first summarised the mathematical approaches to represent a physical domain by the discrete SPH method. The representation of the function and its derivative operators were introduced in different dimensions. Various drawbacks corrections for SPH were recalled. In particular, we implemented the so-called corrected kernel and corrected gradient functions to account for existing domain limits and alternative primary variable formulations. We also implemented a Total Lagrangian version of SPH to solve a large deformations problem (through the Saint Venant-Kirchhoff constitutive model). Moreover, we have proposed a set of validation tests and discussions about the capability of our numerical EDP solver to describe the vibration of elastic solid. The validation tests have presented satisfactory results for simple configuration and boundary conditions compared to analytical and other existing numerical solutions.

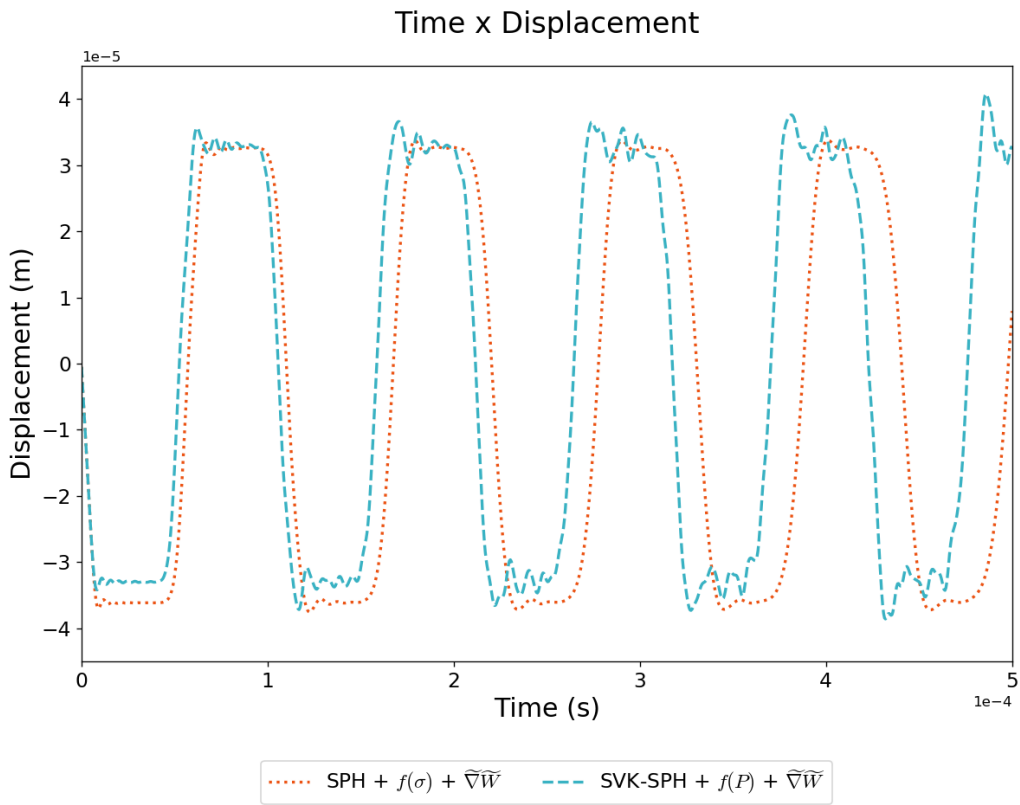


(a) Displacement evolution over time of the last free material point.

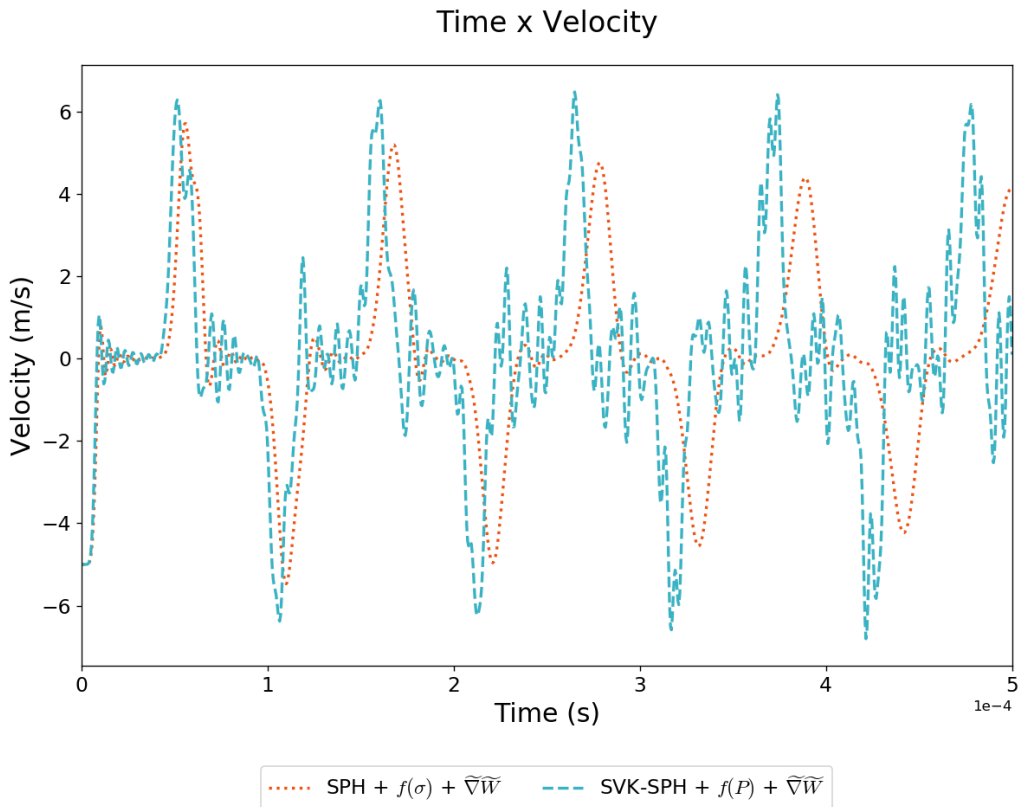


(b) Velocity evolution over time of the last free material point.

Fig. 2.27.: Comparison between Saint Venant-Kirchhoff SPH, FEM (for displacement only), Stress points SPH [59] and Total Lagrangian SPH [26]. The SVK-SPH presented here adopts the mixed normalisation and correction of the kernel functions and a stress-based momentum equation discretisation.

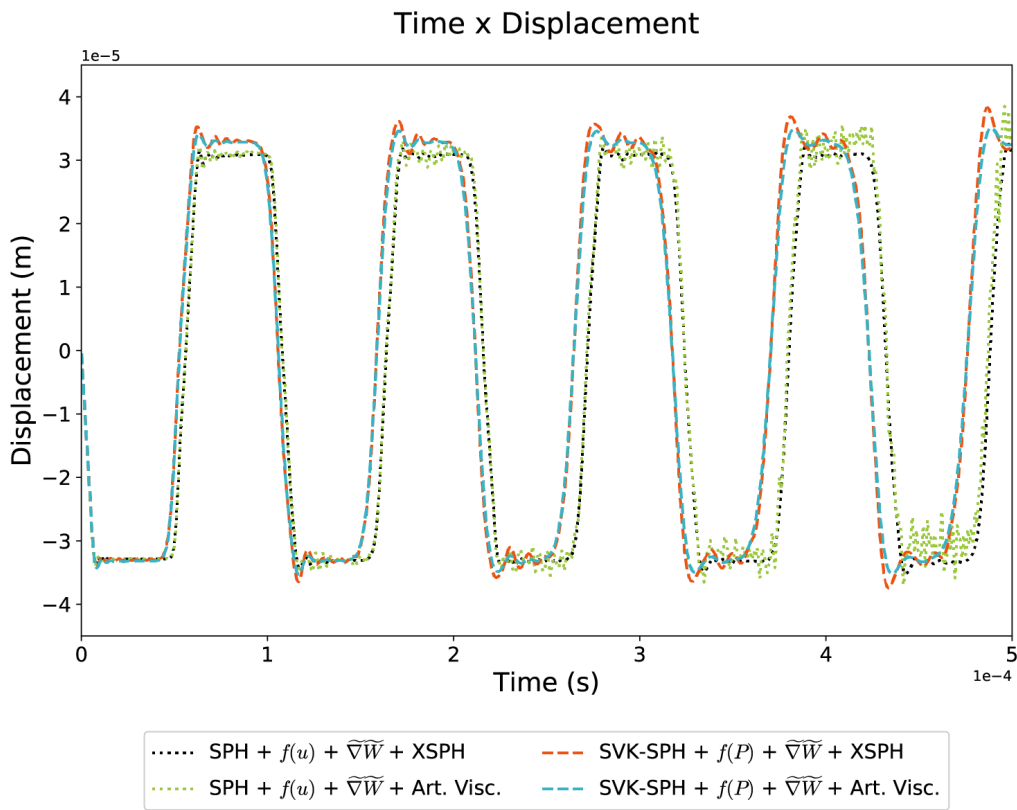


(a) Displacement evolution of the last free material point.

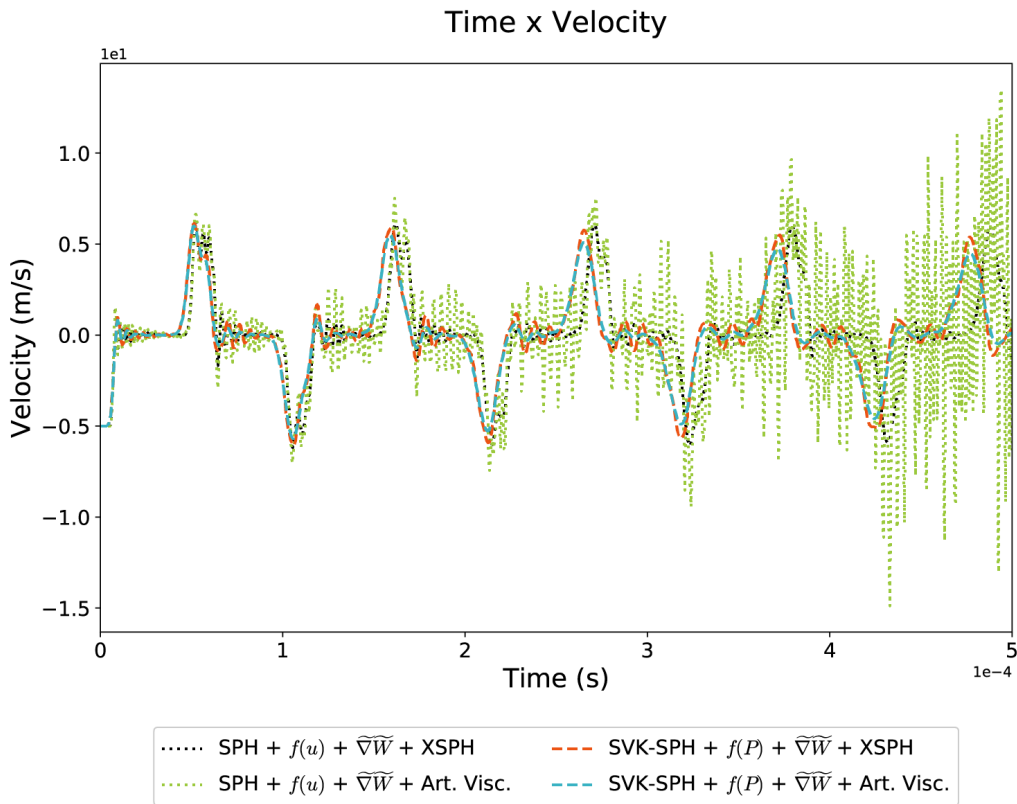


(b) Velocity evolution of the last free material point.

Fig. 2.29.: Mixed normalised and corrected version of the small (SPH) and large deformations (SVK-SPH) approaches compared by their displacement and velocity evolution.



(a) Displacement evolution over time of the last free material point.



(b) Velocity evolution over time of the last free material point.

Fig. 2.30.: Numerical improvements for mixed normalised and corrected versions of small deformations SPH and large deformations SVK-SPH model: XSPH ($\epsilon = 0.5$) and Artificial viscosity ($\check{\alpha} = 0.2$ and $\check{\beta} = 0.4$).

Overview: This chapter consists in a submitted paper that explores the capabilities of the SPH method to deal with non-local effects in elasticity. This is achieved through finite support domains of the SPH kernel function independently of the discretisation. In a 1D vibration problem, SPH results are compared to analytical (discrete and continuous) solutions. Lastly, we investigate the SPH invariance using finite or infinite domain kernel functions and using stress-based or strain-based gradient formulations.

Modelling non-local elasticity in 1D vibrating rods using Smoothed Particle Hydrodynamics method

Rafael C. Deptulski^{a,b,*}, Magdalena Dymitrowska^a and Djimédo Kondo^b

^a*PSE-ENV/SEDRE/LETIS, Institut de Radioprotection et de Sécurité Nucléaire (IRSN), 31 Avenue de la Division Leclerc, 92260 Fontenay-aux-Roses, France*

^b*Sorbonne Université, Institut Jean le Rond d'Alembert - UMR 7190, 4 Place Jussieu, 75005 Paris*

ARTICLE INFO

Keywords:

non-local elasticity
generalized continuum mechanics
vibrating rods
SPH

ABSTRACT

The present study aims to assess the use of the Total Lagrangian Smoothed Particles Hydrodynamics (SPH) method predicting non-local elastic effects in finite deformations. For this aim, we first recall the discrete and continuum analytical solutions of a 1D bar under longitudinal harmonic vibrations with small scale effects. In the SPH approach, the constitutive laws do not present any additional term, and the non-locality is introduced only through the kernel convolution. Contrary to the classical use of the SPH method, the simulations are conducted with a finite smoothing length, which may be related to the characteristic size of the microstructure.

The numerical results obtained from the 1D bar simulations under different boundary conditions demonstrate that the SPH method can capture the non-local effects in dynamics independently of the discretization points density. In detail, it is shown that the numerical results have a good agreement with available analytical solutions. Moreover, it is observed that SPH strain-based and stress-based formulations lead to similar responses. Finally, we provide a discussion about the finite and infinite support kernel functions.

Introduction

Low permeability argillite rocks are commonly studied as potential hosts for geological nuclear waste disposals or CO₂ storage. In nuclear waste disposals, gases (mainly dihydrogen) are expected to be generated, namely by anoxic corrosion of different metallic components of waste packages and disposal structures. The quantity of iron can be used to evaluate the amount of hydrogen released through this process and shows that the gas-phase will probably be formed and could potentially attain significant pressure during several tens or hundreds of thousands of years. Due to inherent argillite properties (like very small pore sizes, high confining pressures, and swelling capabilities related to significant clay fraction), the understanding of gas migration phenomena within them requires to take into account hydro-mechanical coupling.

To this end, it is possible to work directly on the pore-scale level with models describing direct displacement and deformation of different fluid and solid phases. Smoothed Particle Hydrody-

*Corresponding author

✉ rafael.deptulski@gmail.com (R.C. Deptulski); magdalena.dymitrowska@irsn.fr (M. Dymitrowska); djimedo.kondo@sorbonne-universite.fr (D. Kondo)
ORCID(s): 0000-0001-7810-123X (R.C. Deptulski)

namics (SPH) method allows to solve all kinds of partial differential equations within the same formalism and was applied recently to get a model of drainage in initial water-saturated Callovo-Oxfordian argillite (COx). This model considers a 2-phase flow within a realistic poral structure together with an elasticity with damage for the solid part [47]. The poral space was extracted from 3D imaging by FIB/SEM of one COx sample [53]. However, in order to conduct 3D simulations, and due to actual hardware limitations, only relatively small sub-samples can be used (size of about $1 \mu\text{m}^3$ in the case of [47]), which are much too small to account for a REV of the material. In this situation, one of the obvious choices is to work with the biggest possible sub-samples and with a limited numerical resolution with a significant resolution error, allowing rather for qualitative than quantitative results. In the SPH method, the situation is somehow more complicated since it has been shown previously that this method possesses a characteristic internal length is related to non-local effects in damage localisation [57]. Thus, it becomes essential to check the possibility of inducing the non-local effect in purely elastic models with limited resolution. This internal SPH length becomes non-negligible for the system size, which could sum up the discretisation error and destroy even the quantitative reliability of the simulations.

Non-local mechanical theories seek to represent how the large-scale properties and behaviour of materials are affected by deformation heterogeneity at a lower scale [26]. In the 18th century, Lagrange [35, 36] already investigated the presence of small-scale effects in an elastic material using a concentrated microstructure model. In particular, his work linked the fields of lattice models and continuum mechanics and motivated the study of non-local elasticity. Since then numerous contributions (see for instance, [34, 30, 25, 27]) proposed different mathematical models to account for small-scale effect on the corresponding macro-scale properties.

In particular, this domain has known a vast increase of interest since the correspondence was established between Lagrange lattice discrete model and continuum models introduced in the 60s through the integral strain-based model [34, 50]. This approach considers the non-local behaviour as a response computed from a non-local strain variable. However, it requires a more complex mathematical resolution given its kernel-integral form. Some decades later, Eringen has developed the non-local differential stress-based formulation (see, for instance, a compilation of his studies in [29]), which usually results in less complex mathematical expressions due to its differential form. In recent studies, Aydogdu [2, 3] and Challamel et al. [16, 11] have discussed the relations between different formulations of non-local continuum mechanics through a 1D longitudinal vibration problem. Their research focused on the influence of non-local variables present in continuum form on macroscopic responses. [16] also presented the correspondence between Lagrange lattice discrete model and the stress gradient-based non-local model [31].

In the domain of continuum non-local models, a wide discussion about the non-local characteristic parameter (usually denoted by e_0) can be found in the literature. In a configuration of direct interaction between two neighbour cells, Eringen [28] proposed an optimal value of $e_0 \approx 0.386$ through its continuum nonlocal theory based in the Born-Kármán model of lattice dynamics. Rose-neau [51], following Collins [20], have introduced the continualization approach based on different approximation operators which allow to achieve the equivalent non-local wave equation obtained in the method of Eringen. Inspired by the continualization method, Challamel *et al.* [14, 17] and Zhang *et al.* [66] presented in different studies the acquisition of such parameter as equal to $e_0 = \sqrt{1/12} \approx 0.218$ from the microstructured buckling model. Other results presented by Challamel et al. [15, 12] are obtained by the calibration between discrete and continua models. Lazar *et*

al. [37] have obtained the same values of e_0 by using the nonlocal elasticity of bi-Helmholtz type. In addition, different values of e_0 following multiple boundary conditions were presented by Wang *et al.* and [63]. Otherwise, some studies can be found based on different configurations taking into account indirect neighbouring interaction such as n-neighbour lattice interactions [52, 17] or higher-order finite difference formulation [13, 14].

Some studies have recently proposed analytical non-local solutions that can appropriately represent the response of an elastic bar under longitudinal vibrations (see for instance [2, 16]). In addition, the effects of the initial displacement amplitudes under longitudinal-transverse vibrations have been studied by several authors [21, 22, 59, 60]. It is worth noting that the order of magnitude of the vibration displacement may lead to small or large deformations, which we will account for in our investigations.

In this study, we present a new approach to deal with non-local effects by using a specific numerical method: Smoothed Particle Hydrodynamics (SPH). The principles of this method were introduced independently by Lucy [43] and Gingold and Monaghan [32] for treating astrophysical problems. Nowadays, it is widely applied to simulate, with good accuracy, transient dynamic problems with important local deformations of studied domains. Initially SPH has been largely employed in the fields of fluid dynamics [40, 41, 61, 10] including multiphase flows [45, 19]. Applications to solid mechanics have been explored since the 1990s after introducing the structural mechanics framework by Libersky and Petscheck [38, 39]. Besides, applications in other domains have also been made, for instance, in reactive transport [55] and heat transfer [18, 19].

The SPH is constructed as a Lagrangian points method that does not use a fixed grid and where a convolution assesses the properties of a material point with a kernel function over its neighbourhood. There are no predefined points of inter-connectivity that facilitate the treatment of large deformations. Also, the meshless character of the SPH allows an efficient implementation based on CUDA technology for massively parallel computations on GPU. The present work uses an SPH-based framework developed at the Institute for Radiological Protection and Nuclear Safety (IRSN). Following Pazdniakou and Dymitrowska [47], such a method can manage multiphase fluid, rigid, and solid elastic components within the same conceptual framework. We implement in this numerical tool a mixed normalised-corrected form [9] of the SPH Total Lagrangian method [48].

It is worth noting that, inspired by the elasto-damage non-local analytical model proposed by Bažant and Belytschko [7, 5, 6], previous research was performed using SPH to the same purpose by Vignjevic *et al.* [56, 58, 57]. They have demonstrated the non-local character and the absence of mesh dependency on elastic-damage phenomena using an SPH Total Lagrangian form and comparing it to FEM. However, we demonstrate in the present paper that the capability of the SPH method to represent such scale effects is much larger.

The present work focuses on simulations of the non-local elastic response of a one dimension bar under longitudinal harmonic vibrations. Some previous studies have applied the SPH method to solve this problem (for instance, see [24, 49]), but only in its local version, where the SPH is used as a mere solver of a given PDE. In this work, we apply the SPH method to discretize the same PDE, without introducing any additional non-local term in constitutive law, like for instance, the integral or gradient terms present in continuum non-local models [50, 27]. However, we allow λ , the size of the support domain of the kernel function, to become finite and investigate the relation between this numerical parameter and the non-local response in the vibration frequency.

The paper is organised as follows: first, we recall a discrete and then a continuous analytical

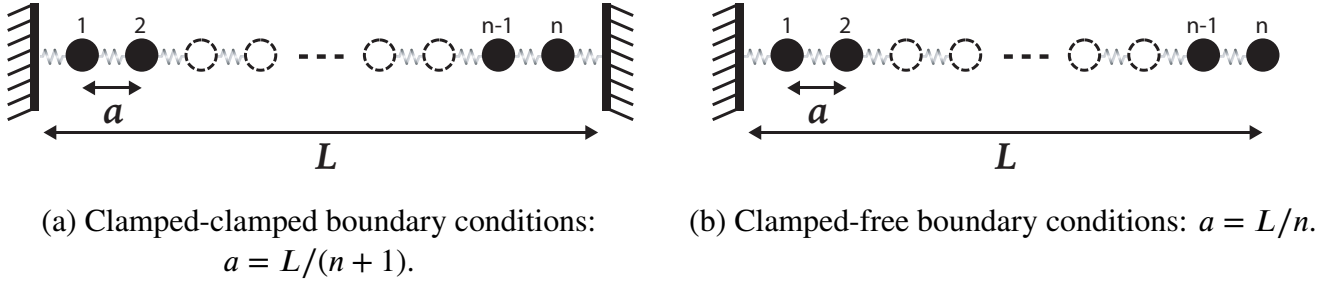


Figure 1: Lattice spring system with concentrated masses.

model that can capture small-scale effects in such a vibration phenomenon. Secondly, the SPH framework is briefly described with some highlights on its advantages and drawbacks. Then, numerical SPH results are compared with the analytical non-local ones, including a discussion about the energy conservation, different SPH kernel functions, and distinct formulae adopted to represent momentum equation. Finally, conclusions and outlooks are presented.

1. Analytical models

This part is devoted to a brief presentation of analytical elasticity models in 1D vibration problems, focusing on a summary of the Lagrange lattice discrete and the continuum models as presented and discussed in recent works by Aydogdu [2, 3] and Challamel [16, 11]. These models will be useful as a test basis for the evaluation of our numerical approach.

1.1. 1D lattice discrete model

Lagrange's investigations of longitudinal vibrations on lattice and discrete spring studies introduced the research of the small scale effect [35, 36]. Consider the equivalent model of concentrated masses constituting a Born-Kármán lattice system of L total length. Clamped-clamped boundary condition system composed of n point masses separated by the distance $a = L/(n + 1)$ (Fig. 1a). Clamped-free configuration has n point masses and $a = L/n$ (Fig. 1b). Consider that all point masses have the same mass m except the free end mass in Fig. 1b which is halved.

The 1D local constitutive law in terms of the axial force N is introduced as:

$$N = EA \frac{\partial u}{\partial x} \quad (1)$$

where u is the local displacement along the x -axis, A is the transverse section surface and E is elastic Young modulus. The momentum equation, in its continuum form, with respect to the local displacement is given by:

$$\rho \frac{\partial^2 u}{\partial t^2} = E \frac{\partial^2 u}{\partial x^2} \quad (2)$$

where $\rho = m/(A \times a)$ is mass per unit of volume and t relates the time. Hence, in order to represent (Eq. 2) in a discrete form, for the left-side, consider harmonic displacement of each i -index mass $u_i(t) = u_i e^{j\omega t}$ where $j = \sqrt{-1}$ and ω is the angular vibration frequency. For the

Modelling non-local elasticity in 1D vibrating rods using Smoothed Particle Hydrodynamics method right-side, consider the finite difference principle for lattice equations. It follows that:

$$u_{n+1} + \left(\frac{a^2}{L^2} \beta^2 - 2 \right) u_n + u_{n-1} = 0 \quad (3)$$

where the non-dimensional local frequency parameter β^2 is defined as:

$$\beta^2 = \frac{\rho}{E} \omega^2 L^2 \quad (4)$$

The discrete displacement of a particle i can be written in the following trigonometric form:

$$u_i = C_1 \cos(i \phi) + C_2 \sin(i \phi) \quad \text{with} \quad \phi = \arccos \left(1 - \frac{a^2}{L^2} \frac{\beta^2}{2} \right) \quad (5)$$

with C_1 and C_2 are some constants. The procedure to obtain this solution and its validity conditions are recalled in Appendix A. In addition, the kinetic energy \hat{T} and the internal or elastic potential energy \hat{W} can be described, respectively, by their continuous and discrete forms (as presented in [16]):

$$\hat{T} = \int_0^L \frac{\rho A}{2} \left(\frac{\partial u}{\partial t} \right)^2 dx = \sum_{i=1}^{n-1} \frac{1}{2} \rho A a \left(\frac{\partial u_i}{\partial t} \right)^2 + \frac{1}{4} \rho A a \left[\left(\frac{\partial u_0}{\partial t} \right)^2 + \left(\frac{\partial u_n}{\partial t} \right)^2 \right] \quad (6a)$$

$$\hat{W} = \int_0^L \frac{EA}{2} \left(\frac{\partial u}{\partial x} \right)^2 dx = \sum_{i=0}^{n-1} \frac{1}{2} EA a \left(\frac{u_{i+1} - u_i}{a} \right)^2 \quad (6b)$$

Furthermore, analytical expressions relate the Lagrange frequency β^2 to $\frac{a}{L}$ value for each of k -th eigen mode of vibration. These expressions are recalled in details in Appendix A.

Furthermore, analytical expressions relate the Lagrange frequency β^2 to $\frac{a}{L}$ value for each of k -th eigenmode of vibration. These expressions are recalled in detail in Appendix A.

Clamped-clamped (CC) longitudinal vibration discrete model: for a discrete lattice chain clamped at both ends $u_0 = u_n = 0$ and the discrete frequency parameter β_{DCC}^2 which takes into account the non-local effect is the following:

$$\beta_{DCC}^2 = \left(2 \frac{L}{a} \sin \left(\frac{k\pi a}{2L} \right) \right)^2 \quad (7)$$

Clamped-free (CF) longitudinal lattice: for clamped-free lattice configuration, one has the following boundary conditions: $u_0 = 0$ and the axial force $N_n = 0$. It leads to the analytical Lagrange-type frequency $\beta_{DCF}^2(k, a/L)$ for the k -th eigen mode:

$$\beta_{DCF}^2 = \left(2 \frac{L}{a} \sin \left(\frac{(2k-1)\pi a}{4L} \right) \right)^2 \quad (8)$$

Furthermore, for both boundary conditions, a/L is equal to the inverse of the number of point masses inside the domain. The asymptotic behaviour of (Eqs. 7 and 8) shows that the values of the frequency parameter β^2 tend to a local value (Eq. 4) when $a/L \rightarrow 0$, otherwise their values decrease with the increase of a/L in both cases. These analytical lattice solutions will be used for comparison with our numerical non-local model.

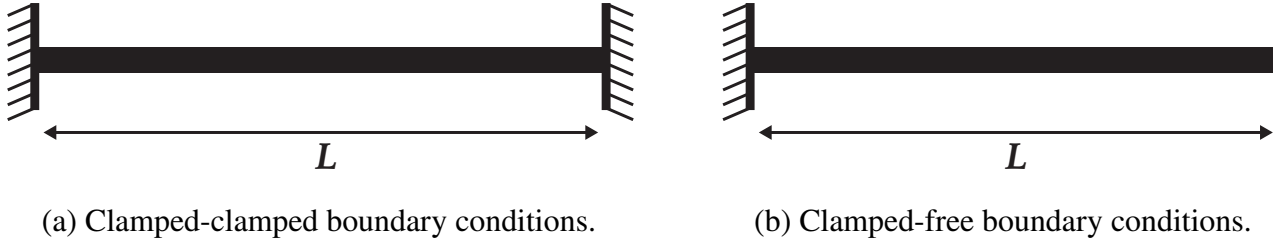


Figure 2: Continuum bar system.

1.2. 1D non-local continuum bar model

Here, the non-local elasticity through the differential stress-based formulation is recalled (as presented by Eringen in [27]), in order to apply it to our problem of 1D a bar of length L and cross-section A under longitudinal vibration (Fig. 2). The detailed procedures to obtain the results described in this section are recalled in Appendix B.

1.2.1. Stress gradient non-local continuum bar model

The non-local wave equation can be written by introducing the non-local form of the axial force $N = N_{nl} - (e_0 a)^2 \frac{\partial^2}{\partial x^2} N_{nl}$ into the local governing equations (Eqs. 1 and 2), such as:

$$EA \frac{\partial^2 u}{\partial x^2} - \rho A \frac{\partial^2 u}{\partial t^2} + \rho A (e_0 a)^2 \frac{\partial^4 u}{\partial t^2 \partial x^2} = 0 \quad (9)$$

where e_0 is a dimensionless parameter that depends on the material properties and a is an internal characteristic length which corresponds to the spring length in lattice model. We observe that when $e_0 a = 0$, this model reduces to the local model (Eq. 2). Consider the longitudinal bar displacement $u(x, t) = U(x) \sin(\omega t)$ (as in [2]), a new form of (Eq. 9) can be obtained as:

$$L^2 \frac{\partial^2 U}{\partial x^2} + \alpha^2 U = 0 \quad (10)$$

where $\alpha^2 = \frac{\beta^2}{1 - (\frac{e_0 a}{L})^2 \beta^2}$ and β^2 is the dimensionless frequency parameter presented in (Eq. 4). Hence, this differential equation yields a solution of the following form:

$$U(x) = C_1 \cos\left(\frac{\alpha}{L} x\right) + C_2 \sin\left(\frac{\alpha}{L} x\right) \quad (11)$$

Clamped-clamped (CC) longitudinal bar: Adopting the boundary conditions for a bar fixed at both extremities ($u(0, t) = u(L, t) = 0$) into (Eq. 10 and 11) leads to the following non-local formulation of the continuum β^2 frequency parameter:

$$\beta_{CC}^2 = \frac{(k\pi)^2}{1 + e_0^2 \left(\frac{a}{L}\right)^2 (k\pi)^2} \quad (12)$$

with the dimensionless factor a/L representing the influence of the small scale on the macro-scale.

Clamped-free (CF) longitudinal bar: Now, introducing clamped-free boundary conditions ($u(0, t) = 0$ and $N(L, t) = 0$) into (Eq. 10 and 11) results in a non-local form of the β^2 frequency parameter for a CF configuration:

$$\beta_{CF}^2 = \frac{\left((2k-1)\frac{\pi}{2}\right)^2}{1 + e_0^2 \left(\frac{a}{L}\right)^2 \left((2k-1)\frac{\pi}{2}\right)^2} \quad (13)$$

1.2.2. Continualization model towards a high-order non-local parameter e_0

We noticed in different analytical studies (see for instance [22, 16, 59, 11]) the adoption of zeroth-order approximation of e_0 in terms of a in the continuum governing equations. It may result in a significant differences between the discrete model (Section 1.1) and the continuum model (Section 1.2), these discrepancies are larger for non-local conditions (*i.e.* $a \gg 0$). We discuss here the importance of e_0 in continuum non-local analytical solutions by adopting the second order centred finite difference form (*i.e.* direct interaction between cells), where the interactions are limited to the closest neighbour of each cell and the inherent scale effects are well reproduced by differential operators. Hence, following Roseneau's development [51], we revisit the right-hand term of the 1D wave equation as presented in (Eq. 2) by introducing a new operator L_D and its expansion L_A , such as:

$$\frac{\partial^2 u}{\partial x^2} \equiv L_D u(x, t) \quad \text{with} \quad L_D \approx L_A D^{(2)} \quad (14)$$

where D traduces a differential operator and the superscript $(.)$ its n-th order (*e.g.* $D^{(2)} = \partial/\partial x^2$). We note that the expansion order of L_A has a direct influence in L_D . Hence, we consider the second-order central finite difference approximation obtained after the sum of the Taylor expansions of $u(x-a)$ and $u(x+a)$ (considering a more important expansion order of L_A though):

$$\frac{u(x+a) - 2u(x) + u(x-a)}{a^2} = \left(1 + \frac{1}{12}a^2 D^{(2)} + \frac{1}{360}a^4 D^{(4)} + \frac{1}{20160}a^6 D^{(6)}\right) D^{(2)}u(x) + \mathcal{O}(a^8) \quad (15a)$$

$$L_A = 1 + \frac{1}{12}a^2 D^{(2)} + \frac{1}{360}a^4 D^{(4)} + \frac{1}{20160}a^6 D^{(6)} \quad (15b)$$

We recall that a is the distance between two discretized points, which corresponds to the spring characteristic length in the discrete lattice model but in continuum models can be interpreted in many different ways (for instance, we present in the next section another interpretation for such quantity when the governing equations are discretized through kernel functions). In order to obtain the non-local form of (Eq. 14), we invert L_A using a Padé approximation [1,6] [54]:

$$L_A^{-1} = 1 - \frac{1}{12}a^2 D^{(2)} + \frac{1}{240}a^4 D^{(4)} - \frac{1}{6048}a^6 D^{(6)} \quad (16)$$

Then, introducing sixth-order expansion (Eq. 16) into (Eq. 14) allows us to find the non-local form of the wave equation (as presented in its 2nd order in Eq. 9):

$$\frac{\partial^2 u}{\partial x^2} - \frac{\rho}{E} \left(1 - \frac{1}{12} a^2 D^{(2)} + \frac{1}{240} a^4 D^{(4)} - \frac{1}{6048} a^6 D^{(6)} \right) \frac{\partial^2 u}{\partial t^2} = 0 \quad (17)$$

We note that when the length-scale parameter $a \rightarrow 0$, this model reduces to the local model (Eq. 2). Hence, considering an 1D harmonic vibration, the analytical longitudinal displacement field (Eq. 11) for different boundary conditions has the following forms:

$$\text{Clamped-clamped (CC): } u(x, t) = C_2 \sin \left(k\pi \frac{x}{L} \right) \sin(\omega t) \quad (18a)$$

$$\text{Clamped-free (CF): } u(x, t) = C_2 \sin \left(\frac{(2k-1)\pi x}{2L} \right) \sin(\omega t) \quad (18b)$$

In addition, by introducing the respective temporal and spatial derivatives of (Eqs. 18) into (Eq. 17), we obtain a dimensionless frequency parameter β^2 determining numerically the values of a high-order form of the non-local parameter e_0 .

Clamped-clamped (CC): For a clamped-clamped bar ($u(0, t) = u(L, t) = 0$), we get the same non-local formulation of the non-local β_{CC}^2 as found in (Eq. 12), but here e_0 has a high-order expansion in terms of a/L :

$$e_{0_{cc}}^2 = \frac{1}{12} + \frac{(k\pi)^2}{240} \left(\frac{a}{L} \right)^2 + \frac{(k\pi)^4}{6048} \left(\frac{a}{L} \right)^4 + \mathcal{O}((a)^6) \quad (19)$$

Clamped-free (CF): Introducing the clamped-free boundary conditions ($u(0, t) = 0$ and $N(L, t) = 0$) into (Eq. 17), results in the following CF non-local form of the β_{CF}^2 , with e_0 depending on a/L represented here in a high-order form:

$$e_{0_{cf}}^2 = \frac{1}{12} + \frac{((2k-1)\pi)^2}{960} \left(\frac{a}{L} \right)^2 + \frac{(2k-1)\pi^4}{96768} \left(\frac{a}{L} \right)^4 + \mathcal{O}((a)^6) \quad (20)$$

It is worth noting that the high-order e_0 values shown in (Eqs. 19 and 20) are exactly equal to the high-order values of e_0 obtained by calibration between continuum and lattice discrete model after Taylor series expansion at $a/L \rightarrow 0$ (this method was adopted by different authors [12, 63, 65]). Some arguments are considered to justify the choice of a 0th order expansion of e_0 : the assumption that the non-local effect is the influence of the infinitesimal value of a/L on the macro-scale properties of a material, which simplifies the solution of the mathematical expressions significantly (see for instance [16, 59, 11]).

In the following, we propose the comparison of solutions with e_0 at different orders, which allows us to reach a larger validity domain (we adopt $0 < a/L \leq 1$). Furthermore, it is worth noting that all non-local constitutive laws might fulfil the translational invariance principle and have normalised forms. Hence, we introduce the treatment of the investigated vibration problem in the next section through our mesh free method to be compared with the analytical models of the present section. Besides, we aim at verifying that the proposed model can well reproduce non-local behaviour in small and large deformations.

2. Non-local behaviour through SPH model

This section presents the elastic model, followed by the numerical framework adopted in this paper. The mechanical approach adopted here constructs the governing equations by using both initial and deformed configurations. In the literature, it is usually called SPH Total Lagrangian method (see [48, 58, 49] for more details).

2.1. 1D large deformations elastic model

In order not to be limited by small vibration amplitudes, we adopt in this work a large deformations Lagrangian approach. For completeness, we recall here classical notations, governing equations as well as constitutive laws that are used. The deformation gradient F is expressed through the displacement $u = x - X$ at time t :

$$F = \frac{\partial x}{\partial X} = 1 + \frac{\partial u}{\partial X} \quad (21)$$

Considering the 1D finite deformation theory in a Lagrangian description, we use the Green-Lagrange strain ϵ^{GL} , which is defined as (see for instance [4]):

$$\epsilon^{GL} = \frac{\partial u}{\partial X} + \frac{1}{2} \left(\frac{\partial u}{\partial X} \right)^2 \quad (22)$$

The equation of conservation of mass uses the Jacobian J to assess the density ρ from the reference configuration ρ_0 :

$$\rho = J^{-1} \rho_0 \quad (23)$$

where J is usually defined as equal to $F = \partial x / \partial X$ for 1D configuration [8], and in 2D or 3D $J = \det |F|$. The momentum conservation in a Total Lagrangian configuration is given through the 1st Piola-Kirchhoff stress P , such as:

$$\frac{\partial^2 u}{\partial t^2} = \frac{1}{\rho_0} \frac{\partial P}{\partial x} \quad (24)$$

The conservation of internal energy e in absence of thermal effects reads [8]:

$$\rho_0 \frac{\partial w}{\partial t} = P \frac{\partial F}{\partial t} = S \frac{\partial \epsilon^{GL}}{\partial t} \quad (25)$$

where the 2nd Piola-Kirchhoff stress S in 1D can be written as $S = F^{-1} P$.

In the considered large deformations framework, different mechanical approaches can be adopted. In the present case, we adopt the 1D energy density function $\rho_0 w$ defined by the Saint Venant-Kirchhoff constitutive model:

$$\rho_0 w = \frac{1}{2} E (\epsilon^{GL})^2 \quad (26)$$

which results in the 1D state law between ϵ^{GL} and S , where E stands for the Young modulus:

$$S = \rho_0 \frac{\partial w}{\partial \epsilon^{GL}} = E \epsilon^{GL} \quad (27)$$

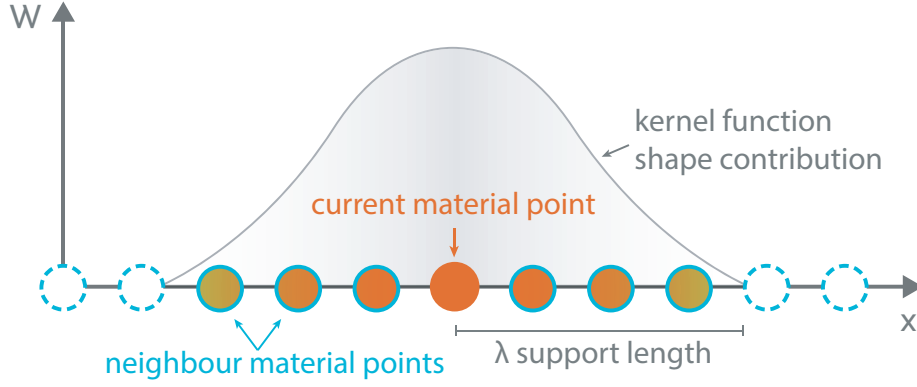


Figure 3: One dimension SPH principle with weighted neighbours contribution following the smoothing kernel function W

2.2. SPH numerical model

The principle of the SPH method is based on approximation of a point of coordinate r of a function f by means of a convolution with a given smoothing function in analogy to the following formula using Dirac's delta function δ .

$$f(r) = \int f(r')\delta(r - r')dr' \quad (28)$$

The value of f is replaced by an integration over a finite size neighbourhood with a kernel function W such that:

$$\langle f(r) \rangle = \int f(r')W(r - r', h)dr' + err_{smoothing} \quad (29)$$

The angle brackets $\langle \cdot \rangle$ denotes the SPH kernel approximation, h is called the smoothing scale and is related to the kernel function support length λ and $err_{smoothing}$ is the approximation error. Usually, function W is chosen such that $err_{smoothing} = \mathcal{O}(h^2)$ (see [41]).

Thus, it is possible to define the smoothed form of f as (Eq. 29) is:

$$\langle f_S(r) \rangle = \int f(r')W(r - r', h)dr' \quad (30)$$

Its derivatives can be obtained in the simplest way from the divergence theorem and the integration by parts ([41]):

$$\langle \nabla f_S(r) \rangle = \int f(r')\nabla W(r - r', h)dr' \quad (31)$$

2.2.1. Smoothing function

Several smoothing kernel functions are commonly used to achieve high accuracy and numerical stability in different applications. In order to ensure the method consistency, W has to fulfil some conditions (Eq. 32): it must converge to the Dirac function when h tends to zero, it usually has a finite support domain and must be normalised, even and positively defined. The fact that W

has to be positively defined inside the support domain has a physical meaning when computing properties by a weighted sum. Moreover, the function W must satisfy (Eq. 32c) which correspond to the conservation of angular and linear momentum.

$$\left\{ \begin{array}{l} \lim_{h \rightarrow 0} W(q, h) = \delta(q) \\ \int W(q, h) dr' = 1 \\ \int (r - r') W(r - r', h) dr' = 0 \end{array} \right. \quad \begin{array}{l} (32a) \\ (32b) \\ (32c) \end{array}$$

The following 1D gaussian function presented by Gingold [32] is a good choice to achieve accuracy and stability, but has a high computation cost given its infinite support domain, which implies the adoption of periodic boundary conditions.

$$W(q, h) = \frac{1}{h\sqrt{\pi}} \exp \left[- \left(\frac{q}{h} \right)^2 \right] \quad (33)$$

For computational convenience, smoothing functions are often represented by truncated polynomial forms. Among the most common formulations are quadratic and cubic spline functions [41] which are frequently employed in hydrodynamics framework (see more in [44]). The following 1D cubic spline smoothing function is used most of the time in the present work.

$$W(q, h) = \frac{1}{h} \begin{cases} \frac{2}{3} - \left(\frac{q}{h}\right)^2 + \frac{1}{2}\left(\frac{q}{h}\right)^3 & \text{if } 0 \leq q < h \\ \frac{1}{6}\left(2 - \frac{q}{h}\right)^3 & \text{if } h \leq q < 2h \\ 0 & \text{if } q \geq 2h \end{cases} \quad (34)$$

Following the characteristics of a kernel function, the relation between λ and h may vary (see [23, 62] for more details). Here, $\lambda = 2\sqrt{2}h$ for Gaussian function and $\lambda = 2h$ for cubic spline function.

2.2.2. Discrete form

Its discrete form can approximate the continuous integral presented in (Eq. 30), where the value of f in discrete material point a is computed using a weighted sum over \hat{N} points b in its neighbourhood (of radius λ).

$$f(r)_a = \sum_b^{\hat{N}} f_b V_b W(r_a - r_b, h) \quad \text{if } |r_a - r_b| < \lambda \quad (35)$$

The volume of each particle is defined by $V_a = m_a/\rho_a$. Furthermore, the sum approximation of continuous integrals presented before generate an error estimated as $err_{integral} = \mathcal{O}(\Delta/h)$, with Δ the length scale characterising the average distance between material points [55]. Fig. 3 presents

the SPH concept of smoothing in one dimension. In addition, the deformation gradient F is the only non-local variable in our system before computing the SVK state law (Eq. 27) which reads in a SPH discrete form:

$$F_a = \left[\sum_{b=1}^{\hat{N}} \frac{m_b}{\rho_{b,0}} (r_b - r_a) \tilde{\nabla}_{a,0} \tilde{W}_{ab,0} \right] + 1 \quad (36)$$

In order to fix some drawbacks often present in elastic solid simulations through the original form of SPH like particle disorder and tensile instability (see for instance [39, 1]), this study adopts a Total Lagrangian form that states the initial state of the system as reference state (see [48, 58, 49] for detailed discussion). Thus, the discrete SPH forms of governing equations (Eqs. 23-25) are respectively:

$$\rho_a = J^{-1} \rho_{a,0} \quad (37a)$$

$$\frac{\partial^2 u_a}{\partial t^2} = -\frac{1}{m_a} \sum_{b=1}^{\hat{N}} \frac{m_a}{\rho_{a,0}} \frac{m_b}{\rho_{b,0}} \left(P_b \tilde{\nabla}_{b,0} \tilde{W}_{ba,0} - P_a \tilde{\nabla}_{a,0} \tilde{W}_{ab,0} \right) \quad (37b)$$

$$\frac{\partial w_a}{\partial t} = \sum_{b=1}^{\hat{N}} \frac{m_a}{\rho_{a,0}} \frac{m_b}{\rho_{b,0}} (v_b - v_a) P_a \tilde{\nabla}_{a,0} \tilde{W}_{ab,0} \quad (37c)$$

The index a and b identify, respectively, each material point of the SPH system and its \hat{N} neighbours, w is the internal energy as introduced in (Eq. 25). We note that $\frac{\partial^2 u_a}{\partial t^2}$ and $\frac{\partial w_a}{\partial t}$ are also computed through SPH interpolation. In addition, the sum of energies E^{TOT} inside an isolated SPH system is given by:

$$E^{TOT} = E^{\hat{T}} + E^{\hat{W}} \quad (38)$$

where the total kinetic energy $E^{\hat{T}}$ and the total internal energy $E^{\hat{W}}$ for a SPH system composed of n material points are written as:

$$E^{\hat{T}} = \sum_a^n \frac{1}{2} m_a v_a^2 \quad (39a)$$

$$E^{\hat{W}} = \sum_a^n \frac{m_a}{\rho_a} w_a \quad (39b)$$

Following Liu *et al.* [42] and Bonet and Lok [9], we use a new corrected form of the kernel function (here denoted by the superscript \sim), and of the kernel gradient. These corrections insure the conservation of the linear and angular moments. For time integration, we implement a Predict-Evaluate-Correct Leap-Frog explicit scheme (as presented in [64]). The time step must respect the

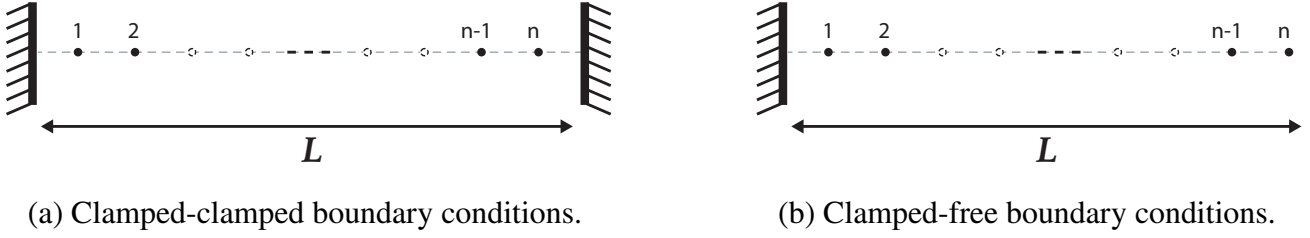


Figure 4: SPH bar system.

Parameter	Sign	Value
Young modulus	E	200 [GPa]
Linear mass density	ρ	7833 [kg/m]
Bar length	L	0.1333 [m]
Number of material points	n	200 [-]
Time step	Δt	10^{-8} [s]

Table 1

Input data for 1D bar SPH simulations

following Courant-Friedrich-Levy conditions to insure the numerical stability (see [46] for more details).

$$\Delta t \leq \begin{cases} 0.25 \frac{h}{|v_{max}|} \\ 0.25 \sqrt{\frac{h}{|a_{max}|}} \\ h \sqrt{\frac{\rho}{E}} \end{cases} \quad (40)$$

Despite several advantages, the straightforward use of SPH for solid elastic simulations presents some drawbacks. Thus, seeking to inhibit the tensile instability in our work, we use a Total Lagrangian formulation. In the following, we use analytical solutions and numerical models previously introduced to present the results of the 1D longitudinal vibration problem.

3. SPH simulations with $\lambda/L \rightarrow 0$

One more time, we consider a bar of length L and discretized by n SPH material points, as presented in previous sections. Two types of boundary conditions are used: clamped at both ends (as presented in Fig. 4a) and clamped-free (as presented in Fig. 4b). Adopting the same material point discretisation over all simulations, this work investigates the influence of the ratio λ/L and its relation with the previously used ratio of a/L . Table 1 presents all parameters considered for SPH simulations.

In this section we validate the Total Lagrangian SPH method, introduced in Sec. 2, with respect to the discrete and continuum analytical solutions from Sec. 1. The cubic spline kernel (Eq. 34) is

being used and all the simulations are conducted in the limit of $\lambda/L \rightarrow 0$. Where $C_2 = L/2000$ is a chosen small constant amplitude and ω is the angular frequency as defined in (Eq. 4). The initial conditions are imposed via the velocity profiles corresponding to the time derivative of (Eqs. 18):

$$\text{Clamped-clamped (CC): } v(x, t) = C_2 \omega \sin\left(k\pi \frac{x}{L}\right) \cos(\omega t) \quad (41a)$$

$$\text{Clamped-free (CF): } v(x, t) = C_2 \omega \sin\left(\frac{(2k-1)\pi x}{2L}\right) \cos(\omega t) \quad (41b)$$

For this simulation, the value of $\lambda/L = 0.025$ and the first mode $k = 1$ are used. The three first periods of oscillation are shown in (Fig. 5) for CC and (Fig. 6) for CF. From the oscillation period τ obtained from local minima (Figs. 5a and 6a) we calculate $\omega = 2\pi/\tau$ in (Eq. 4). We plot the longitudinal displacement over time at different positions along the bar (CC - Fig. 5a and CF - Fig. 6a), computed by means of the SPH method and compared to the analytical solutions (Eqs. 18). Fig. 5b for CC and Fig. 6b for CF, present the velocity over time at the same positions and compared with the analytical solutions (Eqs. 41). Finally, following (Eqs. 38 and 39) we give the total energy evolution over time (CC - Fig. 5c and CF - Fig. 6c) as compared with the analytical solutions (Eqs. 6). It can be seen that the total energy is conserved and we find a very good agreement with the analytical solutions for all variables.

Figs. 5a-6c confirm that the SPH can reproduce with good accuracy the 1D longitudinal vibration phenomenon. The use of a small ratio λ/L results in a close agreement between the numerical and the analytical solutions without non-local effects, showing that, in this limit, the SPH method behaves as expected as a simple PDE solver. It is worth mentioning that the λ values cannot become smaller than the distance between the closest material points, which is a necessary condition for the SPH to compute neighbour contributions during the smoothing procedure.

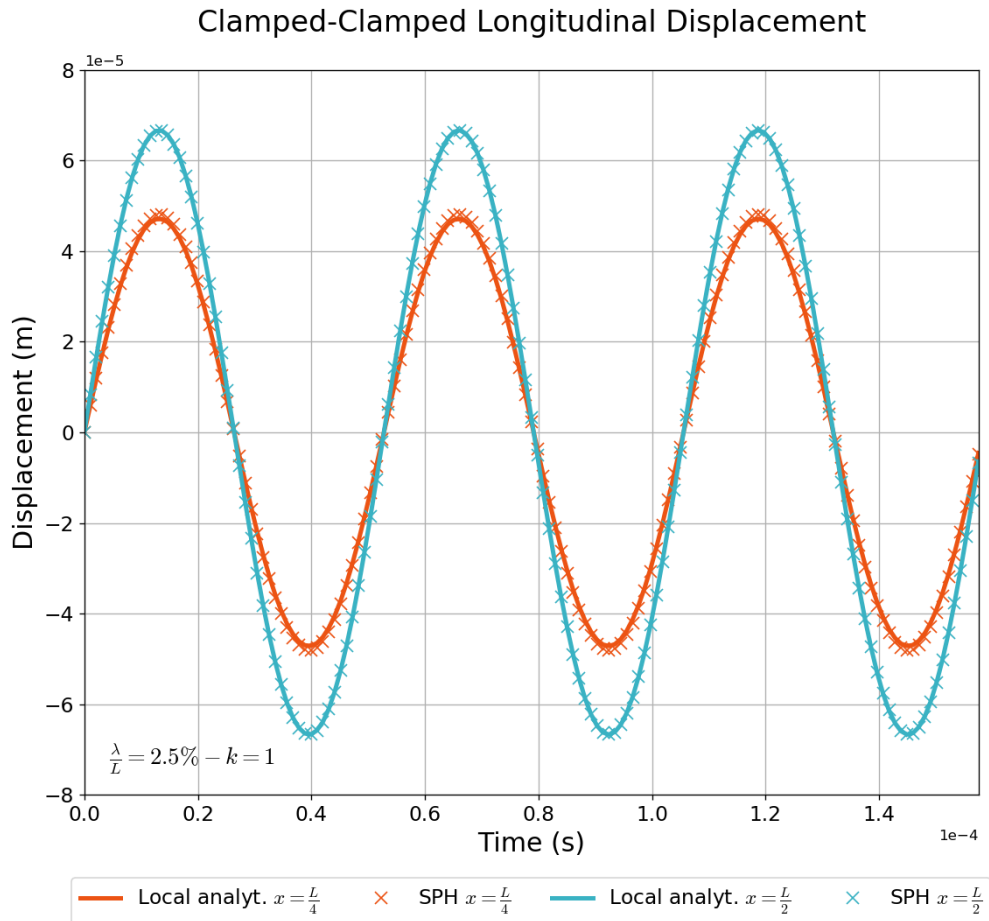
4. Non-local effects using SPH method

In this part, we assess the capability of the SPH method to introduce non-local behaviour when adopting finite λ/L values. Also, some insight is given about the role of different variables and conditions on the observed non-local behaviour.

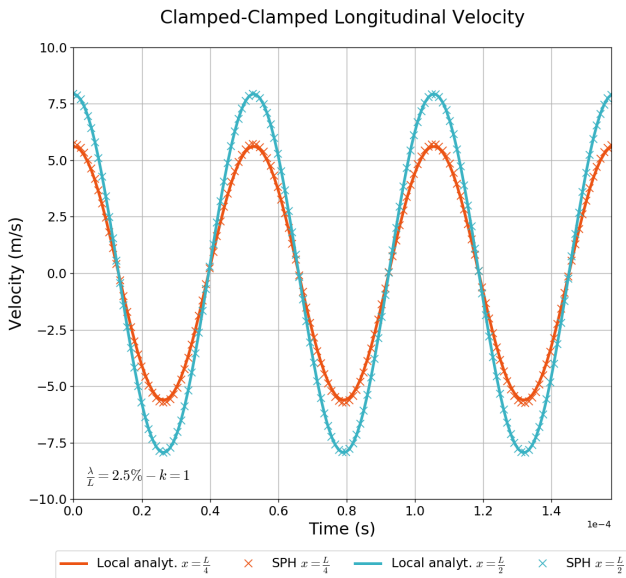
4.1. Simulations with $\lambda/L = O(1)$ towards non-local effects

The small scale effects in a longitudinal vibration problem are expected to change the macroscopic properties of the bar, resulting in a slower vibration and thus in a decrease of the dimensionless frequency parameter β^2 . Hence, we reconsider a clamped-clamped configuration presented in Fig. 4a, with a ratio $\lambda/L = O(1)$ and for $k = 1$.

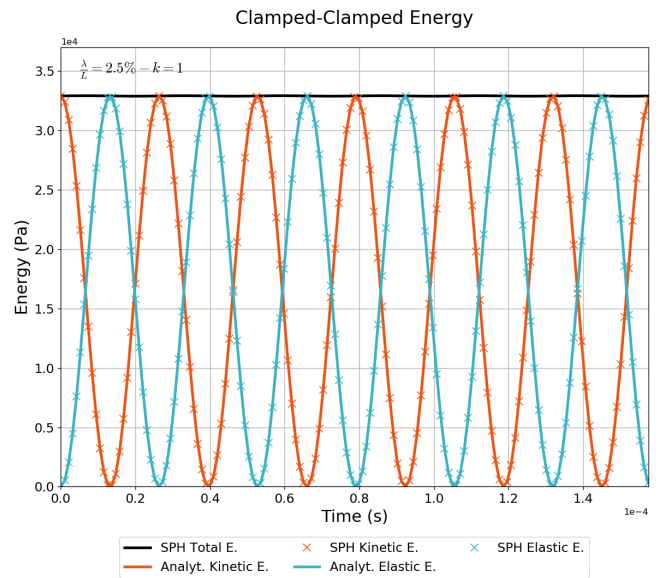
The displacement (Fig. 7a) and the velocity (Fig. 7b) evolution presents an increase of the period τ (thus the angular frequency ω decreases, as expected). The maximal amplitude of the displacement increases compared to the local analytical case ($\lambda/L \rightarrow 0$). This is due to the way we impose the initial conditions, namely by predefining the velocity evolution, the same for all values of λ/L . The amplitudes of displacement and velocity are proportional with the proportionality constant equal to ω . Thus, when the oscillation period changes, the displacement amplitude changes as well. Therefore, these results also confirm the prediction of a change in the vibration frequency (softening). What is more, Fig. 7c shows that the total energy of the system remains



(a) Analytical local displacement (Eq. 18a) x SPH results for CC configuration.

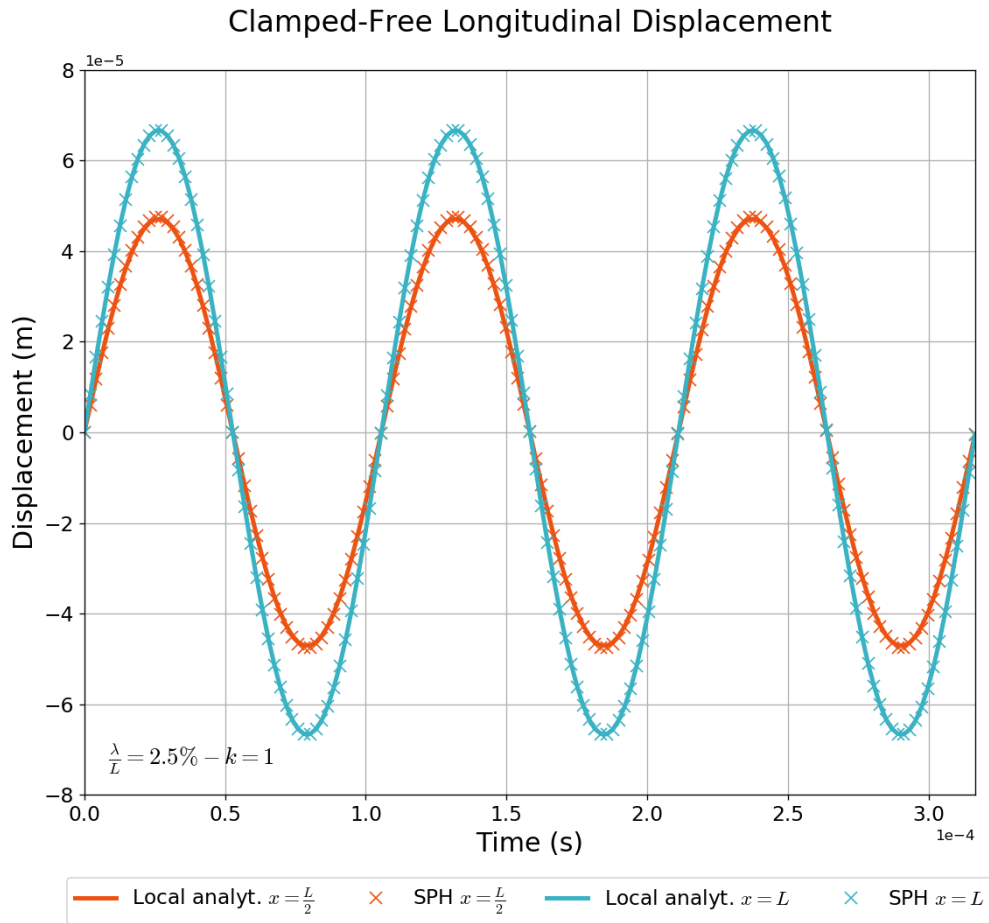


(b) Analytical local velocity (Eq. 41a) x SPH results for CC configuration.

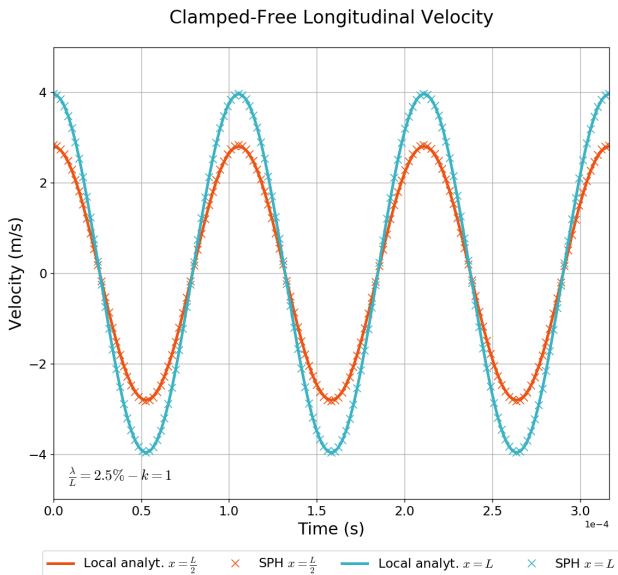


(c) Analytical global kinetics and elastic energy (Eqs. 6) x SPH results for CC configuration.

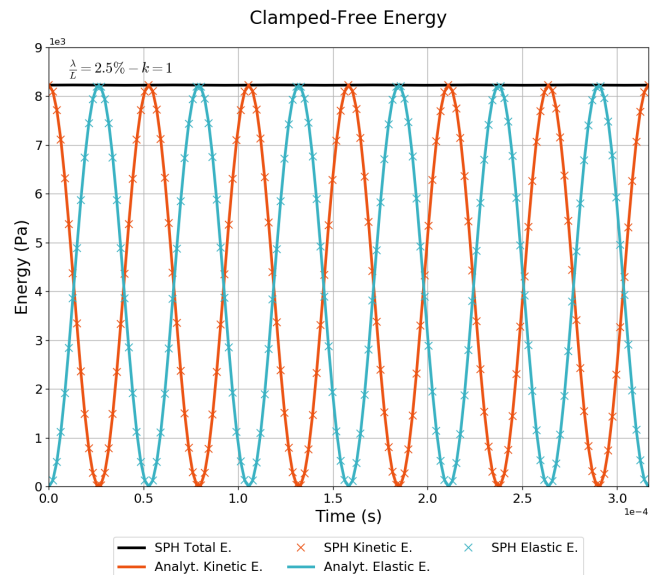
Figure 5: Displacement, velocity and energy evolution in SPH results with λ/L .



(a) Analytical local displacement (Eqs. 18b) x SPH results for CF configuration.

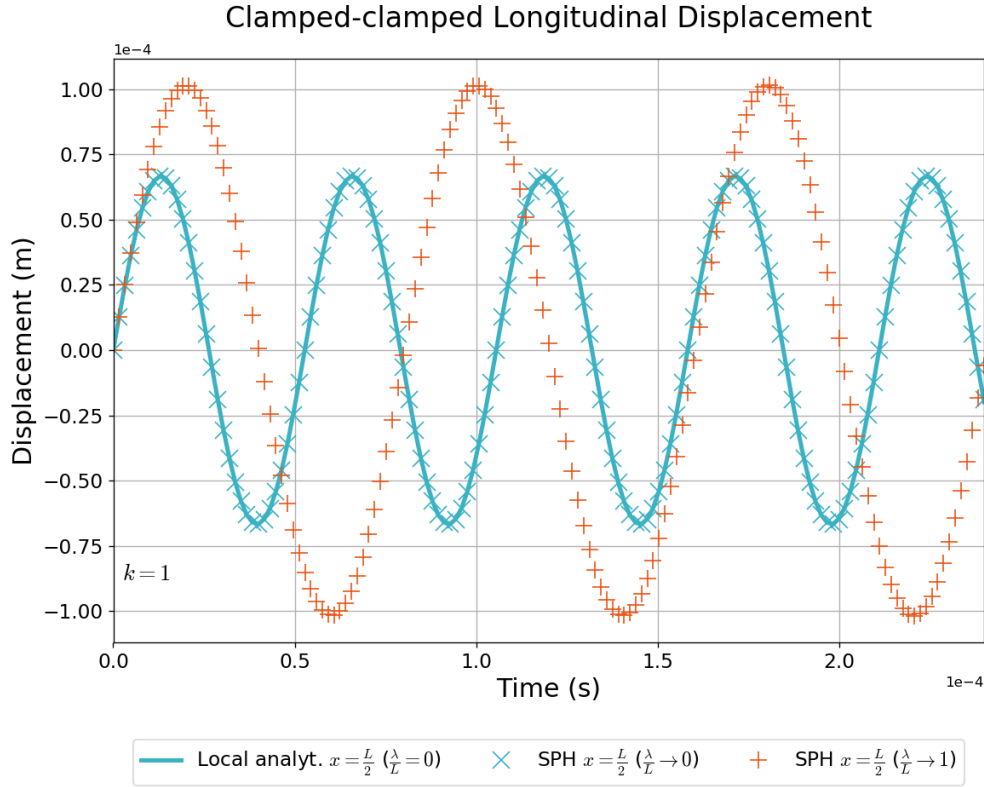


(b) Analytical local velocity (Eq. 41b) x SPH results for CF configuration.

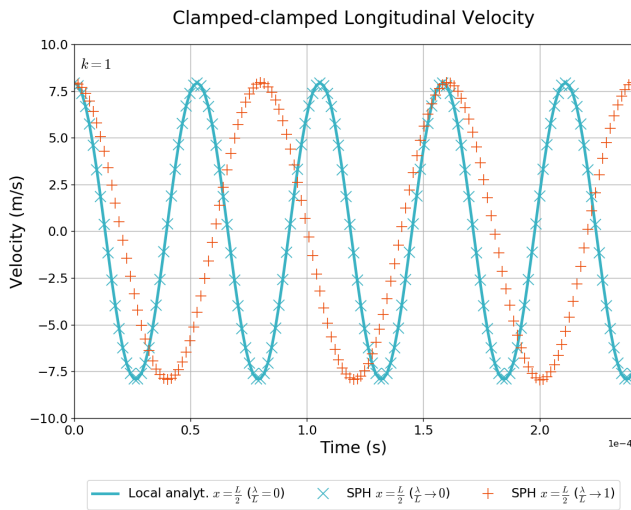


(c) Analytical global kinetics and elastic energy (Eqs. 6) x SPH results for CF configuration.

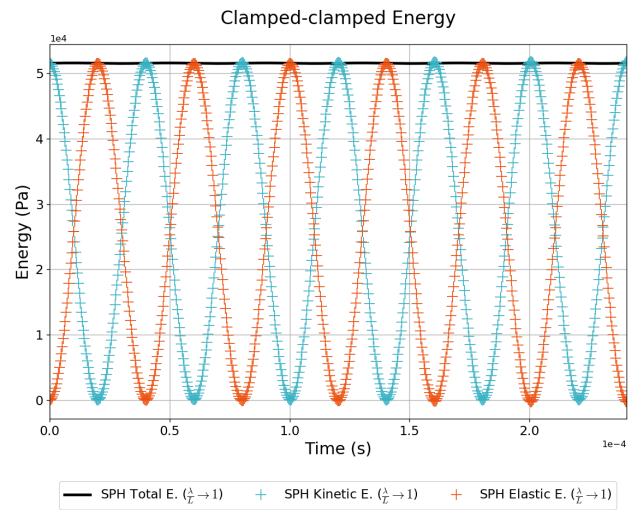
Figure 6: Displacement, velocity and energy evolution in SPH results with λ/L .



(a) SPH longitudinal displacement results versus analytical solution (Eq. 18a).



(b) SPH longitudinal velocity results versus analytical solution (Eq. 41a).



(c) SPH kinetic and elastic energies for $\lambda/L \rightarrow 1$ (Eqs. 6).

Figure 7: SPH method results for $\lambda/L = O(1)$ in a clamped-clamped configuration for the first vibration mode $k = 1$.

constant despite the use of a finite value of λ/L , which might have led to a significant numerical dissipation.

In addition, we observe that the SPH approach allows us to explore non-local effects beyond those studied by the Lagrange lattice spring system as summarised by Challamel *et al.* [16] (where

the discrete variable $n = L/a \leq 2$). Here, λ/L is not only the inverse of n , but becomes a continuous variable with the possibility to exceed $1/2$. This observation justifies the adoption of the ratio λ/L as abscissas in the following subsections. Moreover, in the subsequent results and figures, the subscript *SPH* will be used for all results obtained from the SPH method. For the analytical solutions, the subscripts *l*, *D* and *C* denote, respectively, the local solution ($e_0 a = 0$) and the analytical discrete and continuum non-local solutions ($e_0 a > 0$).

4.2. SPH simulations with finite and infinite support kernel functions

In the previous subsection, it has been shown that the SPH method can account for non-local effects when used with finite λ/L values. Here, we perform multiple simulations to quantify the non-local effects by the variation of the frequency parameter β^2 as a function of λ/L . In this context, we check the influence of the choice of the kernel functions (Gaussian kernel or cubic spline kernel). Fig. 8 shows the variation of β^2 with λ/L for $k = 1$ (a for clamped-clamped and b for clamped-free boundary conditions).

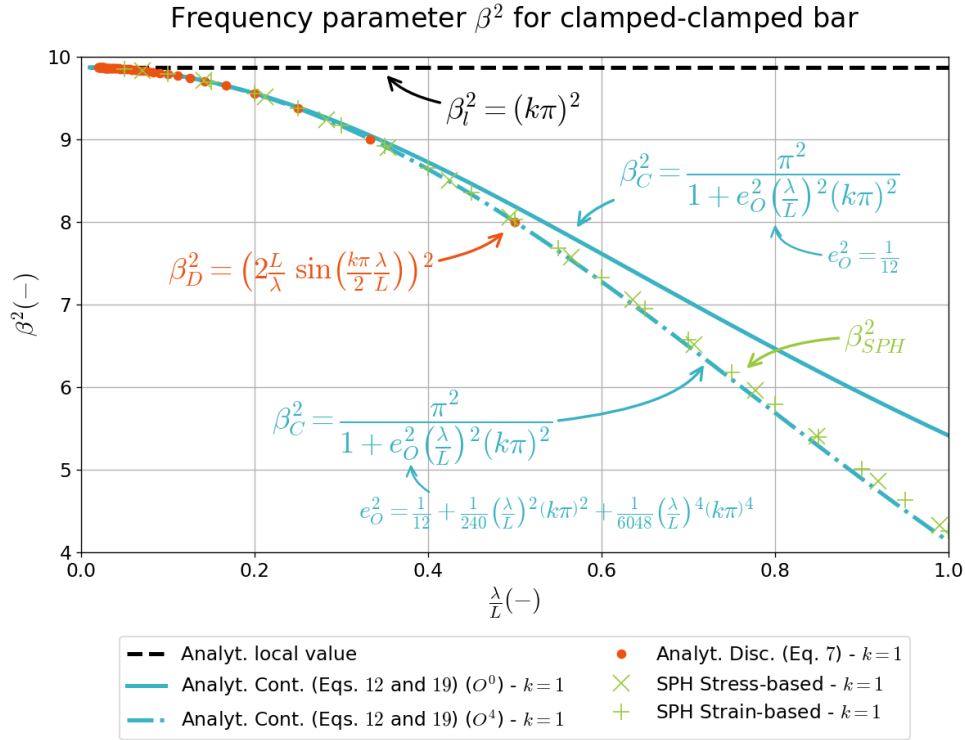
These results prove that the numerical solution using cubic spline kernel (Eq. 34) presents a very similar behaviour to that with the Gaussian kernel (Eq. 33), in spite of much smaller computing cost due to its finite support. For both kernel functions, the increase of the parameter λ/L leads to a significant decrease of β^2 as compared to the local behaviour (constant value, dashed line). Furthermore, we observe that the best agreement between the SPH results and the non-local analytical solutions is obtained by taking $a = \lambda$ in (Eqs. 7, 8, 12 and 13). The dots represent the discrete lattice solution which fits better with the SPH solution for larger λ/L values. The solid lines represent the continuum analytical solution with a development of e_0^2 parameter with respect to λ/L to the order $\mathcal{O}(\lambda/L)^0$ as showed in Eqs. 19 and 20 and adopted by Challamel *et al.* in [16, 11]. In addition, we present also the continuum analytical solution (dash-dotted line) with e_0^2 of $\mathcal{O}(\lambda/L)^4$ order following Eqs. 19 and 20.

It is noteworthy that the discrete solutions for β^2 from (Eqs. 7 and 8) have a domain limited such as $\lambda/L \in]0; 1/2]$ (*i.e.* $n \geq 2$). From these results of β^2 , we observe a rising difference between the discrete and the 0^{th} order continua analytical solutions over the increase of λ/L . The numerical SPH results show a good agreement with the discrete and the 4^{th} order continua analytical solutions. Also, we note that the analytical form with a higher-order of e_0 presents a closer approximation to the lattice discrete analytical solution and good agreement with our numerical model when $a/L \rightarrow 1$.

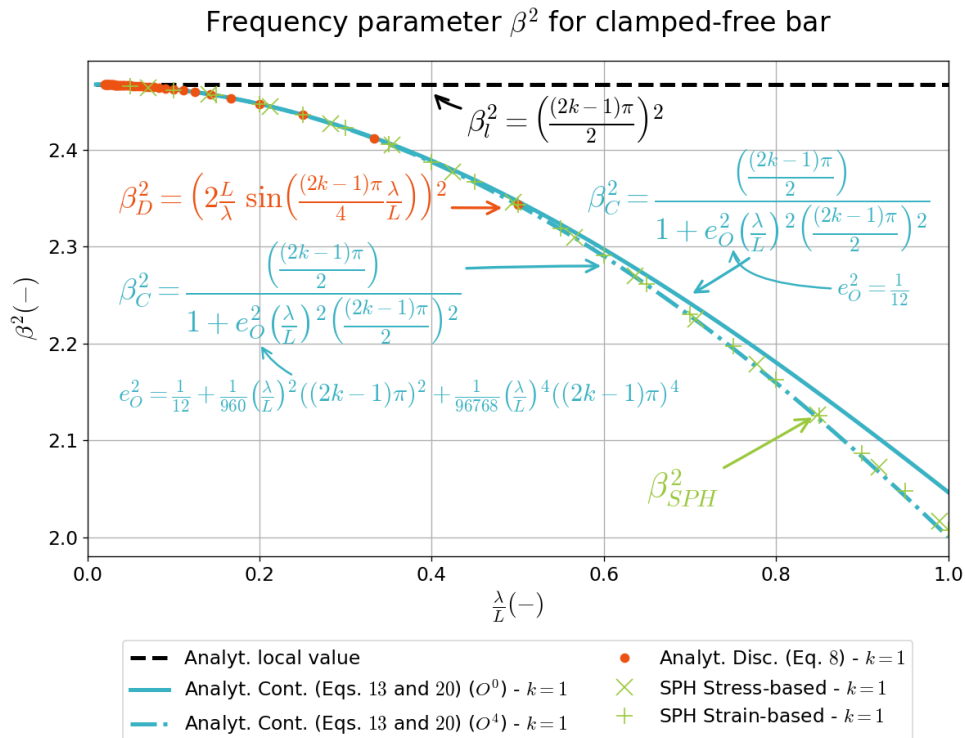
4.3. Effects of initial amplitudes

In the previous subsection, we showed that thanks to the non-local nature of the SPH method, the increase of the ratio λ/L leads to a decrease of the β^2 frequency parameter. On the other hand, Şimşek [21, 22] has stated that the increase of the initial displacement amplitude in a vibration phenomenon of a bar raises the longitudinal stretching due to the large deflections, which implies higher vibration frequencies. This phenomenon is called "spring hardening".

Seeking to investigate such adverse effect, we show in Fig. 9 SPH simulation results with different initial velocity amplitudes C_2 (present in Eqs. 41) for the following non-local parameter values $\lambda/L = 2.5\%$, 12.5% , 22.5% and 32.5% . In order to obtain stable solutions for all configurations, we adopt here a higher number of material points $n = 600$. We observed that beyond $C_2/\lambda \leq 0.5$, the SPH solutions become unstable.



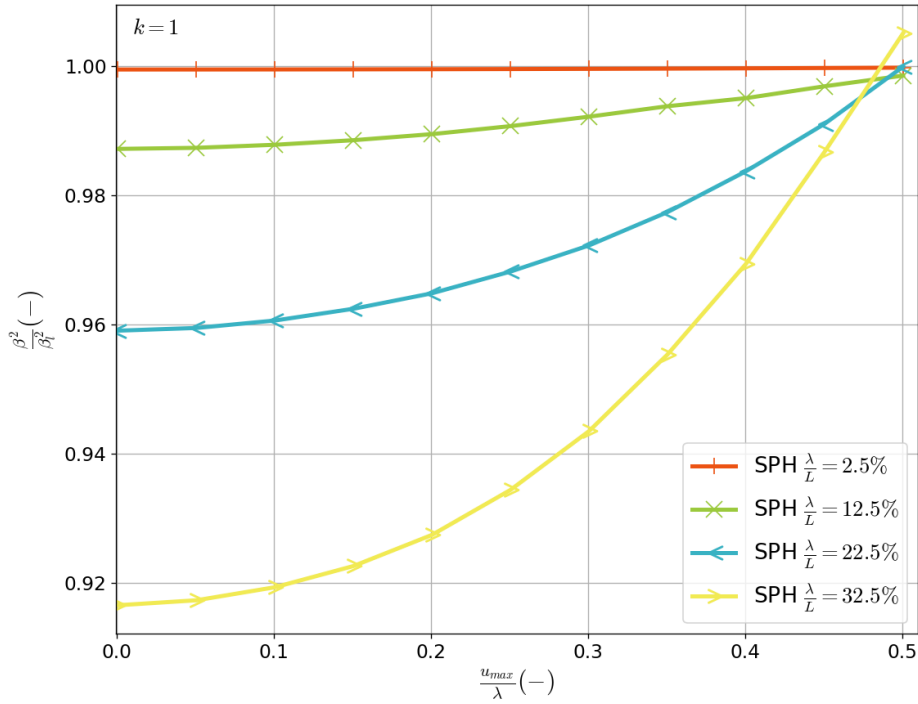
(a) Clamped-clamped configuration: Frequency parameter β^2 found through SPH versus discrete (Eq. 7) and continuum (Eq. 12) analytical solutions.



(b) Clamped-free configuration: Frequency parameter β^2 found through SPH versus discrete (Eq. 8) and continuum (Eq. 13) analytical solutions.

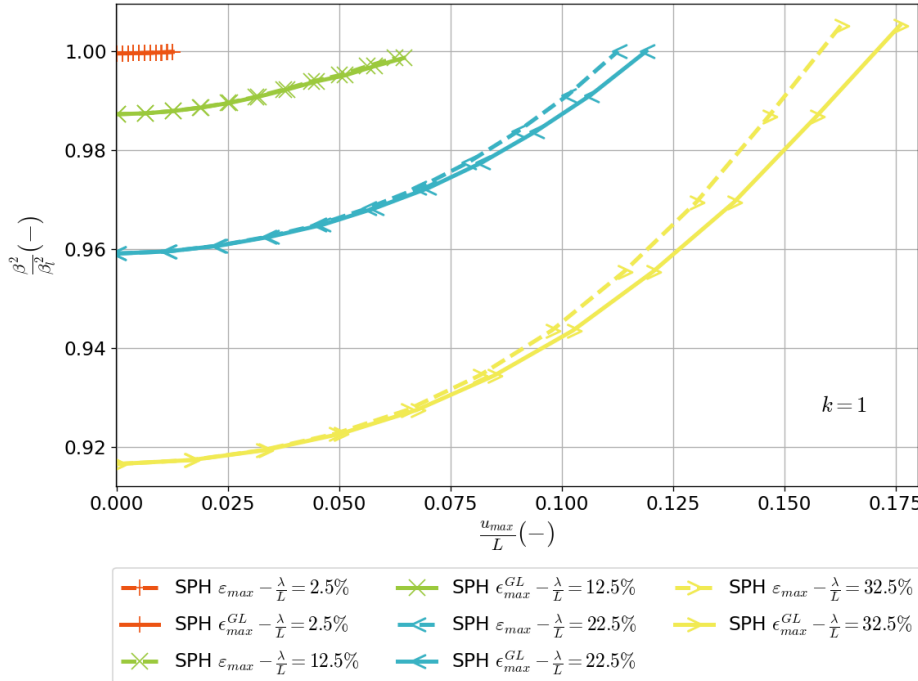
Figure 8: Study of the dimensionless frequency parameter β_{SPH}^2 compared to analytical discrete and continua solutions for two different kernel functions, $k = 1$.

Normalized frequency parameter β^2 for clamped-clamped bar



(a) Normalised frequency β^2 for increasing velocity amplitude ratios C_2/λ in large deformations description.

Normalized frequency parameter β^2 for clamped-clamped bar



(b) Normalised frequency β^2 for different maximal values of small and large deformations longitudinal strains.

Figure 9: Study of the dimensionless frequency parameter β_{SPH}^2 for different initial velocity amplitudes C_2 and $k = 1$.

Table 2

 Analytical and numerical results for $\lambda/L = 0.05$ and $\lambda/L = 0.5$ in a clamped-clamped configuration

	λ/L	β_D^2	$\beta_C^2 [\mathcal{O}(\lambda/L)^0]$	$\beta_C^2 [\mathcal{O}(\lambda/L)^4]$	β_{SPH}^2
$k = 1$	0.05	9.85	9.85	9.85	9.85
	0.5	8.00	8.19	8.00	8.03
$k = 2$	0.05	39.15	39.16	39.15	39.16
	0.5	16.00	21.66	16.54	17.04
$k = 3$	0.05	87.19	87.21	87.19	87.19
	0.5	8.00	31.16	13.23	12.71

Table 3

 Analytical and numerical results for $\lambda/L = 0.05$ and $\lambda/L = 0.5$ in a clamped-free configuration

	λ/L	β_D^2	$\beta_C^2 [\mathcal{O}(\lambda/L)^0]$	$\beta_C^2 [\mathcal{O}(\lambda/L)^4]$	β_{SPH}^2
$k = 1$	0.05	2.47	2.47	2.47	2.47
	0.5	2.34	2.35	2.34	2.34
$k = 2$	0.05	22.10	22.10	22.10	22.10
	0.5	13.66	15.18	13.71	13.90
$k = 3$	0.05	60.90	60.90	60.90	60.98
	0.5	13.66	26.99	15.89	16.35

Fig. 9a presents the normalised β^2 over the dimensionless quantity C_2/λ and shows, as expected from the previous section, that for small initial amplitudes ($C_2/\lambda \rightarrow 0$), the frequency β^2 decreases with the increase of the non-local parameter λ/L . However, increasing initial amplitudes raises the values of β^2 for all λ/L configurations, showing that the amplitude value has a preponderant influence in these cases.

Besides, in Fig. 9b we present the dimensionless frequency over the maximal values of di displacement u_{max} , resulting in the infinitesimal strain ϵ_{max} for a small deformations theory and the large deformations Green-Lagrange strain ϵ_{max}^{GL} obtained with our large deformations SPH method by solving the Saint Venant-Kirchhoff constitutive model. The behaviour of both strain formulations are qualitatively similar, and, as expected, the effect of large deformations becomes more sensible with a higher ratio of λ/L . These tests confirm that our Total Lagrangian SPH approach can represent strain ranges where large-deformation conditions are significant. Moreover, it can also represent with good accuracy and stability both: softening and hardening phenomena, due, respectively, to the non-local parameter and the increase of the initial velocity amplitude.

4.4. Frequency parameter β^2 for different eigen modes

After demonstrating the capacity of the SPH method to introduce non-locality in small and large deformation formulations, our goal is now to investigate further the role of eigen modes. The higher value of k , the steeper are the gradients to be solved, so that the numerical method may be inefficient or unstable. For that, we come back to the parameters presented in Table 1 and consider again a constant small amplitude $C_2 = L/2000$. We obtain β^2 parameter for the three first vibration eigen modes through our numerical model and compare it to both discrete (Eqs. 7 and 8) and continuum (Eqs. 12 and 13) analytical solutions.

Figs. 10 shows the β^2 values in a clamped-clamped boundary condition. For the same boundary

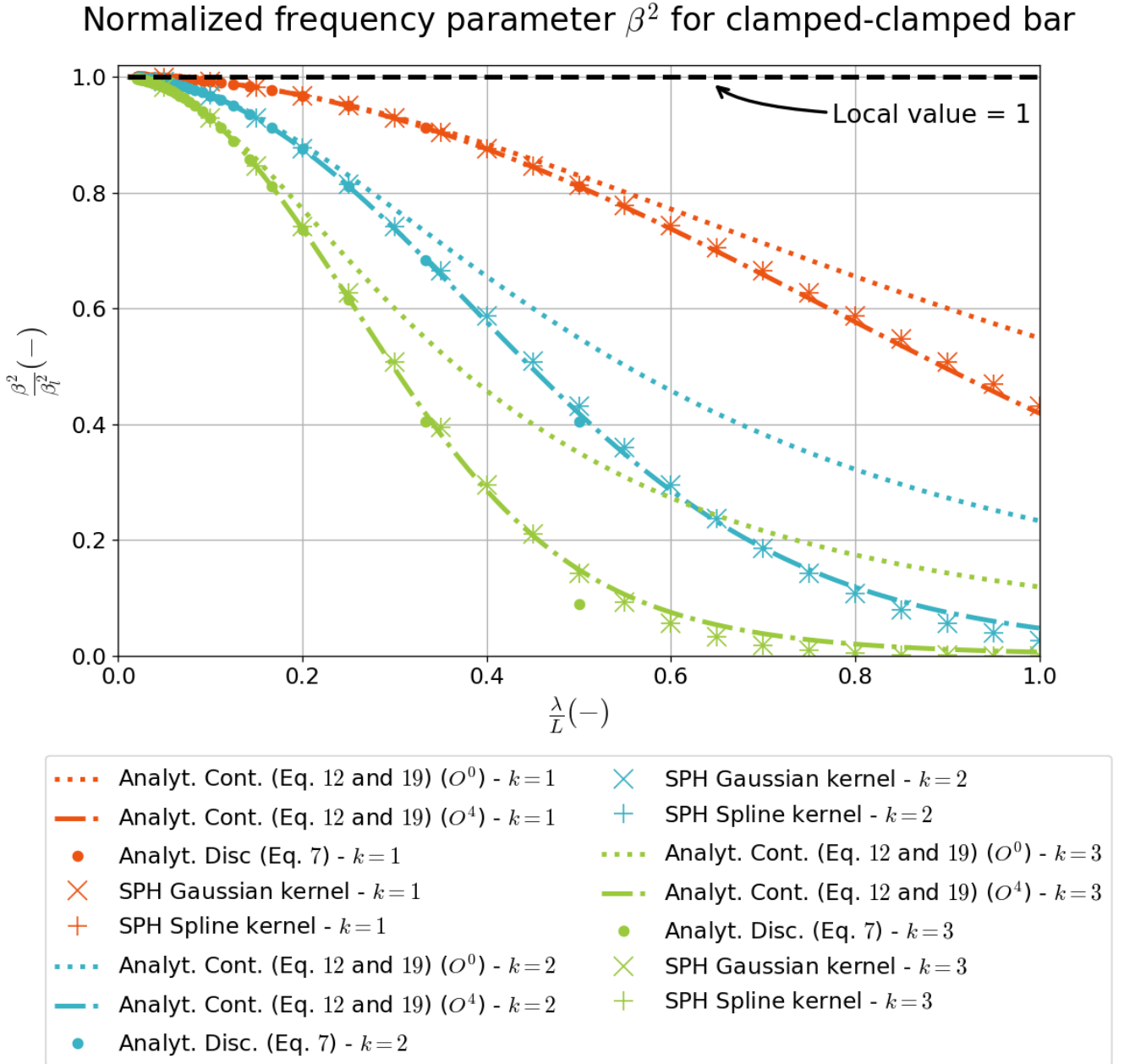


Figure 10: Clamped-clamped configuration: Normalised β^2 obtained by SPH, discrete (Eq. 7) and continuum (Eq. 12) analytical solutions by increasing the ratio λ/L for for $k=1,2$ and 3.

condition, Tab. 2 present the exact values found in two configurations: $\lambda/L = 0.05$ and $\lambda/L = 0.5$. In addition, Figs. 11 and Tab. 3 presents the same information respectively in for the clamped-free configuration.

For both boundary conditions, we obtain stable solutions of the SPH numerical results, and both continua analytical solutions ($\mathcal{O}(\lambda/L)^0$ and $\mathcal{O}(\lambda/L)^4$) are quite close to the discrete analytical solutions. As expected from the analytical models, the decrease of the non-local frequency with λ/L ratios is dependent on the vibration eigenmode, being more important for larger k values.

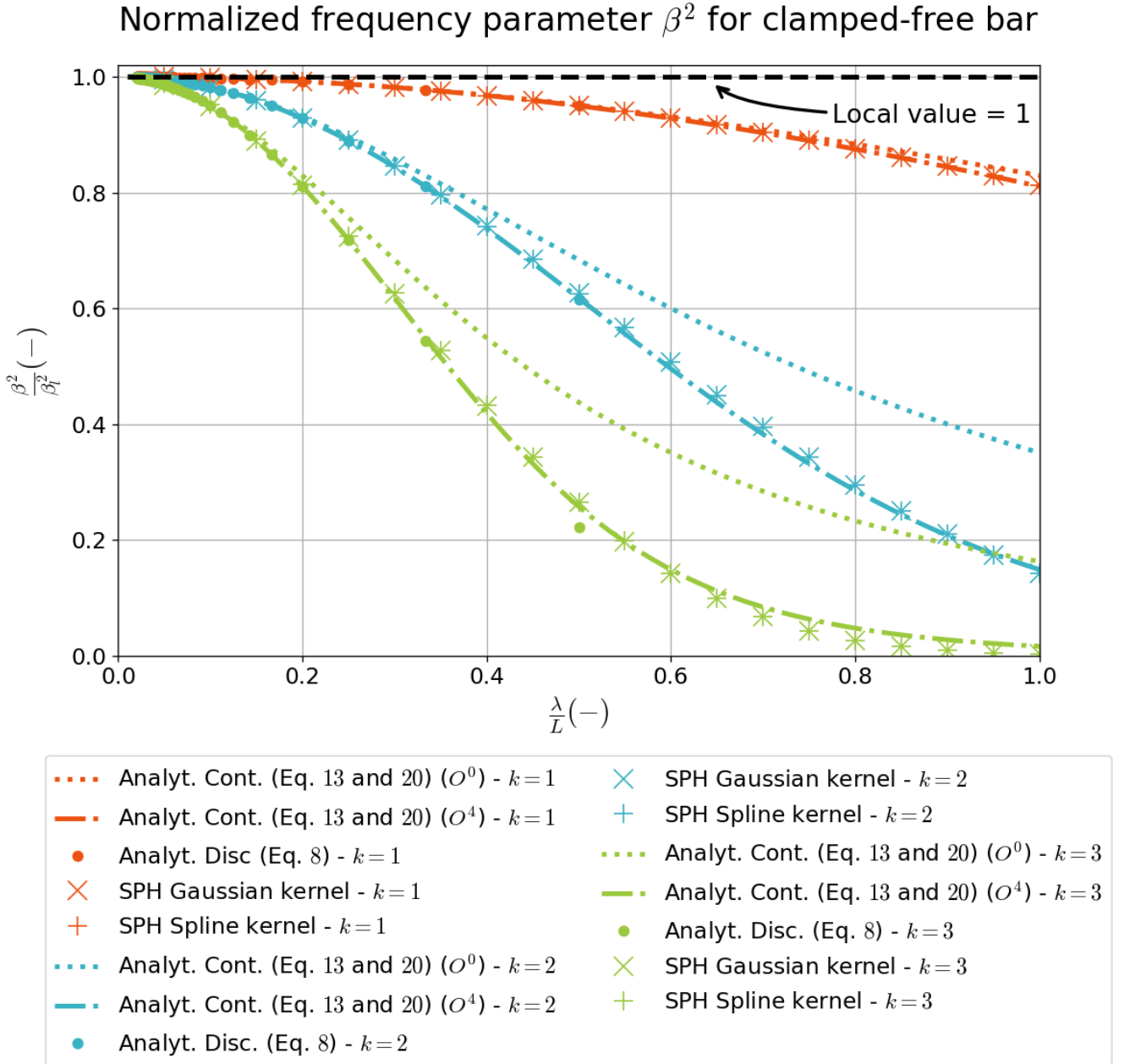


Figure 11: Clamped-free configuration: Normalised β^2 obtained by SPH, discrete (Eq. 8) and continuum (Eq. 13) analytical solutions by increasing the ratio λ/L for $k=1,2$ and 3.

Also, for higher k the difference from this solution appears at lower values of λ/L . These results also highlight the important relative discrepancies of the continuum analytical solutions compared to the discrete analytical solutions for larger values of λ/L . These differences reach maximum values for $k=3$ at $\lambda/L=0.5$. It shows that our SPH model can reach close results to the 4th order continuum model. It also can well represent such phenomena even in larger values of λ/L .

4.5. Stress-based and strain-based non-local models

In this work, we observed that the non-local effect in the SPH numerical framework comes from its smoothed character that can be applied to any local variable. Thus, based on the constitutive law (Eq. 27), different discretizations of the momentum equation can be generate, for instance: stress-based (Eq. 24) or strain-based (Eq. 42) forms. In this section, we investigate the individual behaviour between these two formulations in the context of non-locality.

$$\frac{\partial v}{\partial t} = \frac{E}{\rho_0} \frac{\partial(F\epsilon^{GL})}{\partial x} \quad (42)$$

Fig. 12 presents the frequency parameter β^2 for clamped-clamped (Fig. 12a) and clamped-free (Fig. 12b) configurations for two different momentum equation forms: stress-based and the strain-based.

The excellent agreement of results from both SPH forms confirms the equivalence of these models. Challamel has presented in [11] the equivalence between the displacement-based and the strain-based non-local models. Here, our SPH tool shows that such equivalence is also verified for the stress-based form. Challamel also argued that the incompatibility of the stress-based model in a finite domain is due to the infinite nature of the Gaussian kernel, which does not allow a normalisation in a truncated domain. However, it can be corrected by using periodic boundary conditions. In this work, we adopted a finite support spline kernel and an infinite support Gaussian kernel (with periodic boundary condition), demonstrating that the non-local nature of our numerical SPH solution is inherent, independently of the variable-based or the finite or infinite kernel support domains.

4.6. Higher-order non-local parameter e_0

In this section we come back to the results presented in Sec. 4.2 and Sec. 4.4, but we modify the presentation in order to extract the behaviour of e_0 parameter itself. We show in Figs. 13 the non-local parameter e_0 (represented here by its inverse squared form - for sake of clearness) for λ/L values for $k = 1, 2$ and 3 . These values were obtained by introducing β_{SPH}^2 values into β_C^2 from the continuum analytical model (Eqs. 12 and 13).

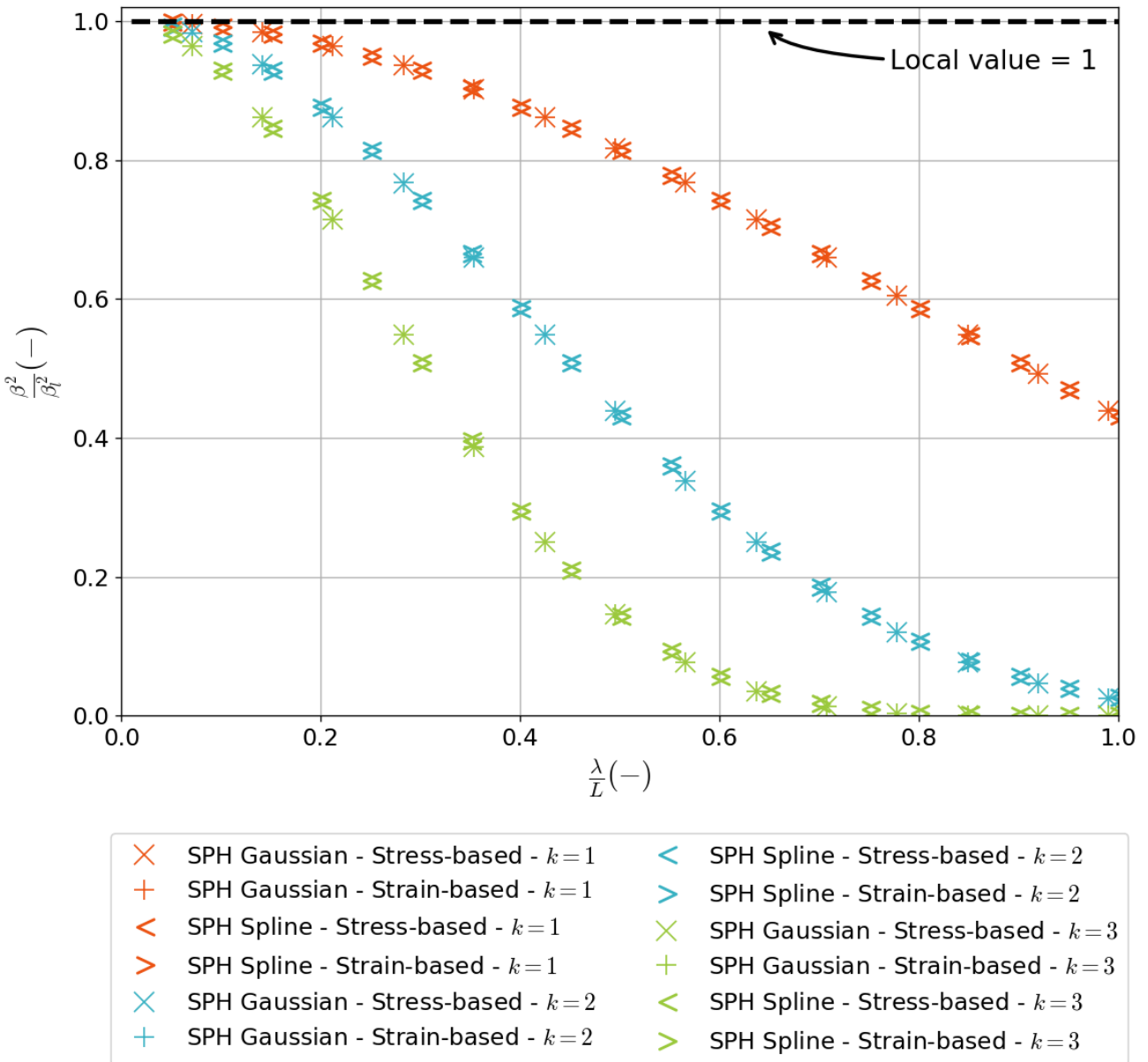
As expected, the non-local parameter found by SPH tends to the zero-th order error analytical solution (Eqs. 19 and 20), represented by the dashed line, when $\lambda/L \rightarrow 0$. However, when $\lambda/L > 0$, the SPH results show that e_0 is not constant with λ/L . Thus, we plot also the 2nd and the 4th order expansions of the analytical solution of e_0 (Eqs. 19 and 20). The highest-order analytical results present good agreement with the SPH model and confirm the sensibility of e_0^2 to λ/L values.

It can be noted some discrepancies around the small values of λ/L . In our code, the material point density is inversely proportional to the λ -support length. Hence, its reduction can generate significant discretisation errors that can be corrected by a higher material point density, demanding though more significant computing cost. Besides, we observe that the adoption of lower-order expansion of e_0 in continuum analytical solutions may become a significant error source.

Concluding remarks

In this paper, we study the numerical properties of the SPH method for non-local elasticity. The physical laws adopted in our numerical model do not present any additional terms to account for

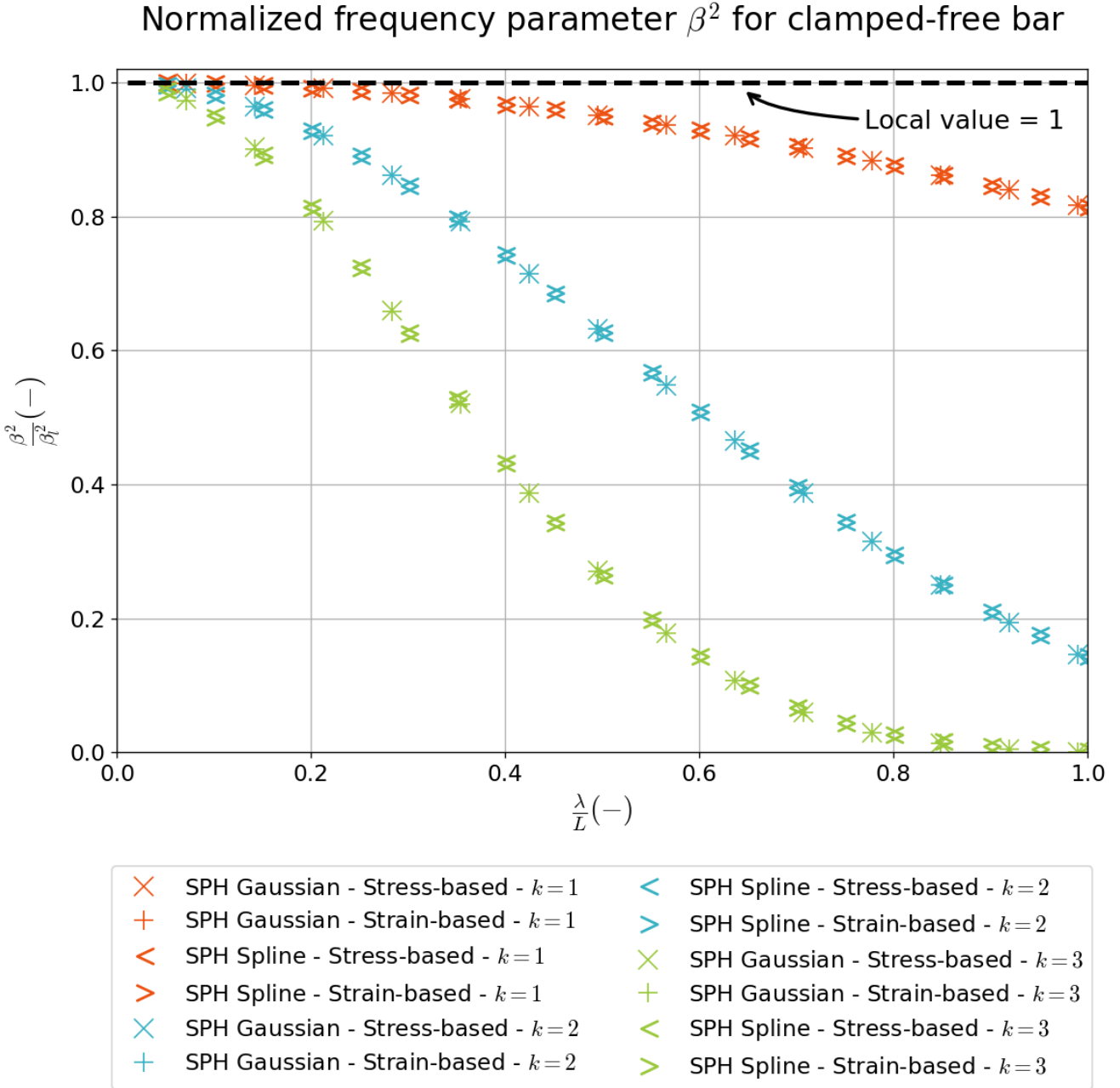
Normalized frequency parameter β^2 for clamped-clamped bar



(a) Clamped-clamped configuration: normalised β^2 obtained by SPH.

the non-locality, and the scale effect is expected to be carried out by the kernel smoothing, which is a fundamental ingredient of the SPH method. However, we do not use the SPH in its classical way (as a mere solver of PDE), which has a proven convergence with the smoothing scale $h \rightarrow 0$, but we explore its properties in a finite h domain. The computations are performed in a 1D bar under longitudinal harmonic vibrations using a mixed normalised-corrected form of the Total Lagrangian SPH method.

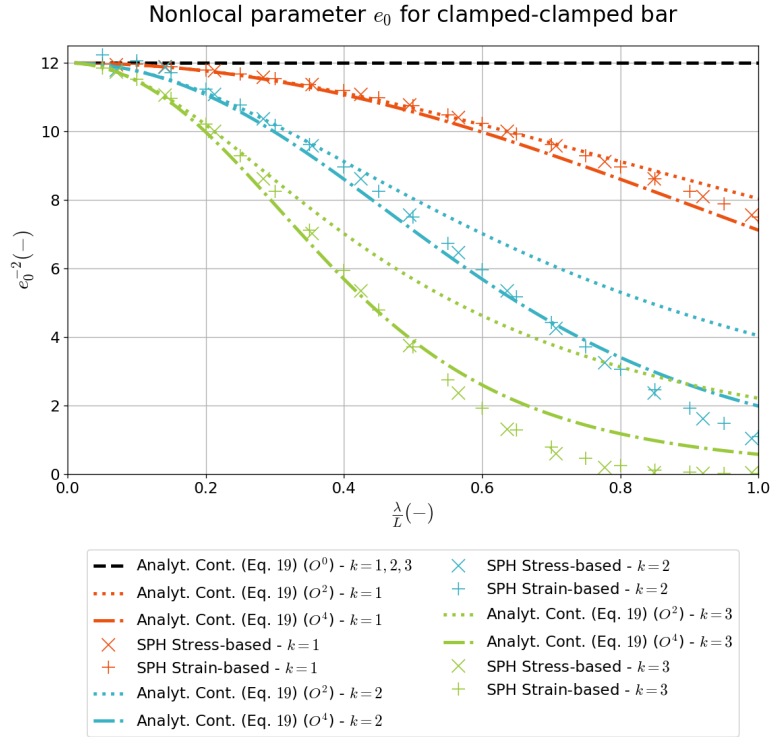
Two analytical methods (a discrete lattice and a continuum non-local model) were recalled in order to validate and discuss our numerical results. The obtained results show that the proposed SPH approach can capture in clamped-clamped and clamped-free boundary conditions problems



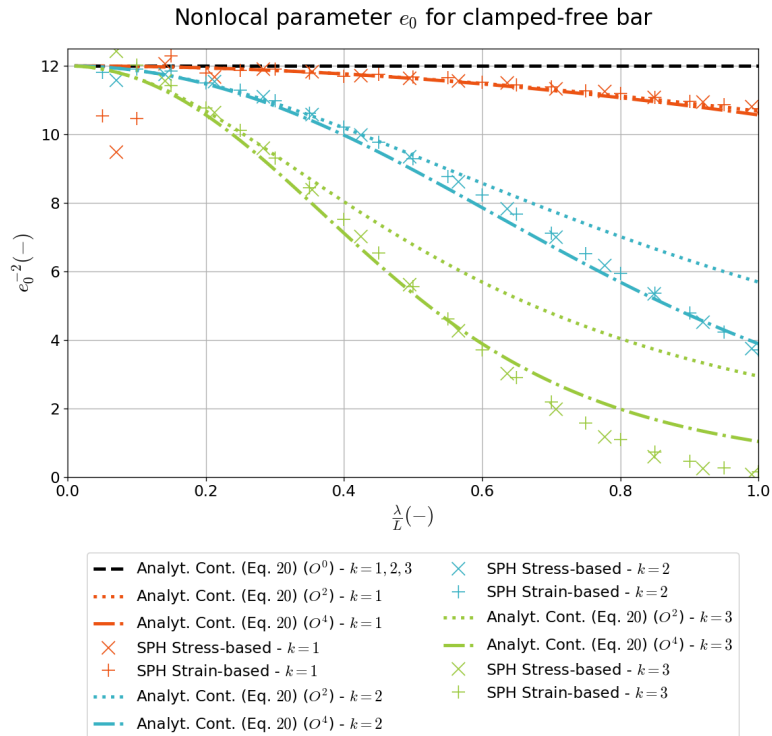
(b) Clamped-free configuration: normalised β^2 obtained by SPH).

Figure 12: Strain and stress-based behaviour of the dimensionless frequency parameter β_{SPH}^2 following strain and stress-based momentum equations for the three first eigen modes.

the expected small-scale influence on vibration frequency with good accuracy and stability for softening effects. In addition, our solver can also capture the hardening effects after the increase of the initial amplitude of vibration. Therefore, we have shown that finite and infinite kernel functions with two distinct formulations for the momentum equation lead to the same conclusions. The introduction of the Saint Venant-Kirchhoff constitutive model in the Total Lagrangian SPH approach has also allowed us to represent strain ranges where large-deformation conditions appear. e_0 ap-



(a) Clamped-clamped configuration: SPH versus different order error analytical continua solutions (Eq. 19)



(b) Clamped-free configuration: SPH versus different order error analytical continua solutions (Eq. 20)

Figure 13: Sensibility analysis of the non local parameter e_0 by increasing the ratio λ/L for $k=1,2$ and 3 .

proximations up to $\mathcal{O}(\lambda/L)^4$ seems to be the best fit for the SPH results, both for this non-local parameter and also for the frequency parameter β^2 .

In our paper, we demonstrated the capability of the SPH method to capture small scale effects is much larger than the well-known damage localisation as shown in previous research [56, 58, 57]. Our methodological study can serve as a starting point to study non-local phenomena with the SPH method without introducing any arbitrary terms into the underlying equations. To better understand the importance of non-local behaviour through SPH, elastic models in higher dimensions deserve to be further investigated. It will also be useful to better analyse the results of SPH models in more complex and coupled applications, like the gas migration in deformable porous media, where the non-locality may appear due to SPH nature and to discretisation limitations. The modeling of such a complex phenomenon has been at the heart of this domain in the last decades, but it is still poorly understood. Such analysis is a key application in the context of nuclear safety assessment and will help better describe the response of clayey rocks (represented by elastic materials) coupled to a multiphase flow.

Acknowledgements

This research has received financial support from the French National Research Agency (ANR) through the HydroGeoDam project under grant no. ANR-17-CE06-0016. We address a grateful acknowledgment to Mr. Frederic DELERUYELLE for his fruitful review and comments.

A. Appendix: Discrete lattice model elements

Based on Goldberg's [33] solution for a finite difference value problem (also resumed in [13]), we write the following auxiliary form of (Eq. 3) where $u_i = C\Psi^i$:

$$\Psi + \left(\frac{a^2}{L^2} \beta^2 - 2 \right) + \frac{1}{\Psi} = 0 \quad (43)$$

We define ϕ such as:

$$\phi = \arccos \left(1 - \frac{a^2}{L^2} \frac{\beta^2}{2} \right) \quad (44)$$

The equation (43) admits two solutions:

$$\Psi_{1,2} = \cos(\phi) \pm j \sin(\phi) \quad (45)$$

with $j = \sqrt{-1}$. Then, considering the Moivre's theorem adapted to this problem:

$$[\cos(\phi) + j \sin(\phi)]^i = \cos(i \phi) + j \sin(i \phi) \quad (46)$$

We can write, with respect to its real part, the discrete displacement u from (Eq. 3) of a i -th particle

$$u_i = C_1 \cos(i \phi) + C_2 \sin(i \phi) \quad (5 \text{ revisited})$$

where C_1 and C_2 are arbitrary constants.

Clamped-clamped boundary conditions: Adopting the boundary conditions clamped at both extremities:

$$u_0 = u_{n+1} = 0 \quad (47)$$

$C_1 = 0$ by applying the boundary conditions (Eq. 47) to (Eq. 5). Thus, noting that $(n + 1) = L/a$, it leads to:

$$C_2 \sin\left(\frac{L}{a} \phi\right) = 0 \implies \frac{L}{a} \phi = k\pi \quad (48)$$

where $k = 1, 2, 3, \dots$ denotes the vibration eigen modes. Considering the trigonometric identity:

$$1 - \cos\left(k\pi \frac{a}{L}\right) = 2 \sin^2\left(\frac{k\pi a}{2L}\right) \quad (49)$$

The introduction of (Eq. 48) into (Eq. 5) leads to a non-local form for the β^2 frequency parameter:

$$\beta_{CC}^2 = \left(2 \frac{L}{a} \sin\left(\frac{k\pi a}{2L}\right)\right)^2 \quad (7 \text{ revisited})$$

Clamped-free boundary conditions: Adopting the clamped-free boundary conditions configuration:

$$u_0 = 0 \quad (50a) \quad N_n = 0 \quad (50b)$$

where N_n is the axial force at the mass of the free end.

Applying the boundary conditions (Eq. 50) into (Eq. 5) we get $C_1 = 0$. Considering $n = L/a$, it results in:

$$C_2 \cos\left(\frac{L}{a} \phi\right) = 0 \implies \frac{L}{a} \phi = (2k - 1) \frac{\pi}{2} \quad (51)$$

Considering again the same trigonometric identity:

$$1 - \cos\left((2k - 1) \frac{\pi a}{2L}\right) = 2 \sin^2\left(\frac{(2k - 1)\pi a}{4L}\right) \quad (52)$$

and introducing (Eq. 51) into (Eq. 44) we obtain the non-local form for the β^2 frequency parameter for this case:

$$\beta_{CF}^2 = \left(2 \frac{L}{a} \sin\left(\frac{(2k - 1)\pi a}{4L}\right)\right)^2 \quad (8 \text{ revisited})$$

B. Appendix: Non-local stress gradient model elements

The non-local stress gradient model, as proposed by Eringen [27], relates the local and the non-local force quantities:

$$N = N_{nl} - (e_0 a)^2 \frac{\partial^2 N_{nl}}{\partial x^2} \quad (53)$$

where e_0 is a dimensionless material parameter and a is an internal characteristic length. Thus, combining the non-local relation (Eq. 53) and the non-local versions of (Eqs. 1 and 2) we obtain a non-local form of the wave equation (as detailed by Aydogdu [2] and Challamel *et al.* [15]):

$$EA \frac{\partial^2 u}{\partial x^2} - \rho A \frac{\partial^2 u}{\partial t^2} + \rho A (e_0 a)^2 \frac{\partial^4 u}{\partial t^2 \partial x^2} = 0 \quad (9 \text{ revisited})$$

We observe that when the non-local parameter $e_0 a = 0$ this model reduces to the local model (Eq. 2). Thus, considering the displacement of a bar in harmonic vibrations after separation of variables (as proposed by [2]).

$$u(x, t) = U(x) \sin(\omega t) \quad (54)$$

A new form of (Eq. 9) in function of $U(x)$, after the introduction of the bar length L , is then defined as:

$$\left(1 - \frac{\rho}{E} \omega^2 (e_0 a)^2\right) L^2 \frac{\partial^2 U}{\partial x^2} + \frac{\rho}{E} \omega^2 L^2 U = 0 \quad (55)$$

from what, we identify the dimensionless frequency parameter $\beta^2 = \frac{\rho}{E} \omega^2 L^2$, such as:

$$L^2 \frac{\partial^2 U}{\partial x^2} + \frac{\beta^2}{1 - e_0^2 \left(\frac{a}{L}\right)^2} U = 0 \quad (56)$$

Thus, introducing a new dimensionless parameter:

$$\alpha^2 = \frac{\beta^2}{1 - e_0^2 \left(\frac{a}{L}\right)^2} \quad (57)$$

It results in the following reduced form of the non-local wave equation:

$$L^2 \frac{\partial^2 U}{\partial x^2} + \alpha^2 U = 0 \quad (10 \text{ revisited})$$

The second degree differential (Eq. 10) yields to a solution of form:

$$U(x) = C_1 \cos\left(\frac{\alpha}{L} x\right) + C_2 \sin\left(\frac{\alpha}{L} x\right) \quad (11 \text{ revisited})$$

Clamped-clamped boundary conditions: Adopting the boundary conditions for a bar fixed at both extremities:

$$u(0, t) = u(L, t) = 0 \quad (58)$$

Applying the boundary conditions (Eq. 58) into (Eqs. 11 and 54), $C_2 \sin(\alpha) = 0$ and $C_1 = 0$. It results in $\alpha_{CC} = k\pi$, where $k = 1, 2, 3, \dots$ denotes the vibration eigen modes. It leads to a non-local formulation of the β^2 frequency parameter:

$$\beta_{CC}^2 = \frac{(k\pi)^2}{1 + e_0^2 \left(\frac{a}{L}\right)^2 (k\pi)^2} \quad (12 \text{ revisited})$$

Clamped-free boundary conditions: Now, considering a clamped-free boundary condition configuration:

$$u(0, t) = 0 \quad (59a)$$

$$N(L, t) = 0 \quad (59b)$$

After introducing (Eqs. 59) into (Eqs. 11 and 54), $C_2 \cos(\alpha) = 0$ and $C_1 = 0$. It yields that $\alpha_{CF} = (2k - 1)\frac{\pi}{2}$, resulting in a non-local form of the β^2 frequency parameter for a CF configuration:

$$\beta_{CF}^2 = \frac{\left((2k - 1)\frac{\pi}{2} \right)^2}{1 + e_0^2 \left(\frac{a}{L} \right)^2 \left((2k - 1)\frac{\pi}{2} \right)^2} \quad (13 \text{ revisited})$$

CRedit authorship contribution statement

Rafael C. Deptulski: Data curation, Software, Writing - Original draft preparation. **Magdalena Dymitrowska:** Data curation, Software. **Djimédo Kondo:** Conceptualization of this study, Methodology.

References

- [1] Attaway, S., Heinstein, M., Mello, F., Swegle, J., 1993. Coupling of smooth particle hydrodynamics with PRONTO, Sandia National Labs., Albuquerque, NM (United States), New Orleans, LA.
- [2] Aydogdu, M., 2009. Axial vibration of the nanorods with the nonlocal continuum rod model. *Physica E: Low-dimensional Systems and Nanostructures* 41, 861 – 864. URL: <http://www.sciencedirect.com/science/article/pii/S1386947709000137>, doi:<https://doi.org/10.1016/j.physe.2009.01.007>.
- [3] Aydogdu, M., 2012. Axial vibration analysis of nanorods (carbon nanotubes) embedded in an elastic medium using nonlocal elasticity. *Mechanics Research Communications* 43, 34 – 40. URL: <http://www.sciencedirect.com/science/article/pii/S009364131200016X>, doi:<https://doi.org/10.1016/j.mechrescom.2012.02.001>.
- [4] Bathe, K.J., Bolourchi, S., 1979. Large displacement analysis of three-dimensional beam structures. *International Journal for Numerical Methods in Engineering* 14, 961–986. URL: <https://onlinelibrary.wiley.com/doi/abs/10.1002/nme.1620140703>, doi:10.1002/nme.1620140703, arXiv:<https://onlinelibrary.wiley.com/doi/pdf/10.1002/nme.1620140703>.
- [5] Bažant, Z.P., 1987. Why continuum damage is nonlocal: justification by quasiperiodic microcrack array. *Mechanics Research Communications* 14, 407–419.
- [6] Bažant, Z.P., 1991. Why continuum damage is nonlocal: Micromechanics arguments. *Journal of Engineering Mechanics* 117, 1070–1087.
- [7] Bažant, Z.P., Belytschko, T.B., 1985. Wave propagation in a strain-softening bar: exact solution. *Journal of Engineering Mechanics* 111, 381–389.
- [8] Belytschko, T., Liu, W.K., Moran, B., Elkhodary, K., 2013. *Nonlinear finite elements for continua and structures*. John Wiley & sons.
- [9] Bonet, J., Lok, T.S., 1999. Variational and momentum preservation aspects of smooth particle hydrodynamic formulations. *Computer Methods in Applied Mechanics and Engineering* 180, 97 – 115. URL: <http://www.sciencedirect.com/science/article/pii/S0045782599000511>, doi:[https://doi.org/10.1016/S0045-7825\(99\)00051-1](https://doi.org/10.1016/S0045-7825(99)00051-1).
- [10] Capone, T., Panizzo, A., Monaghan, J.J., 2010. Sph modelling of water waves generated by submarine landslides. *Journal of Hydraulic Research* 48, 80–84. URL: <https://doi.org/10.1080/00221686.2010.9641248>, doi:10.1080/00221686.2010.9641248, arXiv:<https://doi.org/10.1080/00221686.2010.9641248>.
- [11] Challamel, N., 2018. Static and dynamic behaviour of nonlocal elastic bar using integral strain-based and peridynamic models. *Comptes Rendus Mécanique* 346, 320 – 335. URL: <http://www.sciencedirect.com/science/article/pii/S1631072117302504>, doi:<https://doi.org/10.1016/j.crme.2017.12.014>.
- [12] Challamel, N., Lerbet, J., Wang, C., Zhang, Z., 2014. Analytical length scale calibration of nonlocal continuum from a microstructured buckling model. *ZAMM - Journal of Applied Mathematics and Mechanics / Zeitschrift für Angewandte Mathematik und Mechanik* 94, 402–413. URL: <https://doi.org/10.1002/zamm.201200130>, doi:10.1002/zamm.201200130. publisher: John Wiley & Sons, Ltd.
- [13] Challamel, N., Picandet, V., Collet, B., Michelitsch, T., Elishakoff, I., Wang, C., 2015a. Revisiting finite difference and finite element methods applied to structural mechanics within enriched continua. *European Journal of Mechanics - A/Solids* 53, 107–120. URL: <http://www.sciencedirect.com/science/article/pii/S0997753815000236>, doi:10.1016/j.euromechsol.2015.03.003.

- [14] Challamel, N., Picandet, V., Elishakoff, I., Wang, C.M., Collet, B., Michelitsch, T., 2015b. On nonlocal computation of eigen frequencies of beams using finite difference and finite element methods. *International Journal of Structural Stability and Dynamics* 15, 1540008. ISBN: 0219-4554 Publisher: World Scientific.
- [15] Challamel, N., Rakotomanana, L., Marrecq, L.L., 2009. A dispersive wave equation using nonlocal elasticity. *Comptes Rendus Mécanique* 337, 591–595. URL: <http://www.sciencedirect.com/science/article/pii/S1631072109001041>, doi:<https://doi.org/10.1016/j.crme.2009.06.028>.
- [16] Challamel, N., Wang, C., Elishakoff, I., 2016. Nonlocal or gradient elasticity macroscopic models: A question of concentrated or distributed microstructure. *Mechanics Research Communications* 71, 25–31. URL: <http://www.sciencedirect.com/science/article/pii/S0093641315001792>, doi:<https://doi.org/10.1016/j.mechrescom.2015.11.006>.
- [17] Challamel, N., Wang, C.M., Zhang, H., Kitipornchai, S., 2018. Exact and nonlocal solutions for vibration of axial lattice with direct and indirect neighboring interactions. *Journal of Engineering Mechanics* 144, 04018025. ISBN: 0733-9399 Publisher: American Society of Civil Engineers.
- [18] Chaniotis, A., Poulidakos, D., Koumoutsakos, P., 2002. Remeshed Smoothed Particle Hydrodynamics for the Simulation of Viscous and Heat Conducting Flows. *Journal of Computational Physics* doi:10.1006/jcph.2002.7152.
- [19] Chen, Z., Zong, Z., Liu, M.B., Zou, L., Li, H.T., Shu, C., 2015. An SPH model for multiphase flows with complex interfaces and large density differences. *Journal of Computational Physics* doi:10.1016/j.jcp.2014.11.037.
- [20] Collins, M.A., 1981. A quasicontinuum approximation for solitons in an atomic chain. *Chemical Physics Letters* 77, 342–347. URL: <http://www.sciencedirect.com/science/article/pii/0009261481801613>, doi:[https://doi.org/10.1016/0009-2614\(81\)80161-3](https://doi.org/10.1016/0009-2614(81)80161-3).
- [21] Şimşek, M., 2014. Large amplitude free vibration of nanobeams with various boundary conditions based on the nonlocal elasticity theory. *Composites Part B: Engineering* 56, 621–628. URL: <http://www.sciencedirect.com/science/article/pii/S1359836813005040>, doi:10.1016/j.compositesb.2013.08.082.
- [22] Şimşek, M., 2016. Nonlinear free vibration of a functionally graded nanobeam using nonlocal strain gradient theory and a novel Hamiltonian approach. *International Journal of Engineering Science* 105, 12–27. URL: <http://www.sciencedirect.com/science/article/pii/S0020722516300520>, doi:10.1016/j.ijengsci.2016.04.013.
- [23] Dehnen, W., Aly, H., 2012. Improving convergence in smoothed particle hydrodynamics simulations without pairing instability. *Monthly Notices of the Royal Astronomical Society* 425, 1068–1082. URL: <https://doi.org/10.1111/j.1365-2966.2012.21439.x>, doi:10.1111/j.1365-2966.2012.21439.x.
- [24] Dyka, C.T., Randles, P.W., Ingel, R.P., 1997. Stress points for tension instability in SPH. *International Journal for Numerical Methods in Engineering* doi:10.1002/(SICI)1097-0207(19970715)40:13<2325::AID-NME161>3.0.CO;2-8.
- [25] Eringen, A., 1976. *Continuum physics. volume 4-polar and nonlocal field theories*. New York, Academic Press, Inc., 1976. 288 p.
- [26] Eringen, A., Suhubi, E., 1964. Nonlinear theory of simple micro-elastic solids—i. *International Journal of Engineering Science* 2, 189–203. URL: <http://www.sciencedirect.com/science/article/pii/0020722564900047>, doi:[https://doi.org/10.1016/0020-7225\(64\)90004-7](https://doi.org/10.1016/0020-7225(64)90004-7).
- [27] Eringen, A.C., 1983. On differential equations of nonlocal elasticity and solutions of screw dislocation and surface waves. *Journal of applied physics* 54, 4703–4710.
- [28] Eringen, A.C., 1984. *Theory of nonlocal elasticity and some applications*. Technical Report. Princeton Univ NJ Dept of Civil Engineering.
- [29] Eringen, A.C., 2002. *Nonlocal continuum field theories*. Springer Science & Business Media.
- [30] Eringen, A.C., Edelen, D., 1972. On nonlocal elasticity. *International Journal of Engineering Science* 10, 233–248.
- [31] Eringen, A.C., Kim, B.S., 1977. Relation between non-local elasticity and lattice dynamics.
- [32] Gingold, R.A., Monaghan, J.J., 1977. Smoothed particle hydrodynamics: theory and application to non-spherical stars. *Monthly notices of the royal astronomical society* 181, 375–389.
- [33] Goldberg, S., 1958. *Introduction to difference equations: with illustrative examples from economics, psychology, and sociology*. Wiley. URL: <https://books.google.fr/books?id=0vY4zQEACAAJ>.
- [34] Kunin, I., 1966. Model of an elastic medium of simple structure with three-dimensional dispersion. *Journal of Applied Mathematics and Mechanics* 30, 642–652. URL: <http://www.sciencedirect.com/science/article/pii/0021892867901013>, doi:10.1016/0021-8928(67)90101-3.
- [35] Lagrange, J.L., 1759. *Recherches sur la nature et la propagation du son*. Œuvres complètes ed., Gallica. URL: http://sites.mathdoc.fr/cgi-bin/oeitem?id=OE_LAGRANGE__1_39_0.
- [36] Lagrange, J.L., 1788. *Mécanique Analytique*. Desaint. URL: <http://eudml.org/doc/204580>.
- [37] Lazar, M., Maugin, G.A., Aifantis, E.C., 2006. On a theory of nonlocal elasticity of bi-Helmholtz type and some applications. *International Journal of Solids and Structures* 43, 1404–1421. URL: <http://www.sciencedirect.com/science/article/pii/S0020768305002209>, doi:10.1016/j.ijsolstr.2005.04.027.
- [38] Libersky, L.D., Petschek, A.G., 1991. Smooth particle hydrodynamics with strength of materials, in: *Advances in the free-Lagrange method including contributions on adaptive gridding and the smooth particle hydrodynamics method*. Springer, pp. 248–257.
- [39] Libersky, L.D., Petschek, A.G., Carney, T.C., Hipp, J.R., Allahdadi, F.A., 1993. High strain lagrangian hydrodynamics a three-dimensional SPH code for dynamic material response. *Journal of Computational Physics* doi:10.1006/jcph.1993.1199.
- [40] Liu, M.B., Liu, G.R., 2005. Meshfree particle simulation of micro channel flows with surface tension. *Computational Mechanics* doi:10.1007/s00466-004-0620-y.
- [41] Liu, M.B., Liu, G.R., 2010. Smoothed particle hydrodynamics (SPH): An overview and recent developments. *Archives of Computational Methods in Engineering* doi:10.1007/s11831-010-9040-7, arXiv:1007.3908.
- [42] Liu, W.K., Jun, S., Li, S., Adee, J., Belytschko, T., 1995. Reproducing kernel particle methods for structural dynamics. *International Journal for Numerical Methods in Engineering* doi:10.1002/nme.1620381005.

Modelling non-local elasticity in 1D vibrating rods using Smoothed Particle Hydrodynamics method

- [43] Lucy, L.B., 1977. A numerical approach to the testing of the fission hypothesis. 82, 1013–1024. doi:10.1086/112164.
- [44] Monaghan, J.J., Huppert, H.E., Worster, M.G., 2005. Solidification using smoothed particle hydrodynamics. *Journal of Computational Physics* doi:10.1016/j.jcp.2004.11.039, arXiv:0507472.
- [45] Monaghan, J.J., Kocharyan, A., 1995. SPH simulation of multi-phase flow. *Computer Physics Communications* doi:10.1016/0010-4655(94)00174-Z.
- [46] Morris, J.P., 2000. Simulating surface tension with smoothed particle hydrodynamics. *International Journal for Numerical Methods in Fluids* doi:10.1002/1097-0363(20000615)33:3<333::AID-FLD11>3.0.CO;2-7.
- [47] Pazdniakou, A., Dymitrowska, M., 2018. Migration of gas in water saturated clays by coupled hydraulic-mechanical model. *Geofluids* 2018.
- [48] Rabczuk, T., Belytschko, T., Xiao, S., 2004. Stable particle methods based on Lagrangian kernels. *Meshfree Methods: Recent Advances and New Applications* 193, 1035–1063. URL: <http://www.sciencedirect.com/science/article/pii/S0045782504000088>, doi:10.1016/j.cma.2003.12.005.
- [49] Reveles, J.R., 2007. Development of a total Lagrangian SPH code for the simulation of solids under dynamic loading. Ph.D. thesis. Cranfield University.
- [50] Rogula, D., 1982. *Nonlocal Theory of Material Media*. Springer-Verlag Kg. URL: <https://books.google.fr/books?id=iaEeAQAAIAAJ>.
- [51] Rosenau, P., 1986. Dynamics of nonlinear mass-spring chains near the continuum limit. *Physics Letters A* 118, 222–227. URL: <http://www.sciencedirect.com/science/article/pii/0375960186901702>, doi:[https://doi.org/10.1016/0375-9601\(86\)90170-2](https://doi.org/10.1016/0375-9601(86)90170-2).
- [52] Rosenau, P., 1987. Dynamics of dense lattices. *Physical Review B* 36, 5868–5876. URL: <https://link.aps.org/doi/10.1103/PhysRevB.36.5868>, doi:10.1103/PhysRevB.36.5868. publisher: American Physical Society.
- [53] Song, Y., Davy, C., Troadec, D., Blanchenet, A.M., Skoczylas, F., Talandier, J., Robinet, J., 2015. Multi-scale pore structure of COx claystone: Towards the prediction of fluid transport. *Marine and Petroleum Geology* 65, 63–82. URL: <https://linkinghub.elsevier.com/retrieve/pii/S0264817215001245>, doi:10.1016/j.marpetgeo.2015.04.004.
- [54] Sutmann, G., 2007. Compact finite difference schemes of sixth order for the helmholtz equation. *Journal of Computational and Applied Mathematics* 203, 15–31.
- [55] Tartakovsky, A.M., Trask, N., Pan, K., Jones, B., Pan, W., Williams, J.R., 2016. Smoothed particle hydrodynamics and its applications for multiphase flow and reactive transport in porous media. *Computational Geosciences* 20, 807–834. doi:10.1007/s10596-015-9468-9.
- [56] Vignjevic, R., Campbell, J., Libersky, L., 2000. A treatment of zero-energy modes in the smoothed particle hydrodynamics method. *Computer Methods in Applied Mechanics and Engineering* doi:10.1016/S0045-7825(99)00441-7.
- [57] Vignjevic, R., Djordjevic, N., Gemkow, S., De Vuyst, T., Campbell, J., 2014. Sph as a nonlocal regularisation method: Solution for instabilities due to strain-softening. *Computer Methods in Applied Mechanics and Engineering* 277, 281–304.
- [58] Vignjevic, R., Reveles, J.R., Campbell, J., 2006. SPH in a total lagrangian formalism. *CMES - Computer Modeling in Engineering and Sciences* doi:citeulike-article-id:1967892.
- [59] Vila, J., Fernández-Sáez, J., Zaera, R., 2017. Nonlinear continuum models for the dynamic behavior of 1D microstructured solids. *International Journal of Solids and Structures* 117, 111–122. URL: <http://www.sciencedirect.com/science/article/pii/S0020768317301348>, doi:10.1016/j.ijsolstr.2017.03.033.
- [60] Vila, J., Fernández-Sáez, J., Zaera, R., 2018. Reproducing the nonlinear dynamic behavior of a structured beam with a generalized continuum model. *Journal of Sound and Vibration* 420, 296–314. URL: <http://www.sciencedirect.com/science/article/pii/S0022460X18300488>, doi:10.1016/j.jsv.2018.01.040.
- [61] Violeau, D., Issa, R., 2007. Numerical modelling of complex turbulent free-surface flows with the SPH method: An overview. doi:10.1002/fld.1292, arXiv:fld.1.
- [62] Violeau, D., Leroy, A., 2014. On the maximum time step in weakly compressible SPH. *Journal of Computational Physics* 256, 388–415. URL: <http://www.sciencedirect.com/science/article/pii/S0021999113006050>, doi:10.1016/j.jcp.2013.09.001.
- [63] Wang, C.M., Zhang, H., Challamel, N., Duan, W.H., 2017. Eringen's small length scale coefficient for vibration of axially loaded nonlocal Euler beams with elastic end restraints. *Journal of Modeling in Mechanics and Materials* 1. Publisher: De Gruyter.
- [64] Young, J.R., 2018. Modelling elastic dynamics and fracture with coupled mixed correction Eulerian Total Lagrangian SPH. Ph.D. thesis. The University of Edinburgh.
- [65] Zhang, H., Wang, C., Challamel, N., 2018. Modelling vibrating nano-strings by lattice, finite difference and Eringen's nonlocal models. *Journal of Sound and Vibration* 425, 41–52. URL: <http://www.sciencedirect.com/science/article/pii/S0022460X18302207>, doi:10.1016/j.jsv.2018.04.001.
- [66] Zhang, Z., Wang, C., Challamel, N., Elishakoff, I., 2014. Obtaining Eringen's length scale coefficient for vibrating nonlocal beams via continualization method. *Journal of Sound and Vibration* 333, 4977–4990. URL: <http://www.sciencedirect.com/science/article/pii/S0022460X1400371X>, doi:10.1016/j.jsv.2014.05.002.

Concluding remarks

In this chapter, we have studied a 1D vibration problem for different boundary conditions (clamped-clamped and clamped-free). We have accurately accounted for higher-order (non-local) effects in elasticity compared to analytical lattice discrete and continuous solutions. It has been shown that the non-local effects are directly related to the numerical support-length parameter (inherent to the SPH).

SPH modelling of local elasto-damage

Overview: In this chapter, we aim to extend the capability of our SPH solver to deal with non-local effects due to growing damage in elastic materials. In section 4.1, we established a local energetic-based formulation of the elastic damage model. Unilateral effects in the presence of damage (observed in geomaterials) are included in this formulation. In section 4.2, a 1D problem of a softening bar is treated through the SPH method in order to provide a first characterization of the non-local effects. In section 4.3, a 2D structure (a square plate with a rigid inclusion) is investigated either in quasi-static or dynamics conditions. For these cases, we examine the possibility to predict the transition from damage to fracture. Asymmetric tensile-compressive responses are also discussed. Finally, the role of the numerical parameter (the support length of the SPH kernel function) as a potential characteristic length of the material is discussed.

Despite several research studies carried out recently, the hydromechanical behaviour of clayey rocks is not yet fully understood at the pore scale given the difficulty to observe at lower-scale the initiation of macroscopic fractures and to regenerate conditions existing in-situ. We previously mentioned and discussed that dilatant flows are still poorly characterized both from experimental and theoretical perspectives due to their coupling with damage. Experimental data reported in literature [140], [173] state that the clayey matrix studied here has an elastic response for a deformation range up to an elastic limit value. Beyond this threshold, an irreversible degradation phenomenon may take place. Such a process can occur by widening the existing pore spaces resulting in new micro-cracks, that can become preferential percolation pathways. In the field of clay materials, such problem has been the source of few studies [63], [155].

Concerning the issues related to deep geological disposals, we can decouple, in a first approach, damage and hydromechanics. The damage prediction and its transition towards rupture phenomena constitute an essential subject in itself, even in an unsaturated state. A widespread form of investigating this problem consists of implementing regularised non-local damage models (non-local integral or differential formulations).

The fracture in its classical theory understanding, as introduced by Griffith [71] and enhanced by Irwin [78] and Rice [142], will not be directly investigated here, but will be suitably addressed through localisation of damage. Introduced by Lemaitre and

Chaboche [89], the damage model adopted here (reputed as “local” method) is based in a thermodynamics approach that can be built from two main ingredients: the choice of state variables that construct a thermodynamics potential (giving its energetic evolution) and a damage criterion that governs the degradation process. The numerical modelling of local damage models also presents a few specific aspects. The zones strongly damaged can be assimilated as fractures, but not presenting tough discontinuities of the displacement field. Besides, the damage field tends to be localized in areas of infinitesimal size leading to failure without energy dissipation [15], which can generate major issues in a mesh-based method where the results may depend on the mesh resolution.

In order to overcome this pathological mesh dependence issue, non-local damage models were proposed. In a first non-local method (called as “integral”)[18], [129] the local damage variable (or its conjugated force) is replaced by its non-local version (through a convolution procedure). Francfort and Marigo [65] proposed another solution to the damage problem using a variational approach (reputed as “gradient”), where the solution is based in a minimization of the functional energy function. An approximation of this variational approach (called as “phase-field”) has been proposed by Bourdin *et al.* [30] based on Ambrosio and Tortorelli [1], [2], in which the way to solve the localization problem originated in local models is to “regularise” the functional to be minimized by adding therein an additional term comprising the damage gradient and some material constants (notably a characteristic length that is related to the width of the localization zone). A few years later, this approximation has been interpreted as the variational formulation of a class of gradient damage models [105], [128]. Also, Lorentz and Andrieux [101][102] proposed another alternative to this class of gradient damage model that introduces the characteristic length in a gradient term occurring in the stored energy. Recently, phase-field applications in dynamic conditions are also found in literature [22], [28], [93].

In this thesis, we propose a new form to treat the damage-fracturing problem through our interpolated Smoothed Particle Hydrodynamics (SPH), a meshless method capable of extending the non-local nature to any variable, generating a non-local system. For the reasons just mentioned, an important challenge of this thesis is to investigate the capability to predict rupture phenomena through the SPH method, while accounting for non-local effects but without resorting to a non-local regularisation of the damage law. In this context, a significant question we contribute to answering here is about the role played for the h -length inherent to the SPH solver.

Prediction of damage occurrence and growth in solid elastic materials has motivated various researches based on the stress-based criteria reputed in the continuum damage mechanics [79], [81], [107], [123], [133] or on the energy-based methods following a thermodynamics approach [90], [91]. The coupled *Rankine - Mohr-Coulomb*

criteria allows to treat tensile, compressive and shear loads. Despite its various advantages, this approach may be viewed as the first attempt of modelling. A more advanced strategy consists of a thermodynamics-based formulation that will allow accounting for the very dissipative nature of the damage. We also seek to compare the SPH model firstly adopted in Pazdniakou and Dymitrowska [126] to the results obtained using the thermodynamics approach adopted here. Moreover, for the sake of conciseness, we present here only the small deformations formulations. However, given the similarities between both forms, the large deformations formulations can be achieved through the following equations replacing the small deformations tensors by the large deformations tensors in a similar procedure as presented in Sections 2.4.1 and 2.4.2.

4.1 Thermodynamics-based formulation of damage models

In this section, we aim at presenting the two necessary ingredients to construct a thermodynamic-based damage model in the context of Generalized Standard Materials (GSM) [72].

4.1.1 Free energy and dissipation potential

The choice of the state variables $(\underline{\underline{\varepsilon}}, D)$ is the first required ingredient to constitute the thermodynamics potential (or Helmholtz free energy) of an elasto-damageable material, such as:

$$\rho w(\underline{\underline{\varepsilon}}, D) = \frac{1}{2} \underline{\underline{\varepsilon}} : \mathbb{C}(D) : \underline{\underline{\varepsilon}} \quad (4.1)$$

where $\mathbb{C}(D)$ is the effective stiffness tensor. The state laws can be deduced from the thermodynamics potential becoming the following conjugated reversible forces:

$$\underline{\underline{\sigma}}^{rev} = \rho \frac{\partial w}{\partial \underline{\underline{\varepsilon}}} = \mathbb{C}(D) : \underline{\underline{\varepsilon}} \quad (4.2a)$$

$$\mathcal{Y}^{rev} = \rho \frac{\partial w}{\partial D} = \frac{1}{2} \underline{\underline{\varepsilon}} : \mathbb{C}'(D) : \underline{\underline{\varepsilon}} \quad (4.2b)$$

where the superscript *rev* relates a reversible state and ' designates a material derivative. The evolution law of the internal variable (damage variable D) is then a necessary step within the construction of the damage model. It leads to the expression of the intrinsic dissipation \mathcal{D} as a consequence of the damage increasing.

$$\mathcal{D} = (\underline{\underline{\sigma}} - \underline{\underline{\sigma}}^{rev}) : \dot{\underline{\underline{\varepsilon}}} - \mathcal{Y}^{rev} \dot{D} \quad (4.3)$$

which can be written in function of the irreversible state variables (denoted by the *irr* superscript), such that:

$$\mathcal{D} = (\underline{\underline{\sigma}}^{irr}) : \underline{\underline{\dot{\varepsilon}}} + \mathcal{Y}^{irr} \dot{D} \quad (4.4)$$

It is evident that $\underline{\underline{\sigma}}^{irr} = \underline{\underline{\sigma}} - \underline{\underline{\sigma}}^{rev}$ and $\mathcal{Y}^{irr} = -\mathcal{Y}^{rev}$. Considering a non-viscous behaviour, $\underline{\underline{\varepsilon}}$ is a non-dissipative variable and then $\underline{\underline{\sigma}}^{irr} = 0$. Thus, we are able to evaluate the evolution of the damage variable, as follows:

$$\mathcal{D} = \mathcal{Y}^{irr} \dot{D} \quad (4.5)$$

It results in the irreversible thermodynamic force associated to the damage variable D :

$$\mathcal{Y}^{irr} = -\rho \frac{\partial w}{\partial D} = -\frac{1}{2} \underline{\underline{\varepsilon}} : \mathbb{C}'(D) : \underline{\underline{\varepsilon}} \quad (4.6)$$

It is noteworthy that the first derivatives of the stiffness tensor $\mathbb{C}(D)$ must present negative values in order to represent a degradation on the material properties (*i.e.* $\mathbb{C}'(D) < 0$). Besides, the second derivatives must have positive values (*i.e.* $\mathbb{C}''(D) > 0$) in order to ensure the stability of the model. On the same way, the positivity of the intrinsic dissipation seeks to guarantee the irreversibility of the damage, such as:

$$\mathcal{Y}^{irr} \dot{D} \geq 0 \Rightarrow \dot{D} \geq 0 \quad (4.7)$$

4.1.2 Dissipation pseudo-potential and evolution laws

In order to obtain the second required ingredient in the GSM context, an automatic way to ensure the positivity of \mathcal{D} during degradation evolution is to obtain the differential of \mathcal{Y} with respect to the dissipation pseudo-potential:

$$\varphi(\dot{D}) = \mathcal{Y}_c \dot{D} \quad (4.8)$$

which is convex in \dot{D} , has non-negative scalar values and minima $\dot{D} = 0$ ($\varphi(0) = 0$). For non-differential φ , the dissipative thermodynamic forces read:

$$\mathcal{Y} \in \partial\varphi(\dot{D}) \quad (4.9)$$

in which, we adopt the notation $\mathcal{Y} = \mathcal{Y}^{irr}$ for the sake of simplicity. The dual potential $\varphi^*(\mathcal{Y}, D)$ is given by the *Legendre-Fenchel* transform of $\varphi(\dot{D})$, such as:

$$\begin{aligned}\varphi^*(\mathcal{Y}, D) &= \sup_{\dot{D}} (\mathcal{Y}\dot{D} - \mathcal{Y}_c\dot{D}) \\ &= \begin{cases} 0 & \text{if } \mathcal{Y} - \mathcal{Y}_c \leq 0 \\ +\infty & \text{if } \mathcal{Y} - \mathcal{Y}_c > 0 \end{cases}\end{aligned}\quad (4.10)$$

which is the indicator function of the $\varphi = [0, \mathcal{Y}_c]$ domain. This process leads to a damage criterion (also called as loading function) expressed as:

$$f(\mathcal{Y}) = \mathcal{Y} - \mathcal{Y}_c(D) \leq 0 \quad (4.11)$$

Following the particularity of different damage models, it can be necessary to introduce the dependency on D into \mathcal{Y}_c in Eq. (4.11). Henceforth, from (Eq. 4.6) the loading function can be written in tensorial notation as:

$$f(\mathcal{Y}) = -\frac{1}{2} \underline{\underline{\varepsilon}} : \mathbb{C}'(D) : \underline{\underline{\varepsilon}} - \mathcal{Y}_c(D) \leq 0 \quad (4.12)$$

The damage evolution law is then given by:

$$\dot{D} \in \partial\varphi^*(\mathcal{Y}, D) \quad (4.13)$$

which, owing to (Eq. 4.10) reads:

$$\dot{D} = \begin{cases} 0 & \text{if } \underbrace{f(\mathcal{Y}) < 0}_{\text{elastic regime}} \text{ or } \underbrace{f(\mathcal{Y}) = 0 \text{ and } \dot{f}(\mathcal{Y}) < 0}_{\text{elastic unloading}} \\ \underbrace{\Lambda \frac{\partial f(\mathcal{Y})}{\partial \mathcal{Y}}}_{=1} = \Lambda & \text{if } \underbrace{f(\mathcal{Y}) = 0 \text{ and } \dot{f}(\mathcal{Y}) = 0}_{\text{damage loading}} \end{cases}\quad (4.14)$$

The different cases are illustrated in Fig. 4.1. In (Eq. 4.14), Λ is a positive damage scalar, determined from the consistency condition $\dot{f}(\mathcal{Y}) = 0$, which reads:

$$\begin{aligned}\dot{f}(\mathcal{Y}(\underline{\underline{\varepsilon}}, \dot{D})) &= \frac{\partial f}{\partial \underline{\underline{\varepsilon}}} : \dot{\underline{\underline{\varepsilon}}} + \frac{\partial f}{\partial D} : \dot{D} \\ &= -\mathbb{C}'(D) : \underline{\underline{\varepsilon}} : \dot{\underline{\underline{\varepsilon}}} - \left(\frac{1}{2} \underline{\underline{\varepsilon}} : \mathbb{C}''(D) : \underline{\underline{\varepsilon}} + \mathcal{Y}'_c(D) \right) \dot{D} = 0\end{aligned}\quad (4.15)$$

It follows that in damage loading regime (*i.e.* $f(\mathcal{Y}) = 0$ and $\dot{f}(\mathcal{Y}) = 0$):

$$\dot{D} = \Lambda = \frac{-\mathbb{C}'(D) : \underline{\underline{\varepsilon}} : \dot{\underline{\underline{\varepsilon}}}}{\frac{1}{2} \underline{\underline{\varepsilon}} : \mathbb{C}''(D) : \underline{\underline{\varepsilon}} + \mathcal{Y}'_c(D)} \quad (4.16)$$

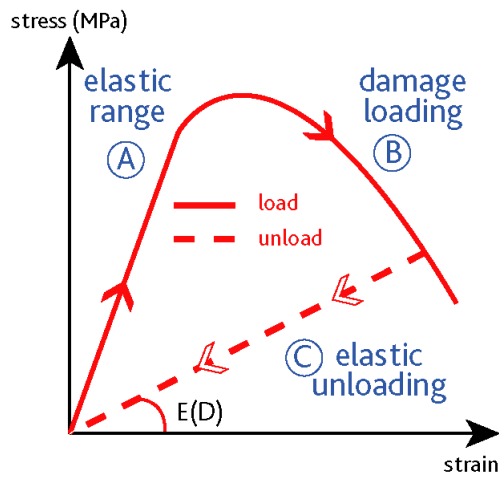


Fig. 4.1.: Strain-stress tensile constitutive law for elasto-damage material

4.1.3 Account of unilateral effects (microcracks closure)

In this part, we aim at describing the asymmetry of the tensile-compressive behaviour observed for several materials, including geomaterials, by introducing the so-called unilateral effect of damage on elastic properties. Fig. 4.2 illustrates such phenomenon under tensile loading (when the damage is presented as open micro-voids), followed by compression loading (for which micro-voids are closed).

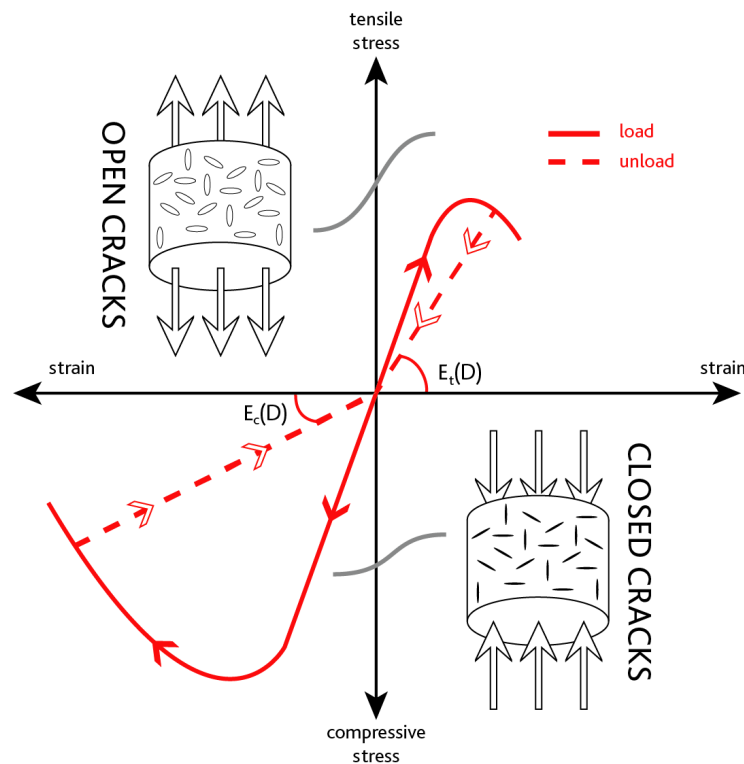


Fig. 4.2.: Strain-stress unilateral effect behaviour

For the derivation of elastic-damage models with unilateral effects which induce different stiffnesses (*i.e.* $\mathbb{C}(\text{D})_t \neq \mathbb{C}(\text{D})_c$)¹ in tensile and compressive regimes, we follow studies by [5], [6], [82], [127]. The reader interested by the mathematical aspect of this topic can refer to [47] in which the conditions of the continuity of the mechanical response of multilinear materials are analysed. For isotropic models, it can be shown that the achievement of the continuity of the mechanical response requires that the transition between "tensile-compressive" regimes must be done at $\text{tr}(\underline{\underline{\varepsilon}}) = 0$.

Let us insist on the fact that despite the existence of the asymmetric behaviour, we seek to ensure the continuity of the mechanical response in the model. Knowing that in the isotropic case, the stiffness tensor \mathbb{C} is decomposed in a spherical part and a deviatoric one, the thermodynamic potential, accounting for the unilateral effects reads:

$$\rho w(\underline{\underline{\varepsilon}}, \text{D}) = \begin{cases} \frac{1}{2}k(\text{D}) \left(\text{tr}(\underline{\underline{\varepsilon}}) \right)^2 + \mu(\text{D}) \underline{\underline{\varepsilon}}^d : \underline{\underline{\varepsilon}}^d & \text{if } \text{tr}(\underline{\underline{\varepsilon}}) \geq 0 \\ \frac{1}{2}k_0 \left(\text{tr}(\underline{\underline{\varepsilon}}) \right)^2 + \mu(\text{D}) \underline{\underline{\varepsilon}}^d : \underline{\underline{\varepsilon}}^d & \text{if } \text{tr}(\underline{\underline{\varepsilon}}) \leq 0 \end{cases} \quad (4.17)$$

where the superscript 0 relates an initial property. Note that at the tensile-compressive transition, this potential is continuous and takes the value: $\mu(\text{D}) \underline{\underline{\varepsilon}}^d : \underline{\underline{\varepsilon}}^d$. The resulting state equations, previously presented in (4.2a) and (4.6), take then the form:

$$\underline{\underline{\sigma}} = \rho \frac{\partial w}{\partial \underline{\underline{\varepsilon}}} = \begin{cases} k(\text{D}) \text{tr}(\underline{\underline{\varepsilon}}) \mathbb{1} + 2\mu(\text{D}) \underline{\underline{\varepsilon}}^d & \text{if } \text{tr}(\underline{\underline{\varepsilon}}) \geq 0 \\ k_0 \text{tr}(\underline{\underline{\varepsilon}}) \mathbb{1} + 2\mu(\text{D}) \underline{\underline{\varepsilon}}^d & \text{if } \text{tr}(\underline{\underline{\varepsilon}}) \leq 0 \end{cases} \quad (4.18a)$$

$$\mathcal{Y} = -\rho \frac{\partial w}{\partial \text{D}} = \begin{cases} -\frac{1}{2} k'(\text{D}) \left(\text{tr}(\underline{\underline{\varepsilon}}) \right)^2 - \mu'(\text{D}) \underline{\underline{\varepsilon}}^d : \underline{\underline{\varepsilon}}^d & \text{if } \text{tr}(\underline{\underline{\varepsilon}}) \geq 0 \\ -\mu'(\text{D}) \underline{\underline{\varepsilon}}^d : \underline{\underline{\varepsilon}}^d & \text{if } \text{tr}(\underline{\underline{\varepsilon}}) \leq 0 \end{cases} \quad (4.18b)$$

with $\underline{\underline{\sigma}} = 2\mu(\text{D}) \underline{\underline{\varepsilon}}^d$ and $\mathcal{Y}^{rev} = -\mu'(\text{D}) \underline{\underline{\varepsilon}}^d : \underline{\underline{\varepsilon}}^d$ at $\text{tr}(\underline{\underline{\varepsilon}}) = 0$. Furthermore, by introducing (4.18b) into (4.11):

$$f(\mathcal{Y}) = \begin{cases} -\frac{1}{2} k'(\text{D}) \left(\text{tr}(\underline{\underline{\varepsilon}}) \right)^2 - \mu'(\text{D}) \underline{\underline{\varepsilon}}^d : \underline{\underline{\varepsilon}}^d - \mathcal{Y}_c(\text{D}) \leq 0 & \text{if } \text{tr}(\underline{\underline{\varepsilon}}) \geq 0 \\ -\mu'(\text{D}) \underline{\underline{\varepsilon}}^d : \underline{\underline{\varepsilon}}^d - \mathcal{Y}_c(\text{D}) \leq 0 & \text{if } \text{tr}(\underline{\underline{\varepsilon}}) \leq 0 \end{cases} \quad (4.19)$$

with $f(\mathcal{Y}) = -\mu'(\text{D}) \underline{\underline{\varepsilon}}^d : \underline{\underline{\varepsilon}}^d - \mathcal{Y}_c(\text{D}) \leq 0$ when $\text{tr}(\underline{\underline{\varepsilon}}) = 0$. Moreover, if being on damage loading (*i.e.* $f(\mathcal{Y}) = 0$ and $\dot{f}(\mathcal{Y}) = 0$):

$$\dot{\text{D}} = \begin{cases} \frac{-k'(\text{D}) \text{tr}(\underline{\underline{\varepsilon}}) \text{tr} \dot{\underline{\underline{\varepsilon}}} - 2\mu'(\text{D}) \underline{\underline{\varepsilon}}^d : \dot{\underline{\underline{\varepsilon}}}}{\frac{1}{2}k''(\text{D}) \left(\text{tr}(\underline{\underline{\varepsilon}}) \right)^2 + \mu''(\text{D}) \underline{\underline{\varepsilon}}^d : \underline{\underline{\varepsilon}}^d + \mathcal{Y}'_c(\text{D})} & \text{if } \text{tr}(\underline{\underline{\varepsilon}}) \geq 0 \\ \frac{-2\mu'(\text{D}) \underline{\underline{\varepsilon}}^d : \dot{\underline{\underline{\varepsilon}}}}{\mu''(\text{D}) \underline{\underline{\varepsilon}}^d : \underline{\underline{\varepsilon}}^d + \mathcal{Y}'_c(\text{D})} & \text{if } \text{tr}(\underline{\underline{\varepsilon}}) \leq 0 \end{cases} \quad (4.20)$$

¹The subscripts *t* and *c* relates, respectively, the tensile and compressive states.

with $\dot{D} = \frac{-2\mu'(D) \underline{\underline{\varepsilon}}^d : \underline{\underline{\dot{\varepsilon}}}^d}{\mu''(D) \underline{\underline{\varepsilon}}^d : \underline{\underline{\varepsilon}}^d + \mathcal{Y}'_c(D)}$ at the transition $\text{tr}(\underline{\underline{\varepsilon}}) = 0$.

4.1.4 Examples of degradation functions and of critical energy release

Two classes of damage models are considered here, where the effective stiffness tensor is assumed to be isotropic (*i.e.* $\mathbb{C}(D) = 3k(D) \mathbb{J} + 2\mu(D) \mathbb{K}$). We adopt formulations based in the models proposed by Ponte-Castaneda and Willis (PCW) [40] and by Ambrosio-Tortorelli (AT) [1], [2], [30], [105]. These models can represent different material response following linear and quadratic evolution of the degradation process. Hence, inspired in the PCW damage model [40], we consider here uniform degradation functions of the shear and bulk modulus, such as:

$$\frac{k(D)}{k_0} = \frac{\mu(D)}{\mu_0} = \frac{1 - \hat{\alpha}D}{1 + \hat{\beta}D} \quad (4.21)$$

with $\hat{\alpha}$ and $\hat{\beta}$ constant parameters allowing to define the damage functions $k(D)$ and $\mu(D)$. Due to different values of the parameters of Eq. (4.21), it can be necessary to introduce the dependency on D parameter into the critical damage energy release \mathcal{Y}_c . In addition, the second damage model is based in the Ambrosio-Tortorelli (AT) model, where for our cases, the degradation functions of the shear and bulk modulus read:

$$\frac{k(D)}{k_0} = \frac{\mu(D)}{\mu_0} = (1 - D)^2 \quad (4.22)$$

The quadratic damage function fulfil the degradation condition of the negative first derivative and the stability condition of positive second derivative.

Additionally, we may have a dependency on D into the critical damage energy release $\mathcal{Y}_c(D)$. Two well-known versions of the critical damage energy release, depending or not on D , can be written as:

$$1^{st} \text{ case: } \mathcal{Y}_c = \mathcal{Y}_c^0 \quad (4.23a)$$

$$2^{nd} \text{ case: } \mathcal{Y}_c(D) = 2D\mathcal{Y}_c^0 \quad (4.23b)$$

where \mathcal{Y}_c^0 is an initial critical damage energy release. In the 1st case, an elastic regime will take place before the damage initiation (this response relates more often the mechanical response obtained for several geomaterials). Otherwise, the 2nd case does not present an elastic range and the degradation process starts once the deformation is different of zero. This formulation-type is widely found in literature (see for instance [6], [66]).

4.1.5 SPH-based algorithm implementation of the damage models

We illustrate here the numerical implementation used to compute the response of an elasto-damageable material in our SPH code. Previously, we illustrated the complete flowchart describing the SPH algorithm for the computing of a solid material response in Fig. 2.9. In Fig. 4.3, we first highlight that the deformation tensor $\underline{\underline{\epsilon}}_a^{t+\Delta t}$ is the primary non-local variable in our computing.

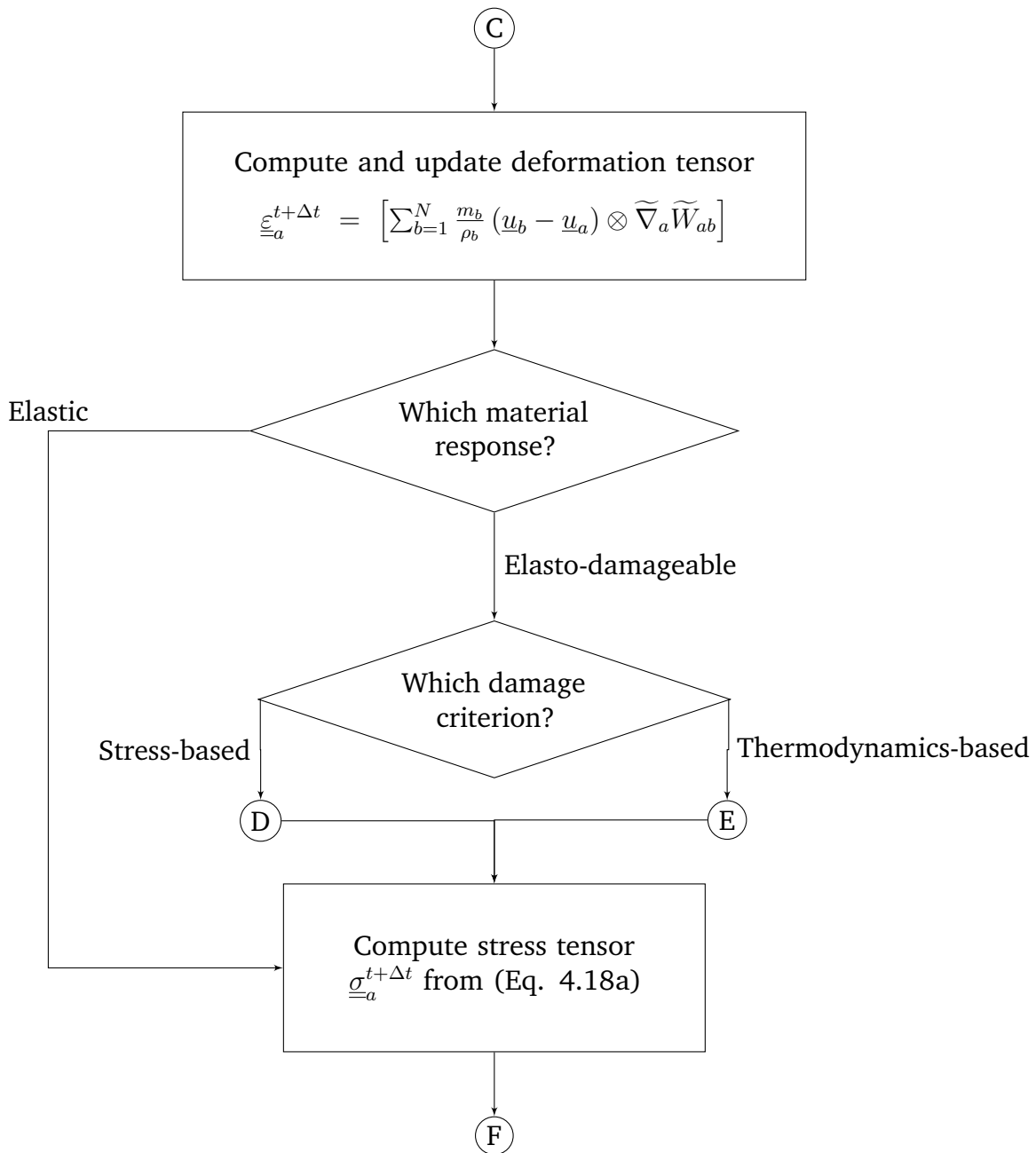


Fig. 4.3.: SPH computing flow chart for solid material points constitutive model and material response

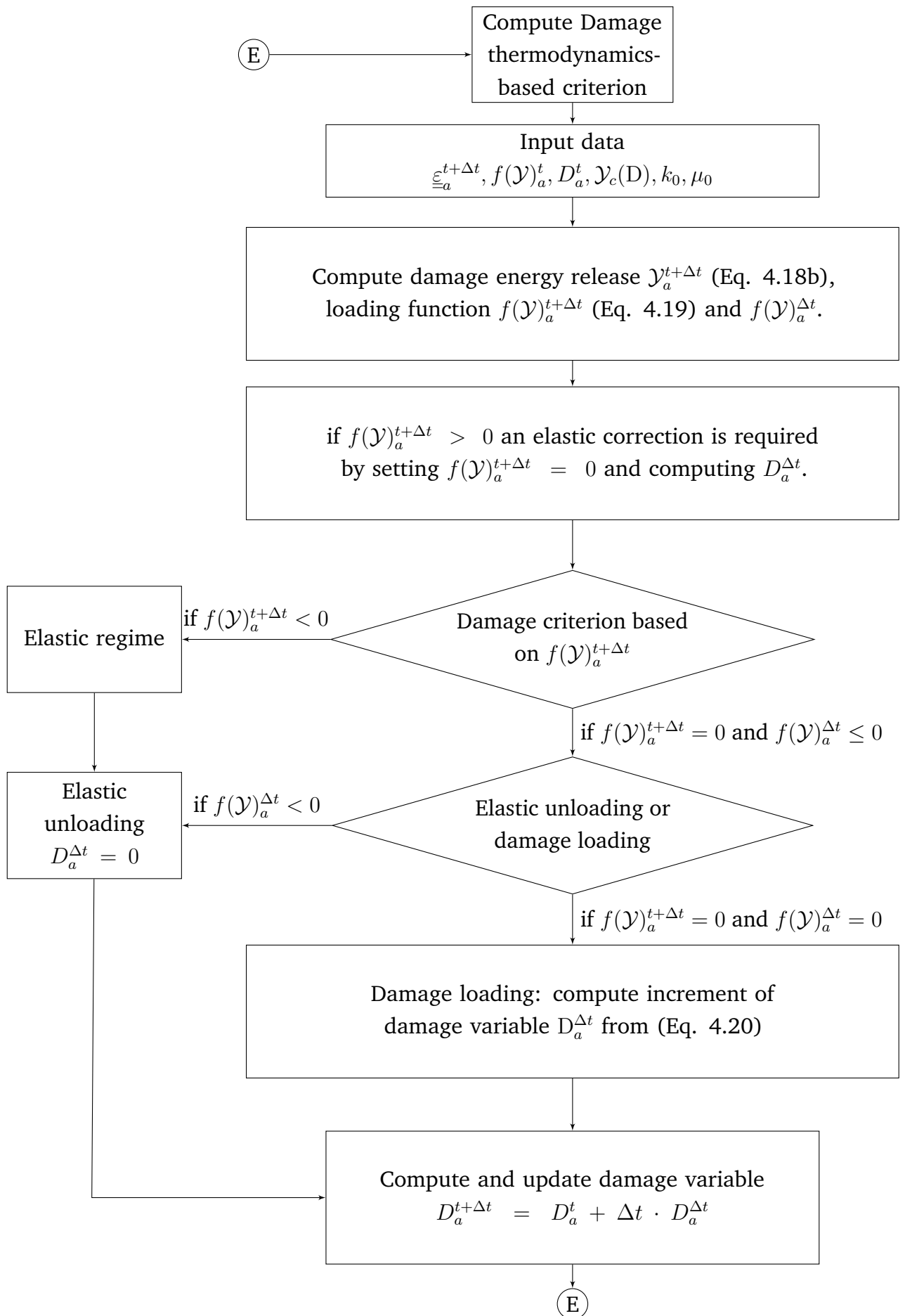


Fig. 4.4.: SPH computing flow chart for thermodynamics-based damage model.

In the following, our SPH code offers a damage criteria choice between a Rankine and Mohr-Coulomb strain-based criterion (detailed in Pazdniakou and Dymitrowska [126] but not used here) or a thermodynamics-based criterion. In Fig. 4.4, we illustrate the algorithm flow chart used to numerically compute the thermodynamics-based damage model described in Sec. 4.1.2.

Hence, to better understand the mechanical response of an elasto-damageable material following the underlying thermodynamics-based damage model, we present, in the following, two numerical tests seeking to validate our damage model. We also aim to analyze and discuss the capabilities of our SPH solver to reproduce non-local effects. We first apply different models to the test case of a softening 1D bar under tensile loads. In the following, we present a 2D fiber reinforced plate problem in which we explore the nucleation and propagation crack phenomena under tensile and compressive loading.

It is noteworthy that SPH is a mesh-free method, however, for minimal values of the numerical h -scale parameter, the interaction between material points can be limited to their closest neighbours, recalling a response of a system with a meshed domain. Such results were highlighted in Chap. 3. In the next applications, we will investigate two capital ingredients in SPH: the h -scale parameter and the role of the material point densities.

4.2 Application to 1D dynamic softening bar

We study here a model of a 1D bar loaded at both ends (see Fig. 4.5) through our SPH solver.

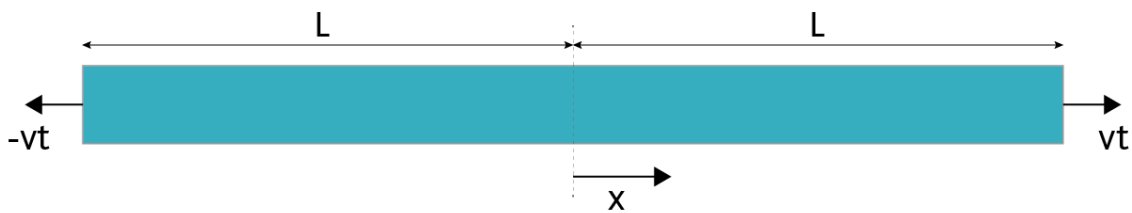


Fig. 4.5.: Bar configuration and boundary conditions

where v being the displacement velocity and the boundary conditions read:

$$\begin{cases} \text{at } x = -L & , \quad \bar{u} = -vt \\ \text{at } x = L & , \quad \bar{u} = vt \end{cases} \quad (4.24)$$

where \bar{u} is the imposed displacement at the left and right end. Bažant and Belytschko [19] were the first to propose an analytical solution to such problem taking into account a softening behaviour of a material. According to them, such boundary condition is the same as for a bar of length L fixed at $x = 0$. Their results shown the damage localisation at the centre of the bar beyond the instant $t > \frac{L}{c_e}$ where c_e being the sound wave velocity in this medium. Few years later, Bažant observed a mesh-dependence pathology when treating damage variable by local methods (*e.g.* Finite Elements - FE). He postulated that the continuous damage variable is not a local variable by bearing on different evidences, for instance a softening response when changing the micro-structure scale (represented by the mesh-density) [16], [17]. Such condition can generate local loss of ellipticity when resolving the differential equations, causing an ill-posed mathematical problem.

Based on Bažant’s analytical solution and on the issue of mesh-dependence of local methods, Vignjevic *et al.* [158] proposed to solve this softening bar problem by using SPH. They compared FE and SPH solutions highlighting the absence of dependency on the material point densities of the last one. Their results were obtained by using a Total Lagrangian SPH formulation (see more in [141]). In a previous work [53], we investigated the same problem using the standard SPH formulation (as presented by Monaghan [116]).

We adopt here different SPH approaches (conventional SPH-based and Total Lagrangian-based) in order to investigate the damage model described in Sec. 4.1. Table 4.1 resumes the simulation parameters adopted as proposed by Vignjevic *et al.* [158].

Parameter	Sign	Value
Bar half-length	L	100 [mm]
Young modulus	E	70.8 [GPa]
Volumetric mass density	ρ	1550 [kg/m ³]
Initial failure strain	ε_{t0}	0.022 [–]
Critical failure strain	ε_{tu}	0.060 [–]

Tab. 4.1.: Input data for dynamic simulation of a softening bar

In addition, we adopt a SPH artificial viscosity (Eq. 2.64) with parameters $\check{\alpha} = 10$ and $\check{\beta} = 1$ in order to reduce the oscillations and enhance the stability of the system. We will illustrate in the different numerical experiments presented in this chapter the evolution of the total energy (*i.e.* the sum of the elastic or bulk energy, the dissipated or surface energy and the kinetic energy). The presence of kinetic energy here is justified

by our dynamic approach. The sum of the energies E^{TOT} inside an isolated SPH system is given by:

$$E^{TOT} = E^{\hat{W}} + E^{\hat{D}} + E^{\hat{T}} \quad (4.25)$$

where the global elastic energy is $E^{\hat{W}}$, the global dissipated energy is $E^{\hat{D}}$ and the global kinetic energy is $E^{\hat{T}}$, for a SPH system composed of n material points, are written as:

$$E^{\hat{W}} = \sum_a^n \frac{m_a}{\rho_a} w_a \quad (4.26a)$$

$$E^{\hat{D}} = \sum_a^n \frac{m_a}{\rho_a} \mathcal{Y}_c^0 \cdot D_a \quad (4.26b)$$

$$E^{\hat{T}} = \sum_a^n \frac{1}{2} m_a v_a^2 \quad (4.26c)$$

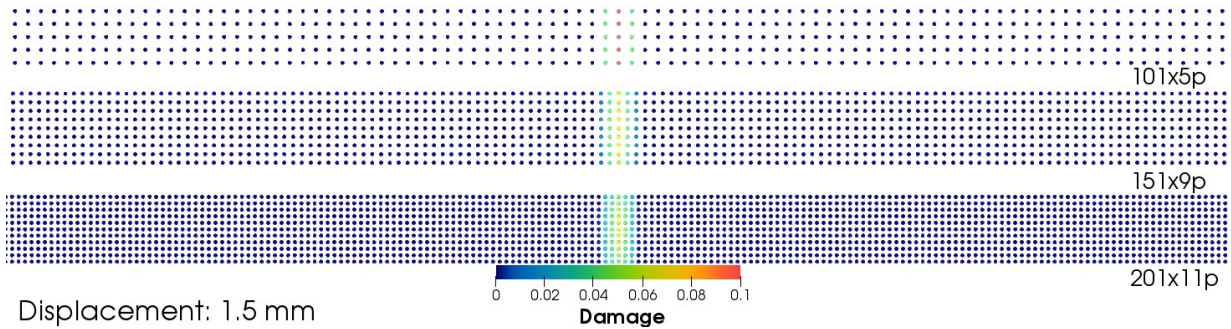
The index a identifies each material point of the SPH system and w is the internal energy as introduced in (Eq. 2.87).

4.2.1 Material point densities independence validation

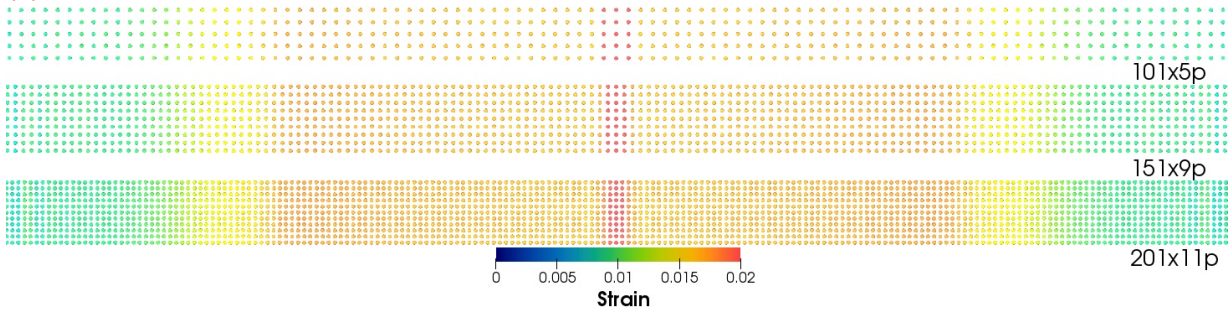
We aim here, first, at validating the use of our Saint-Venant Kirchhoff model through an SPH Total Lagrangian-based formulation taking into account the normalisation of the kernel function and its corrected derivative form. This formulation is called here as SVK SPH. For this simulation, $2h$ -size is equal to $5mm$ for three different material point densities (101x5, 151x9 and 201x11). A displacement velocity of $v = \pm 70 m/s$ is applied at both sides in order to create the bi-tractioned condition. In this part, we adopt the PCW-based damage function (Eq. 4.21) with parameters:

$$\begin{cases} \hat{\alpha} = 1 \\ \hat{\beta} = \frac{\epsilon_u}{\epsilon_0} - 1 \\ \mathcal{Y}_c = \mathcal{Y}_c^0 \end{cases} \quad (4.27)$$

In Fig. 4.6 we present the damage and strain fields for the three proposed discretizations. Although the three different material point densities, the damage zone at the centre of each bar in Fig. 4.6a seems to present the same width. In addition, in the Green-Lagrange strain profile (Fig. 4.6b) the coloured zones follow a similar behaviour. This similar responses on the damage width zone validate the independence for different material point densities, highlighting the inherent non-local nature of SPH. Our results using the SVK-SPH model are close to those showed by Vignjevic *et al.* [158] using a Total Lagrangian SPH. In a more detailed point of view, Fig. 4.7 shows some of the main variables present in this system by a plot over the central line of the bar along their total



(a) Damage D zone lengths for different material point discretizations.



(b) Green-Lagrange deformation ϵ_{GL} for different material point discretizations.

a,b watch

 the video

Fig. 4.6.: 1D softening bar: damage and Strain. damage width zone independence for different material point densities for $2h = 5mm$ at $t = \frac{3L}{2c_e}$.

length. For the three different point discretization, the strain, stress and displacement profiles are quite similar. A more important difference is observed for the peak values at the centre of the bar. In addition, although different peak values, the width of the damaged zone does not depend on the particle densities from the zoomed longitudinal profile of the damage D (top-left side chart).

Another relevant result is the small damage peak values, instead of the $0 - 1$ discontinuity obtained with local methods (see [158]). We note that the peak values obtained in each configuration decreases with the increase of particle density and seems to converge towards the densest configuration monotonously. However, when compared to [158] damage profiles, the same solution is non-monotonous there. The small peak values in this dynamic condition are conditioned to small traction loading. Finally, we highlight the gain on stability by adopting the 201 material points discretization compared to the less dense cases.

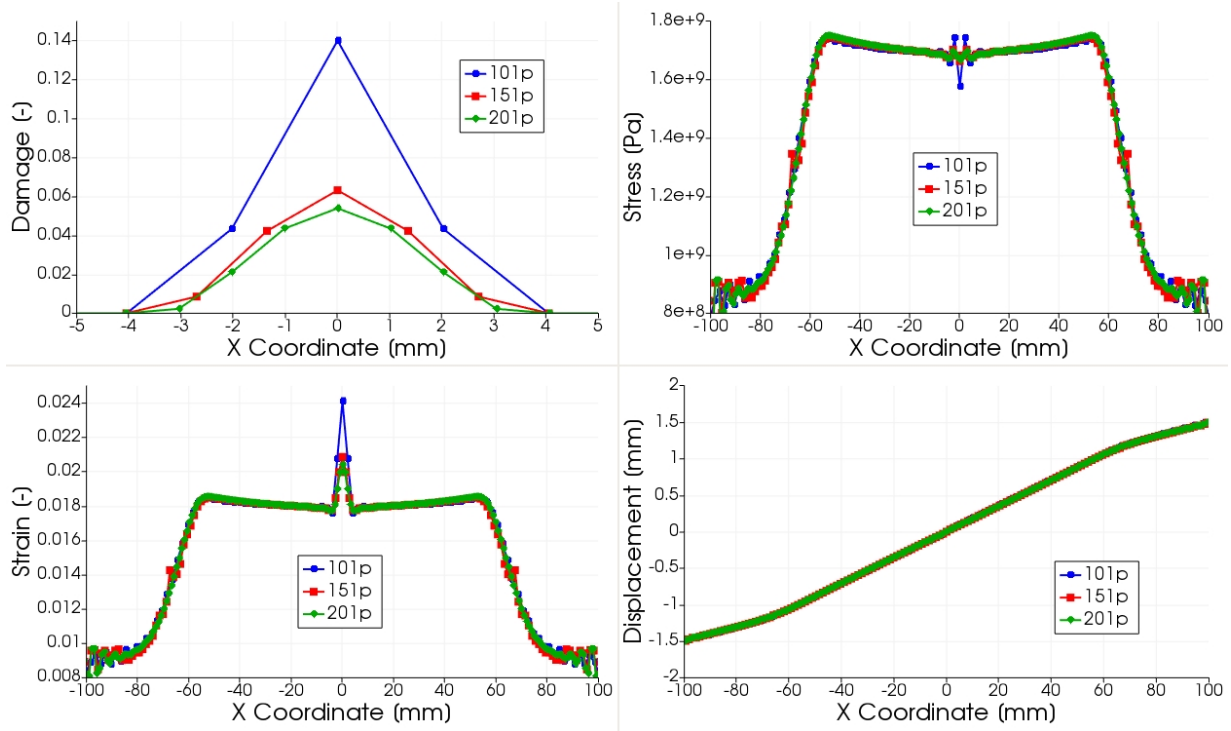


Fig. 4.7.: Damage, stress, strain and displacement at $t = \frac{3L}{2c_e}$. Validation of normalized-corrected SVK SPH by using PCW-based damage function following three density of longitudinal material points: 101, 151 and 201.

Therefore, we illustrate in Fig. 4.8 the evolution of elastic, kinetic, dissipated and total energies for the range of the imposed displacement $\bar{u} \leq 1.5mm$. The x-axis is represented by the absolute imposed displacement \bar{u} at the bar end. Vignjevic *et al.* [158] restricted the energies representation to the internal energies. Nevertheless, our choice to represent the kinetic energy helps to better understand the total energy evolution (dotted line). Although the total energy increases with a constant slope during all the simulation time, the kinetic and the elastic energy present quasi-similar increasing evolution values up to $\bar{u} \leq 1mm$. At $\bar{u} = 1mm$, the displacement wave reaches the centre of the bar generating the damaged zone observed in Fig. 4.6a (the small damage levels there agrees with the small level of dissipated energy here). However, after $\bar{u} \geq 1mm$, the kinetic energy inverse its increasing evolution and starts to decrease following an inverse slope, while the elastic energy presents now around a double of its previous slope value. Such combined evolution of elastic and kinetic energies results in a constant slope of the total energy (given the quasi-negligible dissipated energy), which is coherent with a bar system under constant loading. The three different discretizations present very close values of energy evolution, that is why, for a matter of clarity, we show here only the results for the 201 longitudinal material points configuration.

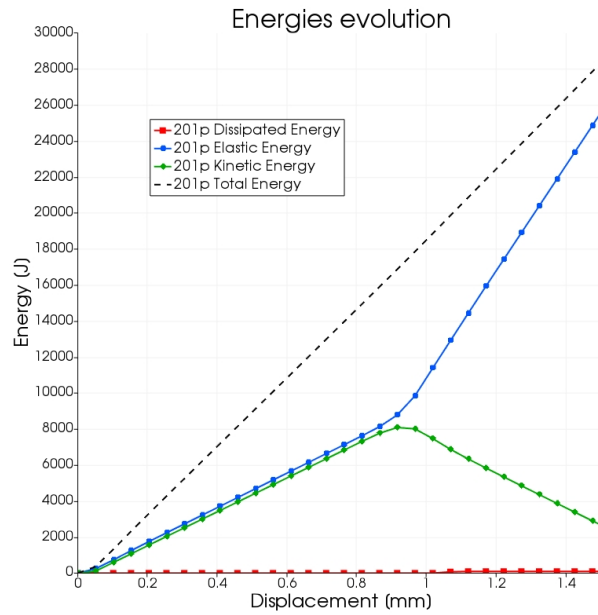


Fig. 4.8.: PCW-based damage model: evolution of elastic, kinetic, dissipated and total energies for $\bar{u} \leq 1.5mm$.

While maintain the same material properties and bar discretization, we investigate now this bi-tractioned problem under a greater displacement velocity of $v = 72m/s$. Fig. 4.9 present the mechanical response of this material through the strain-stress curves of the three different discretization (for the material point localised at the centre of the bar). Such result confirms the absence of discretization dependence on the post-peak evolution of the strain-stress curve.

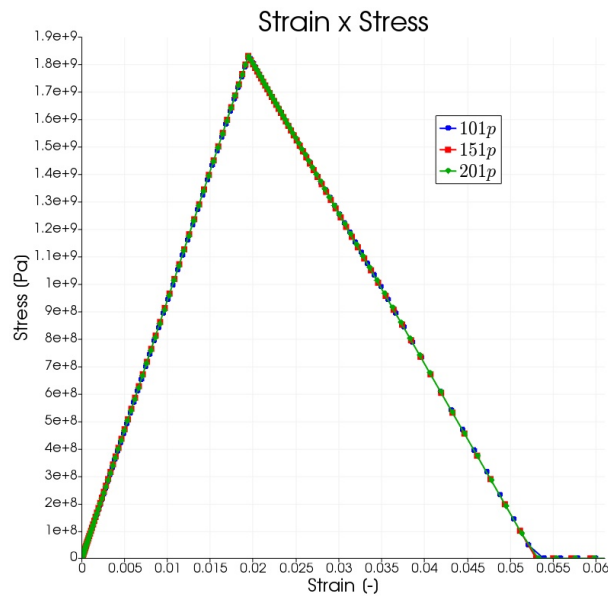


Fig. 4.9.: Strain-stress curve of a elastic bar under a displacement velocity of $v = 72m/s$ for the thermodynamics-based damage model with PCW damage function for different particle densities.

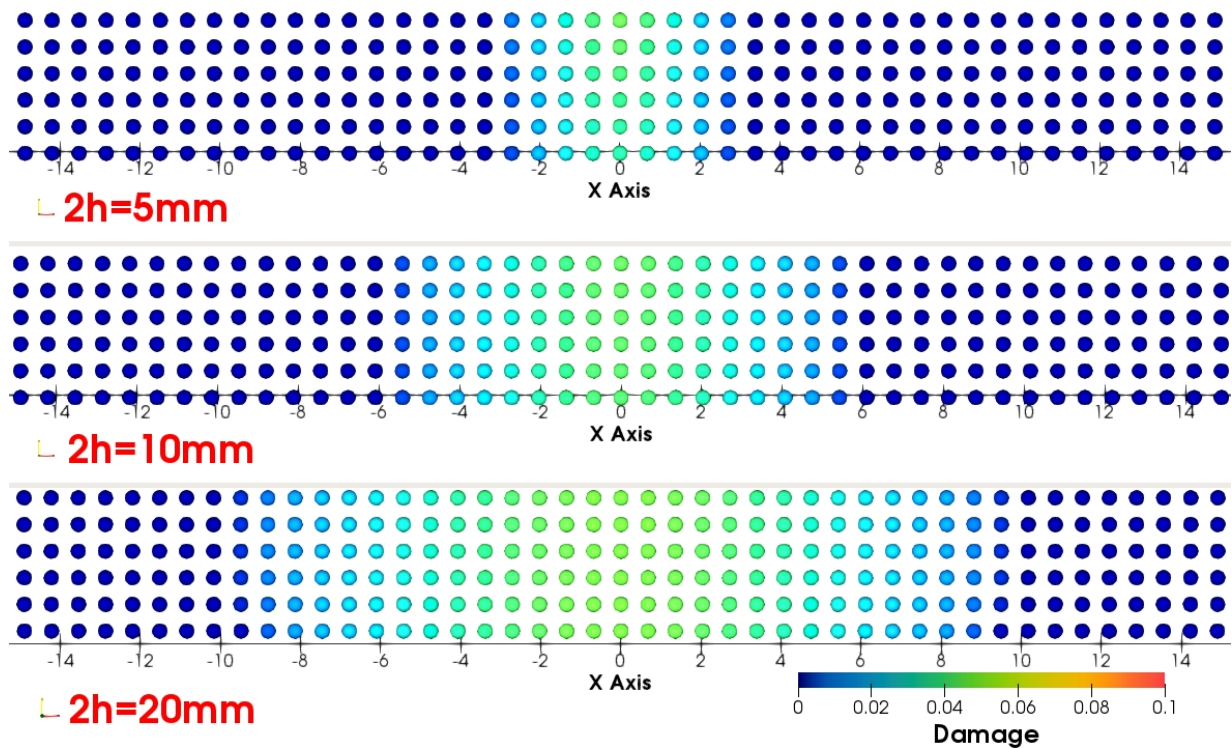
4.2.2 Non-local characterisation by means of the numerical parameter $2h$ -length

Another analysis proposed by Vignjevic *et al.* [158] concern the influence of values of the numerical parameter $2h$ -length for the same bar configuration of 201 longitudinal material points. Their results related the increase of the width of the damaged zone to the increase of the numerical parameter $2h$. Here, we perform a similar simulation using the SVK SPH approach with a more important material point density of 301×17 points resulting in Fig. 4.10. Indeed, the zoom at the zone containing damaged material points (Fig. 4.10a) and the damage profile presented in Fig. 4.10b confirm that the width of the damaged zone follows closely the dimensions of $2h$ even in conditions presenting a higher value of the non-local parameter (*e.g.* $2h=20\text{mm}$). The strain, stress and displacement profiles in Fig. 4.10b show that the adoption of different magnitude orders of the support-length $2h$ have also a mechanical meaning linked to the interpolation zone size. Which can lead to an increase of the oscillations along the bar. Moreover, by comparing energy evolution between the greatest and the smallest values of $2h$ (Fig. 4.11), the increasing of the parameter ($2h = 20\text{mm}$) leads to smaller kinetic energy and greater elastic energy values while $\bar{u} \leq 1\text{mm}$. However, for $\bar{u} > 1\text{mm}$, this role is played by the $2h = 5\text{mm}$ configuration. We note also that besides these variations, the total energies remains quasi-similar during all the simulation.

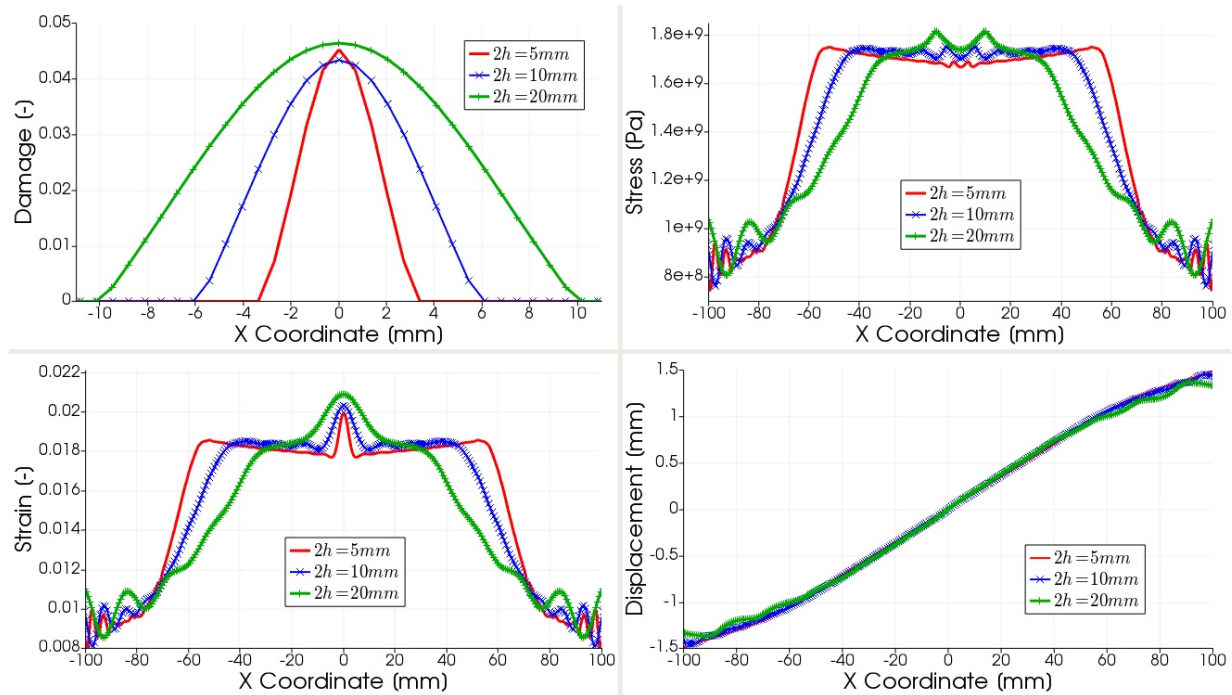
4.2.3 Comparison between different SPH formulations

In Chapter 2, we have introduced the mechanical approaches implemented and used in this thesis. On a first level, we have the small and finite strain formulations, which result, respectively, in conventional SPH and SVK-SPH. Besides, for each approach, we can solve the momentum equations through the displacement-based form (u) or the stress-based form (σ for small deformations and P for large deformations). We adopt artificial viscosity (Eq. 2.64) for all cases, with $\check{\alpha} = 41$ and $\check{\beta} = 1$ for u -based formulations and $\check{\alpha} = 10$ and $\check{\beta} = 1$ for stress-based formulations. These numerical solutions are compared to the analytical solution proposed by Bažant and Belytschko [19].

Thus, for a bar configuration of 201 longitudinal material points, we aim here to investigate the response of the system by means of different computing approaches that can be adopted by our numerical model. Fig. 4.12 illustrates the longitudinal strain profiles for $2h = 5\text{mm}$ at the moments $t = \frac{L}{2c_e}$ and $\frac{3L}{2c_e}$. Qualitatively, the maximum strain presented in this simulation is of around 3% (which is a small strain value to be considered necessary for the use of a large deformations approach). Nevertheless, the use of finite strain formulations in SPH may play an important role of stability and drawback



(a) Damage D zone lengths for increasing $2h$ values.



(b) Damage, strain, stress and displacement longitudinal profiles.

Fig. 4.10.: Width of the damaged zone, strain, stress and displacement profiles for $2h = 5mm, 10mm$ and $20mm$ at $t = \frac{3L}{2c_e}$.

corrections (for instance, Reveles [141] showed that the Total Lagrangian can fix issues like tensile instability). In addition, we propose here the use of a displacement-based

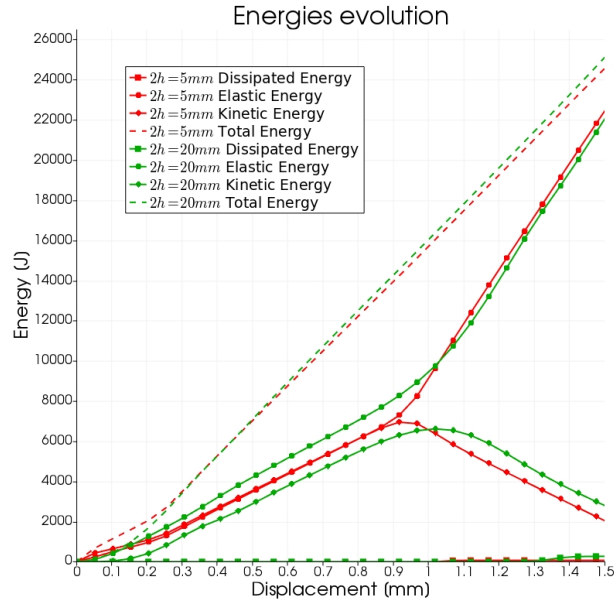
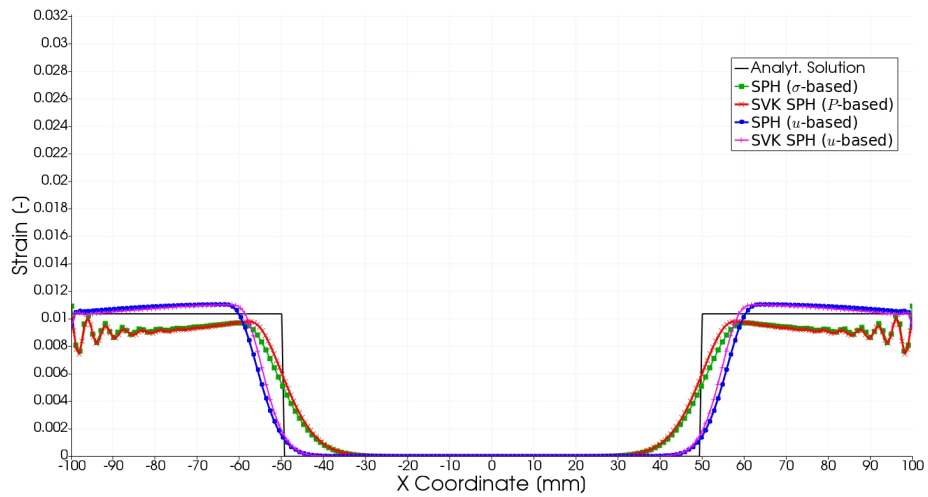


Fig. 4.11.: Evolution of elastic, kinetic, dissipated and total energies for $t < \frac{3L}{2c_e}$.

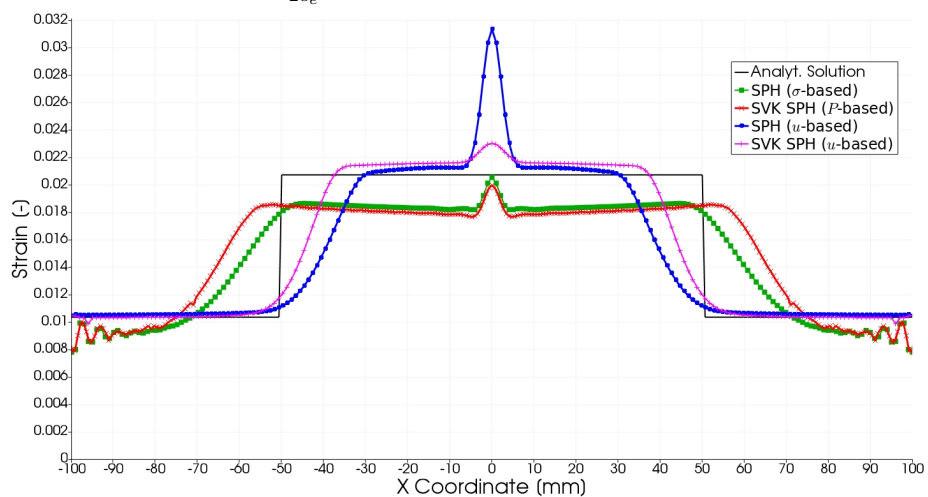
momentum equation in elastic dynamics through SPH, that seems to be more stable and accurate in this problem when comparing to the analytical solutions.

Quantitatively, we see in Fig. 4.12a a more important oscillation presented by the stress-based approaches at the bar bounds. It also highlights a higher velocity of the displacement waves of the stress-based formulations. Besides, we observe in Fig. 4.12b that the displacement-based SPH versions reach closer levels of strain compared to the analytical solution (which are also followed by the other variables) and a much more notably stability. Such stability is essential in complex and coupled systems, that is why we adopt a displacement-based SPH formulation in the following of this thesis.

The present results for this 1D problem show the occurrence of damage growth at low levels. We highlight that, even using a local damage formulation, the damage localization can be done using SPH in diverse discretization densities with a remarkable independence of the discretization. The material point density here seems to be more related to the accuracy of the damage peak values, even in this case, at very low different levels. We demonstrated that the width of the damaged localization zone is related to the parameter $2h$, which is purely numerical. After the present validation and analysis of the potential of SPH method in such a simple case of study, we seek now to apply our proposed numerical model into a multidimensional medium under whether tensile or compressive loading.



(a) Longitudinal strain profile at $t = \frac{L}{2c_e}$.



(b) Longitudinal strain profile at $t = \frac{3L}{2c_e}$.



Fig. 4.12.: Comparison between different SPH formulations. Longitudinal strain profile for $2h = 5\text{mm}$ at $t = \frac{L}{2c_e}$ and $\frac{3L}{2c_e}$.

4.3 Application to 2D fiber reinforced plate

4.3.1 Introduction

Firstly introduced by Bourdin *et al.* [30], this model-problem is reputed in literature as an example of initiation and propagation of complex damage and fracture. Various authors have studied this problem by means of variational approaches, such as gradient model, commonly called phase-field model [5], [6], [52], [66]. In such method, a "phase-field" variable D and a regularisation internal length l_c are introduced into a energy functional \mathcal{E} in a domain Ω [1], [2], [32], such as:

$$\mathcal{E}(\underline{u}, D) = \int_{\Omega} (1 - D)^2 \underline{\underline{\varepsilon}} : \mathbb{C}_0 : \underline{\underline{\varepsilon}} d\Omega + \frac{G_c}{c_w} \int_{\Omega} \left(\frac{w(D)}{l_c} + l_c \nabla D \cdot \nabla D \right) d\Omega \quad (4.28)$$

with \underline{u} a time dependent boundary displacement, G_c a fracture toughness, c_w a normalisation parameter and $w(D)$ a continuous monotonic function. The quadratic damage function as introduced in Sec. 4.1.4 is observed in (Eq. 4.28). This problem can be solved by a minimisation procedure. In addition, the following classes of parameters can be adopted (see for instance Tanné *et al.* [156]):

$$\text{AT-1 type model: } w(D) = D, \quad c_w = \frac{8}{3} \quad (4.29a)$$

$$\text{AT-2 type model: } w(D) = D^2, \quad c_w = 2 \quad (4.29b)$$

In this variational model, two essential ingredients are present: the damage variable can be regularised by means of the internal characteristic length l_c by assuring discretization independence of the damage variable and the fracture yield is determined by G_c .

Unlike to the variational-based methods, SPH method is based in another approach computed over an interpolated mesh-free domain in dynamic conditions. In our SPH formulations, the energy functional does not present the regularisation terms presented at the right-hand-side of (Eq. 4.28). Neither internal length l_c nor tenacity G_c are present in our functional. We advocated in previous sections and validation tests that our regularisation is inherently obtained by means of the interpolation nature of SPH method and that the non-local effects therein can be governed by the numerical parameter $2h$ -support length. Our goal here is to validate the SPH method as a non-local mechanical solver and to discuss its advantages and limitations. For this purpose, we highlight for the two previously cases of the Ambrosio-Tortorelli damage model their respective critical damage energy releases (from 4.23), such that:

$$\text{AT-1 type model: } \mathcal{Y}_c = \mathcal{Y}_c^0 \quad (4.30a)$$

$$\text{AT-2 type model: } \mathcal{Y}_c(D) = 2D\mathcal{Y}_c^0 \quad (4.30b)$$

The form AT-2 type model (Eq. 4.30b) does not present an elastic range and plays a comparison role with existing results [6], [66]. Otherwise, the form AT-1 type model (Eq. 4.30a) present an elastic regime before the damage initiation, which is closer to a mechanical response very often obtained for geomaterials. Also, we note that the change of $\mathcal{Y}_c(D)$ value introduced in (Eq. 4.23) must be taken into account in (Eq. 4.26b) for the computing of dissipated energies.

Although we are able to use SPH to approximate a quasi-static condition by reducing the displacement velocity loading, the internal equilibrium is rarely established (given the acceleration that is commonly not negligible). The use of such an approach for quasi-static conditions is still poorly discussed in the literature. This work aims to highlight some key issues that link dynamic and quasi-static conditions. Fig. 4.13 presents the framework used in this problem: a square plate reinforced in its center with a rigid circular inclusion. The plate has side L and the inclusion has a diameter $L/3$. The

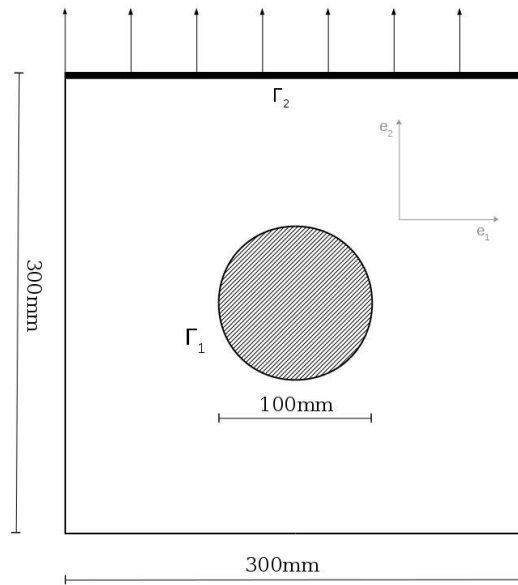


Fig. 4.13.: Set up and boundary conditions of 2D fiber reinforced plate (adapted after Bourdin *et al.* [30]).

boundary conditions considered for this problem read:

$$\begin{cases} \underline{u} = \underline{0} \text{ and } D = 0 & \text{on } \Gamma_1 \\ \underline{u} \cdot \underline{e}_2 = t\bar{u} \cdot \underline{e}_2 \text{ and } \underline{\underline{\sigma}} \cdot \underline{n} \cdot \underline{e}_1 = 0 & \text{on } \Gamma_2 \\ \underline{\underline{\sigma}} \cdot \underline{n} = 0 & \text{on } \partial\Omega / (\Gamma_1 \cup \Gamma_2) \end{cases} \quad (4.31)$$

\underline{u} is the imposed displacement at the top-bound. $\underline{u} \cdot \underline{e}_2$ is positive for tensile loading and negative for compressive loading. \underline{n} is the unity normal, D is the damage variable and $\underline{\sigma}$ is the Cauchy stress tensor. The geometrical and material parameters adopted here (Tab. 4.2) are based on those considered by Freddi and Royer-Carfagni [66]. A damage

Parameter	Sign	Value
Side length	L	300 [mm]
Volumetric mass density	ρ	1000 [mg/mm ³]
Young modulus	E	12000 [N/mm ²]
Poisson coefficient	ν	0.25 [-]
Initial critical energy release	\mathcal{Y}_c^0	2.5×10^{-3} [N/mm ²]
Damage limit bound	s_l	0.99 [-]

Tab. 4.2.: Input data for dynamic simulation of the fiber reinforced plate.

domain such as $0 < D < s_l$ seeking to prevent material disintegration is adopted. In this section, we use an infinitesimal deformation and displacement-based approach through our SPH method. In addition, a SPH artificial viscosity (Eq. 2.64) with parameters $\check{\alpha} = 41$ and $\check{\beta} = 1$ is used in order to improve the system stability. Also, considering the dynamic nature of the SPH method, we account for the kinetic energy in our simulations.

4.3.2 Quasi-static response of fiber reinforced plate

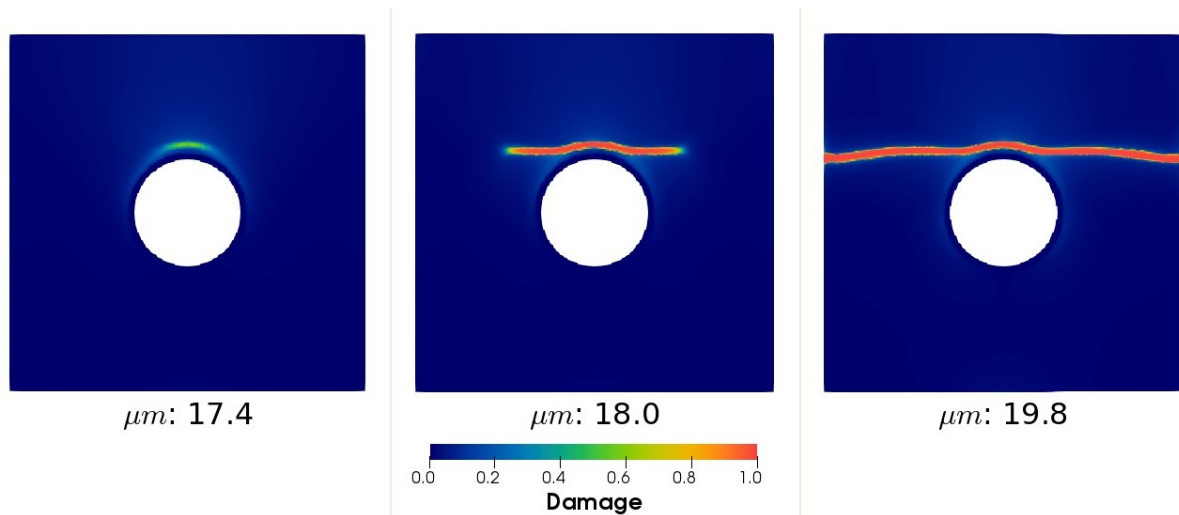
Since our numerical approach presents dynamic terms, we adopt a system under specific loading conditions to closely approximate a quasi-static state. It means that we apply an infinitesimal velocity $v_y = \pm 10^{-7} \cdot L \text{ mm/s}$ at the plate top bound until reach the final fixed displacement $\underline{u} = \pm 10^{-3} \text{ mm}$. We investigate the response of such a system as predicted by the SPH method through the thermodynamics-based damage model with unilateral effect as introduced in previous sections.

This numerical experiment was already presented in analogous conditions but with different material parameters by Amor *et al.* [6], Bourdin *et al.* [30], and Del Piero *et al.* [52]. Here we adopt the simulation parameters from Freddi and Royer-Carfagni [66] that are more reliable to a real case as they stated. We also adopt for this set of simulations for the elastic-damageable plate a discretization of 300x300 material points regularly distributed over the domain, excluding the rigid inclusion. It results in 82476 total points regularly distributed by 1mm of distance. Furthermore, we recall that the interpolated nature of the present system induces a high-order interaction between the material points controlled not by their direct neighbours (as in meshed systems) but by the size of the support domain ($2h$).

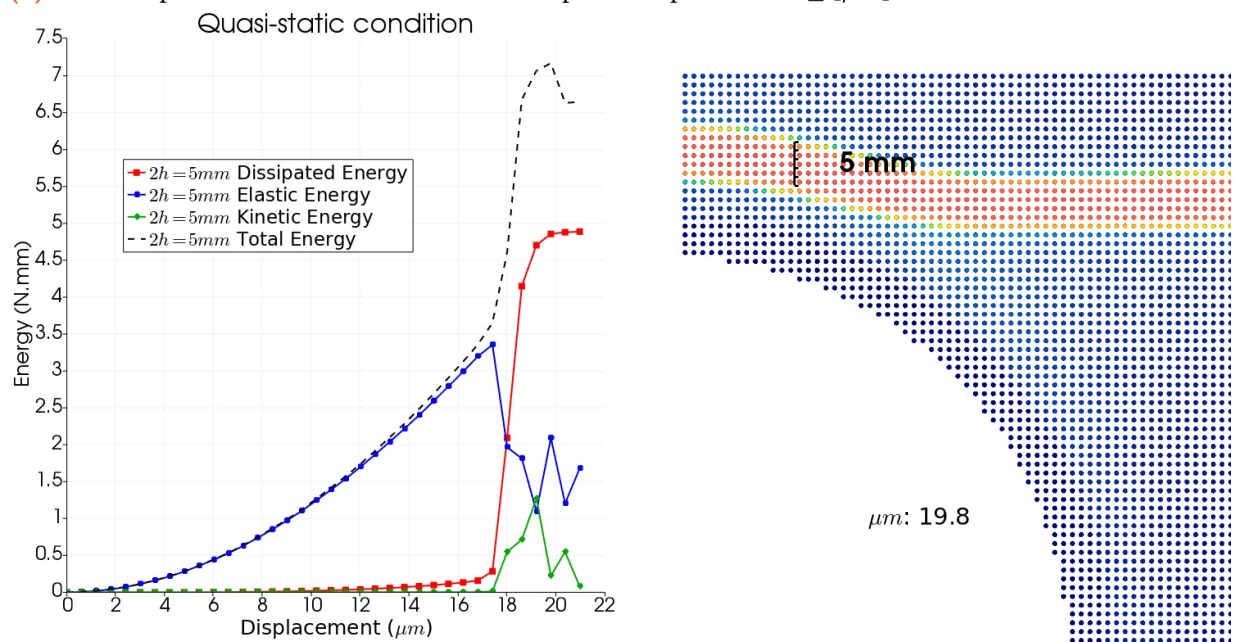
4.3.2.1 Tensile loading

AT-2 type model:

We start presenting two simulations following the support length $2h = 5mm$ for Fig. 4.14 and $2h = 2.5mm$ for Fig. 4.15.



(a) Fracture pattern evolution over different imposed displacements \underline{u} [μm].



(b) Elastic, dissipated, kinetic and total energies evolution.

(c) Zoom in material points scale: width of the damaged zone.



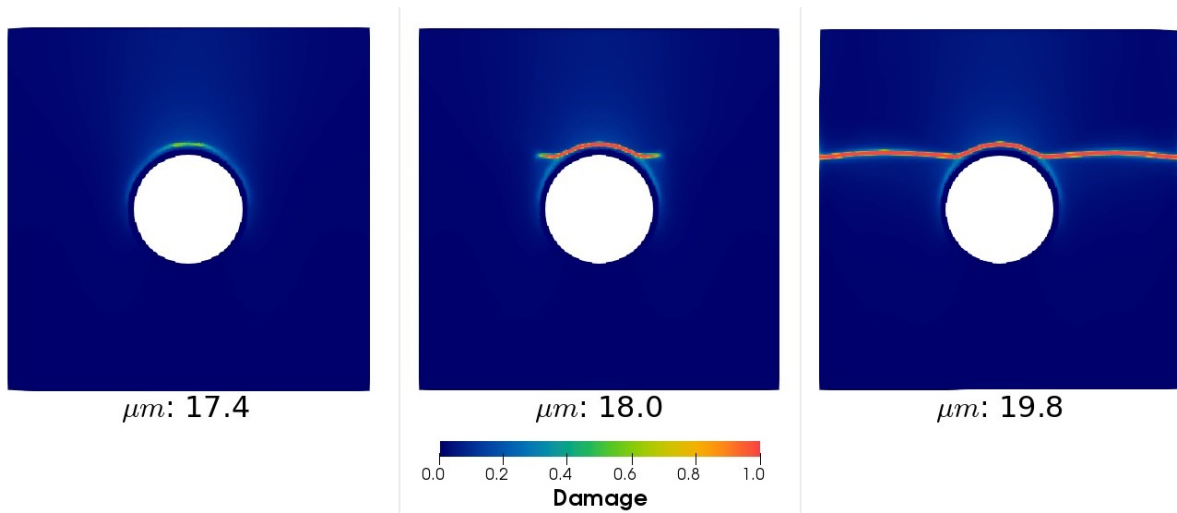
Fig. 4.14.: Tensile quasi-static (AT-2): evolution of damage variable and energies in a plate with rigid inclusion with $2h = 5mm$.

Fig. 4.14a presents the damage field evolution following subsequent imposed displacements \bar{u} . No additional regularisation is introduced into the SPH formulation. We observe the damage growth that starts over the top bound of the inclusion and a crack path that propagates towards the left and right sides of the plate. The fracture pattern is close to those presented by Freddi and Royer-Carfagni [66] using the variational damage model (Eq. 4.28). Differently from Bourdin *et al.* [30] and Amor *et al.* [6] we observe here a symmetry between the left and right-hand-side pattern during the rupture propagation. Hence, after reducing the support length to $2h = 2.5mm$, Fig. 4.15a present a very similar crack pattern evolution but a width of the damaged zone of around a half of the one shown in Fig. 4.14a. This seems to attest that h plays a role similar to that of the internal length used in variational models.

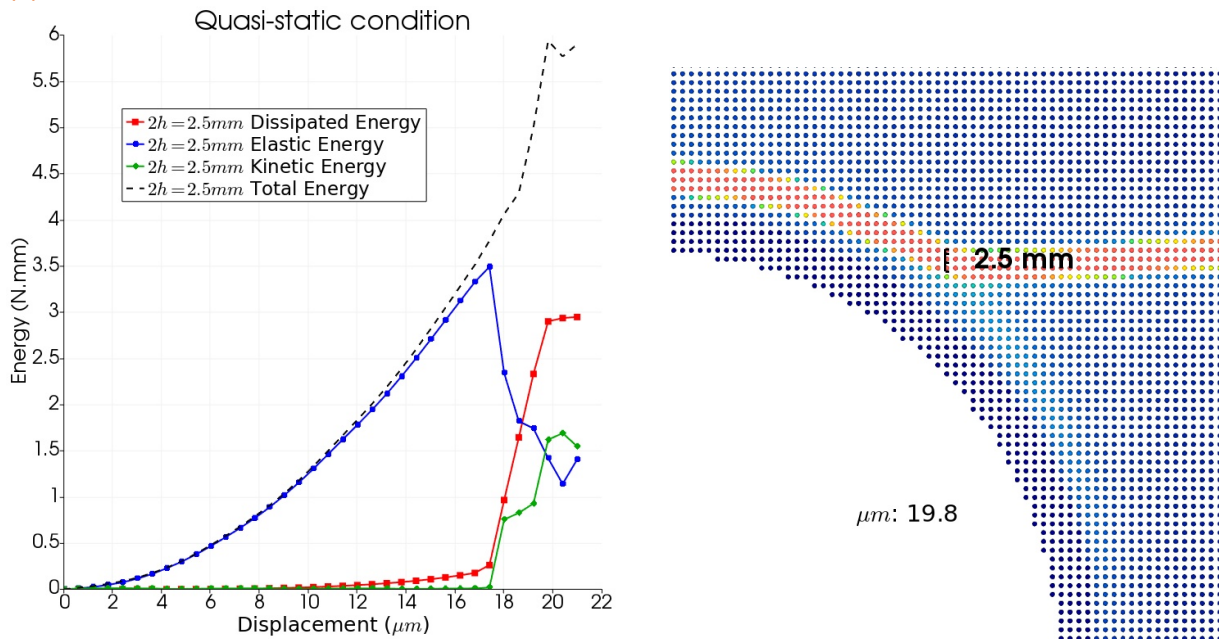
Fig. 4.14b (for $2h = 5mm$) and Fig. 4.15b (for $2h = 2.5mm$) present the evolution of the total, elastic, dissipated and kinetic energies. The occurrence of non-negligible kinetic energies at the exact moment of the rupture initiation is remarkable. Here, this energy has initially the same magnitude order as the elastic energy and decays after a few oscillations. We see a latent oscillation present in the elastic energy that seems to represent the inverse behaviour of the kinetic energy evolution. If the kinetic energy were neglected, such oscillation jumps would be present in the total energy (as shown in Freddi and Royer-Carfagni [66]). Besides, although a qualitatively similar evolution of energies, the differences between elastic and dissipated energy levels and the instant of rupture compared to [66] results can be attributed to the difference of the approaches and damage parameters here adopted (in particular the length-scale h). Moreover, although both configurations present a similar behaviour of the elastic energies for both configurations, the configuration with larger $2h$ parameter present a more important level of the dissipated energy (which is also related to the projected damaged surface).

It is noteworthy the role played by the numerical parameter $2h$ in the system, which is illustrated in Fig. 4.14c for $2h = 5mm$ and Fig. 4.15c for $2h = 2.5mm$. A close proportionality between the support length $2h$ and the width of the damaged zone is observed. This connection has been already noted in a 1D problem (Sec. 4.2) but not yet presented in a multidimensional problem.

In order to better describe the evolution of such degradation phenomenon Fig. 4.16 details the y-displacement [μm] and the maximum principal stress [N/mm^2] in the plate configuration presented in Fig. 4.14. At $\bar{u} = 17.4\mu m$ a tensile stress field has maxima values on the top of the rigid inclusion (which represents the fracture initiation). The vertical displacement has a smooth distribution around the top half part of the inclusion towards the top bound of the plate. In the bottom side of the plate, we see a zone under compression bellow the inclusion, but in a smaller order value than the tensile stress.



(a) Fracture pattern evolution over different imposed displacements \bar{u} [μm].

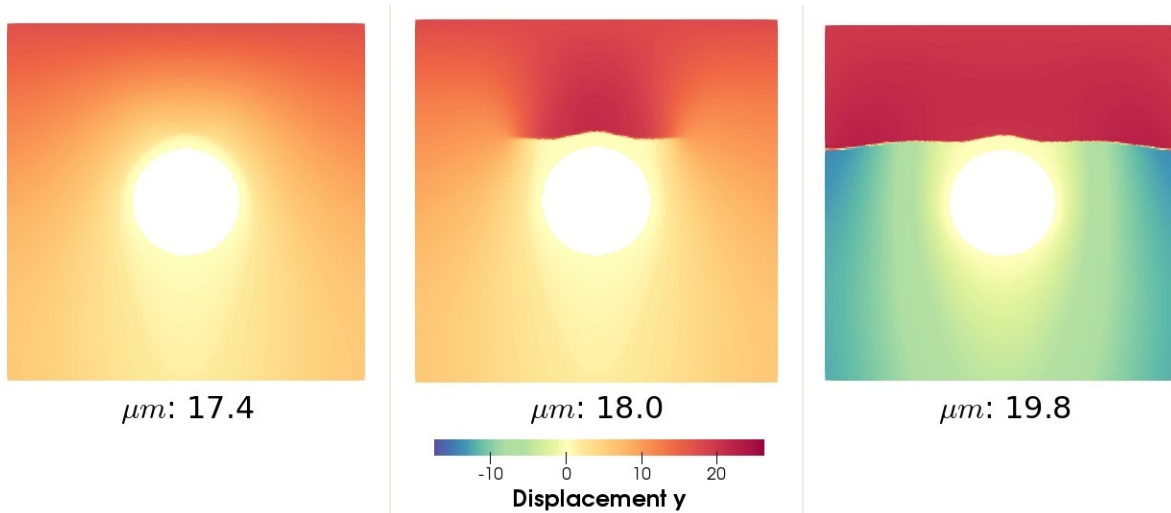


(b) Elastic, dissipated, kinetic and total energies evolution.

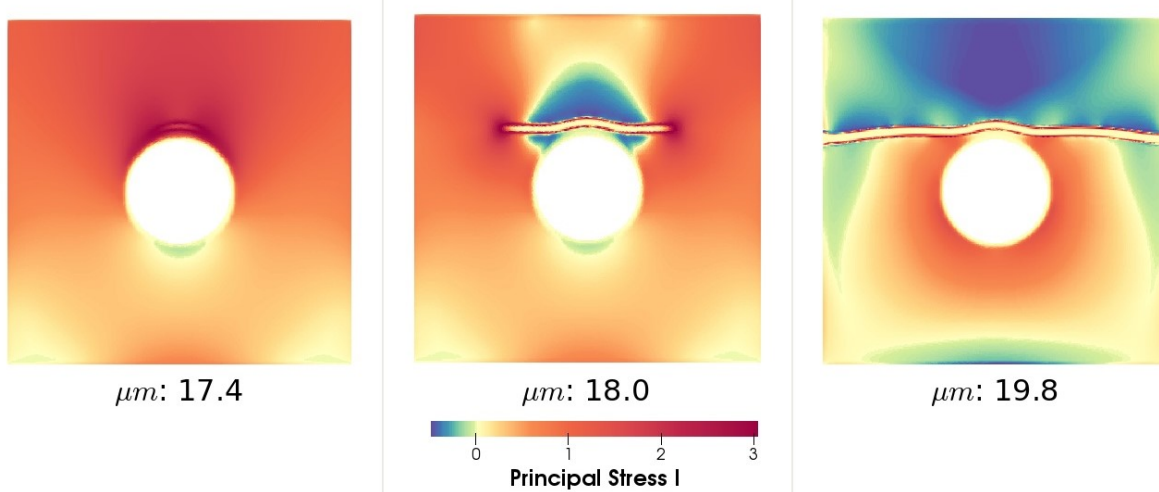
(c) Zoom in material points scale: width of the damaged zone.

Fig. 4.15.: Tensile quasi-static (AT-2): evolution of damage variable and energies in a plate with rigid inclusion with $2h = 2.5\text{mm}$.

In an intermediate evolution instant ($\bar{u} = 18\mu\text{m}$), we observe a strong discontinuity in the y -displacement following both frontiers of the damaged pattern. The maximum principal stress profile shows that, at this moment, the crack tips concentrate the most important tensile stresses in a normal direction to the damage pattern (clarifying the fracture propagation process). The zone at the bottom side of the inclusion and the zones below and above the fracture pattern present now a stronger compressive stress. Finally, at $\bar{u} = 19.8\mu\text{m}$, when the fracture propagation reaches the left and right side boundaries, we observe that the plate seems to be split into two parts by the fractured path, presenting



(a) y-displacement field evolution over different imposed displacements \bar{u} [μm].



(b) Maximum principal stress field evolution over different imposed displacements \bar{u} [μm].



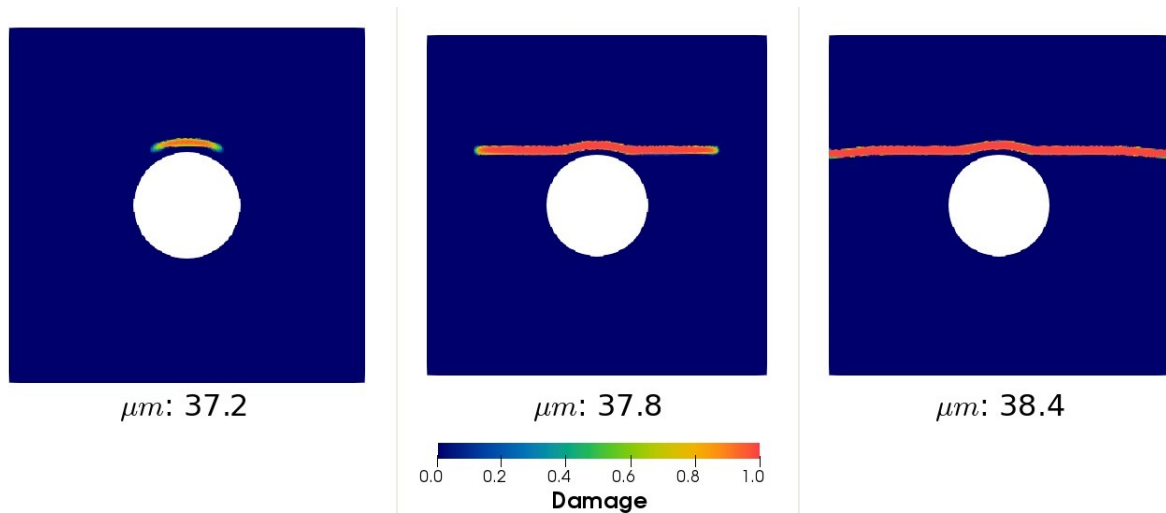
Fig. 4.16.: Tensile quasi-static (AT-2): evolution of the y-displacement and of the maximum principal stress in three key stages: damage growth, half-fractured and completely fractured with $2h = 5mm$.

a quasi-constant and positive value of the y-displacement in the top side and a lower or equal to zero value in the bottom side.

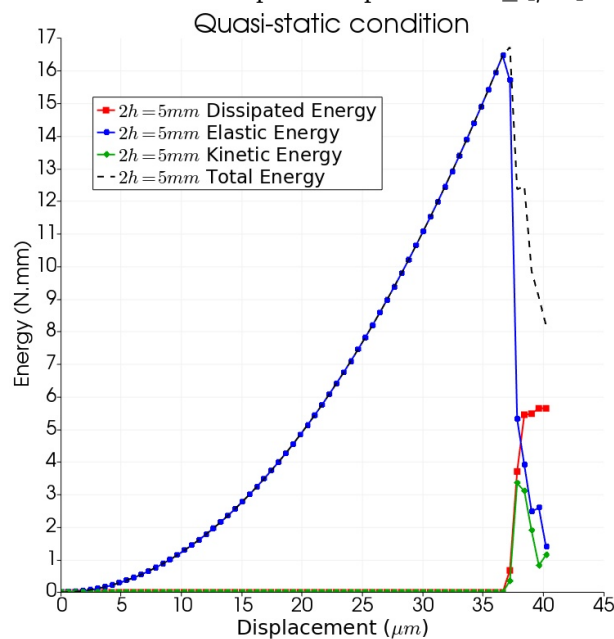
AT-1 type model:

We maintain here the exact conditions and numerical parameters adopted in AT-2 type model by following the support length $2h = 5mm$. Fig. 4.17a presents the damage field evolution for the reinforced fiber plate under a tensile loading. The AT-1 type model has brutal damage and fracturing growth: a range of $1.2\mu m$ of imposed displacement

is necessary from the first damage apparition to the complete fractured sample. The crack pattern presents a similar shape that the one found in the AT-2 type model and the other literature references. We also observe here a symmetry between the left and right-hand-side of the crack pattern. Fig. 4.17b present the evolution of the total, elastic,



(a) Fracture pattern evolution over different imposed displacements \bar{u} [μm].



(b) Elastic, dissipated, kinetic and total energies evolution.

(a) watch



the video

Fig. 4.17.: Tensile quasi-static (AT-1): evolution of damage variable and energies in a plate with rigid inclusion with $2h = 5mm$.

dissipated and kinetic energies. Repeating the phenomenon observed in AT-2 type model, the apparition of a non-negligible kinetic energy at the exact moment of the rupture

initiation is observed here. The level of dissipated energy is here around $5N.mm$, which is expected considering that such energy is related to the projected damaged surface in the sample. Here, both kinetic and dissipated energies present a brutal increase with a close initial slope.

4.3.2.2 Compressive loading

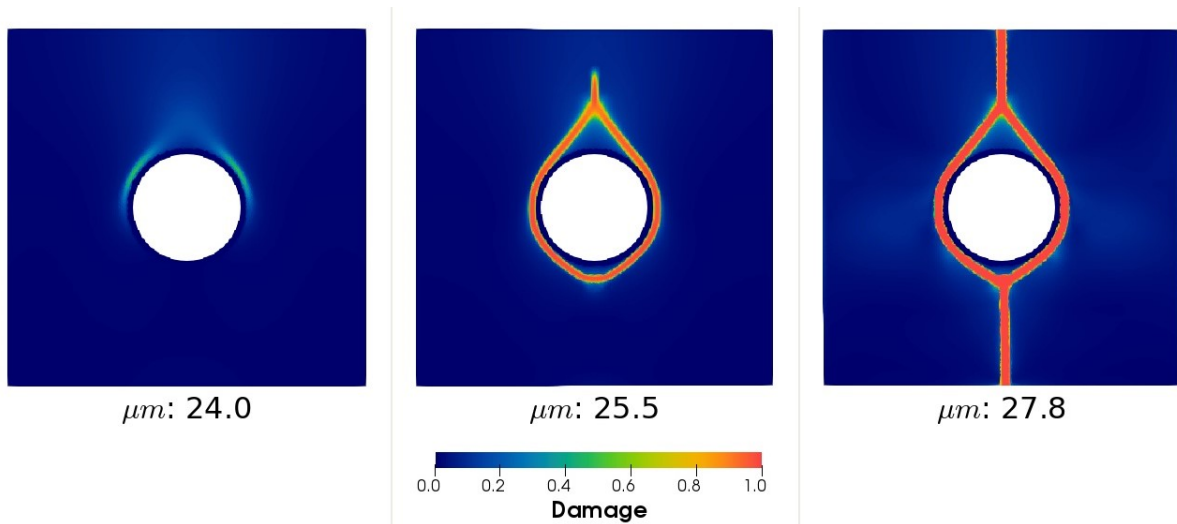
Reversing the loading, we obtain in Fig. 4.18 the damage field evolution after decreasing imposed displacements. The unilateral damage model predicts asymmetric response and is expected to treat the damage evolution differently in tensile and compressive load conditions.

AT-2 type model:

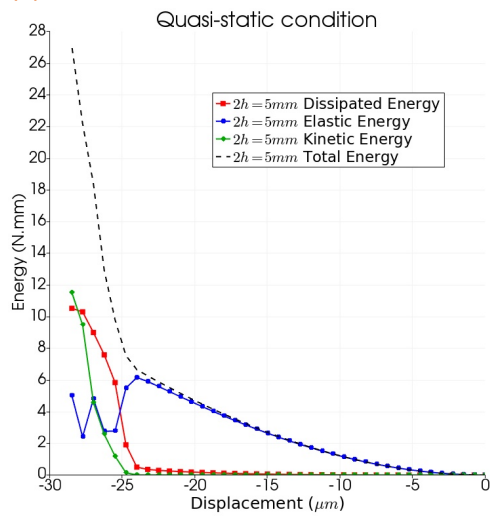
According to Fig. 4.18a, at $\bar{u} = 24.0\mu m$, the elastic solution that was, so far, similar to the tensile load case is followed by a different crack initiation on the top diagonal inclusion boundaries. At $26.2\mu m$ of applied displacement, the cracking pattern evolved to two crack branches, that surround the inclusion by forming different top and bottom angles, propagating towards the top bound in a straight and vertical shape. At the final imposed displacement $\bar{u} = 27.8\mu m$, the crack branch reaches the bottom bound through a shape that seems slightly inclined to the right-hand-side of the plate.

Fig. 4.18b presents level of overall energies greater than those observed in the tensile case. An important rise of the kinetic energy is also noted during fracture propagation. Fig. 4.18c shows a zoom of the damage pattern at the final imposed displacement $\bar{u} = 27.8\mu m$, confirming that the width of the damaged zone also follows the same magnitude order of $2h = 5mm$ under compressive loading.

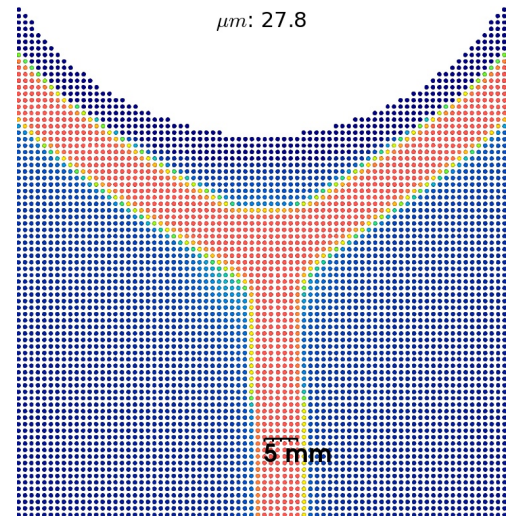
Considering the compressive loading treated here, the unilateral degradation process is better explained in Fig. 4.19 through the horizontal displacement field [μm] (Fig. 4.19a) and the minimum principal stress component [N/mm^2] (Fig. 4.19b). At the displacement $\bar{u} = 24\mu m$, the heterogeneity imposed by the circular inclusion seems to lead to an anti-symmetric division of the x-displacement split in 4 zones coupled to a strong compressive stress field with minima values on the top of the rigid inclusion (which represents the fracture initiation by compression), while below the inclusion, a zone under tensile stress starts growing. At $\bar{u} = 25.5\mu m$ of applied displacement, we observe two new tensile fractures being formed toward the top and the bottom bounds in contrast with the first compressive fracture. The third principal stress field shows that, the crack tips concentrate the most important tensile stresses in a normal direction to the damage pattern. This crack evolution is in agreement with the x-displacement field



(a) Fracture pattern evolution over different imposed displacements \bar{u} [μm].



(b) Elastic, dissipated, kinetic and total energies evolution.



(c) Zoom in material points scale: width of the damaged zone.

(a) watch

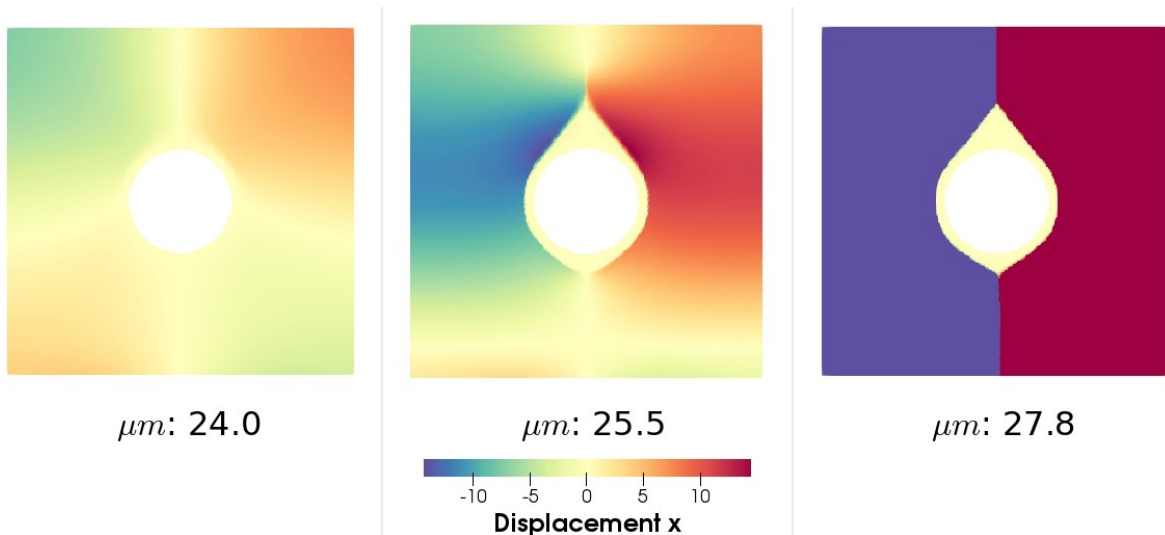
 the video

Fig. 4.18.: Compressive quasi-static (AT-2): evolution of damage, minimum principal stress and energies in a plate with rigid inclusion with $2h = 5mm$.

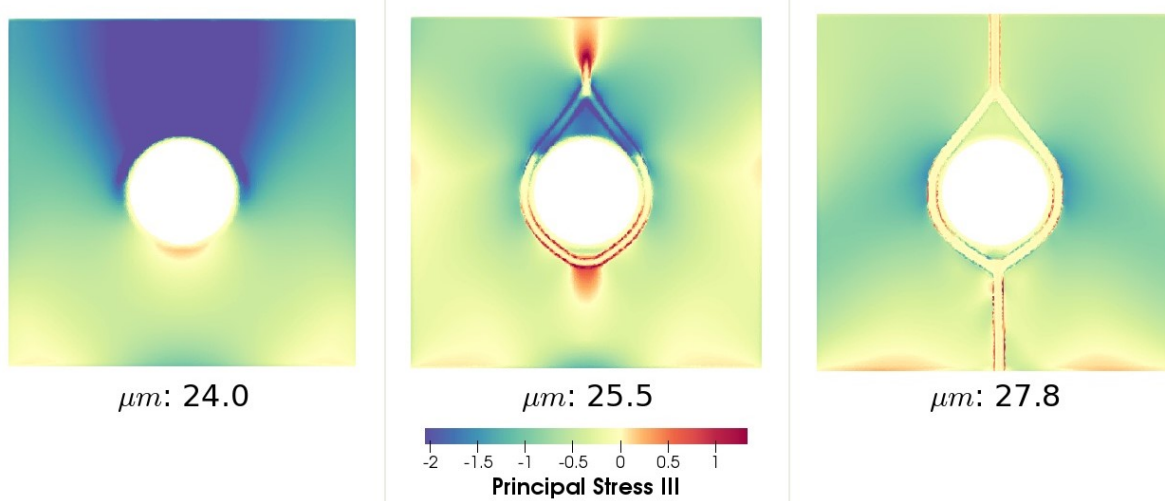
that presents a jump behaviour on the fracture lips creating two zones of more important x-displacement levels at the left and right sides of the inclusion. Lastly, at $\bar{u} = 27.8\mu m$, we observe a suddenly reduction on the stress levels. On the same way, the x-displacement field shows a brutal discontinuity between both sample sides.

AT-1 type model:

The Ambrosio-Tortorelli-based model with critical damage release constant and not dependent on D creates the condition to the damage growth and the crack initiate



(a) x-displacement field evolution over different imposed displacements \bar{u} [μm].



(b) Minimum principal stress field evolution over different imposed displacements \bar{u} [μm].

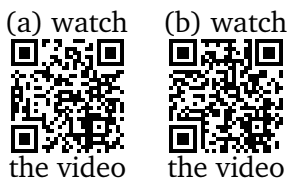
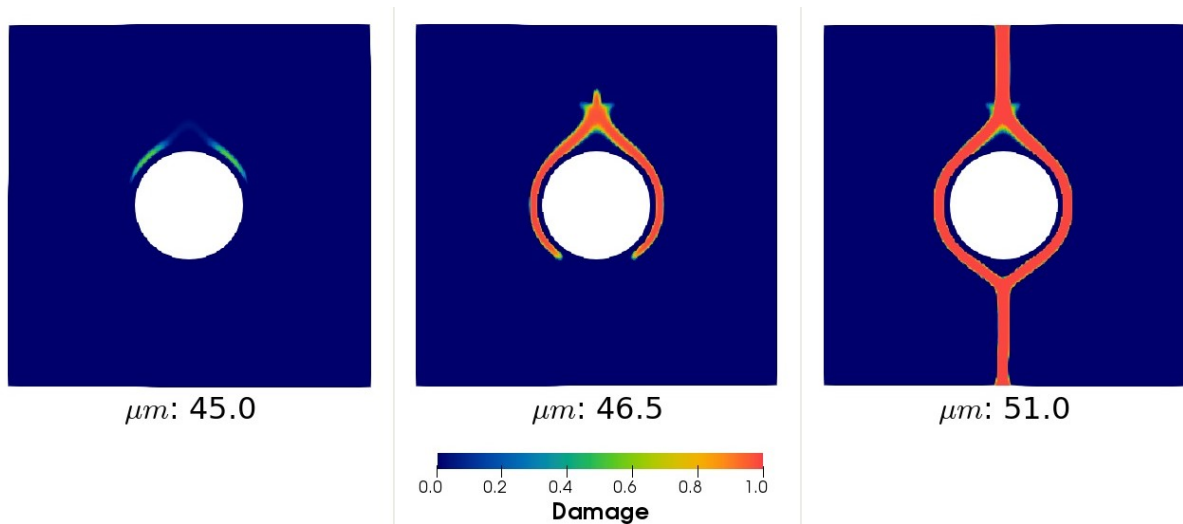
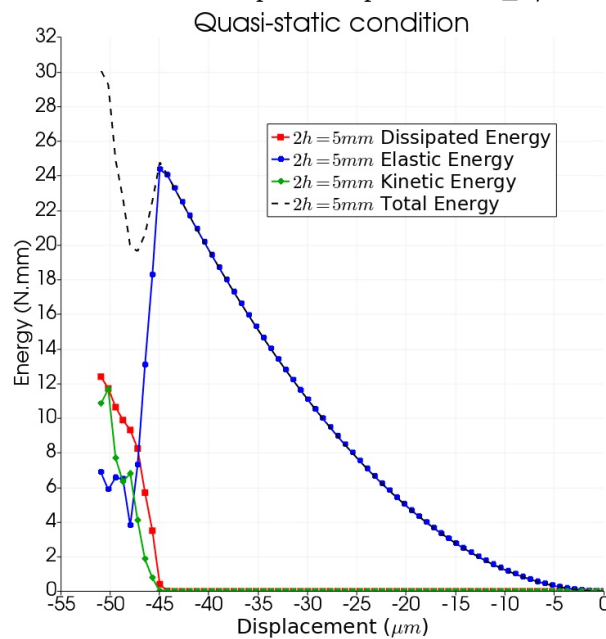


Fig. 4.19.: Compressive quasi-static (AT-2): evolution of the x-displacement and of the minimum principal stress in three key stages: damage growth, half-fractured and completely fractured with $2h = 5mm$.

in a close time interval. This condition is capital to describe the onset of fracturing. In Fig. 4.20a, we observe now that the minimum necessary of imposed displacement to fracture appearance is $45\mu m$ (almost twice larger than in AT-2 type model). The final crack pattern present the same shape than AT-2 type model, with much less diffuse damage around the sample. The crack pattern after a brutal fracturing have a quite symmetric evolution. Fig. 4.20b shows that the adoption of different \mathcal{Y}_c laws does not change the dissipated energy description. We note from Fig. 4.18b and Fig. 4.20b that for imposed displacements of about $\sim 24\mu m$ both models present close elastic energy levels of about $\sim 6N.mm$. However, at this displacement, AT2 model (Fig. 4.18b) starts fracturing, while



(a) Fracture pattern evolution over different imposed displacements \bar{u} [μm].



(b) Elastic, dissipated, kinetic and total energies evolution.

(a) watch



the video

Fig. 4.20.: Compressive quasi-static (AT-1): evolution of damage, minimum principal stress and energies in a plate with rigid inclusion with $2h = 5mm$.

AT-1 type model (Fig. 4.20b) lasts under elastic regime until an imposed displacement of about $\sim 44\mu m$ (which results in a much more important elastic energy level for AT-1 type model). The kinetic energy here seems to be in agreement with the AT-2 type model, remaining in a close evolution behaviour and maximum peak.

4.3.2.3 Analysis of SPH discretization independence and limit values for SPH support-length

Non-local damage models are reputed to overcome the mesh dependence in meshed domains. For this purpose, a common strategy adopted in such problem is to add a non-local term in the energy state function (see Lorentz and Andrieux [101] or Marigo *et al.* [105] for instance). Alternatively, SPH solves the non-locality problem through its interpolated nature and does not need any additional term in their equations to take into account such phenomenon.

In this section, we aim to investigate SPH spatial discretization independence and, for very small and very large values of $2h$, the capability of our method to localize damage even in extreme configurations. Using the same simulation parameters from Sec. 4.3.2.1 and adopting the AT-2 type model, we illustrate in Fig. 4.21 a zoomed part at the top bound of the rigid inclusion for four different material point discretizations (a), (b), (c) and (d) for respectively 200, 300, 400 and 500 material points by side of each plate. In all figures, we note the same width of the damaged zone directly related to $2h = 5\text{mm}$ and a similar shape independent of the discretization.

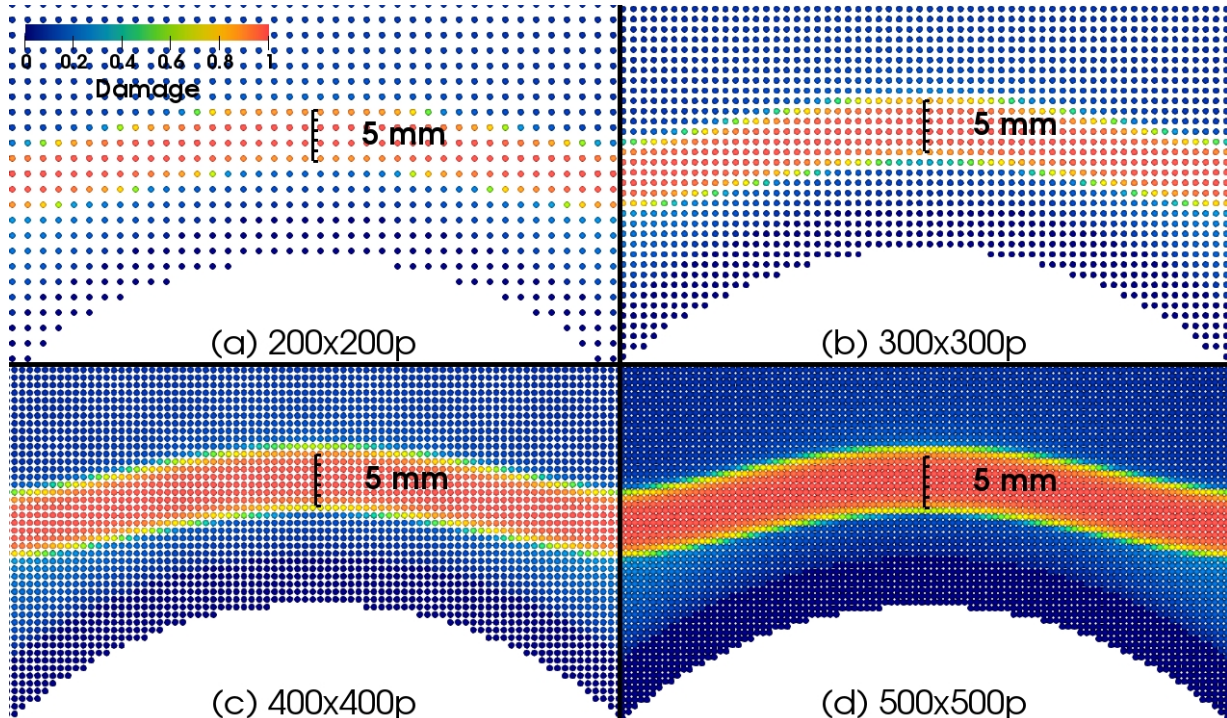


Fig. 4.21.: SPH discretization independence analysis: zoomed area of the top bound of the inclusion showing the discretization independence of the width of the damaged zone for $2h = 5\text{mm}$. Material point discretizations by side of the plate: (a)200, (b)300, (c)400 and (d)500 material points.

In addition, Fig. 4.22 confirms also for the energies quantities the independence of the results on the discretization. We observe a convergence of energy values for discretizations greater or equal to 300 material points by each side of the plate.

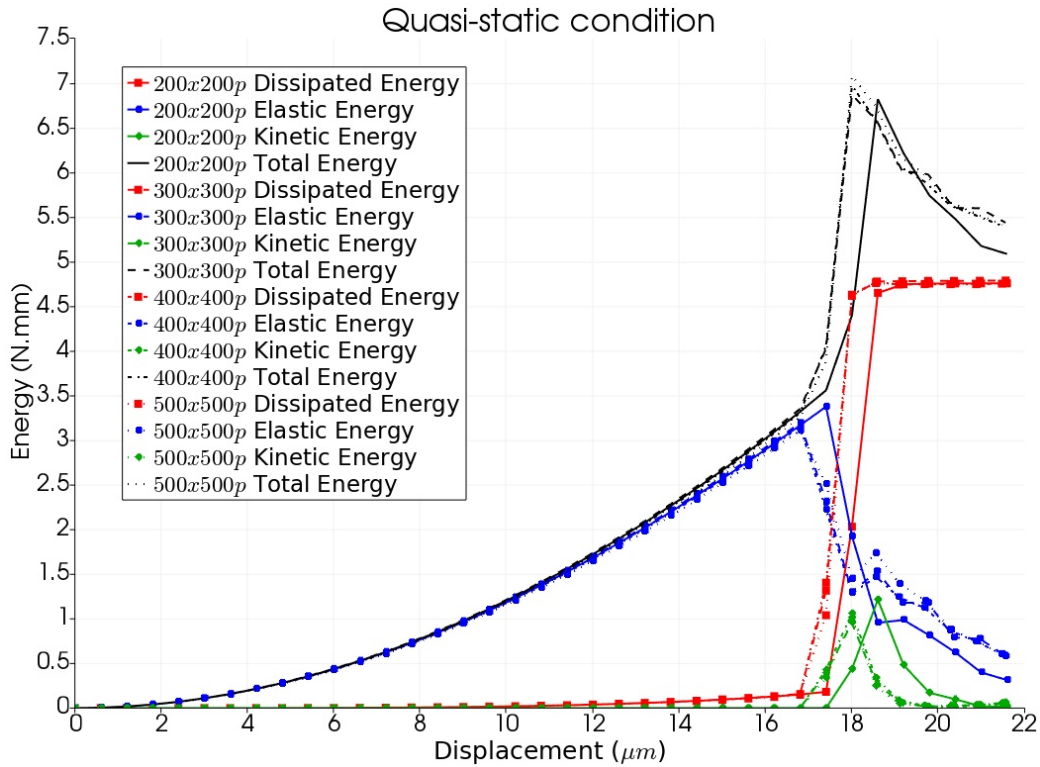
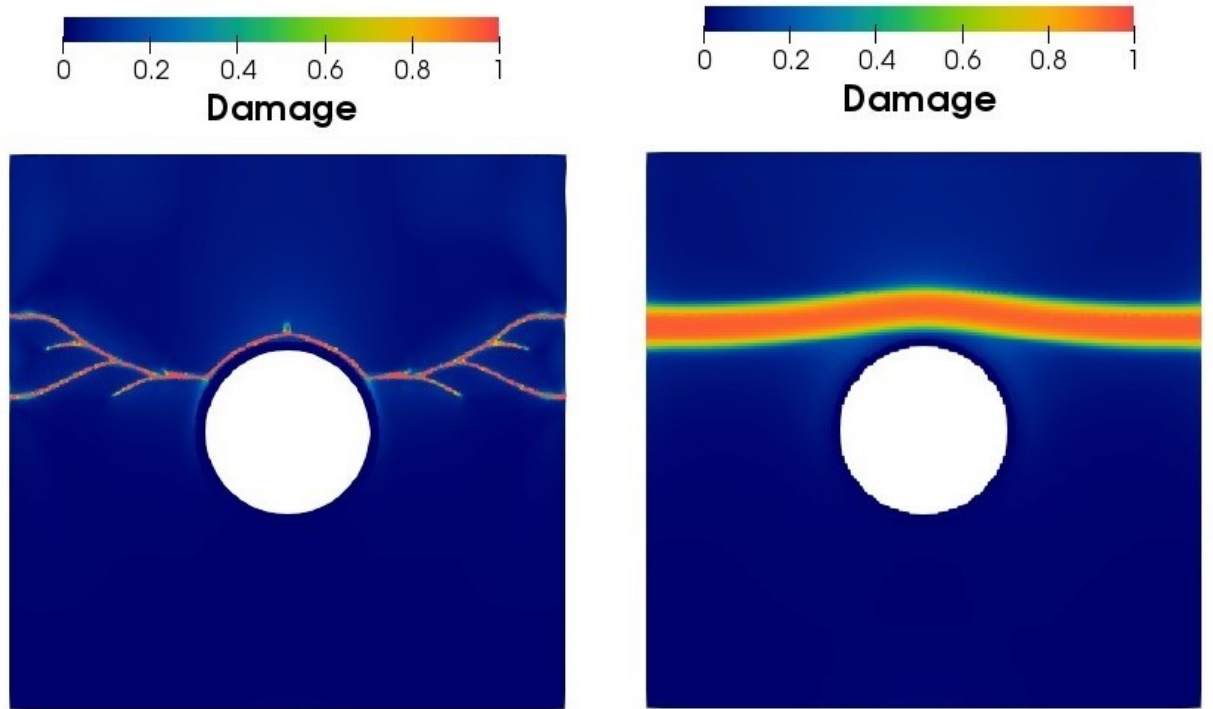


Fig. 4.22.: SPH discretization independence analysis: elastic, dissipated, kinetic and total energies for $2h = 5mm$.

Moreover, we propose another analysis to represent the asymptotic behaviour for minimal and finite values of the numerical parameter $2h$. We noted previously that our quasi-static condition is an approximation of the naturally dynamic SPH solver by reducing in some magnitude orders the kinetic phenomena present therein. Nevertheless, we do not avoid kinetic responses given to a brutal phenomenon, and we showed in previous results that these kinetic responses could be non-negligible in the fracturing regime. In Fig. 4.23, we present two simulations with $2h = 1.25mm$ (Fig. 4.23a) and $2h = 20mm$ (Fig. 4.23b) and the same previous material properties.

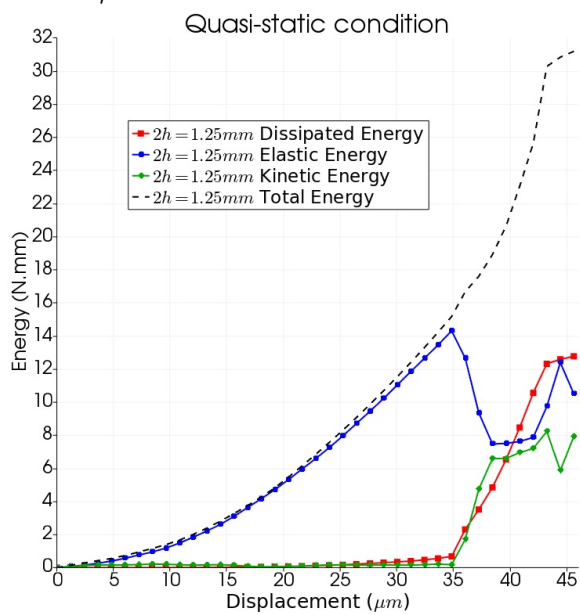
Comparing kinetic energy values from Fig. 4.23c, we observe a rise of kinetic energy with the reduction of the damage width zone (related to $2h$). Again, it is notable that the SPH explicitly captures such dynamic phenomena² even in a quasi-static conditions by the crack branching presented in Fig. 4.23a. This multiple crack branching is also manifested by the higher level of dissipated energy in Fig. 4.23c. Otherwise, Fig.

²Several discussions about crack branching in dynamic conditions can be found in literature (see for instance [20], [28], [93], [152]). In the next section we seek to contribute to this debate investigating such feature through explicit dynamic conditions.

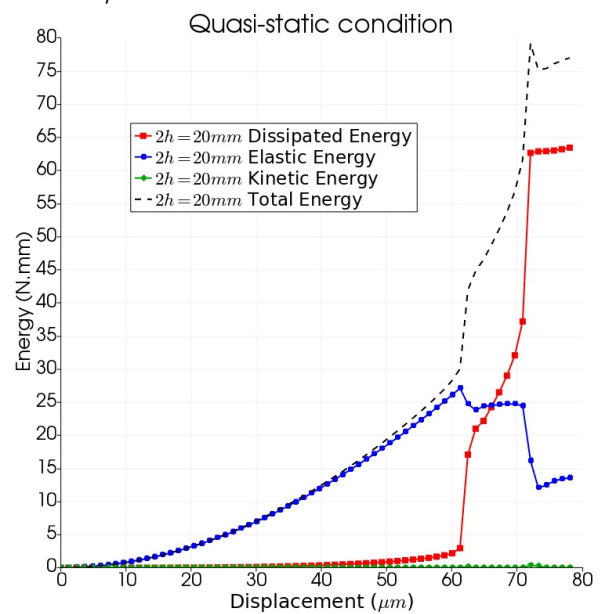


(a) Final fracture pattern for $2h = 1.25\text{mm}$ at $\bar{u} = 45.6\mu\text{m}$.

(b) Final fracture pattern for $2h = 20\text{mm}$ at $\bar{u} = 78.0\mu\text{m}$.



(c) Elastic, dissipated, kinetic and total energies for $2h = 1.25\text{mm}$.



(d) Elastic, dissipated, kinetic and total energies for $2h = 20\text{mm}$.

Fig. 4.23.: Non-local analysis in quasi-static conditions: final fracture pattern and energies evolution for imposed tensile loading with $2h = 1.25\text{mm}$ and $2h = 20\text{mm}$.

4.23d shows that for a large value of $2h$, a higher level of dissipated energy and a very low level of kinetic energy.

4.3.3 Dynamic response of fiber reinforced plate

We adopt now a system under dynamic conditions. We apply a velocity $v_y = \pm 10^{-6} \cdot L \text{ mm/s}$ at the top bound until reaching the final fixed displacement $\bar{u} = \pm 10^{-3} \text{ mm}$. We focus here on investigating the response of such a system by using the SPH method through the energy-based damage model with unilateral effects. We simulate the plate with rigid inclusion under tensile and compressive loads in order to highlight the dynamic response of the system. As before, an infinitesimal strain hypothesis is adopted. A first study of crack propagation in solids under dynamic conditions can be found in [139]. In the following, analytical, experimental, and numerical models [138], [152], [164] were investigated.

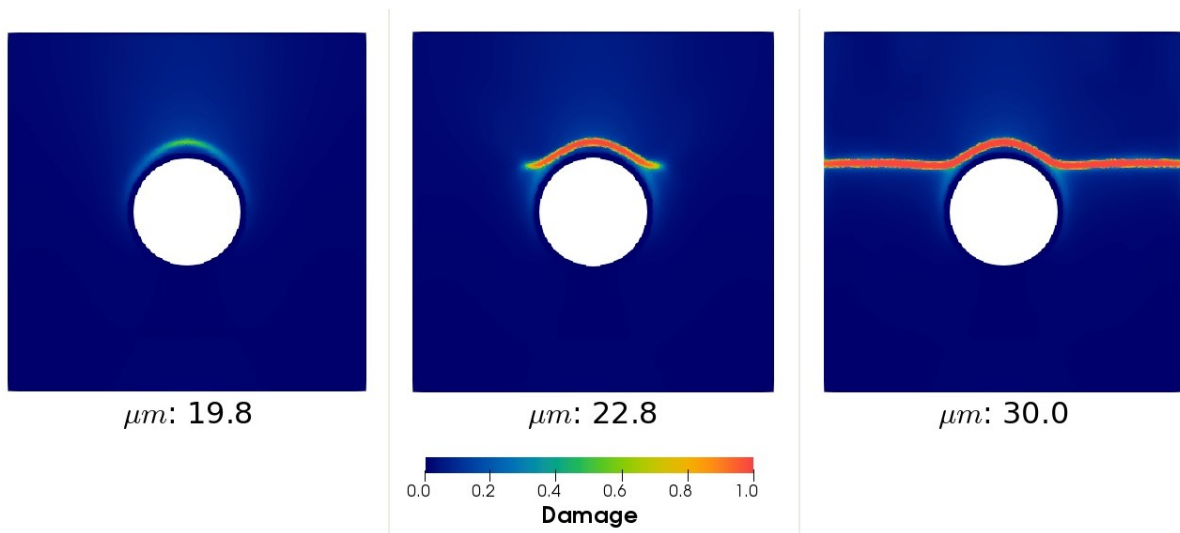
4.3.3.1 Tensile loading

We perform here simulations under tensile dynamic conditions with the same material properties and numerical parameters as in quasi-static (QS) conditions (except for the imposed displacement \bar{u}).

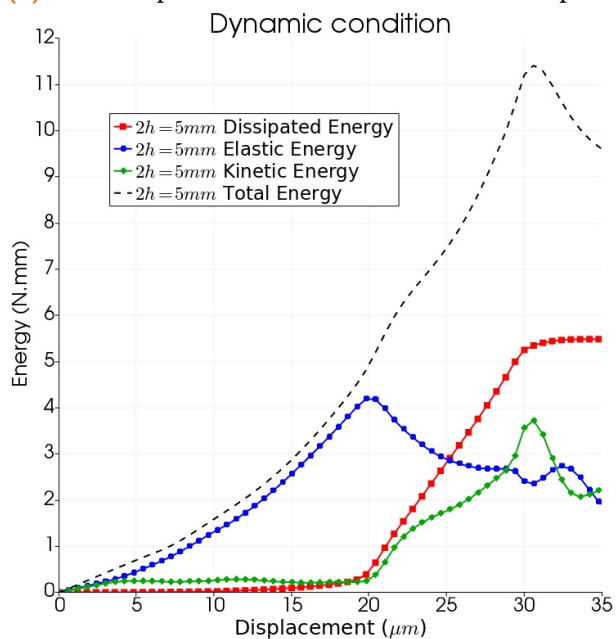
AT-2 type model:

Fig. 4.24a presents the damage field evolution for the plate with an embedded rigid inclusion (for $2h = 5\text{mm}$). As a general observation, a quite similar process of damage growth and propagation is observed as in QS conditions: the damage starts over the top bound of the inclusion and reaches the left and right sides of the plate symmetrically. Notwithstanding, two major differences are observed: the range of imposed displacement between the initiation and the complete damage propagation that was $\bar{u} < 3\mu\text{m}$ in QS is now $\bar{u} > 10\mu\text{m}$; the damage pattern, this time, surrounds more the circular inclusion and then evolves to the lateral bounds in a more straight shape. Such pattern is closer to those obtained in the refereed studies by Amor *et al.* [6] and Freddi and Royer-Carfagni [66] under QS conditions. When the numerical parameter is changed to $2h = 2.5\text{mm}$, a width of the damaged zone of around 2.5mm and a similar crack pattern evolution (but surrounding even more the rigid inclusion) is observed. The propagation towards the lateral boundaries is no more straight and present henceforth crack branching initiations.

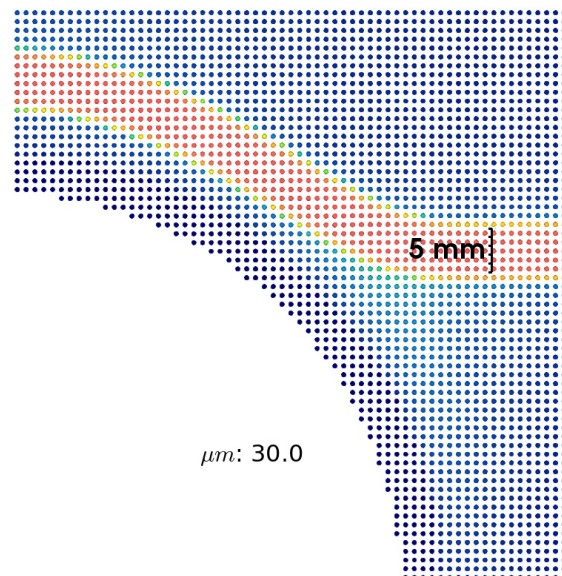
Fig. 4.24b presents the evolution of the total, elastic, dissipated and kinetic energies. The non-negligible kinetic energies present in a post-fracturing instant in QS conditions are normally present now during all the simulation time. Although the dissipated and elastic energies evolved less brutally than from QS conditions, the energetic response of the structure present values of the same order concerning their peak values.



(a) Fracture pattern evolution over different imposed displacements \bar{u} [μm].



(b) Elastic, dissipated, kinetic and total energies evolution.



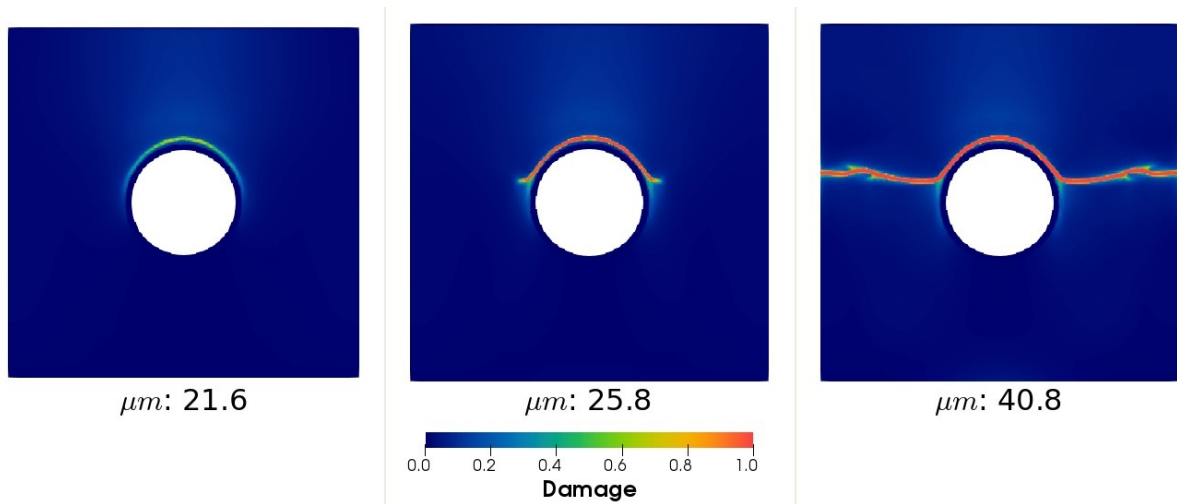
(c) Zoom in material points scale: width of the damaged zone.

(a) watch

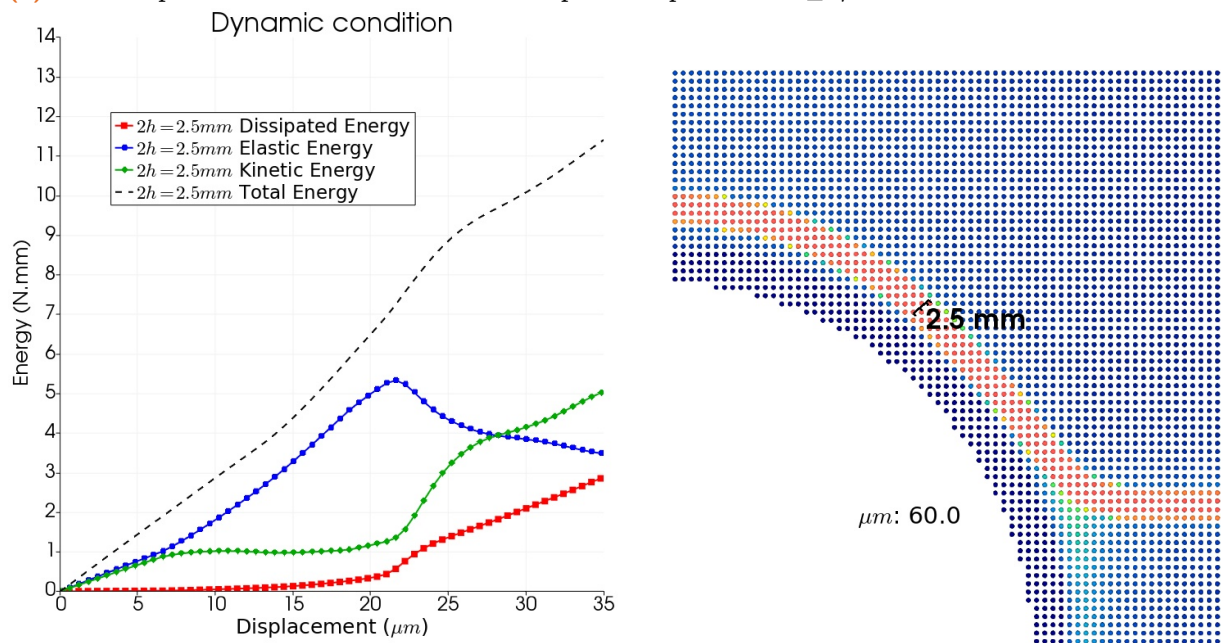
 the video

Fig. 4.24.: Tensile dynamic (AT-2): evolution of damage variable and energies in a plate with rigid inclusion with $2h = 5\text{mm}$.

Considering very similar final damage patterns and energy peaks, it appears that the dynamic conditions play a role especially related to the velocity of evolution of the whole phenomena. We also observe that, also in dynamic conditions, the increase of the dissipated energy values are directly related to the increase of the support-length $2h$.



(a) Fracture pattern evolution over different imposed displacements \bar{u} [μm].



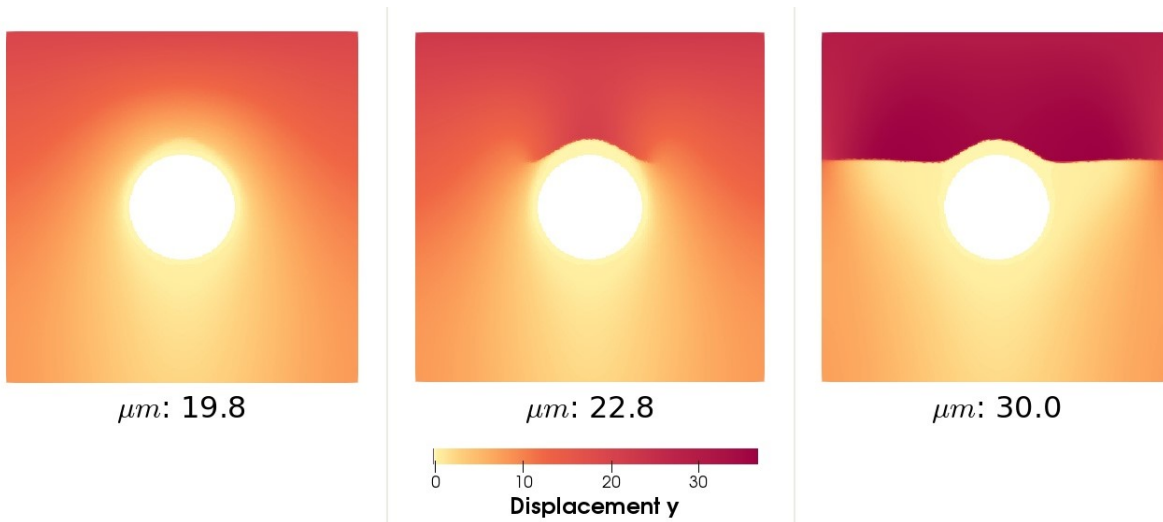
(b) Elastic, dissipated, kinetic and total energies evolution.

(c) Zoom in material points scale: width of the damaged zone.

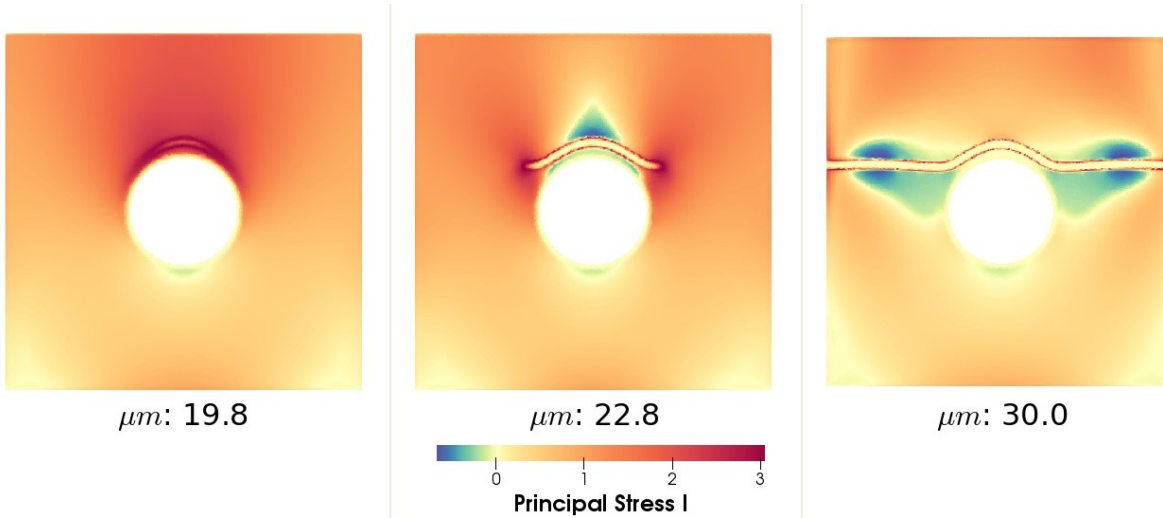
Fig. 4.25.: Tensile dynamic (AT-2): evolution of damage variable and energies in a plate with rigid inclusion with $2h = 2.5mm$.

Moreover, it is worth noting the effect of the numerical parameter $2h$ in the damage characterisation does not change when we switch from quasi-static to dynamic conditions. Fig. 4.24c for $2h = 5mm$ and Fig. 4.25c for $2h = 2.5mm$ confirm a strong relation between the support length $2h$ and the width of the damaged zone at the end of the crack propagation. A discretization independence of SPH under dynamic conditions is also noted.

Fig. 4.26 present, respectively, the displacement [μm] and the maximum principal stress [N/mm^2] in the plate configuration presented in Fig. 4.24a. We see here a



(a) y-displacement field over different imposed displacements \bar{u} [μm].



(b) Maximum principal stress field over different imposed displacements \bar{u} [μm].

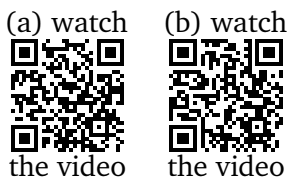


Fig. 4.26.: Tensile dynamic (AT-2): evolution of the y displacement [μm] and of the maximum principal stress [N/mm^2] in three key stages: damage growth, half-fractured and completely fractured with $2h = 5mm$.

smoother gradient of the fields around the plate, the greatest principal stresses presented in Fig. 4.26b and the y-displacement field (Fig. 4.26a) present a similar behaviour that was presented in quasi-static conditions for the two first instants. However, the dynamic behaviour post-failure is much softer at the final time step. We highlight here, as consequence of the dynamic condition, a smoothed variation of these fields all over the plate.

AT-1 type model:

The damage pattern of predicted by AT-1 type model in dynamic conditions (Fig. 4.27a) surrounds less the inclusion than the AT-2 type model. We emphasize the common instant of damage and fracture initiation that requires a higher level of imposed displacement. The energies evolution (Fig. 4.27b) shows a quasi-similar level of dissipated energy when compared to AT-2 type model, but a much more important level of elastic energy, given by the higher displacement before the first damage occurs. Considering that a more brutal crack phenomenon is observed, the kinetic energy is here more pronounced than in AT-2 type model.

4.3.3.2 Compressive loading

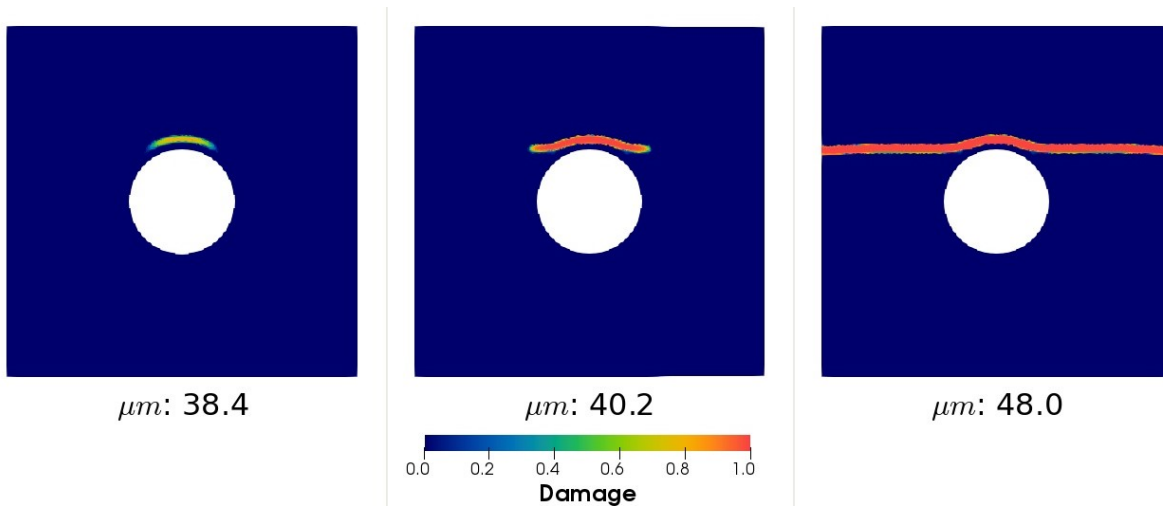
In this section, we consider compressive loading by changing the sense of the imposed displacements. In this context, the extended version of the model will be helpful.

AT-2 type model:

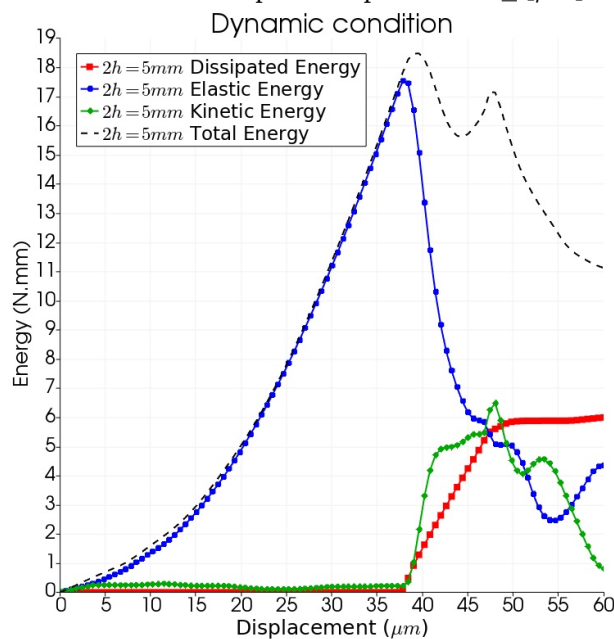
Indeed, the unilateral aspect plays here the same role than in QS conditions, the damage and crack evolution under tensile and compressive conditions being affected. Again, an important difference between the values imposed displacement at the initiation, and the final damage state ($> 30\mu m$) is noted. In quasi-static conditions, this range is lower than $4\mu m$. However, we observe from Fig. 4.28a a similar damage pattern and overall behaviour this time when compared to the QS conditions. Although Fig. 4.28b presents here a smoother energy evolution when compared to QS conditions, it remains at the same energy level values. Finally, Fig. 4.28c confirms again that the width of the damaged zone follows the same magnitude order of $2h = 5mm$ independently of the load conditions. The x-displacements and the minimum principal stresses presented in Fig. 4.29 also present a similar behaviour that was presented in QS conditions. In the same way from the simulation with tensile loading, we observe also a less brutal variation of such fields around the inclusion, which highlights the less established nature of the dynamic condition (in the sense of quasi-static evolving happens slowly enough for the system to remain in internal equilibrium).

AT-1 type model:

Damage evolution as predicted in AT-1 type model, under compressive loading, shows in Fig. 4.30 a similar fracture nucleation than other conditions and models in Fig.



(a) Fracture pattern evolution over different imposed displacements \bar{u} [μm].



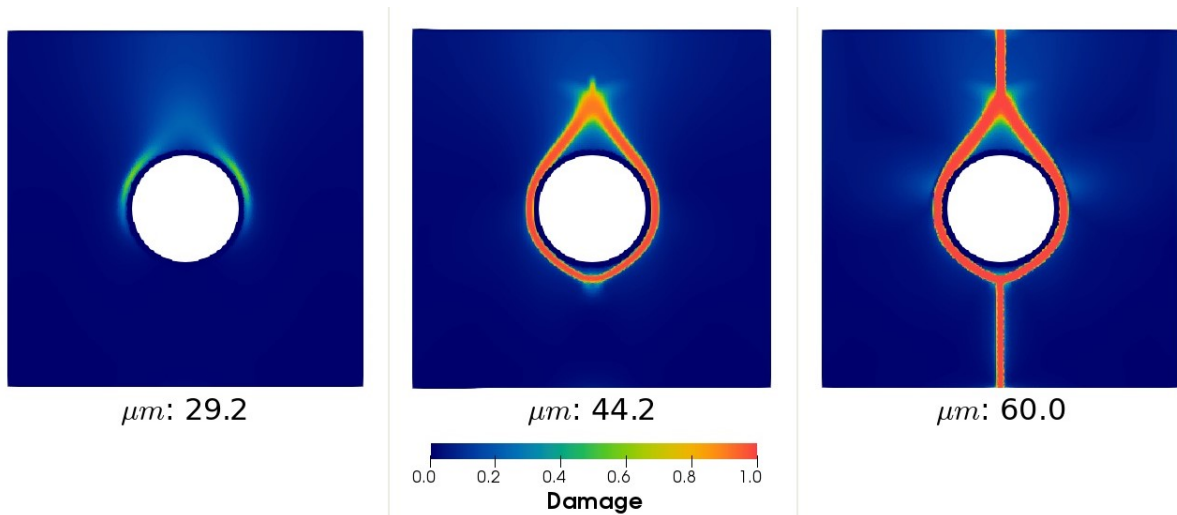
(b) Elastic, dissipated, kinetic and total energies evolution.

(a) watch

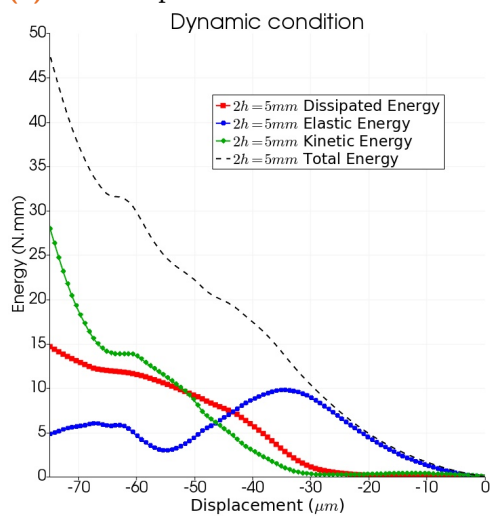
 the video

Fig. 4.27.: Tensile dynamic (AT-1): evolution of damage variable and energies in a plate with rigid inclusion with $2h = 5\text{mm}$.

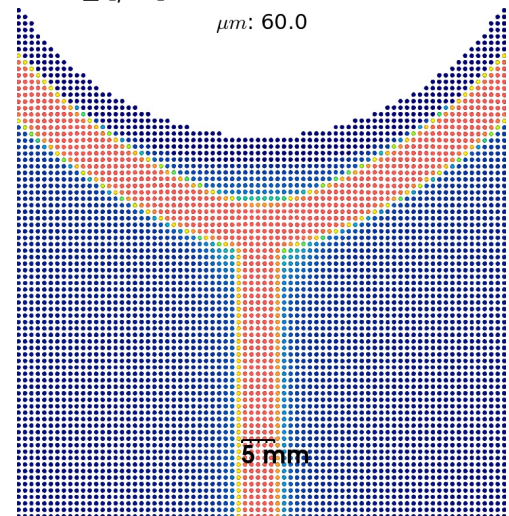
4.30a at an imposed displacement of $51\mu\text{m}$. However, a first crack branching at $58.5\mu\text{m}$ towards the top bound and a second crack branching at $75\mu\text{m}$ towards the bottom bound are predicted. Although we observed such branching phenomena for $2h$ smaller value in Fig. 4.25 or much smaller value in Fig. 4.23a (both in tensile loads), the brutal crack propagation predicted by the AT-1 type model is capable to reproduce crack branching also in compressive load conditions. In addition to the crack branching feature, an asymmetric



(a) Fracture pattern evolution over different imposed displacements \bar{u} [μm].



(b) Elastic, dissipated, kinetic and total energies evolution.



(c) Zoom in material points scale: width of the damaged zone.

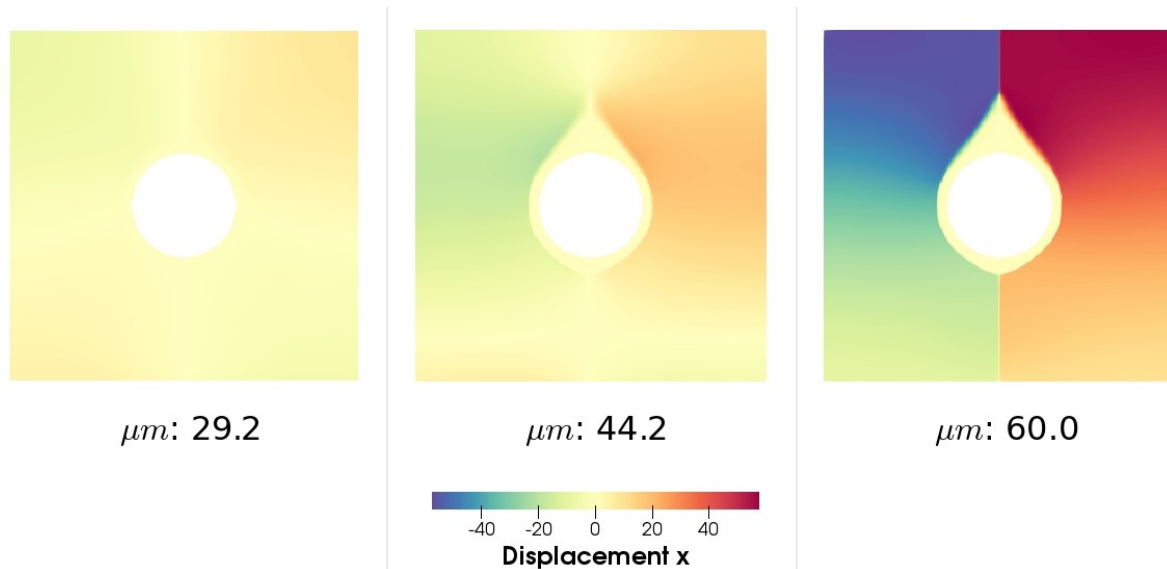
(a) watch



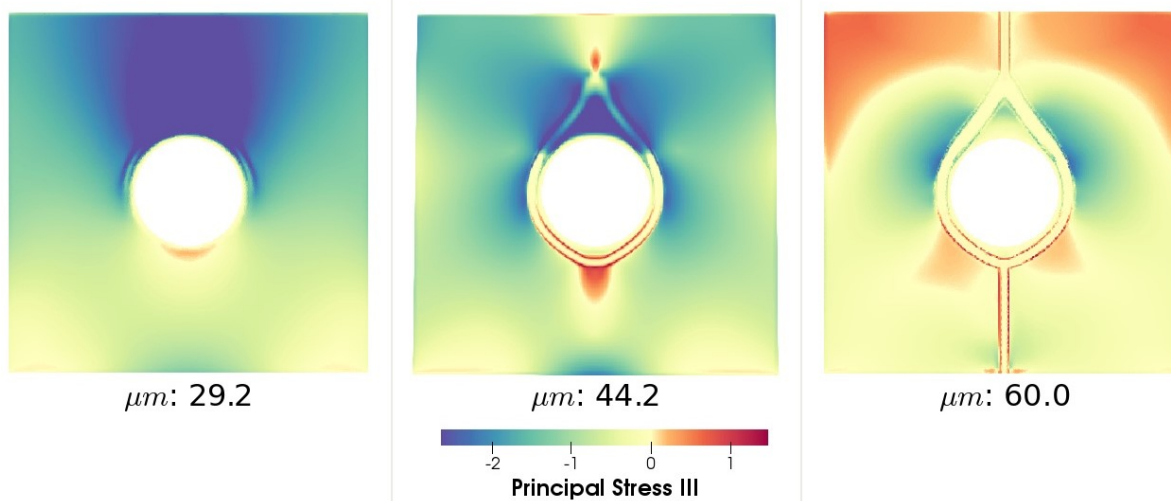
the video

Fig. 4.28.: Compressive dynamic (AT-2): evolution of damage variable, minimum principal stress and energies in a plate with rigid inclusion with $2h = 5mm$.

evolution in the bottom side has been noted. Close crack patterns can also be found in Freddi and Royer-Carfagni [66] despite the use of the AT-2 type model there. Fig. 4.27b show a close dissipated energy level when compared to AT-2 type model. We note that at $75\mu m$ the crack propagation did not reach the bottom boundary. This does not allow us to compare the peaks of dissipated and kinetic energies.



(a) x-displacement field evolution over different imposed displacements \bar{u} [μm].



(b) Minimum principal stress field evolution over different imposed displacements \bar{u} [μm].

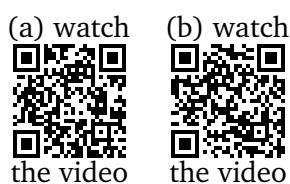
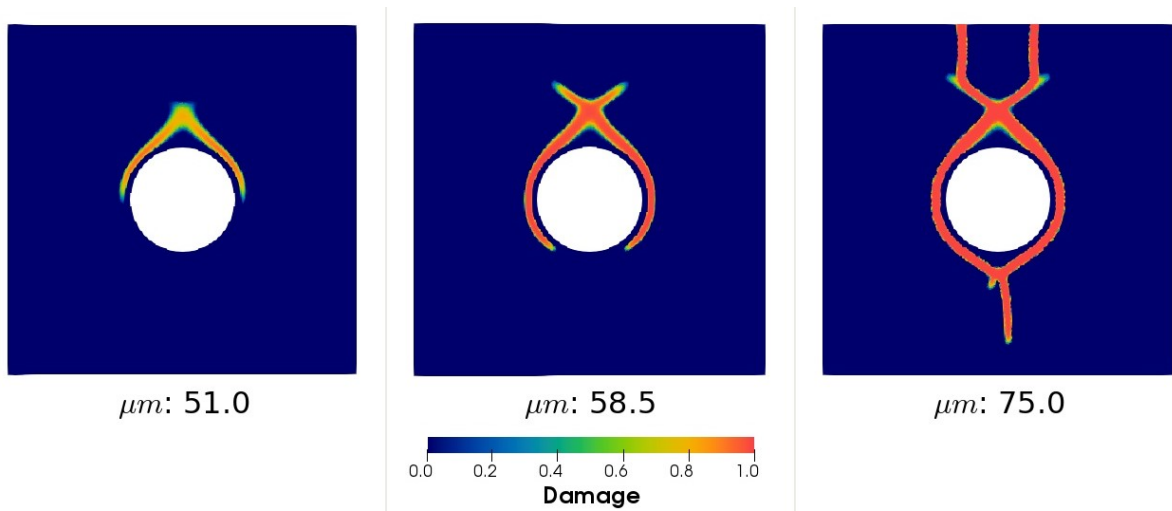


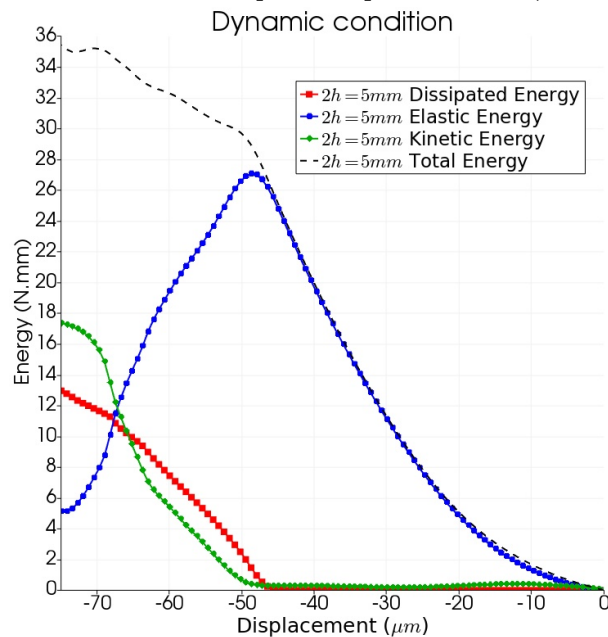
Fig. 4.29.: Compressive dynamic (AT-2): evolution of the x-displacement and of the maximum principal stress in three key stages: damage growth, half-fractured and completely fractured with $2h = 5mm$.

4.3.3.3 Analysis of limit values for SPH support-length

Repeating the procedure of presenting the responses for very small and finite values of the numerical parameter $2h$, we use here dynamics conditions by adopting the AT-2 type model. This time, the imposed displacements reach a value of $120\mu m$. We seek in this section to investigate through asymptotic values of $2h$ the capability of our SPH solver localise damage even in extreme configurations. Fig. 4.31 illustrates two simulations corresponding to $2h = 1.25mm$ (Fig. 4.31a) and $2h = 20mm$ (Fig. 4.31b).



(a) Fracture pattern evolution over different imposed displacements \bar{u} [μm].



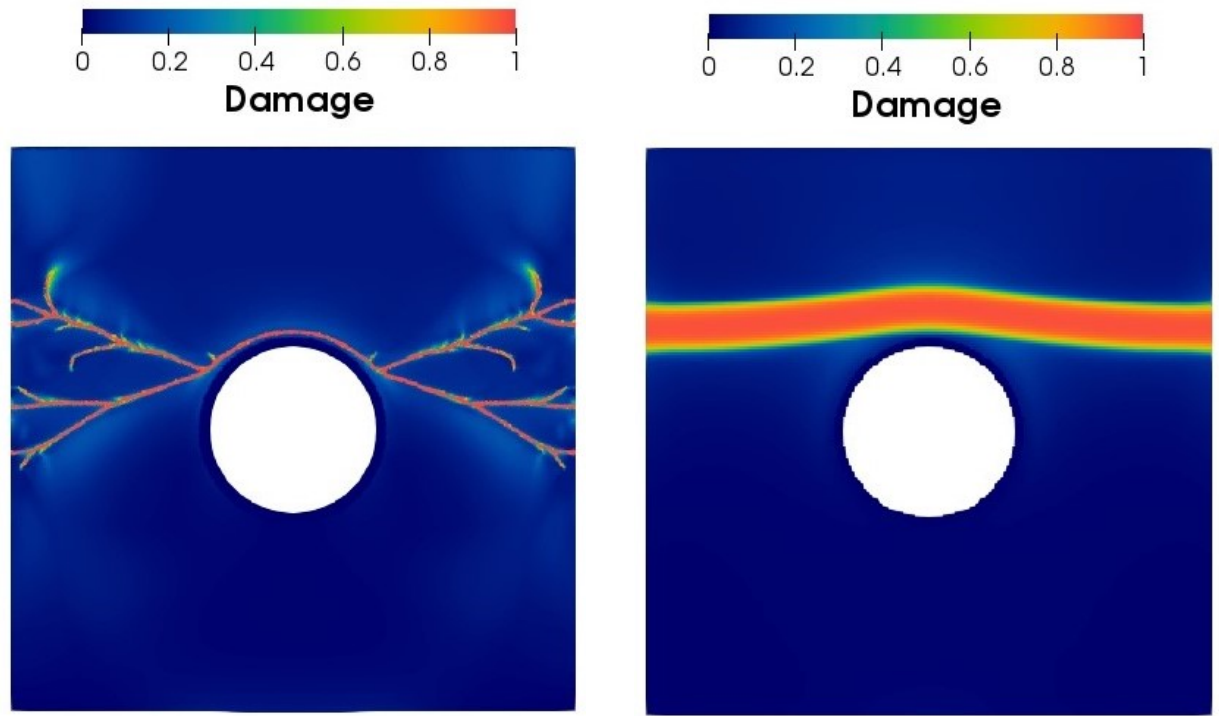
(b) Elastic, dissipated, kinetic and total energies evolution.

(a) watch

 the video

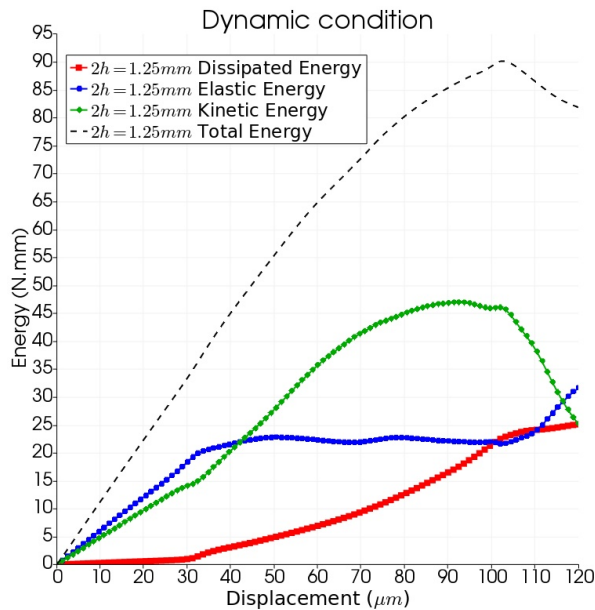
Fig. 4.30.: Compressive dynamic (AT-1): evolution of damage variable and energies in a plate with rigid inclusion with $2h = 5mm$.

The kinetic energy values from Fig. 4.31c present higher levels than the elastic and dissipated energies which can be related to the crack branching and propagation, particularly in dynamic conditions (as illustrated in Fig. 4.31a). On the other side, adopting a very large non-local parameter $2h = 20mm$ leads to a very important decreasing of the kinetic energy values. Besides, the dissipated energy presents a more brutal

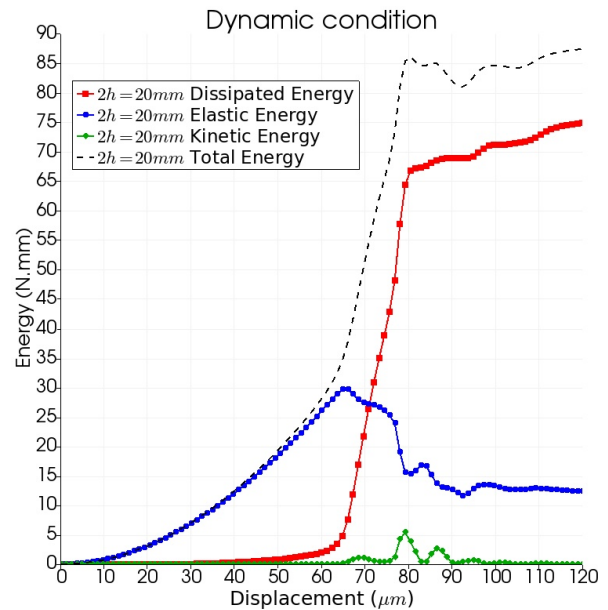


(a) Final fracture pattern for $2h = 1.25mm$ at $\bar{u} = 120.0\mu m$.

(b) Final fracture pattern for $2h = 20mm$ at $\bar{u} = 120.0\mu m$.



(c) Elastic, dissipated, kinetic and total energies for $2h = 1.25mm$.



(d) Elastic, dissipated, kinetic and total energies for $2h = 20mm$.

Fig. 4.31.: Non-local analysis in dynamic conditions: final fracture pattern (at imposed displacement of $120\mu m$) and energies evolution for imposed tensile loading with $2h = 1.25mm$ and $2h = 20mm$.

increasing and a very high peak value (related to the width of the damaged zone and the support-domain $2h$).

For the sake of conciseness, we present in Appendix B supplementary validations of Ponte-Castaneda and Willis based damage model (as recalled in Sec. 4.1.4) in an analogous procedure described in this section. Such validations will be helpful to the clay matrix applications presented in next chapter.

Concluding remarks

In this chapter, we have proposed and implemented, through an SPH framework, a local elastic damage model. In this approach, the non-local regularisation has been performed numerically. It became then possible to treat damage growth, its localization and transition to fracture nucleation and propagation. Two test cases were studied: a 1D vibration bar and a 2D square plate with a rigid inclusion. In both cases, the damage localization was obtained, and it was observed that the width of the damaged zone is related to the numerical parameter support-length ($2h$). In the 2D test case, both for tensile and compressive conditions, the fracture nucleation and propagation which follow the damage localization was accompanied by a non-negligible increase of kinetic energy. Note also that during the fracture propagation, a discontinuity in the displacement fields was observed. As a consequence of the unilateral effects, asymmetric structural responses were observed and proved to be in agreement with existing results. With the SPH method, we have naturally performed simulations under dynamic conditions in which complex fracture patterns with crack branching have been obtained.

Since the numerical parameter $2h$ (the support length of the SPH kernel function) plays the role of a characteristic length of the material, an interesting question concerns its determination from mechanical data. More precisely, it will be helpful to perform an in-depth investigation of the link between this characteristic length $2h$, the fracture toughness G_c and the critical damage energy release rate \mathcal{Y}_c .

Simulations of drainage coupled with damage in a sample of clay rock

Overview: This chapter gathers the progress acquired in the description of an elasto-damageable material from Chapters 3 and 4 in order to simulate a drainage within a clay rock pore-space. In section 5.1, the discrete SPH forms of the fluid dynamics equations are recalled. The description of the numerical sample of a clay matrix is provided in section 5.2. In the following, we present a set of drainage simulations. In section 5.3, we describe the clay matrix as a purely elastic solid medium in order to obtain the reference stress field. In section 5.4, we consider an elasto-damage response to investigate damage growth and fracture propagation under two different confining stresses. Lastly, in section 5.5, a two isolated pores configuration is studied to verify if the model can generate a percolating flow path.

We perform here simulations of drainage coupled with damage in a sample of clay rock (Fig. 5.1). In addition to the elasto-damage formulations presented in previous chapters, SPH forms of the governing equations used to model the behaviour of fluids, and their interactions are resumed in the next section. For the sake of conciseness, we devote the Appendix A to resume the governing equations of rigid bodies.

We resume here the SPH based governing equations of the fluid phases representing the pore-water and hydrogen as adopted in Pazdniakou and Dymitrowska [126].

5.1 SPH fluid phases: pore-water and hydrogen

The continuity equation (1.1) may be discretized into two different versions using the spatial derivatives in the form (2.42):

$$\dot{\rho}_a = \rho_a \sum_b \frac{m_b}{\rho_b} (\underline{v}_a - \underline{v}_b) \cdot \nabla_a W_{ab} \quad (5.1a)$$

$$\dot{\rho}_a = \sum_b m_b (\underline{v}_a - \underline{v}_b) \cdot \nabla_a W_{ab} \quad (5.1b)$$

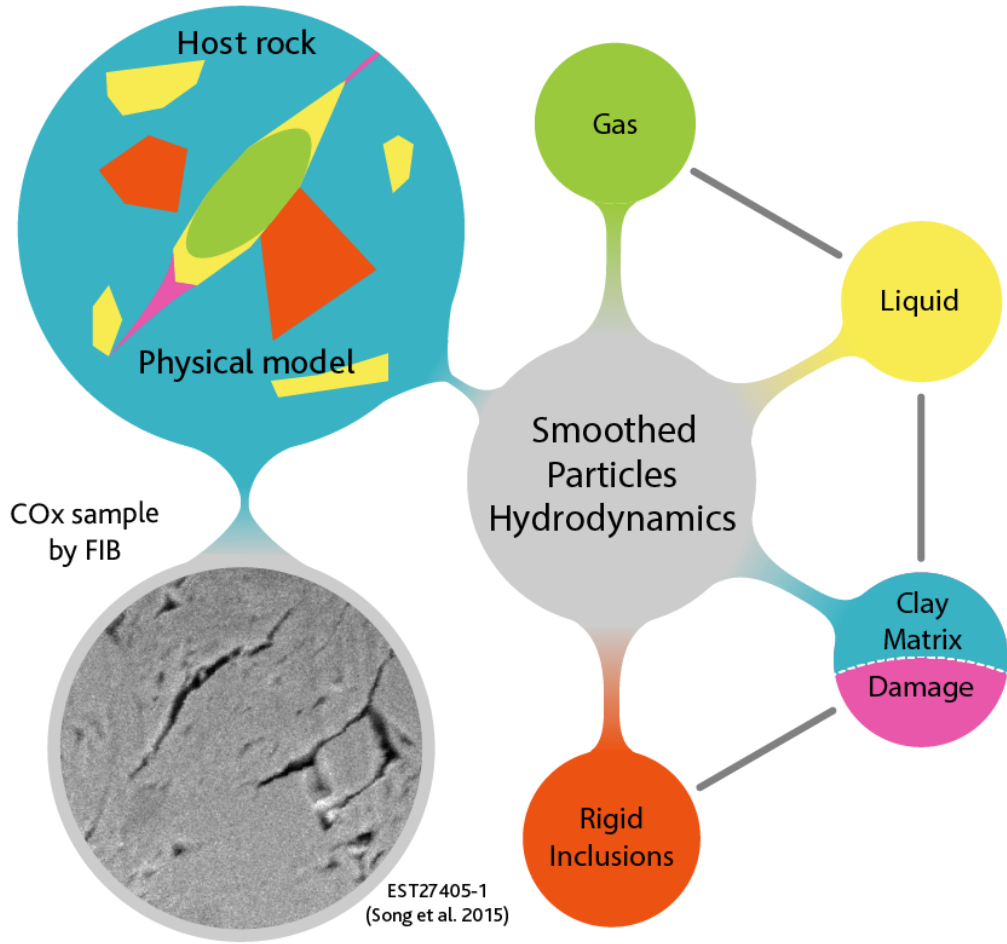


Fig. 5.1.: Physical configuration and SPH numerical model with elasto-damage coupling

It is clear that in a multiphase flow case, the first one provides a better accuracy (even though in all cases the error is of h^2 order). Therefore, by using (2.40) we can discretize the momentum conservation equation (1.3) where the pressure gradient term ∇p can be represented, amongst others, by the following formulations:

$$\nabla p_a = \sum_b \frac{m_b}{\rho_b} (p_a + p_b) \nabla_a W_{ab} \quad (5.2a)$$

$$\nabla p_a = \rho_a \sum_{b=1}^N m_b \left(\frac{p_b}{\rho_b^2} + \frac{p_a}{\rho_a^2} \right) \nabla_a W_{ab} \quad (5.2b)$$

According to Monaghan [117], (5.2b) provides a more stable system with respect to particles disorder, although both formulations have the same accuracy. Furthermore, the

viscous dissipation term present in (1.3) can be discretized by using (2.43) or (2.46), where the last one provides better numerical stability and accuracy.

$$\mu \nabla^2 v_a = 2\mu \sum_{b=1}^N \frac{m_b}{\rho_b} v_{ab} \mathcal{F}_{ab} \quad (5.3)$$

At the two-fluid interface, we can express the viscous dissipation term based on the arithmetic mean; the harmonic mean can be introduced if we need a better precision:

$$\mu \nabla^2 v_a = \sum_{b=1}^N \frac{4\mu_a \mu_b}{\mu_a + \mu_b} \frac{m_b}{\rho_b} v_{ab} \mathcal{F}_{ab} \quad (5.4)$$

Finally, the complete discretization of momentum conservation equation (1.3) can be described as:

$$\begin{aligned} \ddot{u}_a = & - \sum_{b=1}^N \left(\frac{p_b}{\rho_b^2} + \frac{p_a}{\rho_a^2} \right) m_b \nabla_a W_{ab} \\ & + \sum_{b=1}^N \frac{4\mu_a \mu_b}{\mu_a + \mu_b} \frac{m_b}{\rho_b \rho_a} v_{ab} \mathcal{F}_{ab} + \underline{g} + \frac{\check{F}_s}{\rho_a} \end{aligned} \quad (5.5)$$

where \check{F}_s is the surface tension force, that was introduced in section 1.3.1. Its value can be calculated by the introduction of the color function (as shown in Eq. 1.8). Thus, the liquid and gas particles will have their color values of $\check{c}_l = 1$ and $\check{c}_g = -1$, respectively. The SPH discretized expression of the color function can be written as:

$$\check{c}_a = \sum_{b=1}^N \frac{m_b}{\rho_b} \check{c}_b W_{ab} \quad (5.6)$$

where, the unit normal \vec{n} is calculated as:

$$\vec{n}_a = \sum_b \frac{m_b}{\rho_b} (\check{c}_b - \check{c}_a) \nabla_a W_{ab} \quad (5.7)$$

and the discretization of the interface local curvature $\check{\kappa}$ (1.6) is written as:

$$\check{\kappa}_a = \frac{1}{\|\vec{n}_a\|^2} \sum_b \frac{m_b}{\rho_b} (\vec{n}_b \|\vec{n}_a\| - \vec{n}_a \|\vec{n}_b\|) \cdot \nabla_a W_{ab} \quad (5.8)$$

There are several ways to describe the boundary conditions present between different phases in the SPH approach. Combined elastic and fluid models are presented in [4], [12], [120]. The fluid-rigid solid couple can be found in [3], [148]. As a general rule, the velocity of the two different phases at their contact point is supposed to be the same (no-slip condition for viscous fluids), and solid-fluid interface condition is used as

presented by [12] where all types of interacting particles have extended the summation in momentum conservation equations.

5.2 Numerical sample and parameters for drainage simulations

Due to the mezzoscopic pore-scale adopted here, the elastic phase voxels are larger than the Representative Elementary Volume (REV) of the clayey matrix. This assumption allows us to consider it as a homogeneous phase and to disregard all under-size structures visible or not at this scale. Such condition leads to a qualitative analysis of our coupled problem, and it contributes to a better understanding of mechanisms acting at this small scale. In this thesis, we will not attempt the upscaling to the macro scale, even though this is the ultimate aim of this approach.

Our simulation domain is a part of the Callovo-Oxfordian sample EST27405-1 (see in [154]) measuring $5.64 \times 7.96 \times 1.03 \mu\text{m}^3$ with a porosity of 0.0307 ± 0.0039 . As discussed in Sec. 1.3, for this material the most significant part of poral space possesses a few nanometer sizes, which is not large enough to be observed by FIB imaging with a resolution of about 10nm . Therefore, at this scale, only a part of the total porosity is visible with many connections missing, which leads to the observation of mainly disconnected pores. The reconstruction of the percolating poral network from [126] shows several disjoint pores that connect opposite sides of the sample (Fig. 5.2). This set of percolating

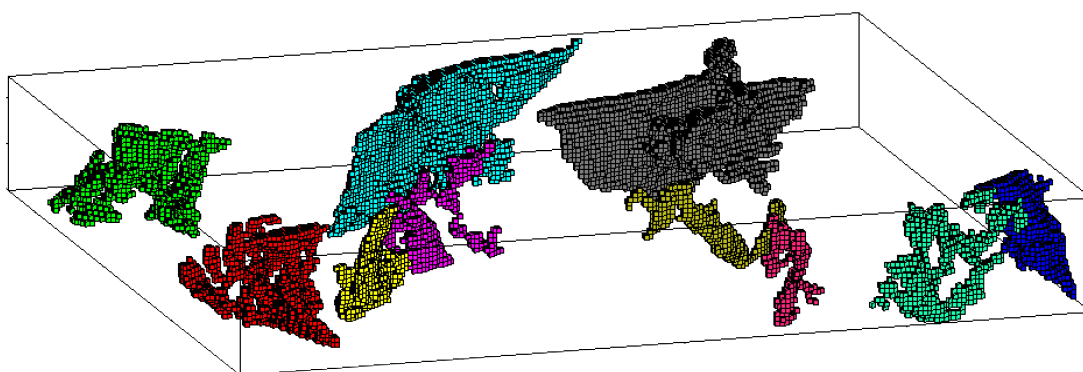


Fig. 5.2.: A total set of percolating pores in a Callovo-Oxfordian clay sample after [126].

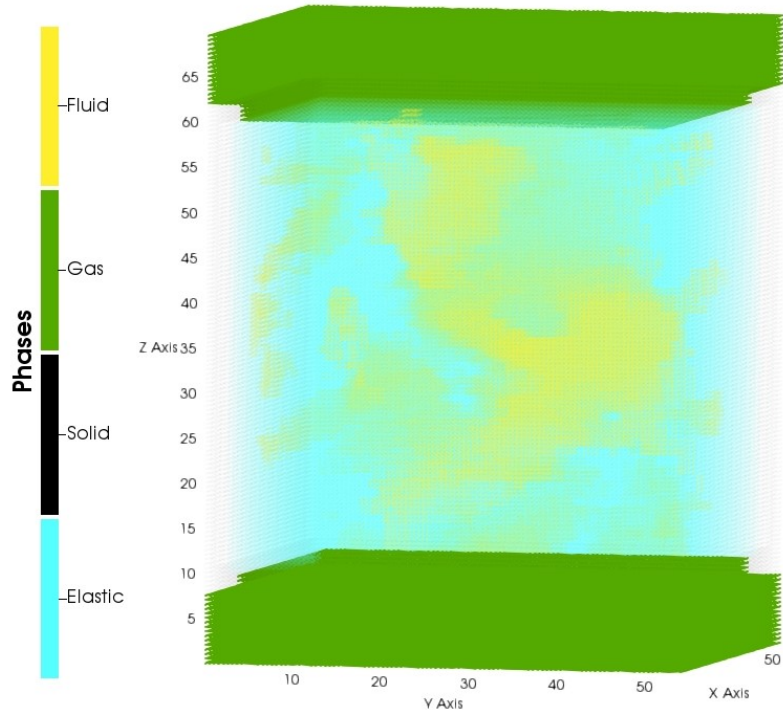
pores is converted in a numerical sample of resolution $8.49 \times 10.78 \times 10\text{nm}^3$ per voxel resulting in a 3D sample of $771 \times 739 \times 103$ voxels. This configuration presents more than 58 million of voxels and is much too big for the actual memory limitations. Thus, to reduce the size and the simulation time, a coarsening of the original sample is adopted reducing the sample to $1/8$ of the original volume (*i.e.* $385 \times 369 \times 51$ voxels). Besides,

the phase identification is set to segment only two different phases: solids and pores. It means that, in this approach, the clay matrix and the rigid inclusions are considered parts of one REV.

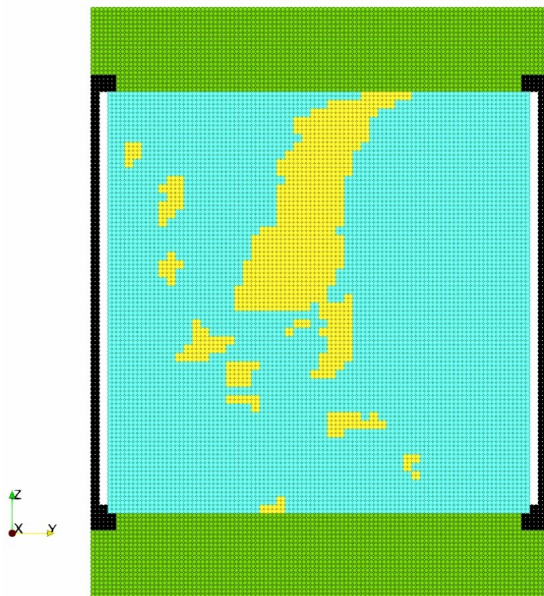
In Pazdniakou and Dymitrowska [126], the authors have simulated different sample boundary conditions, such as constant or free volume, confining stress or non-confining stress applied. Considering the in-situ conditions for Callovo-Oxfordian resumed in Chap. 1, we select the most appropriate configuration with imposed constant confining stress.

To further reduce memory usage and calculation time we limit our study domain to a sub-sample of Fig. 5.2 with one percolating pore (the blue one at the bottom-right corner) with its surrounding disconnected pores. This sub-sample has a new dimension of $50h \times 50h \times 50h$ that is now related to the SPH h -scale length being taken here $h = 20nm$. Of course, as stated in Pazdniakou and Dymitrowska [126], such sample is not a REV, and thus the drainage simulation results for it or for any other sub-sample can not be generalised to bigger scales because of different shapes of pores. The 3D configuration of the studied sample is presented in Fig. 5.3a. The clayey matrix is assimilated to an elastic material (blue material points). The pore space is initially water-saturated (yellow colour) and, on the top and bottom sides, two gas reservoirs (green colour) containing enough particles to fill the entire pore space are disposed. In order to apply the confining stress and allow the volume changes, the sample is placed between fixed solid walls (black colour) except for the z-top and z-bottom borders. These borders are composed of rigid plates. A yz-cut at $x = 27h$ and a xy-cut at $z = 45h$ are respectively illustrated in Fig. 5.3b and Fig. 5.3c. A set of different pores types is visible here: around the principal percolating pore, several medium and small-sized isolated pores are present. Finally, by applying a fixed pressure drop between both gas reservoirs, we create multiphase flow conditions.

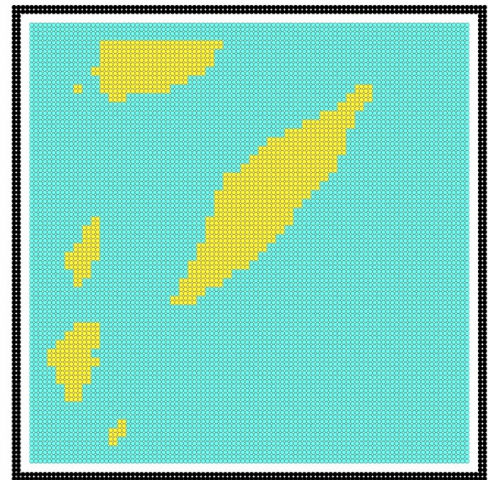
Silva *et al.* [150] studied in a numerical framework the influence of the confinement stress on the capillary pressure during immiscible multiphase flow in a rough fracture. They highlighted that the power spectral density of the capillary pressure could be adopted to qualitatively characterise the heterogeneity of a fracture. The simulations conducted in Pazdniakou and Dymitrowska [126], though very preliminary, were able to reproduce the expected effect of the confining stresses. They showed that the increase of confining stress leads to an increase of percolation time and a decrease of the gas saturation in the same simulation. With lower confining stresses, the pore-space is allowed to dilate more, which increases percolating gas flow. In our model, such pore-space dilation can be reversible (with purely elastic response) or irreversible (with the elasto-damage model). The influence of the confining stress on drainage will be discussed in more details in the next sections.



(a) 3D numerical sub-sample



(b) yz cross-section at $x = 27h$

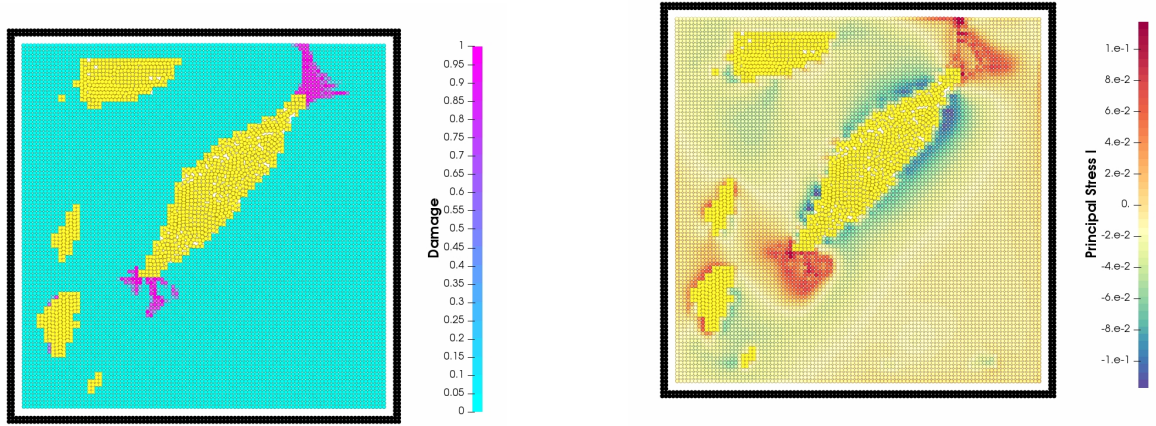


(c) xy cross-section at $z = 45h$

Fig. 5.3.: 3D and orthogonal cuts of the numerical sub-sample containing elastic, water and hydrogen phases.

First of all, we reproduce results from [126] to further validate our code and provide a fully appropriate reference case. We use the same sub-sample from [126]. The elasto-damage behaviour of the clayey matrix is defined by a mixed Rankine (tensile) and Mohr-Coulomb (compression and shear) damage criteria a reversible damage (which is not the case for the present study). All the physical and numerical parameters are taken from [126] and will be recalled and discussed later in this chapter. We present the sample

cross-sections at $t = 4s$ after the onset of drainage for damage (Fig. 5.4a: blue for sound and pink for completely damaged material points) and first principal stress (Fig. 5.4b: blue for compression and red for traction loads). We observe a damage apparition around tips of the pore-space. This observation corresponds well to the experimental evidences of damage initiation (see for instance Wiseall *et al.* [165]). However, the damaged zone is too diffuse and not adapted to capture a localised crack propagation.



(a) Damage field: xy cross-section at $z = 45h$ (b) Maximum principal stress field: xy-cut at $z = 45h$

Fig. 5.4.: Damage (a) and maximum principal stress field (b) in COx sample during drainage with Rankine and Mohr-Coulomb damage model at $t = 4s$.

In the rest of this chapter, we will treat the clay matrix response by adopting a thermodynamics-based damage model with unilateral-effects (as presented in Chap. 4) in order to improve the damage localisation and to better represent the propagation of fractures. Hence, inspired in Ponte-Castaneda and Willis based damage model (PCW) [40], we consider here uniform degradation functions of the shear and bulk modulus, such as:

$$\frac{k(D)}{k_0} = \frac{\mu(D)}{\mu_0} = \frac{1 - \hat{\alpha}D}{1 + \hat{\beta}D} \quad (4.21 \text{ revisited})$$

with $\hat{\alpha}$ and $\hat{\beta}$ constant parameters allowing to define the damage functions $k(D)$ and $\mu(D)$, such as:

$$\begin{cases} \hat{\alpha} = 1 \\ \hat{\beta} = \frac{\epsilon_u}{\epsilon_0} - 1 \end{cases} \quad (5.9)$$

in which the critical damage energy release (after Eq. 4.22) reads:

$$\mathcal{Y}_c = \mathcal{Y}_c^0 \quad (5.10)$$

For the sake of conciseness, we present in Appendix B the complementary validations of PCW damage model in order to use such model to predict damage and rupture occurrence in the present clay matrix application.

Let's now present the physical and numerical parameters used for our drainage simulations. In Tab. 5.1 we recall the COx clay properties as proposed by [126] after [7], [8]. However, the adoption of the strict real values from Tab. 5.1 would induce a

Parameter	Symbol	Value	Unity
Young modulus	E	3	GPa
Poisson ratio	ν	0.1	—
Tensile strength	f_t	4	MPa
Uniaxial compressive strength	f_c	20	MPa
Strain at elastic limit	ε_{t0}	0.0013	—
Ultimate tensile strain	ε_{tu}	0.0026	—
Compressive strain at elastic limit	ε_{c0}	0.015	—
Internal friction angle	ϕ	25	$^\circ$

Tab. 5.1.: Expected COx properties after [126].

calculation cost not yet available in our existing calculation means, especially due to the explicit time integration schema presented in Sec. 2.2.3 that imposes the CFL condition that would limit the time step to about $10^{-12}s$ (which is highly prohibitive). We will base our modelling on the fact that the behaviour of the multiphase flow in porous media can be described by some dimensionless numbers (see for instance [92]). That is why we will adapt the simulation parameters in such a way to both respect the physical flow regimes defined by the dimensionless numbers [74] and to easy the simulations. For the sake of completeness, we recall bellow these dimensionless number for original physical parameters and those retained for simulations. These simulation dimensionless numbers were obtained with the following fluid-gas parameters (Tab. 5.2), that we retain for the present simulations. The Bond number (Bo) measures the importance of interfacial forces

Parameter	Symbol	Value	Unity
Liquid dynamic viscosity	μ_l	10^{-7}	$Pa \cdot s$
Gas dynamic viscosity	μ_g	10^{-9}	$Pa \cdot s$
Mean gas velocity	v_g	$5 \cdot 10^{-5}$	m/s
Surface tension coefficient	$\check{\gamma}$	$4 \cdot 10^{-10}$	N/m
Average pore size	L	$\sim 1 \cdot 10^{-6}$	m

Tab. 5.2.: Simulation input parameters for fluids adopted in this work following [126].

with respect to external forces (like gravity); it also describes the shape of bubbles:

$$Bo = \frac{(\rho_l - \rho_g) \cdot g \cdot L^2}{\check{\gamma}} \quad (5.11a)$$

$$\text{Bo}_{exp} = 4.7 \cdot 10^{-6} \ll 1 \quad (5.11b)$$

$$\text{Bo}_{sim} = 0 \ll 1 \quad (5.11c)$$

where the subscripts l and g relate, respectively, to liquid and gas phases, ρ is the density, g is the gravitational acceleration and L is a characteristic length which is usually the pore size. The capillary number (Ca) represents the ratio between the viscous drag forces and the surface tension forces at a liquid-gas interface:

$$\text{Ca} = \frac{\mu_g \cdot v_g}{\check{\gamma}} \quad (5.12a)$$

$$\text{Ca}_{phy} = 7.2 \cdot 10^{-10} \ll 1 \quad (5.12b)$$

$$\text{Ca}_{sim} \approx 1.25 \cdot 10^{-4} \ll 1 \quad (5.12c)$$

with μ the dynamic viscosity and $\check{\gamma}$ the coefficient of surface tension. The mobility M is the ratio of the viscous forces of the invading liquid (gas) with respect to the receding one (liquid) [74]:

$$M = \frac{\mu_g}{\mu_l} \quad (5.13a)$$

$$M_{phy} = 1 \cdot 10^{-2} \ll 1 \quad (5.13b)$$

$$M_{sim} = 1 \cdot 10^{-2} \ll 1 \quad (5.13c)$$

Finally, the Reynolds number is the ratio of inertial forces to viscous forces:

$$\text{Re} = \frac{\rho_g \cdot v_g \cdot L}{\mu_g} \quad (5.14a)$$

$$\text{Re}_{phy} = 4 \cdot 10^{-5} \ll 1 \quad (5.14b)$$

$$\text{Re}_{sim} \approx 5 \cdot 10^{-1} \quad (5.14c)$$

where v is the characteristic velocity. According to [126], the changes in magnitude orders between the physical and the simulation values of Bo and Re do not change the flow regime. Henceforth, with respect to the boundary conditions in Fig. 5.3, the complete sub-sample has dimensions of $54h \times 54h \times 70h$; the top and bottom gas reservoirs are connected by periodic boundary conditions along the z -axis and have height of $H_r = 10h$ each. The percolation phenomenon is created due to a pressure gradient imposed between these gas reservoirs by means of a body force F_z applied to every gas material point in reservoirs ($z < 10h$ or $z > 60h$). The sound velocities in both fluids are taken equal to $c_s = 0.5m/s$. Indeed, this quantity must be small enough not to decrease too much the

maximal time steps, leading to long simulation times. In the same time, c_s is must be high enough to prevent important density variations.

After parameterize fluid phases, we need to do the same for solid-phase in connection with mechanical loads applied to the system. The gas entry pressure expected for COx found in the literature is about $10MPa$ and the vertical confinement is of about $12MPa$ [169]. Here, we consider a slightly higher gas pressure of $\Delta P_g = 15MPa$ in order to expose the COx sample to a load for which fracturing would be possible. This choice is also interesting to accelerate drainage and therefore reduce the simulation time. In the same way, we propose a scaling factor of 2×10^{-8} between physical and simulation parameters by maintaining a constant ratio between the gas pressure ΔP_g and the clay matrix elastic response (represented by Young modulus E). These rescaled properties are presented in Tab. 5.3. The different confining stresses σ_{conf} simulated are also rescaled in the same way. In addition, the simulation time and the sample dimensions are scaled by 10^{-4} . For all drainage simulations, we use Cuda GPU parallelisation in order to reduce computing time substantively. In the next sections, we present drainage

Parameter	Physical	Simulation	Unity
E	3×10^9	60	Pa
f_t	4×10^6	8×10^{-2}	Pa
f_c	20×10^6	4×10^{-1}	Pa
ΔP_g	15×10^6	3×10^{-1}	Pa

Tab. 5.3.: Physical and simulation mechanical parameters for drainage simulations.

simulations results with all the improvements introduced in previous chapters for elastic and elasto-damage materials through a displacement-based infinitesimal version of our non-local SPH solver. We seek to better describe the three fundamental phenomena for the multiphase flow coupled to solid damaged at a pore scale. First, a non-damageable version of the present sub-sample (Fig. 5.3) is used in order to discuss the elastic responses in terms of stress localisation that are a necessary step towards the second part: the damage characterisation and the transition between damage and fracturing.

5.3 Drainage with purely elastic clay matrix

In this section, we present drainage simulations with an exclusively elastic response of the clayey matrix. For these simulations, a gas pressure drop of $\Delta P_g = 15MPa$ is applied between the two gas reservoirs and a confining stress $\sigma_{conf} = 8MPa$ is applied to the lateral sides of the sample. Pazdniakou and Dymitrowska [126] observed in their work that the adoption of the elastic response of the solid material (instead of a rigid one) leads to a faster percolation, in relation with the expected pore-space dilation. Such

a dilation can also be measured by the porosity evolution or, in a less evident manner, by the gas saturation inside the pore-space. The pressurised gas phase pushes the liquid phase towards the bottom of the sample until a complete percolation (when the top and the bottom reservoirs have a continuum gas-phase connection through the pore-space). Fig. 5.5 present a 3D view of the water-saturated pore space being percolated by the gas phase at three different moments. The water (yellow) and the clay matrix (blue) have reduced colour opacities in order to highlight the evolution of the gas phase.

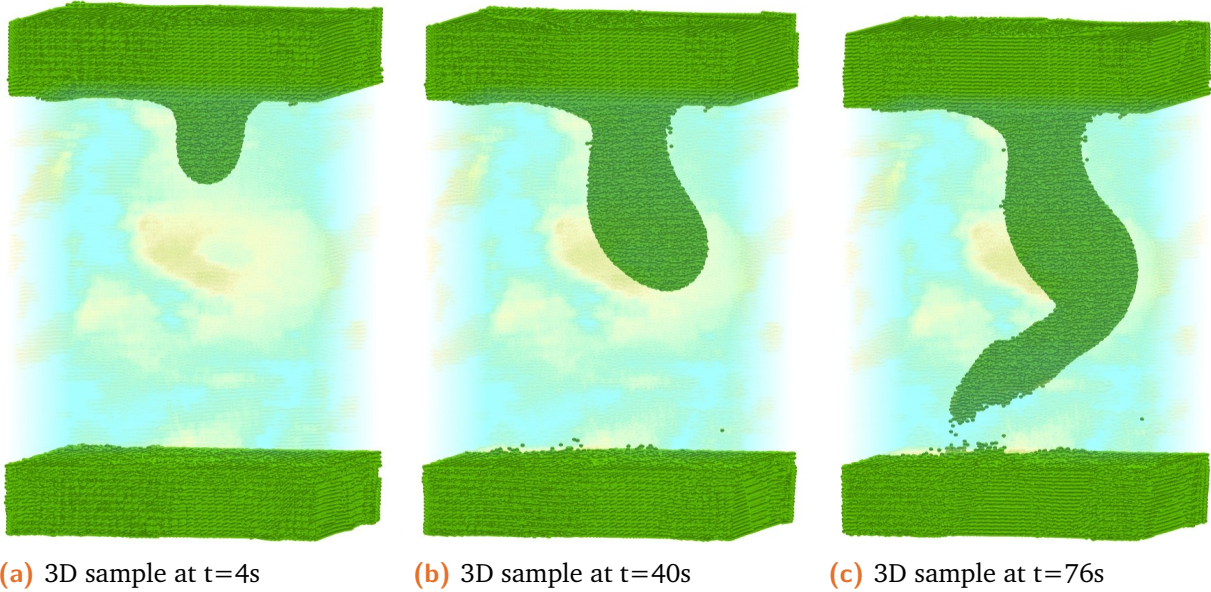
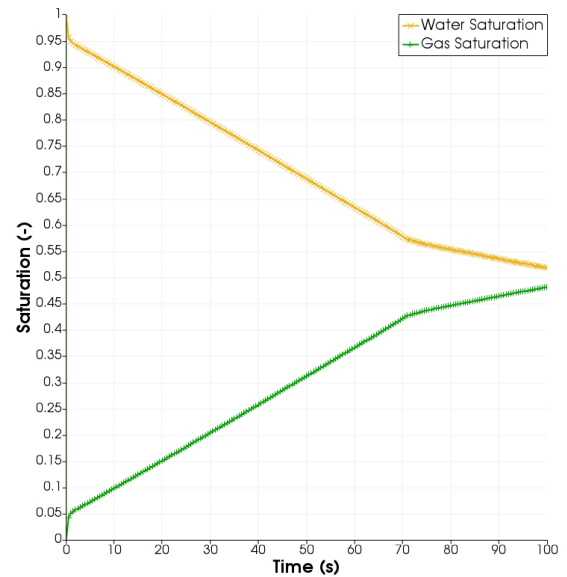
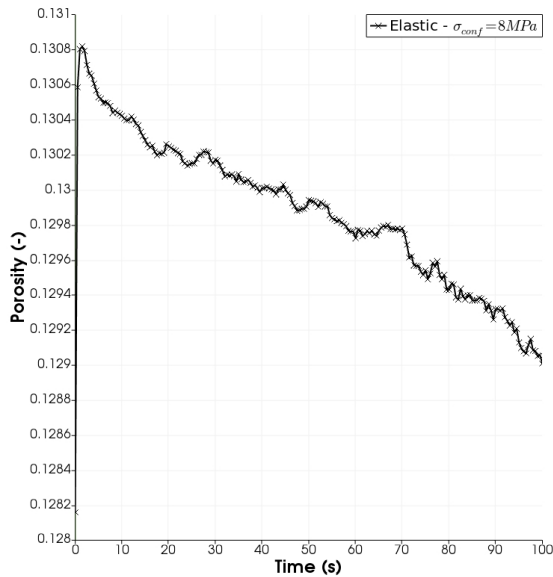


Fig. 5.5.: Elastic matrix: drainage under $\sigma_{conf} = 8MPa$. 3D view of solid and fluid phases.

In this drainage phenomenon through a purely elastic clayey matrix, we note that the main pore has a complex morphology with different section diameters. Between the first (Fig. 5.5a) and the last (Fig. 5.5c) percolation instants the gas phase fills the pore space as represented by increasing gas saturation and consequently decreasing water saturation in Fig. 5.6b with a quasi-linear slope until the percolation at respectively, 0.43 and 0.67. From this point, the gas-water saturation evolves with the same increasing-decreasing behaviour but with much less important slopes. The porosity (Fig. 5.6a) instantly jumps from the initial value of 0.128 at the beginning of drainage to 0.131. This rapid jump is followed by a slow reduction all over the drainage lasting beyond the percolation moment. This observation is to be compared with experiments from Wiseall *et al.* [165], where authors concluded that pathways begin to close once the gas breakthrough occurs.



(a) Porosity evolution.

(b) Water and gas saturation evolution.

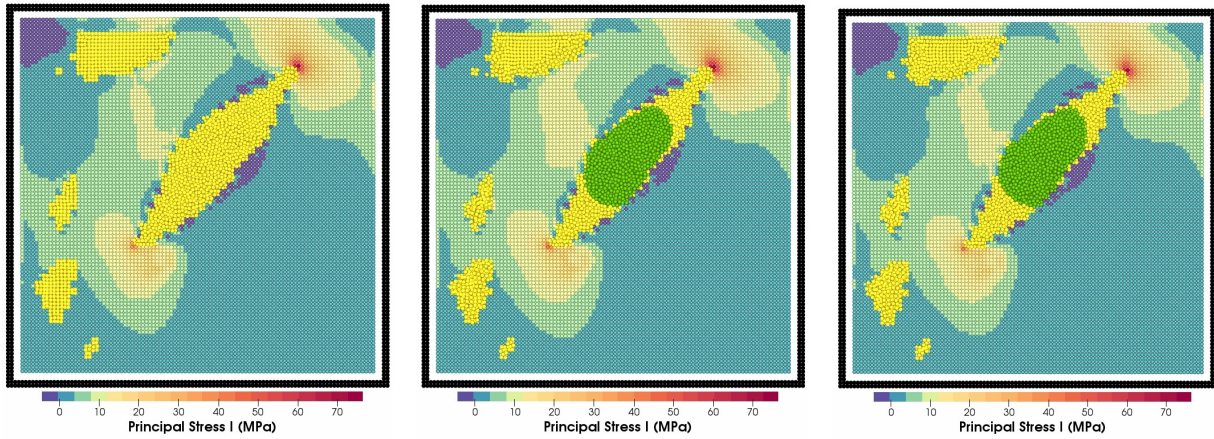
Fig. 5.6.: Elastic matrix: Porosity and saturation evolution during drainage under $\sigma_{conf} = 8MPa$.

In agreement with the porosity evolution, we observe a quick installation of the maximum principal stress field (Fig. 5.7a, Fig. 5.7b and Fig. 5.7c) that evolves only slightly during drainage. High values of tensile stress are located at the pore tips corresponding to a traction zone. Beside that, the rest of the solid material does not present important stresses. In the same way, we observe only a slow evolution of the x-displacement field, that is illustrated in Fig. 5.7d, Fig. 5.7e and Fig. 5.7f. A quite similar distribution is found during all drainage with a maxima and minima values at the lateral borders of the main pore well illustrating the pore-space dilation.

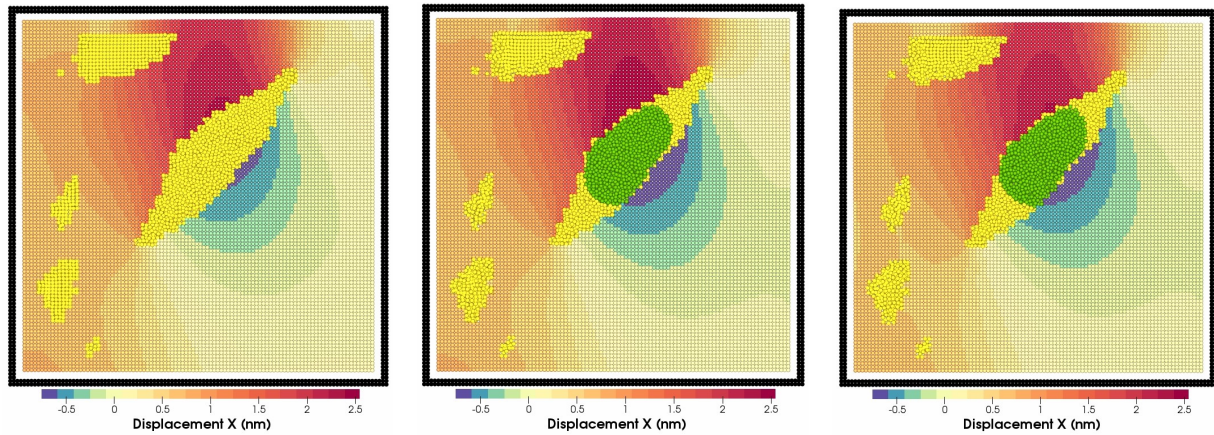
It will be important for the next section and should be retained from Fig. 5.6 and Fig. 5.7 that the maximal and minimal loads in this framework happen at the beginning of the drainage when the gas invasion onsets. In the following sections, the elasto-damage response for the clay matrix will be investigated in order to describe how the damage and fracturing can be initiated and developed by the model itself (as shown in Sec. 4.3).

5.4 Drainage with elasto-damage clay matrix

In this section, drainage simulations are performed by setting an elasto-damageable response of the clayey matrix. We keep the same elastic/damage properties for the clay matrix for all simulations here and the applied pressure drop of $\Delta P_g = 15MPa$. The only parameter that will be varied is the confining stress σ_{conf} , which is expected to impact the sample behaviour significantly. Thus the simulations at two different confining stresses will verify if our model can represent such physical dependency.



(a) Maximum principal stress field at $t=4s$ (b) Maximum principal stress field at $t=40s$ (c) Maximum principal stress field at $t=76s$



(d) Maximum principal stress field at $t=4s$ (e) Maximum principal stress field at $t=40s$ (f) Maximum principal stress field at $t=76s$

(a-c) watch the video (d-f) watch the video

Fig. 5.7.: Elastic matrix: drainage under $\sigma_{conf} = 8MPa$. Maximum principal stress (a, b and c) and x-displacement fields (d, e and f) on a xy cross-section at $z = 45h$.

5.4.1 Confining stress of $\sigma_{conf}=8 MPa$

In this configuration, a confining stress of $8MPa$ is applied to the lateral borders of the numerical sample. Fig. 5.8 shows a 3D drainage evolution of the water-saturated pore space being invaded by the gas at three subsequent times. The overall picture turns out to be qualitatively similar to the purely elastic case presented in Fig. 5.5.

However, we observe several quantitative differences between the two cases when we compare the evolution of porosity in Fig. 5.9a and of water and gas saturation in Fig. 5.9b. Despite similar percolation times, the gas saturation reaches here 0.47 at that moment, which means an increase of 5% compared to the purely elastic matrix. However,

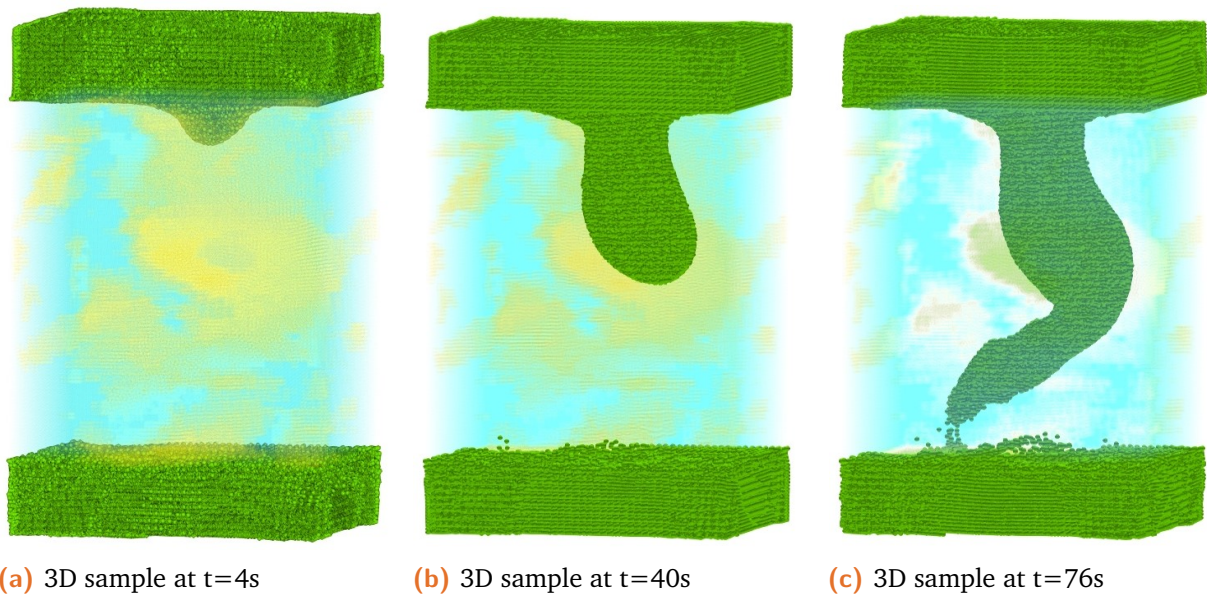
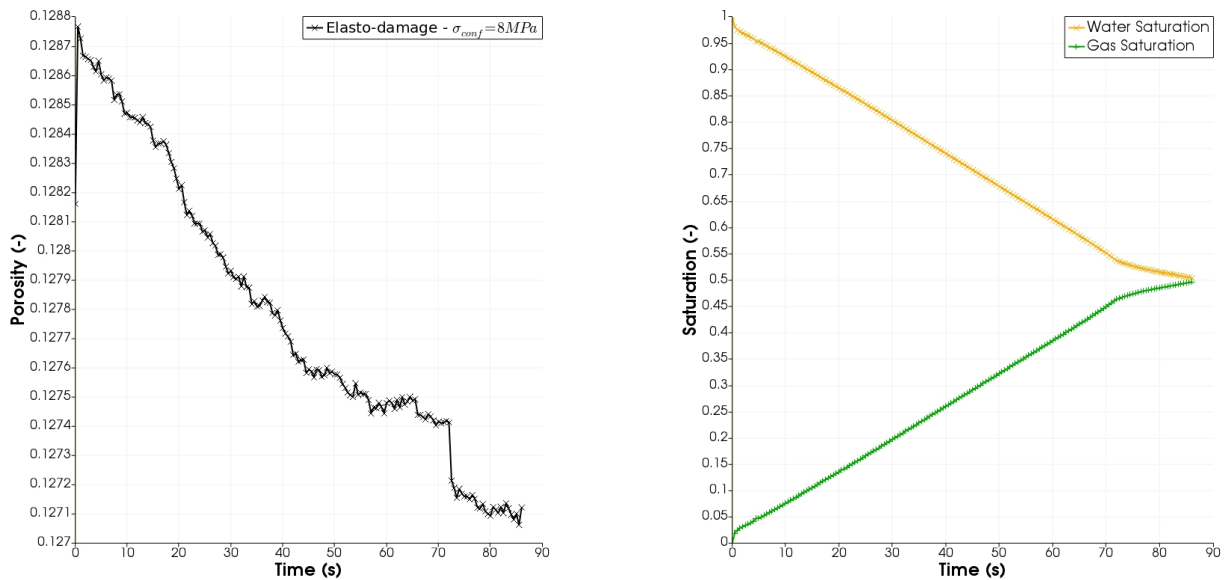


Fig. 5.8.: Drainage under $\sigma_{conf} = 8MPa$ in elasto-damage clay matrix. 3D view of solid and fluid phases.

the porosity evolution in Fig. 5.9a presents a maximal value of 0.128, which is less than the value obtained in the purely elastic matrix case. The percolation moment is visible on the porosity curve with a negative jump, which was not the case before.



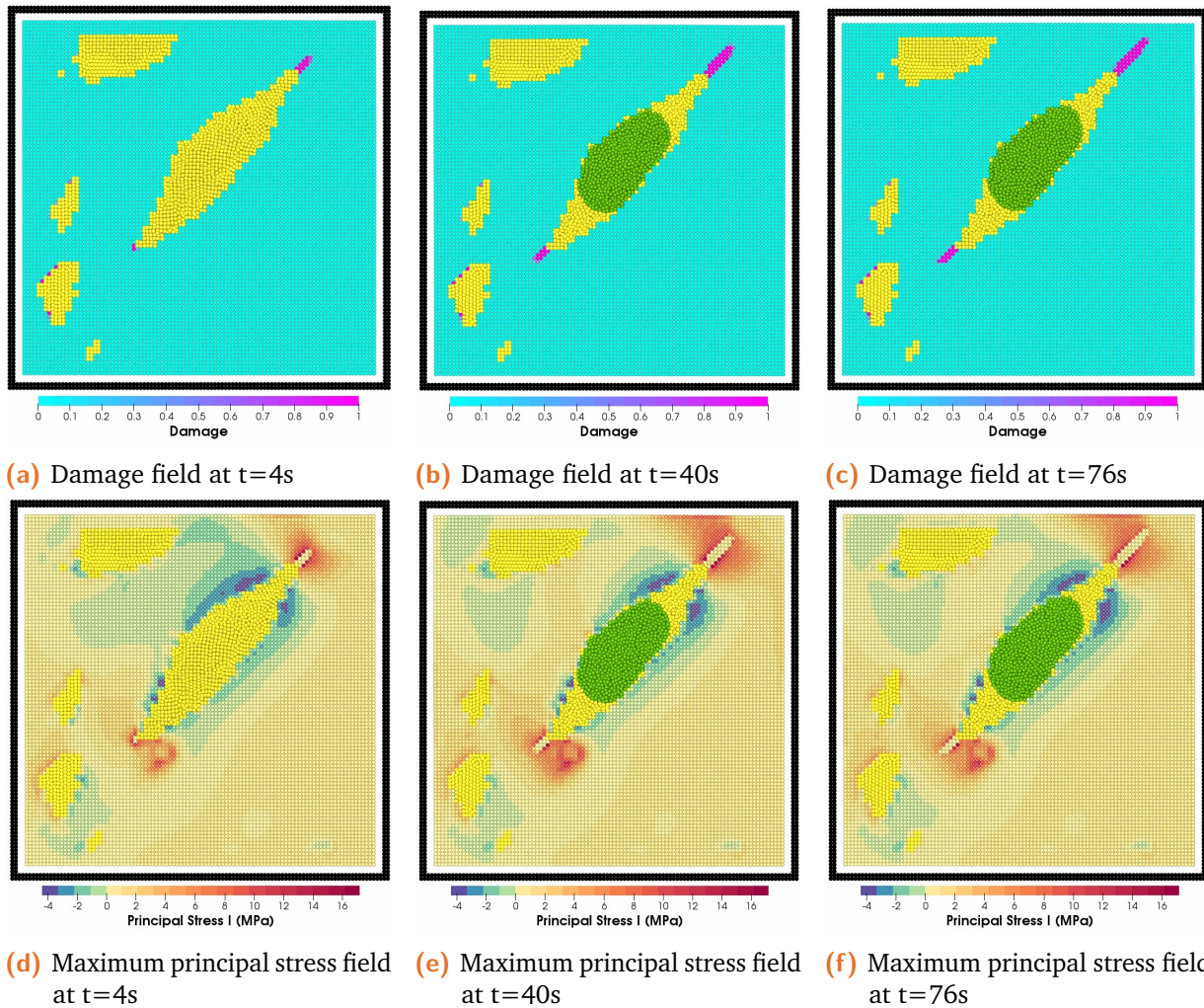
(a) Porosity evolution.

(b) Water and gas saturation evolution.

Fig. 5.9.: Elasto-damage matrix: porosity and saturation for drainage under $\sigma_{conf}=8$ MPa.

In the clay matrix elasto-damage stress and damage fields from Fig. 5.10, we see for the first time the initiation of the damage in Fig. 5.10a at the pore-space tips (as

expected from the results of purely elastic matrix). At the following times, we observe that the evolving drainage leads to the propagation of localised damage zones parallel to the principal pore axis, which may be considered precursors of crack initiation. The first principal stress fields presented in Fig. 5.10d - Fig. 5.10f illustrate a low level of stresses everywhere except for the pore-space tips zones, where the damage is localised. But even in these zones, the maximal values of stress are much lower than in the purely elastic case.



(a-c) watch the video

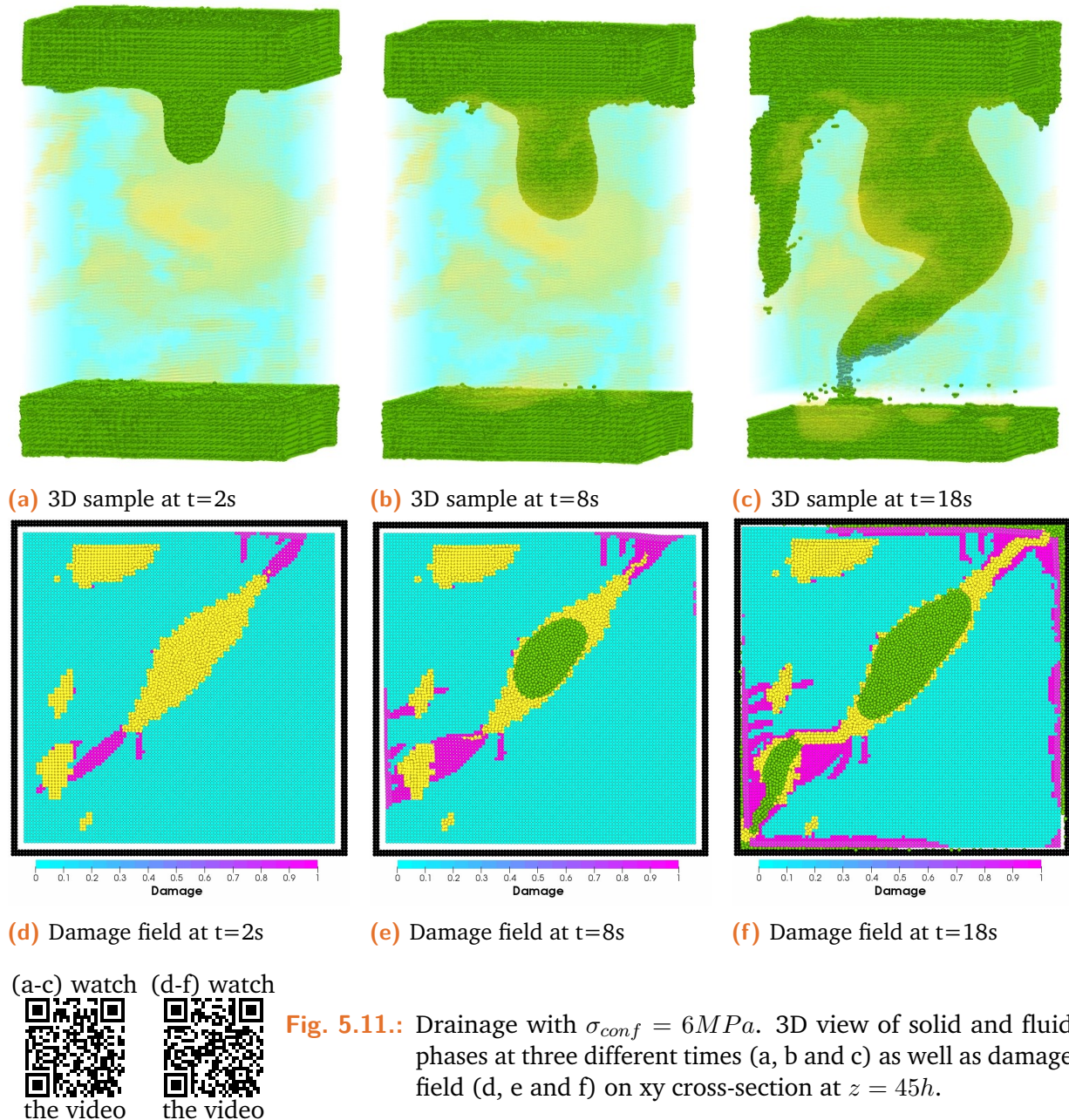
(d-f) watch the video

Fig. 5.10.: Drainage under $\sigma_{conf} = 8MPa$. Damage (a, b and c) and maximum principal stress fields (d, e, and f) on xy cross-section at $z = 45h$.

5.4.2 Confining stress of $\sigma_{conf}=6 MPa$

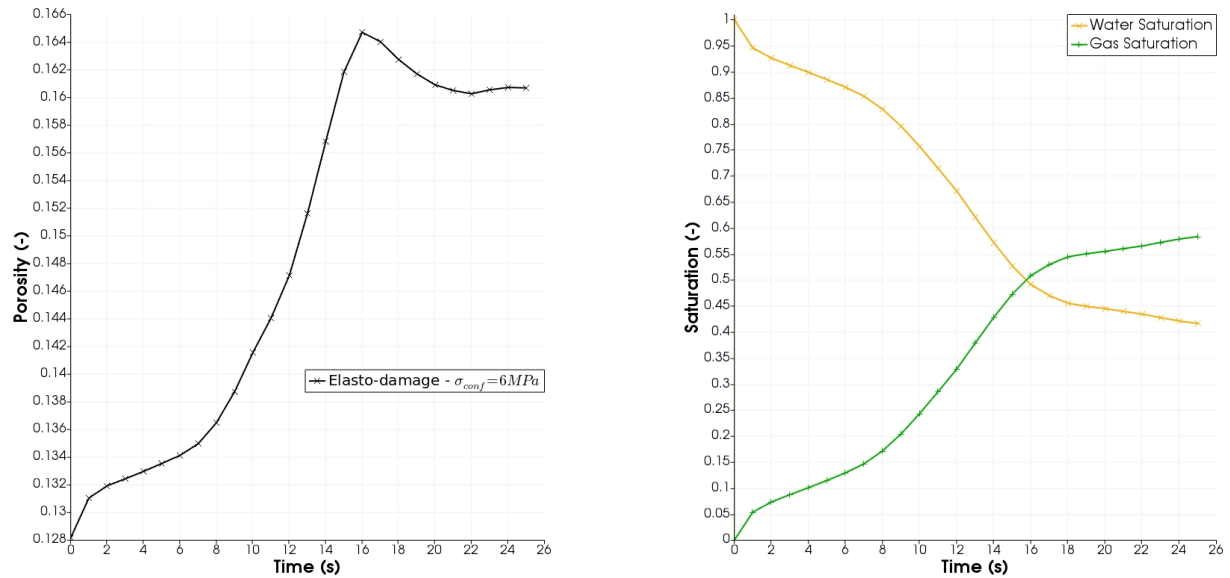
We reduce now the confining stress applied to lateral sides of the sample from $\sigma_{conf}=8 MPa$ to $\sigma_{conf}=6 MPa$ while maintaining all the other parameters identical to

the previous simulation. The overall drainage evolution presented in a 3D view in Fig. 5.11 shows that a lower confining stress leads to an entirely different flow behaviour with more dilation of pore-space and creation of new pathways. Also, we observe that the percolation time is here about 4 times shorter than in previous configurations with $\sigma_{conf} = 8$ MPa.



In Fig. 5.11d we observe that the load caused by the gas invasion is strong enough to create two main damage localisation zones towards the sample boundary on the top-right side and towards an isolated pore on the bottom-left side. At the next time instant (Fig. 5.11e), we see that a few water material points start to propagate through damaged zones at both sides. This can be interpreted as the creation of new pores or

cracks within the damaged zones, which was not observed in our previous simulations. Finally, at percolation time Fig. 5.11f, the main pore is completely connected by a new pore-space to the isolated pore. There is also a new gas flow path taking place in the new pore-space. However, due to the limited size of our numerical sample, we observe many interactions with sample boundaries, which must be considered numerical artefacts.



(a) Porosity evolution.

(b) Water and gas saturation evolution.

Fig. 5.12.: Elasto-damage matrix: Porosity and saturation for drainage under $\sigma_{conf} = 6MPa$.

The most spectacular quantitative difference concerning the case of $\sigma_{conf} = 8MPa$ is related to the porosity evolution presented in Fig. 5.12a. A constant increase of the porosity is observed from the initial value (12.8%) until the maximum porosity value (16.5%) when the gas reaches the bottom gas reservoir. This result is, of course, related to the creation of new pore-space with large fracturing phenomena. This also results in a much faster percolation time. Finally, the gas saturation increases quicker and reaches the end of the simulation almost 60% (see Fig. 5.12b).

The fracturing phenomena are also well visible in the first principal stress and displacement fields, as presented in Fig. 5.13. The stress field shows similar maximal values as in the elasto-damage case with $\sigma_{conf} = 8MPa$. It should be noted that the average stress values are particularly lower after the cracks occurrence (see in Fig. 5.13c when the sample appears to be split into two parts). Similarly, the x-displacement field in Fig. 5.13f contains two zones with values of opposite signs, confirming the apparent loss of interaction between these two parts of the sample.

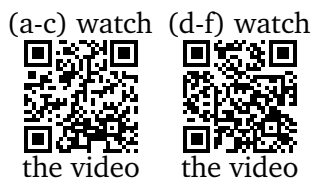
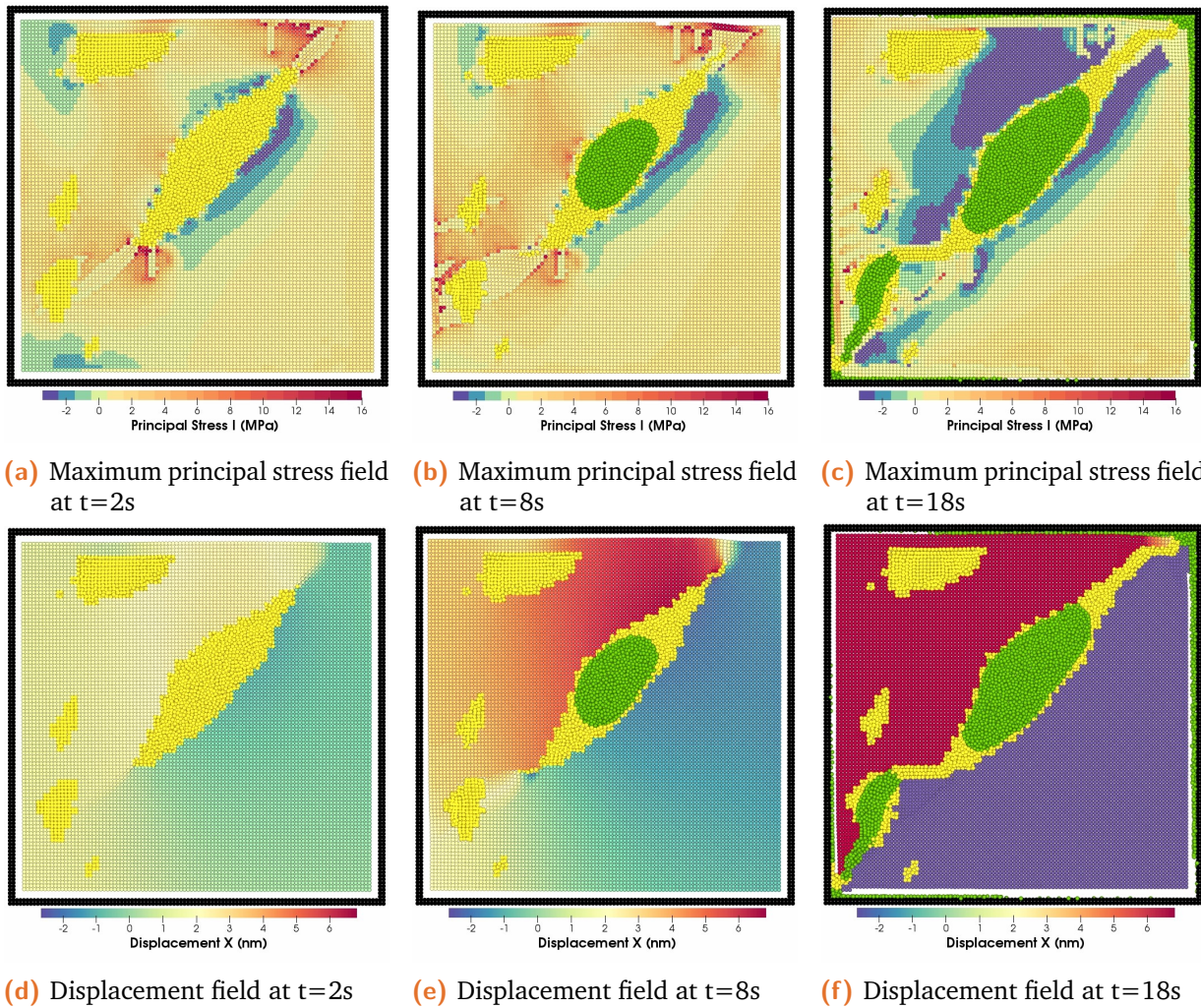
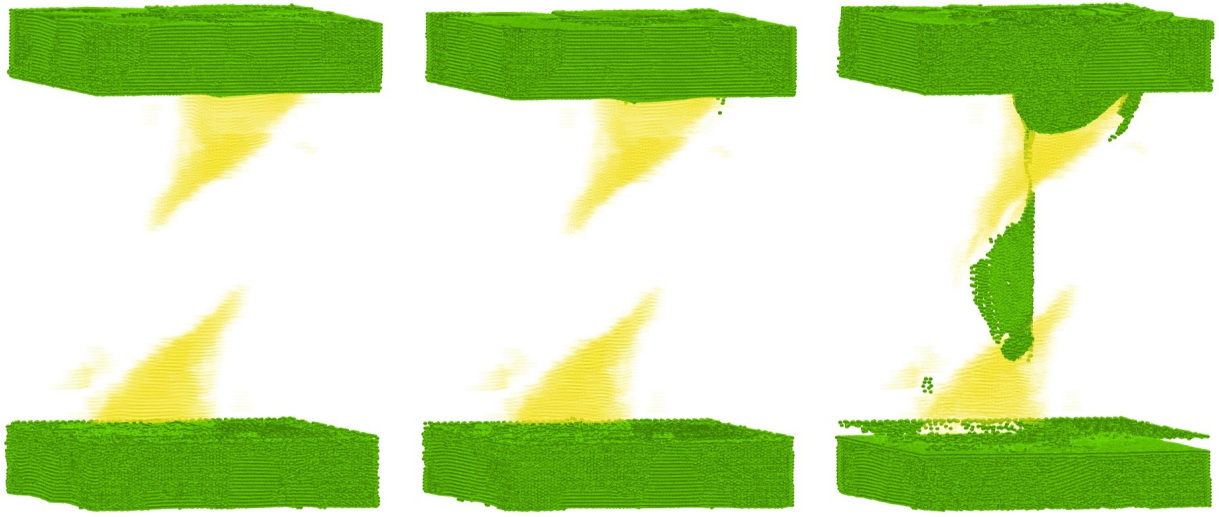


Fig. 5.13.: Drainage at $\sigma_{conf} = 6MPa$. Maximum principal stress (a, b and c) and x-displacement fields (d, e and f) on xy cross-section at $z = 45h$.

5.5 Drainage of a sample with disconnected pores

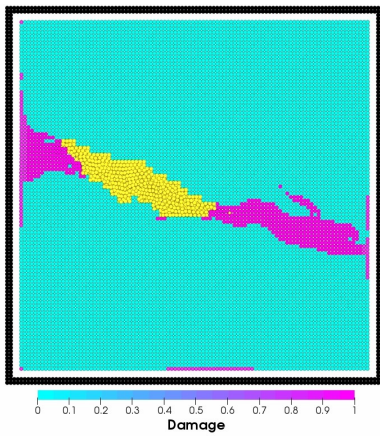
In this last section, we study a manually modified sample with two disconnected pores. Indeed, since our model has proved to be able to create new pore-space, the question we want to answer now is the possibility to generate a percolating path in initially non-percolating samples. We remain here the exact properties, parameters and confining stress adopted in the previous section 5.4.2. Such a numerical sample was created to maintain the pore-space morphology (by reflecting and flipping the bottom part of the pore space presented in previous sections).



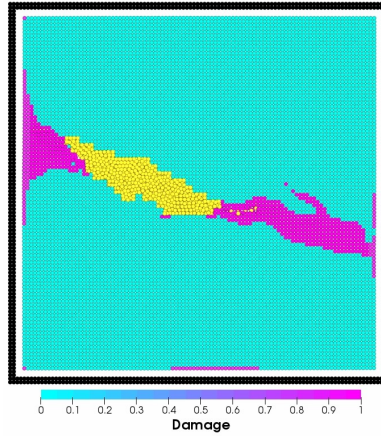
(a) 3D sample at t=1s

(b) 3D sample at t=20s

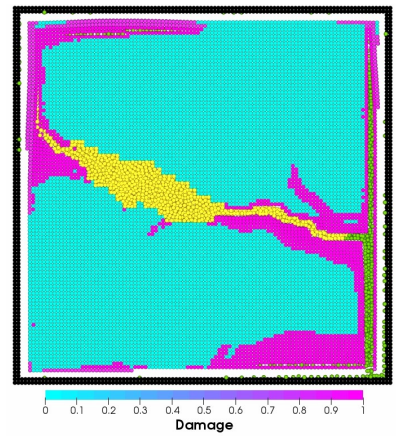
(c) 3D sample at t=50s



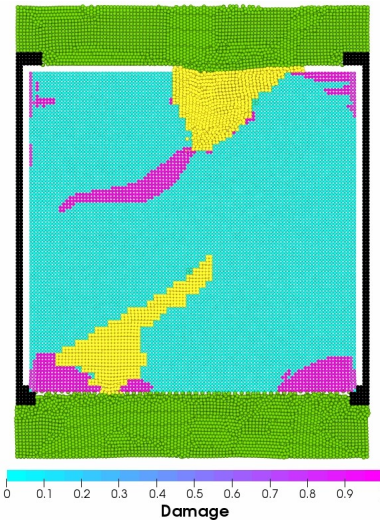
(d) Damage field at t=1s



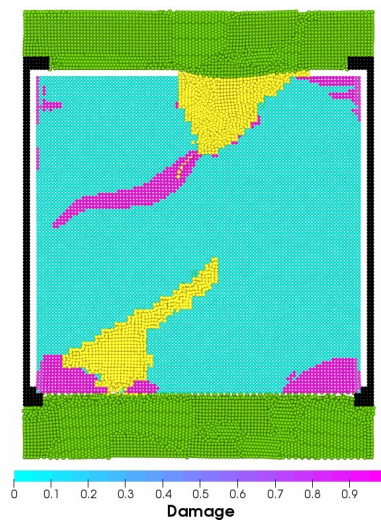
(e) Damage field at t=20s



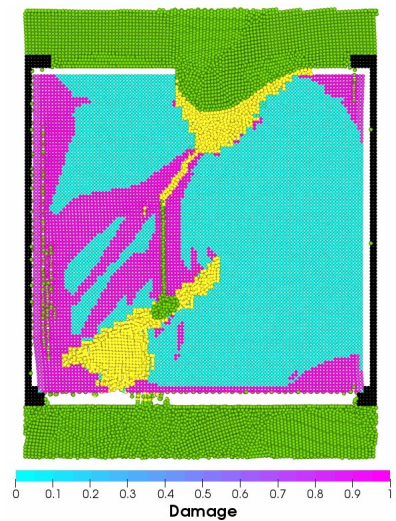
(f) Damage field at t=50s



(g) Damage field at t=1s



(h) Damage field at t=20s

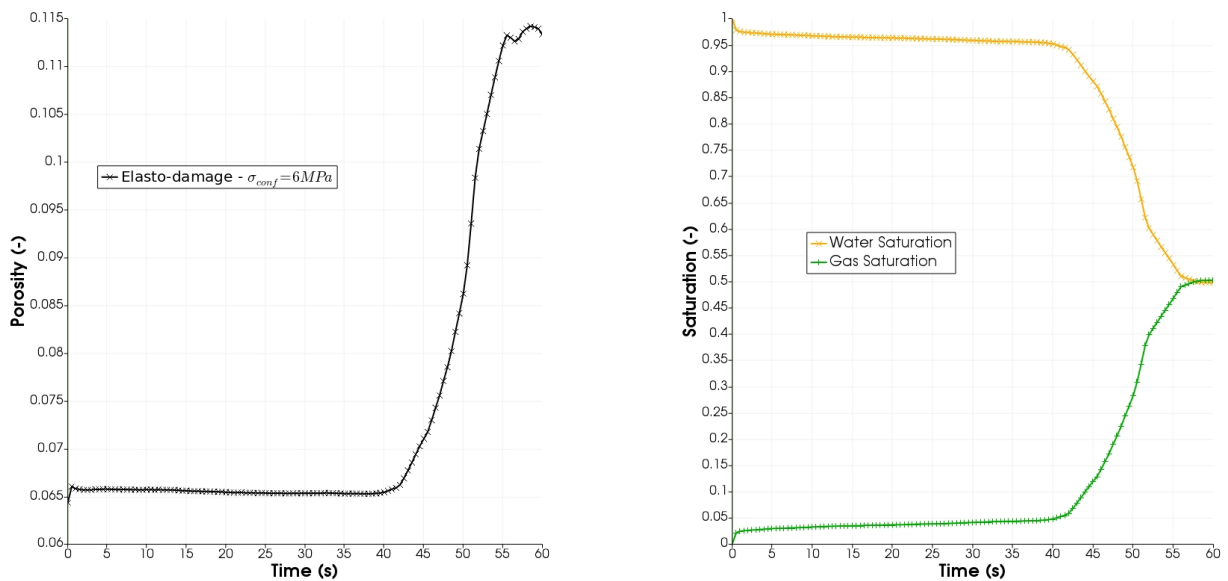


(i) Damage field at t=50s

(a-c) watch the video  (g-i) watch the video 

Fig. 5.14.: Fracturing between isolated pores under $\sigma_{conf} = 6MPa$. 3D view of fluid phases (a, b and c). Solid and fluid phases and damage field through xy cross-section at $z = 45h$ (d, e and f) and xz cross-section at $y = 17h$ (g, h and i).

In Fig. 5.14 we see at the sub-sample centre, the two-pore tips turned to different sides of the sample in order to avoid an easily predictable pathway. The elastic phase in this 3D view is transparent to highlight the geometry of pores and the evolution of the water-gas phases. For the first presented time $t = 1s$, we can look at the evolution of drainage in the 3D view (Fig. 5.14a), on a xy -cut at $z = 45h$ (Fig. 5.14d) and on a 30° inclined xz -cut at $y = 17h$. The initial load caused by the gas invasion is high enough to rapidly damage and propagate cracks that reach the lateral sides around the upper pore. Another important crack is observed in a diagonal direction following the upper pore-space tip. At time $t = 20s$, the 3D view (Fig. 5.14b) does not show yet an important gas intrusion. However, the horizontal and diagonal cross-sections highlight small intrusions of the water phase through the damaged (and fractured) paths. Finally, at $t = 50s$, a vertical fracture (possibly related the ordered material points) is created linking directly the so far isolated pore-spaces. Thus, in this new configuration, we observe that a new percolating pore is generated. In this different sample morphology, the porosity



(a) Porosity evolution.

(b) Water and gas saturation evolution.

Fig. 5.15.: Fracturing between isolated pores: porosity and saturation for drainage under $\sigma_{conf} = 6MPa$.

evolution in Fig. 5.15a is almost constant until the fracturing event, from this point a significant increase of porosity can be observed. The gas saturation in Fig. 5.15b presents a slight increase until 40s of simulation, and since the new preferential pathway is created, a substantial increase is observed reaching more than 50% at the end of the simulation.

Concluding remarks

Through an application to drainage a CO_x sample, our SPH method has shown its capabilities to simulate two-phase flow within an elasto-damage solid matrix. The numerical tool has provided very stable results in various conditions. In the case of an elastic matrix, we have observed pore-space dilation during gas percolation. Also, two different confining stress were imposed on the same numerical sample with elasto-damage response. We have shown that the confining stress can affect the onset of fracturing with new pore space creation. Additionally, for reduced confining stress, it was possible to connect initially isolated pores and to generate new percolating pathways in a non-percolating numerical sample.

Conclusion and Outlooks

The safety assessment of radioactive waste disposal facility installed in very low permeable clay rocks is one of the major issues to which this work aims to contribute. We focused here on studying the mechanical response of the host rock in a coupled hydromechanical phenomena related to the gas migration at pore-scale. The literature review highlighted a lack of studies about the transfer characterisation and the preferential pathway phenomenon at the pore-scale of the CO_x clay. To contribute to this point, we presented a physical model including main phases present in the host rock to represent the preferential pathway phenomenon modelled in this work by a multiphase flow coupled to the damage of the clay matrix.

To detail the numerical procedures used here, we summarised the Smoothed Particle Hydrodynamics method accompanied by various improvements needed to overcome SPH drawbacks showed up while resolving the solid mechanics equations. In particular, we implemented the so-called corrected kernel and corrected gradient functions to account for existing domain limits and alternative primary variable formulations. We also implemented a Total Lagrangian version of SPH to solve a large deformations problem (through the Saint Venant-Kirchhoff constitutive model). Moreover, we performed validation tests on purely elastic cases for which the support length of the kernel function was set to minimal values compatible with material points density. This led to exact EDP solutions, presenting satisfactory results compared to analytical solutions.

An investigation of an elastic material response for finite values of the kernel support length was also performed. This allowed characterising higher-order effects (also called non-local effects). We have accurately accounted for higher-order effects in elasticity through a 1D problem of vibrating bar treated with an SPH model compared to analytical lattice discrete and continua solutions: stress gradient and continualized models. Clamped-clamped and clamped-free boundary conditions were considered. The non-local effects appear to be directly related to parameter $2h$, which is purely numerical (and inherent to the SPH).

We also proposed a non-local SPH-based approach to compute damage and fracture. In this context, the proposed model maintained the local formulation of the damage model, while the non-local regularisation has been performed numerically. Two test cases were simulated in 1D and 2D configurations. Small and large deformation approaches were considered. In both test cases, it has been shown that the damage localisation is achieved and the width of the localised damage zone is independent of the discretisation. This width is related to the support-length $2h$, which confirms that this numerical parameter plays a physical role and may be adjusted to the considered material properties. In quasi-static simulations, it was observed that the fracture propagation, which follows the damage localisation, was accompanied by an increase of kinetic energy. Asymmetric responses related to the unilateral effects of damage was also demonstrated, and the predictions compared well to existing results. It is noticeable that the displacement fields presented a discontinuity during the fracture propagation. Finally, by taking advantage of the SPH method, we were able to perform several simulations in dynamic conditions naturally. We observed in these conditions more complex fracture patterns in which crack branching occurred.

All the improvements introduced into our SPH model were considered to simulate drainage phenomena within a realistic porous material with an elasto-damage solid phase. These phenomena were translated by a multiphase flow coupled to the mechanical response of a clayey rock at the pore scale. We observed that the drainage led to the pore-space dilation during gas percolation. Also, two different confining stresses were imposed on the same clay matrix sample. We showed that the confining stress can affect the onset of fracturing with new pore space creation. We demonstrated that it was possible to connect initially isolated pores for reduced confining stress and generate new percolating pathways in an initially non-percolating sample. With the results and discussions presented in this thesis, we have demonstrated new possibilities opened using the SPH method for studying coupled phenomena arising in mechanics, hydromechanics and geomaterials fields. At this step, several important outlooks for future works can be identified:

- The use of SPH method is an exciting option for studying the damage localisation in various configurations and dimensions. Also, most non-local problems are solved in quasi-static conditions, while SPH can easily access the solutions in dynamic conditions. In particular, the study of damage and fracture in geomaterials will deserve attention. The calibration of the damage model parameters for the studied material will be done by comparing model predictions with experimental data. The clay matrix model considered here as an elasto-damageable material must account for its rigid mineral inclusions. The developed code can easily handle such

a configuration. Moreover, accounting for the plastic deformation of the clay matrix could be interesting.

- Concerning the preferential pathway phenomenon in a clayey pore-space, several steps must be taken to move from the actual state of a “toy model” to a predictive tool:
 - To take into account porewater filling all invisible pores - introducing poromechanics for the solid matrix.
 - To be able to treat larger numerical samples, more representative of the real material, coming closer to a REV of argillite – optimisation of code, for example by introducing variable h approach (equivalent to refining procedure), also modification of GPU parallelisation in order to be able to make simulations on more than one GPU card.
- Another possible application to coupled problems could be simulating desiccation cracks in porous materials. All necessary ingredients are already present in the code, including the diffusion equation for water vapour. The only algorithmic challenge would be to manage fluxes and mass conservation at the interfaces between liquid and gas phases.

Appendix: Rigid bodies (mineral inclusions)

A.1 Continua equations

Given its inhomogeneous nature state, argillaceous rocks present several rigid inclusions at the micro-scale. The interface zones between these elements and the clayey matrix are understood as possible sites for emergence of damage or cracks and such problem is source of further research in this work. In this study, the mineral inclusions (carbonates or silicates) can be treated as rigid bodies. The Newton-Euler equations can fully represent the rigid body dynamics, where the position of the centre of mass can be found as:

$$\underline{r}_{CM} = \frac{1}{m_B} \int \rho(\underline{r}) \underline{r} d^3 \underline{r} \quad (\text{A.1})$$

where the subscript CM represent the center of mass, B the rigid body material property and m the mass of the body. The tensor of the moment of inertia \underline{I}_B is given by:

$$\underline{I}_B = \int \rho(\underline{r}) \left[(\underline{r} - \underline{r}_{CM})^2 \underline{\mathbb{1}} - (\underline{r} - \underline{r}_{CM})(\underline{r} - \underline{r}_{CM})^T \right] d^3 \underline{r} \quad (\text{A.2})$$

The total torque \underline{T}_B acting on the body can be expressed as

$$\underline{T}_B = \int (\underline{r} - \underline{r}_{CM}) \times \hat{\underline{F}} d^3 \underline{r} \quad (\text{A.3})$$

where $\hat{\underline{F}}$ is the external force density. It results in the translation update of the rigid body, described as:

$$\dot{\underline{v}}_{CM} = \frac{\hat{\underline{F}}_B}{m_B} \quad (\text{A.4a})$$

$$\dot{\underline{r}}_{CM} = \underline{v}_{CM} \quad (\text{A.4b})$$

and the time increment of the angular velocity $\underline{\dot{\omega}}$ and of the angle between the body axes and the reference axes $\underline{\dot{\phi}}$ read:

$$\underline{\dot{\omega}}_B = \underline{I}_B^{-1} \left(\underline{T}_B - \underline{\omega}_B \times \underline{I}_B \underline{\omega}_B \right) \quad (\text{A.5a})$$

$$\underline{\dot{\phi}}_B = \underline{\omega}_B \quad (\text{A.5b})$$

In addition, the interface conditions between a rigid body and an elastic phase is given by:

$$\underline{\sigma}_B \cdot \underline{n}_B = -\underline{\sigma}_e \cdot \underline{n}_e \quad (\text{A.6})$$

where the subscripts B and e mean, respectively, rigid body and elastic solid phase. Hence, for the sake of simplicity, the friction force between solid phases is neglected, although such phenomenon is an interesting outlook for further studies.

A.2 Discrete equations

By definition the mechanical properties of any part of a rigid body are constant, thus it is possible to describe such bodies by taking into account only the boundary particles which may experience forces from external particles from other phases. This way of doing may also help to decrease the computation time.

Thus, the discrete SPH forms of equations from Sec. A.1 for a rigid body represented by a set of N points of mass m_s are the following starting with the position of the of the centre of mass:

$$\underline{r}_{CM} = \frac{1}{M_B} \sum_{i=1}^N m_s \underline{r}_a \quad (\text{A.7})$$

The SPH tensor of the momentum of inertia \underline{I}_B is given by:

$$\underline{I}_B = \sum_{i=1}^N m_s \left[(\underline{r}_a - \underline{r}_{CM})^2 \underline{I} - (\underline{r}_a - \underline{r}_{CM})(\underline{r}_a - \underline{r}_{CM})^T \right] \quad (\text{A.8})$$

The total torque \underline{T}_B acting on the body can be expressed as:

$$\underline{T}_B = \sum_{i=1}^N (\underline{r}_a - \underline{r}_{CM}) \times (m_s \underline{a}_a) \quad (\text{A.9})$$

where \underline{a}_a is the acceleration of the point due to external forces. Moreover, the total external force \underline{F}_B acting on the rigid body is given by:

$$\underline{F}_B = \sum_{i=1}^N m_s \underline{a}_a \quad (\text{A.10})$$

Furthermore, the Newton-Euler equations introduced in (A.4) can be integrated using the Leapfrog algorithm as shown in [3]. In this case, given the centre of mass, its linear \underline{a}_{CM} and angular $\underline{\alpha}_B$ accelerations at time t are written as:

$$\underline{a}_{CM}^t = \frac{\underline{F}_B^t}{M_B} \quad (\text{A.11a})$$

$$\underline{\alpha}_B^t = \underline{I}_B^{t-1} \left(\underline{T}_B^t - \underline{\omega}_B^{t-\Delta t/2} \times \underline{I}_B^t \underline{\omega}_B^{t-\Delta t/2} \right) \quad (\text{A.11b})$$

Thus, its linear \underline{v}_{CM} and angular $\underline{\omega}_B$ velocities are updated as:

$$\underline{v}_{CM}^{t+\Delta t/2} = \underline{v}_{CM}^{t-\Delta t/2} + \underline{a}_{CM}^t \Delta t \quad (\text{A.12a})$$

$$\underline{\omega}_B^{t+\Delta t/2} = \underline{\omega}_B^{t-\Delta t/2} + \underline{\alpha}_B^t \Delta t \quad (\text{A.12b})$$

Finally, its new centre of mass position is given by:

$$\underline{r}_{CM}^{t+\Delta t} = \underline{r}_{CM}^t + \underline{v}_{CM}^{t+\Delta t/2} \Delta t \quad (\text{A.13})$$

Therefore, one can obtain the new velocities and positions of the rigid body particles as:

$$\underline{v}_a^{t+\Delta t/2} = \underline{v}_{CM}^{t+\Delta t/2} + \underline{\omega}_B^{t+\Delta t/2} \times (\underline{r}_a^t - \underline{r}_{CM}^t) \quad (\text{A.14a})$$

$$\underline{r}_a^{t+\Delta t} = \underline{r}_{CM}^{t+\Delta t} + \underline{r}_B^{t+\Delta t/2} \cdot (\underline{r}_a^t - \underline{r}_{CM}^t) \quad (\text{A.14b})$$

where \underline{r}_B is the rotation matrix tensor, which can be computed as:

$$\underline{r}_B^{t+\Delta t/2} = \underline{r}_x(\omega_{B,x}^{t+\Delta t/2} \Delta t) \underline{r}_y(\omega_{B,y}^{t+\Delta t/2} \Delta t) \underline{r}_z(\omega_{B,z}^{t+\Delta t/2} \Delta t) \quad (\text{A.15})$$

where $\underline{r}_{x,y,z}(\theta)$ are the tensors which yield the rotation around the principal axis coordinates:

$$\underline{r}_x(\theta) = \begin{pmatrix} 1 & 0 & 0 \\ 0 & \cos(\theta) & -\sin(\theta) \\ 0 & \sin(\theta) & \cos(\theta) \end{pmatrix} \quad (\text{A.16a})$$

$$\underline{r}_y(\theta) = \begin{pmatrix} \cos(\theta) & 0 & \sin(\theta) \\ 0 & 1 & 0 \\ -\sin(\theta) & 0 & \cos(\theta) \end{pmatrix} \quad (\text{A.16b})$$

$$\underline{r}_z(\theta) = \begin{pmatrix} \cos(\theta) & -\sin(\theta) & 0 \\ \sin(\theta) & \cos(\theta) & 0 \\ 0 & 0 & 1 \end{pmatrix} \quad (\text{A.16c})$$

A.3 Interface conditions

The speed of sound in a rigid solid phase reads:

$$c_s = \sqrt{\frac{k_s}{\rho_{0,solid}}} \quad (\text{A.17})$$

where k_s is the solid bulk modulus. Thus, we can obtain the pressure in a solid by introducing c_s into (Eq. 1.4). The fact that the bulk modulus in a rigid solid material is around one magnitude order greater than the bulk modulus in an elastic material ensures the no-slip and non-penetration boundary condition at their interfaces.

Furthermore, the interface interaction forces between different solid phases are based on the *Lennard-Jones* potential as proposed in [116] or alternatively on repulsive forces as introduced by [3], [117]; and the resulting pairwise interparticle force can be constructed in the following way:

$$\underline{F}_a = -\frac{m_b}{m_a + m_b} B(r_a) \underline{n}_a \quad (\text{A.18})$$

where \underline{F}_a is the resultant force, B is a symmetric function that defines the interaction strength based on physical model as described before and \underline{n}_a is the local boundary normal.

Appendix: Complements of simulation results with PCW-based elastic-damage model

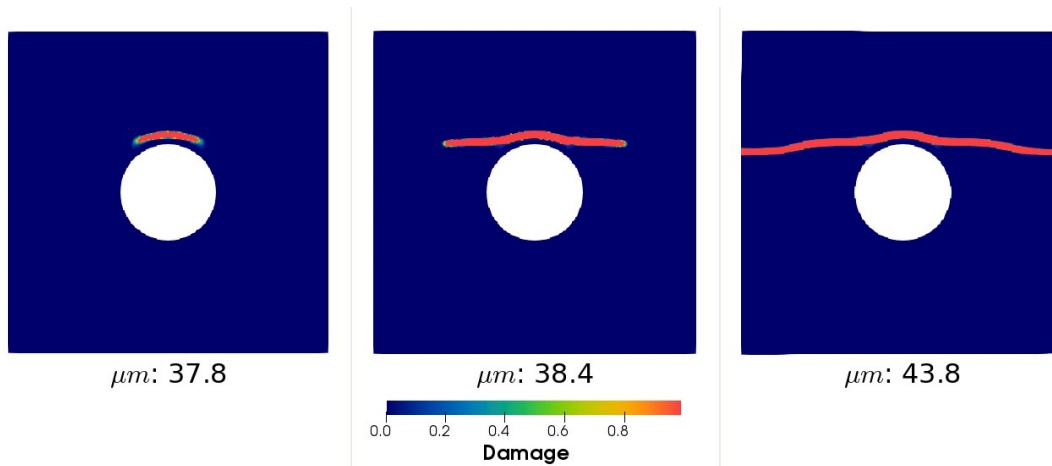
This appendix deploys a few tests using the Ponte-Castaneda and Willis damage model (PCW) [40]. The main purpose of this section is to present a validation of the PCW-based model in a multidimensional problem under tensile and compressive loading. This results will be useful for using this damage model to treat the elastic-damage response to be investigated using the COx clay matrix in Chap. 5. Thus, we summarize here the results of the problem of the square plate with a rigid inclusion (first presented in Chap. 4 through the Ambrosio-Tortorelli damage models). We recall that due to different values of the parameters of Eq. (4.21), it can be necessary to introduce the dependency on D parameter into the critical damage energy release \mathcal{Y}_{crit} . Our damage function will be constructed through (Eq. 4.21) with the following parameters:

$$\begin{cases} \hat{\alpha} = 1 \\ \hat{\beta} = \frac{\varepsilon_u}{\varepsilon_0} - 1 \\ \mathcal{Y}_c = \mathcal{Y}_c^0 \end{cases} \quad (\text{B.1})$$

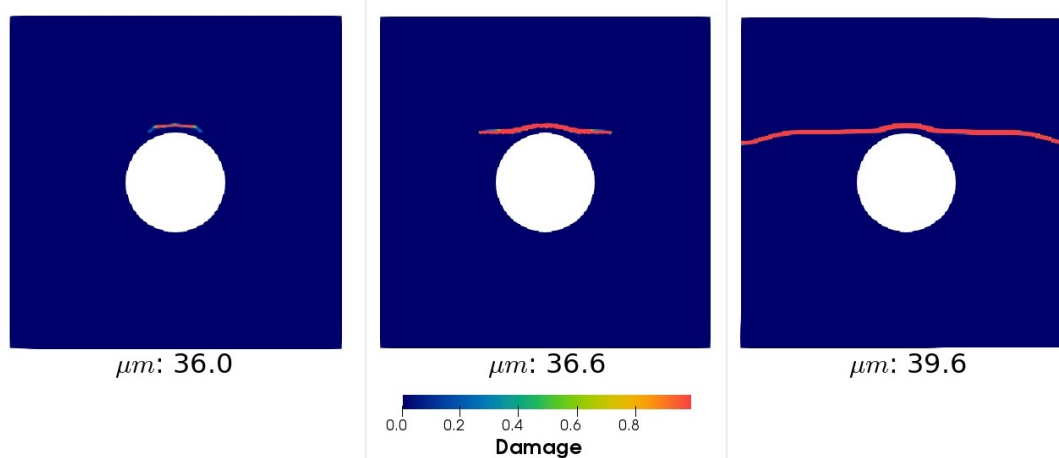
We adopt here the same ratio $\varepsilon_u/\varepsilon_0 = 2$ found in Tab. 5.1 for COx properties. For the sake of conciseness, we will focus the analysis in this appendix in the central aspects that differs from those that was already discussed in chapter 4. Although this PCW damage model has \mathcal{Y}_c constant (the same for AT-2 model), it follows a linear damage function (differently of the quadratic damage function present in AT models).

B.1 Quasi-static conditions

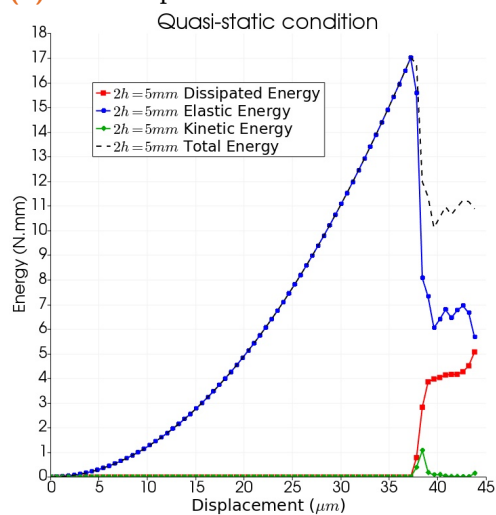
We perform here two simulations adopting the same parameters used in Section 4.3. The evolution of the fracture propagation after an imposed displacement of $60\mu m$ are given in Fig. B.1a (for $2h = 5mm$) and in Fig. B.1b (for $2h = 2.5mm$). We observe that the fracture patterns recall the shape of those obtained with AT-models, with a symmetry between the left and the right-hand-side patterns.



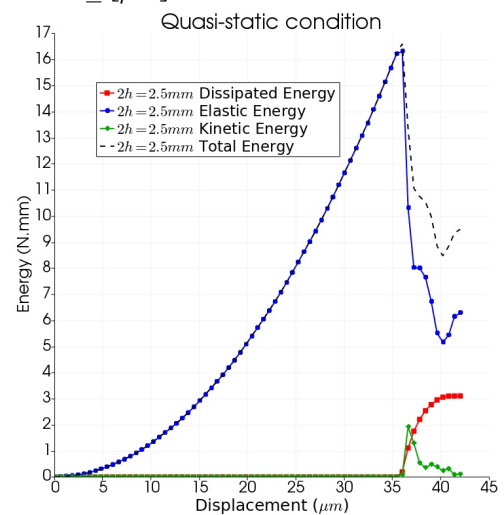
(a) Fracture pattern evolution over different imposed displacements \bar{u} [μm] with $2h = 5mm$.



(b) Fracture pattern evolution over different imposed displacements \bar{u} [μm] with $2h = 2.5mm$.



(c) Elastic, dissipated, kinetic and total energies evolution for $2h = 5mm$.



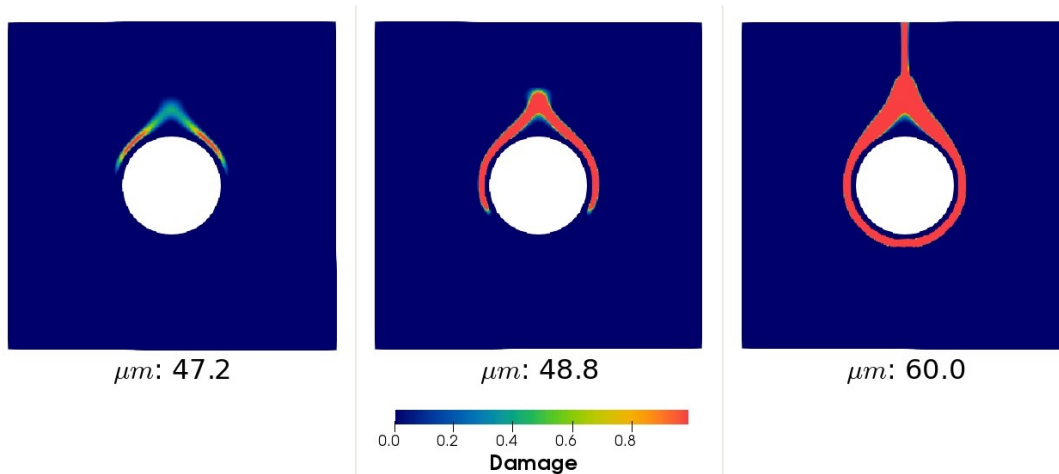
(d) Elastic, dissipated, kinetic and total energies evolution for $2h = 2.5mm$.

Fig. B.1.: Tensile quasi-static (PCW): evolution of the damage variable and energies in a plate with a rigid inclusion with $2h = 5mm$ and $2h = 2.5mm$.

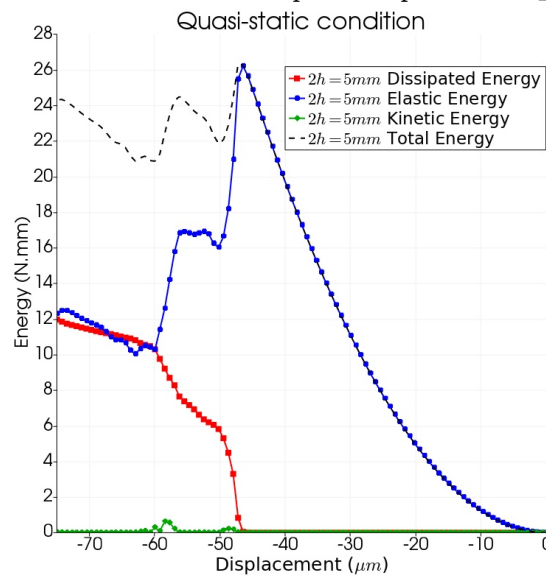
Fig. B.1c and Fig. B.1d highlight, in a similar manner from the AT validations in Sec. 4.3, that an important kinetic energy rises at the exact moment of the rupture

initiation, this energy has a lower order of magnitude this time. The configuration with larger $2h$ presents a more important level of dissipated energy.

Reversing the load, Fig. B.2a (PCW-1) and Fig. B.2a (PCW-2) show the fracture propagation after a negative imposed displacement at the top border. We adopt the support-length $2h = 5mm$. This time, we observe a brutal crack propagating towards the top side of the plate and around the inclusion, but not reaching, this time the bottom bound at the final moment. Fig. B.2b presents the evolution of the total, elastic, dissipated



(a) Fracture pattern evolution over different imposed displacements \bar{u} [μm] with $2h = 5mm$.



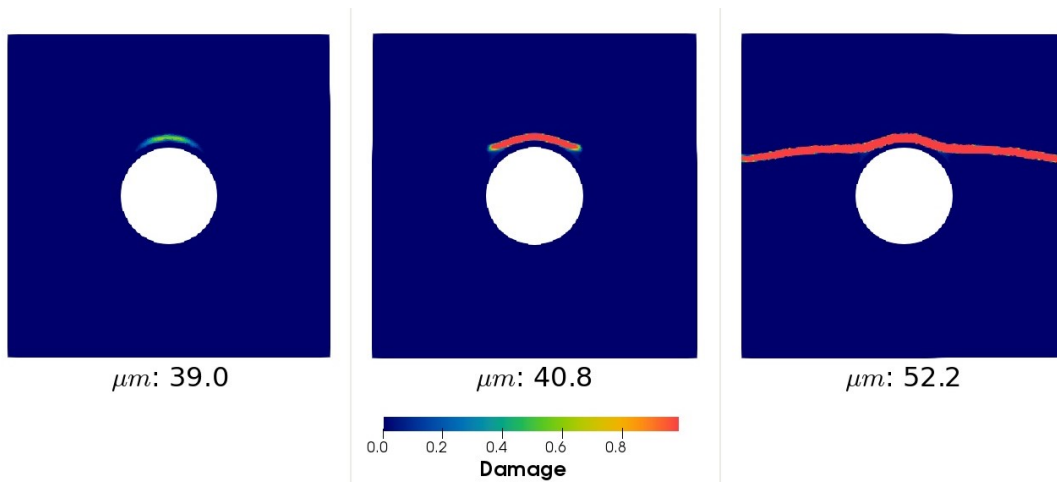
(b) Damage model 2: Elastic, dissipated, kinetic and total energies for $2h = 5mm$.

Fig. B.2.: Compressive quasi-static (PCW): evolution of the damage variable and energies in a plate with a rigid inclusion with $2h = 5mm$.

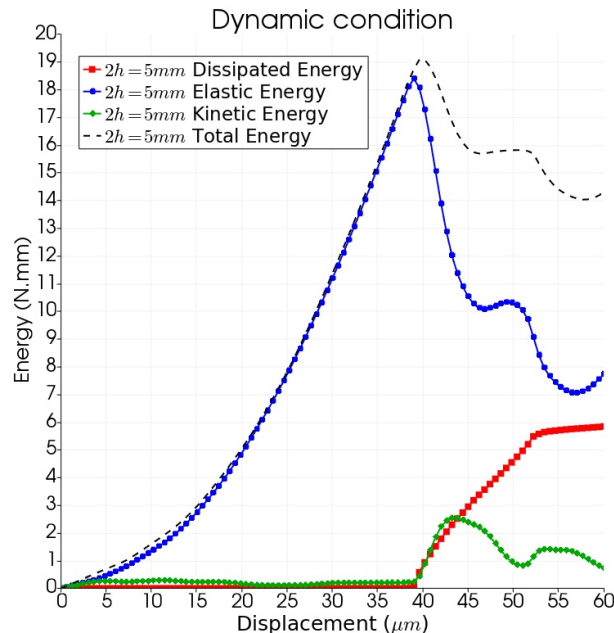
and kinetic energies. The post-fracturing evolution of elastic and dissipated energies seems to be achieved in two consecutive steps. Although a non-negligible kinetic energy, it does not reach higher levels.

B.2 Dynamic conditions

In a system under dynamic conditions, we reproduce here the same simulations presented in Sec. 4.3 using a PCW damage model. The evolution of the fracture propagation after tensile loading is given in Fig. B.3a for $2h = 5mm$. In general, the results here are quite similar to those observed in QS conditions, with an exception for the pattern shape, that follows the same behaviour that the AT-2 model that surrounds more the rigid inclusion.



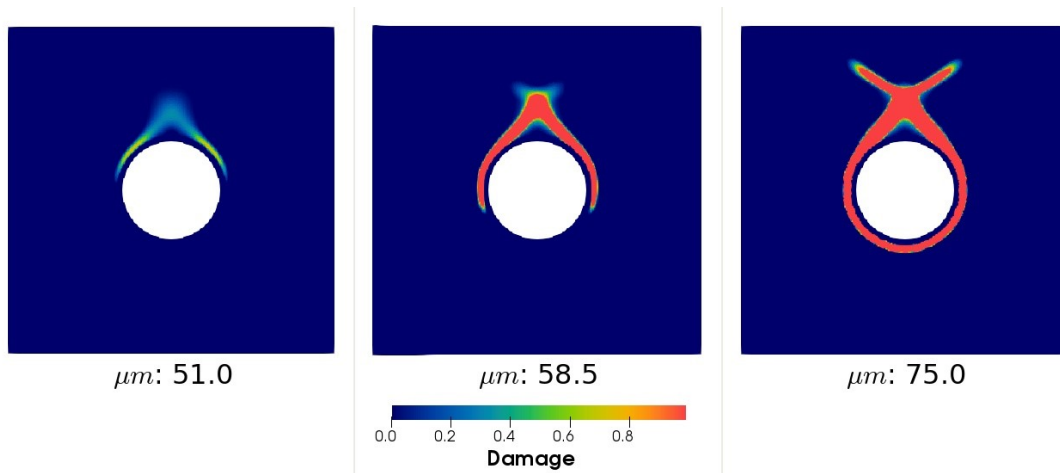
(a) Fracture pattern evolution over different imposed displacements \bar{u} [μm] with $2h = 5mm$.



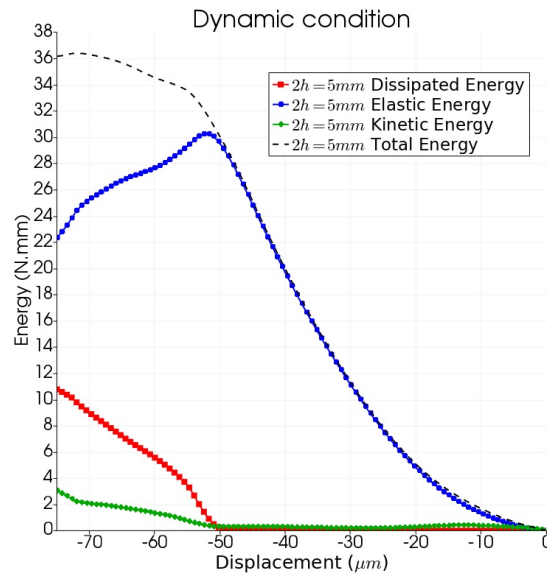
(b) Elastic, dissipated, kinetic and total energies evolution with $2h = 5mm$.

Fig. B.3.: Tensile dynamic (PCW): evolution of the damage variable and energies in a plate with a rigid inclusion with $2h = 5mm$.

Reversing the load in dynamic conditions, the fracture pattern illustrated in Fig. B.4a shows a double diagonal pattern towards the top bound of the matrix. This fracture pattern can also be observed in Amor *et al.* [6] or it is even more explicit in [66].



(a) Fracture pattern evolution over different imposed displacements \bar{u} [μm] with $2h = 5mm$.



(b) Elastic, dissipated, kinetic and total energies evolution with $2h = 5mm$.

Fig. B.4.: Compressive dynamic (PCW): evolution of the damage variable and energies in a plate with a rigid inclusion with $2h = 5mm$.

Finally, a smoother energy evolution when compared to QS conditions is observed in Fig. B.4b remaining at the same energy level values. The present validations do not aim to perform an in-depth investigation of the PCW-based damage models, but to verify good stability and damage responses of the material in quasi-static and dynamic conditions. It allows us to use the damage model in the practical application in Chap. 5.

List of Figures

1.1	Strategies of the French government for management of disposal of radioactive waste (from [77], modified).	6
1.2	Cigéo deep geological facility for disposal of radioactive waste (from [10], modified) at the stage of the Safety Option Dossier, 2016.	7
1.3	Geological log of the Cigéo site (from [7]).	9
1.4	SEM image of COx microstructure (a) and segmented image presenting each component (b) (from [143], modified).	10
1.5	Pore size distribution by a mercury intrusion test supplemented with nitrogen intrusion test (from [8], modified).	11
1.6	Dihydrogen gas production over 100.000 years (from [8], modified).	12
1.7	Gas transport processes in clayey rock: phenomenological description based on the micro-structural concept, geomechanical regime and preferential pathways evolution framework (from [106] and [48], modified).	13
1.8	Adapted from Wiseall <i>et al.</i> [165] images of the evolution of dilatant pathways, chronologically, from a to d.	14
1.9	(a) Regular pore network system and (b) phase diagram of drainage of different invasion patterns by pore network system results (from Holtzman and Juanes [75], adapted).	16
1.10	COx sample by FIB and physical model of the host rock.	19
1.11	General 3D rotation and deformation of a domain from an initial to a current state.	21
2.1	Physical configuration and SPH numerical model	28
2.2	An conceptual example of 2D SPH ordered material points with the smoothing length $\hat{\kappa}h$ around a central point (a) and the neighbour contribution weights following a smoothing function W (b)	29
2.3	Randomly generated data following $f(x) = \tan(x)$ with a standard deviation of 1/4 and its linear and polynomial regressions.	31
2.4	Randomly generated data following $f(x) = \tan(x)$ with a standard deviation of 1/4 and its cubic spline kernel regression with $h = 0.05$	32
2.5	Randomly generated data following $f(x) = \tan(x)$ with a standard deviation of 1/4 and its cubic spline kernel size of $h = 2$	33

2.6	Randomly generated data following $f(x) = \tan(x)$ with a standard deviation of 1/4 and its linear and polynomial and optimal cubic spline kernel ($h = 0.46$) regressions.	33
2.7	2D SPH disordered material points, the smoothing scale h and the neighbour contribution weight following a smoothing function W	38
2.8	SPH boundary particle particles for the one-dimensional case	43
2.9	SPH computing flow chart for solid particles	52
2.9	SPH computing flow chart for solid particles	53
2.9	SPH computing flow chart for solid particles	54
2.10	1D bar of length 1m discretized into $N = 5$ equally spaced of δx material points [171]	55
2.11	Velocity divergence of a 5-points bar under a constant velocity field.	57
2.12	Velocity divergence of a 5-points bar under a linear velocity field.	58
2.13	Velocity divergence of a 5-points bar under a quartic velocity field.	59
2.14	Relative error (Eq. 2.93) of velocity divergence of a 5-points bar under a quartic velocity field.	59
2.15	Velocity divergence computed by mixed correction kernel gradient of a 5-points bar under a quartic velocity field.	60
2.16	Velocity divergence computed by mixed correction kernel gradient of a 50-points bar under a quartic velocity field.	61
2.17	Velocity divergence computed by mixed correction kernel gradient of a 500-points bar under a quartic velocity field.	61
2.18	Velocity divergence computed by mixed correction kernel gradient of a 5 randomly distributed particles bar under a quartic velocity field.	62
2.19	Velocity divergence computed by mixed correction kernel gradient of a 50 randomly distributed particles bar under a quartic velocity field	62
2.20	Velocity divergence computed by mixed correction kernel gradient of a 500 randomly distributed particles bar under a quartic velocity field	63
2.21	2D and 3D particles distribution	64
2.22	2D Velocity divergence computed by mixed correction kernel gradient of a 25 particles discretized plan under a linear velocity field	65
2.23	3D Velocity divergence computed by mixed correction kernel gradient of a 125 particles discretized volume under a linear velocity field	65
2.24	2D Velocity divergence computed by mixed correction kernel gradient of a 25 particles discretized plan under a quartic velocity field	66
2.25	3D Velocity divergence computed by mixed correction kernel gradient of a 125 particles discretized volume under a quartic velocity field	66
2.26	Clamped-free boundary conditions of a 40 material points bar for SPH validation as EDP solver.	67

2.28	Mixed normalised and corrected versions of the small deformations SPH models: stress-based and displacement-based	69
2.27	Comparison between Saint Venant-Kirchhoff SPH, FEM (for displacement only), Stress points SPH [59] and Total Lagrangian SPH [26]. The SVK-SPH presented here adopts the mixed normalisation and correction of the kernel functions and a stress-based momentum equation discretisation.	71
2.29	Mixed normalised and corrected version of the small (SPH) and large deformations (SVK-SPH) approaches compared by their displacement and velocity evolution.	72
2.30	Numerical improvements for mixed normalised and corrected versions of small deformations SPH and large deformations SVK-SPH model: XSPH ($\epsilon = 0.5$) and Artificial viscosity ($\check{\alpha} = 0.2$ and $\check{\beta} = 0.4$).	73
4.1	Strain-stress tensile constitutive law for elasto-damage material	116
4.2	Strain-stress unilateral effect behaviour	116
4.3	SPH computing flow chart for solid material points constitutive model and material response	119
4.4	SPH computing flow chart for thermodynamics-based damage model.	120
4.5	Bar configuration and boundary conditions	121
4.6	1D softening bar: damage and Strain. damage width zone independence for different material point densities for $2h = 5mm$ at $t = \frac{3L}{2c_e}$	124
4.7	Damage, stress, strain and displacement at $t = \frac{3L}{2c_e}$. Validation of normalized-corrected SVK SPH by using PCW-based damage function following three density of longitudinal material points: 101, 151 and 201.	125
4.8	PCW-based damage model: evolution of elastic, kinetic, dissipated and total energies for $\bar{u} \leq 1.5mm$	126
4.9	Strain-stress curve of a elastic bar under a displacement velocity of $v = 72m/s$ for the thermodynamics-based damage model with PCW damage function for different particle densities.	126
4.10	Width of the damaged zone, strain, stress and displacement profiles for $2h = 5mm, 10mm$ and $20mm$ at $t = \frac{3L}{2c_e}$	128
4.11	Evolution of elastic, kinetic, dissipated and total energies for $t < \frac{3L}{2c_e}$	129
4.12	Comparison between different SPH formulations. Longitudinal strain profile for $2h = 5mm$ at $t = \frac{L}{2c_e}$ and $\frac{3L}{2c_e}$	130
4.13	Set up and boundary conditions of 2D fiber reinforced plate (adapted after Bourdin <i>et al.</i> [30]).	132
4.14	Tensile quasi-static (AT-2): evolution of damage variable and energies in a plate with rigid inclusion with $2h = 5mm$	134
4.15	Tensile quasi-static (AT-2): evolution of damage variable and energies in a plate with rigid inclusion with $2h = 2.5mm$	136

4.16	Tensile quasi-static (AT-2): evolution of the y-displacement and of the maximum principal stress in three key stages: damage growth, half-fractured and completely fractured with $2h = 5mm$	137
4.17	Tensile quasi-static (AT-1): evolution of damage variable and energies in a plate with rigid inclusion with $2h = 5mm$	138
4.18	Compressive quasi-static (AT-2): evolution of damage, minimum principal stress and energies in a plate with rigid inclusion with $2h = 5mm$	140
4.19	Compressive quasi-static (AT-2): evolution of the x-displacement and of the minimum principal stress in three key stages: damage growth, half-fractured and completely fractured with $2h = 5mm$	141
4.20	Compressive quasi-static (AT-1): evolution of damage, minimum principal stress and energies in a plate with rigid inclusion with $2h = 5mm$	142
4.21	SPH discretization independence analysis: zoomed area of the top bound of the inclusion showing the discretization independence of the width of the damaged zone for $2h = 5mm$. Material point discretizations by side of the plate: (a)200, (b)300, (c)400 and (d)500 material points.	143
4.22	SPH discretization independence analysis: elastic, dissipated, kinetic and total energies for $2h = 5mm$	144
4.23	Non-local analysis in quasi-static conditions: final fracture pattern and energies evolution for imposed tensile loading with $2h = 1.25mm$ and $2h = 20mm$	145
4.24	Tensile dynamic (AT-2): evolution of damage variable and energies in a plate with rigid inclusion with $2h = 5mm$	147
4.25	Tensile dynamic (AT-2): evolution of damage variable and energies in a plate with rigid inclusion with $2h = 2.5mm$	148
4.26	Tensile dynamic (AT-2): evolution of the y displacement [μm] and of the maximum principal stress [N/mm^2] in three key stages: damage growth, half-fractured and completely fractured with $2h = 5mm$	149
4.27	Tensile dynamic (AT-1): evolution of damage variable and energies in a plate with rigid inclusion with $2h = 5mm$	151
4.28	Compressive dynamic (AT-2): evolution of damage variable, minimum principal stress and energies in a plate with rigid inclusion with $2h = 5mm$	152
4.29	Compressive dynamic (AT-2): evolution of the x-displacement and of the maximum principal stress in three key stages: damage growth, half-fractured and completely fractured with $2h = 5mm$	153
4.30	Compressive dynamic (AT-1): evolution of damage variable and energies in a plate with rigid inclusion with $2h = 5mm$	154
4.31	Non-local analysis in dynamic conditions: final fracture pattern (at imposed displacement of $120\mu m$) and energies evolution for imposed tensile loading with $2h = 1.25mm$ and $2h = 20mm$	155

5.1	Physical configuration and SPH numerical model with elasto-damage coupling	158
5.2	A total set of percolating pores in a Callovo-Oxfordian clay sample after [126].	160
5.3	3D and orthogonal cuts of the numerical sub-sample containing elastic, water and hydrogen phases.	162
5.4	Damage (a) and maximum principal stress field (b) in COx sample during drainage with Rankine and Mohr-Coulomb damage model at $t = 4s$	163
5.5	Elastic matrix: drainage under $\sigma_{conf} = 8MPa$. 3D view of solid and fluid phases.	167
5.6	Elastic matrix: Porosity and saturation evolution during drainage under $\sigma_{conf} = 8MPa$	168
5.7	Elastic matrix: drainage under $\sigma_{conf} = 8MPa$. Maximum principal stress (a, b and c) and x-displacement fields (d, e and f) on a xy cross-section at $z = 45h$.	169
5.8	Drainage under $\sigma_{conf} = 8MPa$ in elasto-damage clay matrix. 3D view of solid and fluid phases.	170
5.9	Elasto-damage matrix: porosity and saturation for drainage under $\sigma_{conf} = 8MPa$	170
5.10	Drainage under $\sigma_{conf} = 8MPa$. Damage (a, b and c) and maximum principal stress fields (d, e, and f) on xy cross-section at $z = 45h$	171
5.11	Drainage with $\sigma_{conf} = 6MPa$. 3D view of solid and fluid phases at three different times (a, b and c) as well as damage field (d, e and f) on xy cross-section at $z = 45h$	172
5.12	Elasto-damage matrix: Porosity and saturation for drainage under $\sigma_{conf} = 6MPa$	173
5.13	Drainage at $\sigma_{conf} = 6MPa$. Maximum principal stress (a, b and c) and x-displacement fields (d, e and f) on xy cross-section at $z = 45h$	174
5.14	Fracturing between isolated pores under $\sigma_{conf} = 6MPa$. 3D view of fluid phases (a, b and c). Solid and fluid phases and damage field through xy cross-section at $z = 45h$ (d, e and f) and xz cross-section at $y = 17h$ (g, h and i).	175
5.15	Fracturing between isolated pores: porosity and saturation for drainage under $\sigma_{conf} = 6MPa$	176
B.1	Tensile quasi-static (PCW): evolution of the damage variable and energies in a plate with a rigid inclusion with $2h = 5mm$ and $2h = 2.5mm$	188
B.2	Compressive quasi-static (PCW): evolution of the damage variable and energies in a plate with a rigid inclusion with $2h = 5mm$	189
B.3	Tensile dynamic (PCW): evolution of the damage variable and energies in a plate with a rigid inclusion with $2h = 5mm$	190
B.4	Compressive dynamic (PCW): evolution of the damage variable and energies in a plate with a rigid inclusion with $2h = 5mm$	191

List of Tables

2.1	Velocity divergence of the pair contributions for a linear velocity (Eq. 2.92b).	56
2.2	Velocity divergence of the pair contributions for a quartic velocity (Eq. 2.92c).	56
2.3	Input data for a 1D bar problem for SPH validation as a local EDP solver. . .	67
4.1	Input data for dynamic simulation of a softening bar	122
4.2	Input data for dynamic simulation of the fiber reinforced plate.	133
5.1	Expected COx properties after [126].	164
5.2	Simulation input parameters for fluids adopted in this work following [126].	164
5.3	Physical and simulation mechanical parameters for drainage simulations. . .	166

Bibliography

- [1] L. Ambrosio and V. M. Tortorelli, „Approximation of functional depending on jumps by elliptic functional via t-convergence,“ *Communications on Pure and Applied Mathematics*, vol. 43, no. 8, pp. 999–1036, 1990. DOI: 10.1002/cpa.3160430805.
- [2] ———, „On the approximation of free discontinuity problems,“ *BOLLETTINO DELLA UNIONE MATEMATICA ITALIANA*, vol. 6B, no. 1, pp. 105–123, 1992.
- [3] A. Amicarella, R. Albano, D. Mirauda, *et al.*, „A smoothed particle hydrodynamics model for 3d solid body transport in free surface flows,“ *Computers Fluids*, vol. 116, pp. 205–228, 2015. DOI: <https://doi.org/10.1016/j.compfluid.2015.04.018>.
- [4] Y. Amini, H. Emdad, and M. Farid, „A new model to solve fluid–hypo-elastic solid interaction using the smoothed particle hydrodynamics (sph) method,“ *European Journal of Mechanics - B/Fluids*, vol. 30, no. 2, pp. 184–194, 2011. DOI: <https://doi.org/10.1016/j.euromechflu.2010.09.010>.
- [5] H. Amor, „Variational approach of Griffith and Paris laws via non-local damage models : Theoretical study and numerical implementation,“ French, Ph.D. dissertation, Université Paris-Nord - Paris XIII, 2008.
- [6] H. Amor, J.-J. Marigo, and C. Maurini, „Regularized formulation of the variational brittle fracture with unilateral contact: Numerical experiments,“ *Journal of the Mechanics and Physics of Solids*, vol. 57, no. 8, pp. 1209–1229, 2009. DOI: 10.1016/j.jmps.2009.04.011.
- [7] ANDRA, „Dossier 2005 argile. évaluation de la faisabilité du stockage géologique en formation argileuse,“ French, Agence Nationale pour la gestion des Déchets Radioactifs, Tech. Rep., 2005.
- [8] ———, „Dossier 2005 argile. tome évaluation phénoménologique du stockage géologique,“ French, Agence Nationale pour la gestion des Déchets Radioactifs, Tech. Rep., 2005.

- [9] —, „Dossier d’options de sûreté - Partie exploitation (DOS-AF),“ French, Agence Nationale pour la gestion des Déchets Radioactifs, Tech. Rep. CG-TE-D-NTE-AMOA-SR2-0000-15-0062/A, 2016, p. 467.
- [10] —, „Dossier d’options de sûreté - Partie exploitation (DOS-Expl),“ French, Agence Nationale pour la gestion des Déchets Radioactifs, Tech. Rep. CG-TE-D-NTE-AMOA-SR1-0000-15-0060, 2016, p. 519.
- [11] M. Angeli, M. Soldal, E. Skurtveit, and E. Aker, „Experimental percolation of supercritical CO₂ through a caprock,“ *Greenhouse Gas Control Technologies* 9, vol. 1, no. 1, pp. 3351–3358, 2009. DOI: 10.1016/j.egypro.2009.02.123.
- [12] C. Antoci, M. Gallati, and S. Sibilla, „Numerical simulation of fluid–structure interaction by sph,“ *Computers Structures*, vol. 85, no. 11, pp. 879–890, 2007, Fourth MIT Conference on Computational Fluid and Solid Mechanics. DOI: <https://doi.org/10.1016/j.compstruc.2007.01.002>.
- [13] J. Autio, P. Gribi, L. Johnson, and P. Marschall, „Effect of excavation damaged zone on gas migration in a KBS-3H type repository at Olkiluoto,“ *MIGRATION 2005, The 10th international conference on the chemistry and migration of actinides and fission products in the geosphere*, vol. 31, no. 10, pp. 649–653, 2006. DOI: 10.1016/j.pce.2006.04.016.
- [14] C. Bauer-Plaindoux, D. Tessier, and M. Ghoreychi, „Propriétés mécaniques des roches argileuses carbonatées: Importance de la relation calcite-argile,“ French, *Comptes Rendus de l’Académie des Sciences-Series IIA-Earth and Planetary Science*, vol. 326, no. 4, pp. 231–237, 1998.
- [15] Z. P. Bažant, „Instability, ductility, and size effect in strain-softening concrete,“ English (US), *Journal of Engineering Mechanics - ASCE*, vol. 102, no. 2, pp. 331–344, 1976.
- [16] —, „Why continuum damage is nonlocal: Justification by quasiperiodic microcrack array,“ *Mechanics Research Communications*, vol. 14, no. 5-6, pp. 407–419, 1987.
- [17] —, „Why continuum damage is nonlocal: Micromechanics arguments,“ *Journal of Engineering Mechanics*, vol. 117, no. 5, pp. 1070–1087, 1991.
- [18] —, „Nonlocal damage theory based on micromechanics of crack interactions,“ *Journal of Engineering Mechanics*, vol. 120, no. 3, pp. 593–617, 1994. DOI: 10.1061/(ASCE)0733-9399(1994)120:3(593).
- [19] Z. P. Bažant and T. B. Belytschko, „Wave propagation in a strain-softening bar: Exact solution,“ *Journal of Engineering Mechanics*, vol. 111, no. 3, pp. 381–389, 1985.

- [20] T. Belytschko, H. Chen, J. Xu, and G. Zi, „Dynamic crack propagation based on loss of hyperbolicity and a new discontinuous enrichment,“ *International Journal for Numerical Methods in Engineering*, vol. 58, no. 12, pp. 1873–1905, 2003, Publisher: John Wiley & Sons, Ltd. DOI: 10.1002/nme.941.
- [21] E. Bemmerl, P. Longuemare, and O. Vincké, „Poroelastic parameters of meuse/haute marne argillites: Effect of loading and saturation states,“ *Applied Clay Science*, vol. 26, no. 1, pp. 359–366, 2004, Clays in Natural and Engineered Barriers for Radioactive Waste Confinement. DOI: 10.1016/j.clay.2003.12.012.
- [22] J. Bleyer, C. Roux-Langlois, and J.-F. Molinari, „Dynamic crack propagation with a variational phase-field model: Limiting speed, crack branching and velocity-toughening mechanisms,“ *International Journal of Fracture*, vol. 204, no. 1, pp. 79–100, 2017.
- [23] M. Blunt, B. Bijeljic, H. Dong, *et al.*, „Pore-scale imaging and modelling,“ *Advances in Water Resources*, vol. 51, pp. 197–216, 2013, cited By 825. DOI: 10.1016/j.advwatres.2012.03.003.
- [24] J. Bolander and S. Saito, „Fracture analyses using spring networks with random geometry,“ *Engineering Fracture Mechanics*, vol. 61, no. 5, pp. 569–591, 1998. DOI: 10.1016/S0013-7944(98)00069-1.
- [25] J. Bonet and T.-S. Lok, „Variational and momentum preservation aspects of smooth particle hydrodynamic formulations,“ *Computer Methods in Applied Mechanics and Engineering*, vol. 180, no. 1, pp. 97–115, 1999. DOI: 10.1016/S0045-7825(99)00051-1.
- [26] J. Bonet and S. Kulasegaram, „Remarks on tension instability of Eulerian and Lagrangian corrected smooth particle hydrodynamics (CSPH) methods,“ *International Journal for Numerical Methods in Engineering*, vol. 52, no. 11, pp. 1203–1220, 2001, Publisher: John Wiley & Sons, Ltd. DOI: 10.1002/nme.242.
- [27] J. Bonet and R. D. Wood, *Nonlinear continuum mechanics for finite element analysis*. Cambridge university press, 1997.
- [28] M. J. Borden, C. V. Verhoosel, M. A. Scott, T. J. Hughes, and C. M. Landis, „A phase-field description of dynamic brittle fracture,“ *Computer Methods in Applied Mechanics and Engineering*, vol. 217-220, pp. 77–95, 2012. DOI: 10.1016/j.cma.2012.01.008.
- [29] P. Boulin, „Expérimentation et Modélisation du Transfert d’hydrogène à travers des argiles de centre de stockage de déchets radioactifs,“ French, Ph.D. dissertation, 2008.

- [30] B. Bourdin, G. Francfort, and J.-J. Marigo, „Numerical experiments in revisited brittle fracture,“ *Journal of the Mechanics and Physics of Solids*, vol. 48, no. 4, pp. 797–826, 2000. DOI: 10.1016/S0022-5096(99)00028-9.
- [31] J. Brackbill, D. Kothe, and C. Zemach, „A continuum method for modeling surface tension,“ *Journal of Computational Physics*, vol. 100, no. 2, pp. 335–354, 1992. DOI: 10.1016/0021-9991(92)90240-Y.
- [32] A. Braides *et al.*, *Approximation of free-discontinuity problems*, 1694. Springer Science & Business Media, 1998.
- [33] L. Brookshaw, „A method of calculating radiative heat diffusion in particle simulations,“ *Publications of the Astronomical Society of Australia*, vol. 6, no. 2, pp. 207–210, 1985.
- [34] L. Brookshaw, „Solving the heat diffusion equation in sph,“ *Memorie della Societa Astronomica Italiana*, vol. 65, p. 1033, 1994.
- [35] T. Capone, A. Panizzo, and J. J. Monaghan, „Sph modelling of water waves generated by submarine landslides,“ *Journal of Hydraulic Research*, vol. 48, no. sup1, pp. 80–84, 2010. DOI: 10.1080/00221686.2010.9641248.
- [36] S. Cariou, Z. Duan, C. Davy, F. Skoczylas, and L. Dormieux, „Poromechanics of partially saturated cox argillite,“ *Applied Clay Science*, vol. 56, pp. 36–47, 2012. DOI: 10.1016/j.clay.2011.11.021.
- [37] S. Cariou, „Hydro-mechanical coupling and transport in Meuse/Haute-Marne argillite : experimental and multiscale approaches,“ French, Thesis, Ecole des Ponts ParisTech, 2010.
- [38] F. J. Carrillo, I. C. Bourg, and C. Soulaine, „Multiphase flow modeling in multiscale porous media: An open-source micro-continuum approach,“ *Journal of Computational Physics: X*, vol. 8, 2020. DOI: <https://doi.org/10.1016/j.jcpx.2020.100073>.
- [39] É. Cartan, „Les systemes differentiels exterieure et leur applications geometriques,“ *sdea*, p. 1, 1945.
- [40] P. P. Castañeda and J. Willis, „The effect of spatial distribution on the effective behavior of composite materials and cracked media,“ *Journal of the Mechanics and Physics of Solids*, vol. 43, no. 12, pp. 1919–1951, 1995. DOI: 10.1016/0022-5096(95)00058-Q.
- [41] A. Chaniotis, D. Poulidakos, and P. Koumoutsakos, „Remeshed smoothed particle hydrodynamics for the simulation of viscous and heat conducting flows,“ *Journal of Computational Physics*, vol. 182, no. 1, pp. 67–90, 2002. DOI: <https://doi.org/10.1006/jcph.2002.7152>.

- [42] Z. Chen, Z. Zong, M. Liu, *et al.*, „An sph model for multiphase flows with complex interfaces and large density differences,” *Journal of Computational Physics*, vol. 283, pp. 169–188, 2015. DOI: <https://doi.org/10.1016/j.jcp.2014.11.037>.
- [43] P. W. Cleary and J. J. Monaghan, „Conduction modelling using smoothed particle hydrodynamics,” *Journal of Computational Physics*, vol. 148, no. 1, pp. 227–264, 1999.
- [44] A. Colagrossi and M. Landrini, „Numerical simulation of interfacial flows by smoothed particle hydrodynamics,” *Journal of Computational Physics*, vol. 191, no. 2, pp. 448–475, 2003. DOI: [10.1016/S0021-9991\(03\)00324-3](https://doi.org/10.1016/S0021-9991(03)00324-3).
- [45] B. D. Coleman and W. Noll, „The Thermodynamics of Elastic Materials with Heat Conduction and Viscosity,” in *The Foundations of Mechanics and Thermodynamics: Selected Papers*, W. Noll, Ed., Berlin, Heidelberg: Springer Berlin Heidelberg, 1974, pp. 145–156. DOI: [10.1007/978-3-642-65817-4_9](https://doi.org/10.1007/978-3-642-65817-4_9).
- [46] A. Corkum and C. Martin, „The mechanical behaviour of weak mudstone (opalinus clay) at low stresses,” *International Journal of Rock Mechanics and Mining Sciences*, vol. 44, no. 2, pp. 196–209, 2007. DOI: [10.1016/j.ijrmms.2006.06.004](https://doi.org/10.1016/j.ijrmms.2006.06.004).
- [47] A. Curnier, Q.-C. He, and P. Zysset, „Conewise linear elastic materials,” *Journal of Elasticity*, vol. 37, no. 1, pp. 1–38, 1994.
- [48] R. Cuss, J. Harrington, R. Giot, and C. Auvray, „Experimental observations of mechanical dilation at the onset of gas flow in Callovo-Oxfordian claystone,” *Clays in Natural and Engineered Barriers for Radioactive Waste Confinement. Geological Society, London, Special Publications*, vol. 400, no. iii, pp. 507–519, 2014. DOI: [10.1144/SP400.26](https://doi.org/10.1144/SP400.26).
- [49] R. J. Cuss and J. F. Harrington, „An experimental study of the potential for fault reactivation during changes in gas and pore-water pressure,” *International Journal of Greenhouse Gas Control*, vol. 53, pp. 41–55, 2016. DOI: [10.1016/j.ijggc.2016.07.028](https://doi.org/10.1016/j.ijggc.2016.07.028).
- [50] C. Davy, S. M’Jahad, F. Skoczylas, and J. Talandier, „Migration de gaz au travers de l’argilite de Bure : Mise en évidence d’un passage discontinu,” fr, in *Rencontres AUGC*, 2013, p. 8.
- [51] W. Dehnen and H. Aly, „Improving convergence in smoothed particle hydrodynamics simulations without pairing instability,” *Monthly Notices of the Royal Astronomical Society*, vol. 425, no. 2, pp. 1068–1082, 2012. DOI: [10.1111/j.1365-2966.2012.21439.x](https://doi.org/10.1111/j.1365-2966.2012.21439.x).

- [52] G. Del Piero, G. Lancioni, and R. March, „A variational model for fracture mechanics: Numerical experiments,” *Journal of the Mechanics and Physics of Solids*, vol. 55, no. 12, pp. 2513–2537, 2007, ISBN: 0022-5096 Publisher: Elsevier.
- [53] R. C. Deptulski, M. Dymitrowska, and D. Kondo, „Modeling the behavior of deformable elastic matrix with damage model using particulate method (SPH),“ French, Brest, 2019.
- [54] G. A. Dilts, „Moving-least-squares-particle hydrodynamics—i. consistency and stability,” *International Journal for Numerical Methods in Engineering*, vol. 44, no. 8, pp. 1115–1155, 1999. DOI: [https://doi.org/10.1002/\(SICI\)1097-0207\(19990320\)44:8<1115::AID-NME547>3.0.CO;2-L](https://doi.org/10.1002/(SICI)1097-0207(19990320)44:8<1115::AID-NME547>3.0.CO;2-L).
- [55] —, „Moving least-squares particle hydrodynamics ii: Conservation and boundaries,” *International Journal for Numerical Methods in Engineering*, vol. 48, no. 10, pp. 1503–1524, 2000. DOI: [https://doi.org/10.1002/1097-0207\(20000810\)48:10<1503::AID-NME832>3.0.CO;2-D](https://doi.org/10.1002/1097-0207(20000810)48:10<1503::AID-NME832>3.0.CO;2-D).
- [56] P. A. M. Dirac, „The physical interpretation of the quantum dynamics,” *Proceedings of the Royal Society of London. Series A, Containing Papers of a Mathematical and Physical Character*, vol. 113, no. 765, pp. 621–641, 1927.
- [57] L. Dormieux and D. Kondo, „Approche micromécanique du couplage perméabilité-endommagement,” *Comptes Rendus Mécanique*, vol. 332, no. 2, pp. 135–140, 2004. DOI: [10.1016/j.crme.2003.11.003](https://doi.org/10.1016/j.crme.2003.11.003).
- [58] C. T. Dyka, P. W. Randles, and R. P. Ingel, „Stress points for tension instability in SPH,” *International Journal for Numerical Methods in Engineering*, 1997. DOI: [10.1002/\(SICI\)1097-0207\(19970715\)40:13<2325::AID-NME161>3.0.CO;2-8](https://doi.org/10.1002/(SICI)1097-0207(19970715)40:13<2325::AID-NME161>3.0.CO;2-8).
- [59] C. Dyka and R. Ingel, „An approach for tension instability in smoothed particle hydrodynamics (SPH),” *Computers & Structures*, vol. 57, no. 4, pp. 573–580, 1995. DOI: [10.1016/0045-7949\(95\)00059-P](https://doi.org/10.1016/0045-7949(95)00059-P).
- [60] P. Espanol and M. Revenga, „Smoothed dissipative particle dynamics,” *Physical Review E*, vol. 67, no. 2, p. 026 705, 2003.
- [61] R. C. Ewing, R. A. Whittleston, and B. W. Yardley, „Geological disposal of nuclear waste: A primer,” *Elements*, vol. 12, no. 4, p. 233, 2016. DOI: [10.2113/gselements.12.4.233](https://doi.org/10.2113/gselements.12.4.233).
- [62] S. Fagbemi, P. Tahmasebi, and M. Piri, „Numerical modeling of strongly coupled microscale multiphase flow and solid deformation,” *International Journal for Numerical and Analytical Methods in Geomechanics*, vol. 44, no. 2, pp. 161–182, 2020. DOI: [10.1002/nag.2999](https://doi.org/10.1002/nag.2999).

- [63] M. Fall, O. Nasir, and T. Nguyen, „A coupled hydro-mechanical model for simulation of gas migration in host sedimentary rocks for nuclear waste repositories,“ *Engineering Geology*, vol. 176, pp. 24–44, 2014.
- [64] S. Fityus and O. Buzzi, „The place of expansive clays in the framework of unsaturated soil mechanics,“ *Applied Clay Science*, vol. 43, no. 2, pp. 150–155, 2009. DOI: 10.1016/j.clay.2008.08.005.
- [65] G. A. Francfort and J.-J. Marigo, „Revisiting brittle fracture as an energy minimization problem,“ *Journal of the Mechanics and Physics of Solids*, vol. 46, no. 8, pp. 1319–1342, 1998.
- [66] F. Freddi and G. Royer-Carfagni, „Regularized variational theories of fracture: A unified approach,“ *Journal of the Mechanics and Physics of Solids*, vol. 58, no. 8, pp. 1154–1174, 2010. DOI: 10.1016/j.jmps.2010.02.010.
- [67] G. Ganzenmüller, M. Sauer, M. May, and S. Hiermaier, „Hourglass control for Smooth Particle Hydrodynamics removes tensile and rank-deficiency instabilities,“ *The European Physical Journal Special Topics*, vol. 225, no. 2, pp. 385–395, 2016. DOI: 10.1140/epjst/e2016-02631-x.
- [68] A. Gastelum, P. Delmas, M. Lefrancq, *et al.*, „Visualising 3d porous media fluid interaction using x-ray ct data and smooth particles hydrodynamics modelling,“ in *25th International Conference of Image and Vision Computing New Zealand*, 2010, pp. 1–8. DOI: 10.1109/IVCNZ.2010.6148861.
- [69] R. A. Gingold and J. J. Monaghan, „Smoothed particle hydrodynamics: Theory and application to non-spherical stars,“ *Monthly notices of the royal astronomical society*, vol. 181, no. 3, pp. 375–389, 1977.
- [70] B. Grambow, „Geological disposal of radioactive waste in clay,“ *Elements*, vol. 12, no. 4, p. 239, 2016. DOI: 10.2113/gselements.12.4.239.
- [71] A. A. Griffith, „The phenomena of rupture and flow in solids,“ *Philosophical transactions of the royal society of london. Series A, containing papers of a mathematical or physical character*, vol. 221, no. 582-593, pp. 163–198, 1921.
- [72] B. Halphen and Q. S. Nguyen, „Sur les matériaux standard généralisés,“ *Journal de Mécanique*, vol. 14, pp. 39–63, 1975.
- [73] J. F. Harrington, A. E. Milodowski, C. C. Graham, J. C. Rushton, and R. J. Cuss, „Evidence for gas-induced pathways in clay using a nanoparticle injection technique,“ *Mineralogical Magazine*, vol. 76, no. 8, pp. 3327–3336, 2012, Edition: 2018/07/05 Publisher: Cambridge University Press. DOI: 10.1180/minmag.2012.076.8.45.

- [74] S. B. H. Hassine, M. Dymitrowska, V. Pot, and A. Genty, „Gas Migration in Highly Water-Saturated Opalinus Clay Microfractures Using a Two-Phase TRT LBM,” en, *Transport in Porous Media*, vol. 116, no. 3, pp. 975–1003, 2017. DOI: 10.1007/s11242-016-0809-5.
- [75] R. Holtzman and R. Juanes, „Crossover from fingering to fracturing in deformable disordered media,” *Physical Review E*, vol. 82, no. 4, p. 046305, 2010.
- [76] D. Hoxha, A. Giraud, F. Homand, and C. Auvray, „Saturated and unsaturated behaviour modelling of meuse-haute/marne argillite,” *International Journal of Plasticity*, vol. 23, no. 5, pp. 733–766, 2007. DOI: 10.1016/j.ijplas.2006.05.002.
- [77] IRSN, „Radioactive waste management. collecting, sorting, treating, conditioning, storing and disposing safely radioactive waste,” Institut de Radioprotection et de Sûreté Nucléaire, Tech. Rep., 2013.
- [78] G. R. Irwin, „Analysis of stresses and strains near the end of a crack transversing a plate,” *Trans. ASME, Ser. E, J. Appl. Mech.*, vol. 24, pp. 361–364, 1957.
- [79] J. Janson and J. Hult, „Damage mechanics and fracture mechanics: A combined approach,” *J. Mec. Appl*, vol. 1, pp. 69–84, 1977.
- [80] Z. Jiang, M. van Dijke, S. Geiger, *et al.*, „Pore network extraction for fractured porous media,” *Advances in Water Resources*, vol. 107, pp. 280–289, 2017. DOI: 10.1016/j.adwatres.2017.06.025.
- [81] L. M. Kachanov, „On the time to failure under creep conditions, izv,” *AN SSSR, Otd. Tekhn. Nauk*, vol. 8, no. 26-31, p. 8, 1958.
- [82] D. Kondo, H. Welemene, and F. Cormery, „Basic concepts and models in continuum damage mechanics,” *Revue Européenne de Génie Civil*, vol. 11, no. 7-8, pp. 927–943, 2007. DOI: 10.1080/17747120.2007.9692970.
- [83] P. Kunz, I. Zarihos, N. Karadimitriou, *et al.*, „Study of multi-phase flow in porous media: Comparison of sph simulations with micro-model experiments,” *Transport in Porous Media*, vol. 114, no. 2, pp. 581–600, 2016, cited By 35. DOI: 10.1007/s11242-015-0599-1.
- [84] J. Kwon, „Smoothed particle hydrodynamics model for simulating miscible multi-fluid flow,” *Journal of Computational Physics*, vol. 384, pp. 114–133, 2019. DOI: 10.1016/j.jcp.2018.12.007.
- [85] M. Lahooti, A. Pishavar, and M. Saidi, „A novel 2d algorithm for fluid solid interaction based on the smoothed particle hydrodynamics (sph) method,” *Scientia Iranica*, vol. 18, no. 3, pp. 358–367, 2011. DOI: <https://doi.org/10.1016/j.scient.2011.05.025>.

- [86] Y. Le Bray and M. Prat, „Three-dimensional pore network simulation of drying in capillary porous media,“ *International Journal of Heat and Mass Transfer*, vol. 42, no. 22, pp. 4207–4224, 1999. DOI: 10.1016/S0017-9310(99)00006-X.
- [87] J.-B. Leblond, *Mécanique de la rupture fragile et ductile*, fre, ser. Études en mécanique des matériaux et des structures. Paris: Hermes science publications Lavoisier.
- [88] P. Lefort, „Etude des déplacements eau-gaz dans les argilites du callovo-oxfordien a l'aide de la théorie de percolation en gradient,“ French, Ph.D. dissertation, Institut National Polytechnique de Toulouse (INP Toulouse), 2014.
- [89] J. Lemaitre and J.-L. Chaboche, „Aspect phénoménologique de la rupture par endommagement,“ *J Méc Appl*, vol. 2, no. 3, 1978.
- [90] J. Lemaitre, „A continuous damage mechanics model for ductile fracture,“ *Journal of engineering materials and technology*, vol. 107, no. 1, pp. 83–89, 1985.
- [91] J. Lemaitre and J.-L. Chaboche, *Mechanics of solid materials*. Cambridge university press, 1994.
- [92] R. Lenormand, E. Touboul, and C. Zarcone, „Numerical models and experiments on immiscible displacements in porous media,“ *Journal of Fluid Mechanics*, vol. 189, pp. 165–187, 1988. DOI: 10.1017/S0022112088000953.
- [93] T. Li, J.-J. Marigo, D. Guilbaud, and S. Potapov, „Gradient damage modeling of brittle fracture in an explicit dynamics context,“ *International Journal for Numerical Methods in Engineering*, vol. 108, no. 11, pp. 1381–1405, 2016, Publisher: John Wiley & Sons, Ltd. DOI: 10.1002/nme.5262.
- [94] L. D. Libersky and A. G. Petschek, „Smooth particle hydrodynamics with strength of materials,“ in *Advances in the Free-Lagrange Method Including Contributions on Adaptive Gridding and the Smooth Particle Hydrodynamics Method*, H. E. Trease, M. F. Fritts, and W. P. Crowley, Eds. 1991, vol. 395, pp. 248–257. DOI: 10.1007/3-540-54960-9_58.
- [95] L. D. Libersky, A. G. Petschek, T. C. Carney, J. R. Hipp, and F. A. Allahdadi, „High strain lagrangian hydrodynamics: A three-dimensional sph code for dynamic material response,“ *Journal of Computational Physics*, vol. 109, no. 1, pp. 67–75, 1993. DOI: <https://doi.org/10.1006/jcph.1993.1199>.
- [96] M. B. Liu and G. R. Liu, „Meshfree particle simulation of micro channel flows with surface tension,“ *Computational Mechanics*, vol. 35, no. 5, pp. 332–341, 2005. DOI: 10.1007/s00466-004-0620-y.
- [97] —, „Smoothed Particle Hydrodynamics (SPH): An Overview and Recent Developments,“ *Archives of Computational Methods in Engineering*, vol. 17, no. 1, pp. 25–76, 2010. DOI: 10.1007/s11831-010-9040-7.

- [98] —, „Restoring particle consistency in smoothed particle hydrodynamics,“ *Applied Numerical Mathematics*, vol. 56, no. 1, pp. 19–36, 2006. DOI: 10.1016/j.apnum.2005.02.012.
- [99] W. K. Liu, S. Jun, S. Li, J. Adee, and T. Belytschko, „Reproducing kernel particle methods for structural dynamics,“ *International Journal for Numerical Methods in Engineering*, 1995. DOI: 10.1002/nme.1620381005.
- [100] L. Lobovský and J. Křen, „Smoothed particle hydrodynamics modelling of fluids and solids,“ *Applied and Computational Mechanics*, vol. 1, no. 2, pp. 521–530, 2007.
- [101] E. Lorentz and S. Andrieux, „A variational formulation for nonlocal damage models,“ *International Journal of Plasticity*, vol. 15, no. 2, pp. 119–138, 1999. DOI: [https://doi.org/10.1016/S0749-6419\(98\)00057-6](https://doi.org/10.1016/S0749-6419(98)00057-6).
- [102] E. Lorentz and V. Godard, „Gradient damage models: Toward full-scale computations,“ *Computer Methods in Applied Mechanics and Engineering*, vol. 200, no. 21, pp. 1927–1944, 2011. DOI: <https://doi.org/10.1016/j.cma.2010.06.025>.
- [103] L. B. Lucy, „A numerical approach to the testing of the fission hypothesis,“ *The Astronomical Journal*, vol. 82, pp. 1013–1024, 1977. DOI: 10.1086/112164.
- [104] S. M’Jahad, „Impact de la fissuration sur les propriétés de rétention d’eau et de transport de gaz des géomatériaux : Application au stockage géologique des déchets radioactifs,“ French, Ph.D. dissertation, Ecole Centrale de Lille, 2012.
- [105] J.-J. Marigo, C. Maurini, and K. Pham, „An overview of the modelling of fracture by gradient damage models,“ *Meccanica*, vol. 51, no. 12, pp. 3107–3128, 2016, Publisher: Springer.
- [106] P. Marschall, S. Horseman, and T. Gimmi, „Characterisation of gas transport properties of the Opalinus Clay, a potential host rock formation for radioactive waste disposal,“ *Oil and Gas Science and Technology*, vol. 60, no. 1, pp. 121–139, 2005. DOI: 10.2516/ogst:2005008.
- [107] J. Mazars, „A description of micro-and macroscale damage of concrete structures,“ *Engineering Fracture Mechanics*, vol. 25, no. 5-6, pp. 729–737, 1986.
- [108] Y. Mehmani and H. A. Tchelepi, „Multiscale formulation of two-phase flow at the pore scale,“ *Journal of Computational Physics*, vol. 389, pp. 164–188, 2019. DOI: 10.1016/j.jcp.2019.03.035.
- [109] M. Mohajerani, „Etude expérimentale du comportement thermo-hydro-mécanique de l’argilite du callovo-oxfordien,“ French, Ph.D. dissertation, Université Paris-Est, 2011.

- [110] J. J. Monaghan, „Smoothed particle hydrodynamics,“ *Annual Review of Astronomy and Astrophysics*, vol. 30, no. 1, pp. 543–574, 1992. DOI: 10.1146/annurev.aa.30.090192.002551.
- [111] ———, „Smoothed Particle Hydrodynamics,“ *Annual Review of Astronomy and Astrophysics*, vol. 30, no. 1, pp. 543–574, 1992, Publisher: Annual Reviews. DOI: 10.1146/annurev.aa.30.090192.002551.
- [112] J. J. Monaghan and A. Kocharyan, „SPH simulation of multi-phase flow,“ *Computer Physics Communications*, 1995. DOI: 10.1016/0010-4655(94)00174-Z.
- [113] J. J. Monaghan and J. C. Lattanzio, „A refined particle method for astrophysical problems,“ *Astronomy and Astrophysics*, vol. 149, pp. 135–143, 1985.
- [114] J. Monaghan and R. Gingold, „Shock simulation by the particle method SPH,“ *Journal of Computational Physics*, vol. 52, no. 2, pp. 374–389, 1983. DOI: 10.1016/0021-9991(83)90036-0.
- [115] J. Monaghan, „Sph and riemann solvers,“ *Journal of Computational Physics*, vol. 136, no. 2, pp. 298–307, 1997. DOI: 10.1006/jcph.1997.5732.
- [116] J. J. Monaghan, „Simulating free surface flows with sph,“ *Journal of computational physics*, vol. 110, no. 2, pp. 399–406, 1994.
- [117] J. J. Monaghan, H. E. Huppert, and M. G. Worster, „Solidification using smoothed particle hydrodynamics,“ *Journal of Computational Physics*, vol. 206, no. 2, pp. 684–705, 2005. DOI: <https://doi.org/10.1016/j.jcp.2004.11.039>.
- [118] H. Montes, J. Duplay, L. Martinez, S. Escoffier, and D. Rousset, „Structural modifications of callovo-oxfordian argillite under hydration/dehydration conditions,“ *Applied Clay Science*, vol. 25, no. 3-4, pp. 187–194, 2004.
- [119] J. P. Morris, „Simulating surface tension with smoothed particle hydrodynamics,“ *International Journal for Numerical Methods in Fluids*, vol. 33, no. 3, pp. 333–353, 2000. DOI: [https://doi.org/10.1002/1097-0363\(20000615\)33:3<333::AID-FLD11>3.0.CO;2-7](https://doi.org/10.1002/1097-0363(20000615)33:3<333::AID-FLD11>3.0.CO;2-7).
- [120] M. Müller, S. Schirm, M. Teschner, B. Heidelberger, and M. Gross, „Interaction of fluids with deformable solids,“ *Computer Animation and Virtual Worlds*, vol. 15, no. 3-4, pp. 159–171, 2004. DOI: <https://doi.org/10.1002/cav.18>.
- [121] A. Neimark, „Multiscale percolation systems,“ *Zh. Eksp. Teor. Fiz*, vol. 96, pp. 1386–1396, 1989.
- [122] V. J. Neumann and R. Richtmyer, „A method for the numerical calculations of hydrodinamical shocks,“ *J. Appl. Phys*, vol. 21, p. 232, 1950.
- [123] F. K. Odqvist and J. Hult, *Kriechfestigkeit metallischer Werkstoffe*. Berlin, Heidelberg: Springer Berlin Heidelberg, 1962. DOI: 10.1007/978-3-642-52432-5_4.

- [124] M. Ostoja-Starzewski, P. Sheng, and K. Alzebdeh, „Spring network models in elasticity and fracture of composites and polycrystals,” *Computational Materials Science*, vol. 7, no. 1, pp. 82–93, 1996. DOI: 10.1016/S0927-0256(96)00064-X.
- [125] A. N. Parshikov and S. A. Medin, „Smoothed Particle Hydrodynamics Using Interparticle Contact Algorithms,” *Journal of Computational Physics*, vol. 180, no. 1, pp. 358–382, 2002. DOI: 10.1006/jcph.2002.7099.
- [126] A. Pazdaniakou and M. Dymitrowska, „Migration of gas in water saturated clays by coupled hydraulic-mechanical model,” *Geofluids*, vol. 2018, 2018.
- [127] K. Pham and J.-J. Marigo, „Approche variationnelle de l’endommagement : I. les concepts fondamentaux,” *Comptes Rendus Mécanique*, vol. 338, no. 4, pp. 191–198, 2010. DOI: <https://doi.org/10.1016/j.crme.2010.03.009>.
- [128] —, „From the onset of damage to rupture: construction of responses with damage localization for a general class of gradient damage models,” *Continuum Mechanics and Thermodynamics*, vol. 25, no. 2-4, pp. 147–171, 2013. DOI: 10.1007/s00161-011-0228-3.
- [129] G. Pijaudier-Cabot and Z. P. Bažant, „Nonlocal damage theory,” *Journal of Engineering Mechanics*, vol. 113, no. 10, pp. 1512–1533, 1987. DOI: 10.1061/(ASCE)0733-9399(1987)113:10(1512).
- [130] M. Prodanović and S. L. Bryant, „A level set method for determining critical curvatures for drainage and imbibition,” *Journal of Colloid and Interface Science*, vol. 304, no. 2, pp. 442–458, 2006. DOI: 10.1016/j.jcis.2006.08.048.
- [131] N. J. Quinlan, M. Basa, and M. Lastiwka, „Truncation error in mesh-free particle methods,” *International Journal for Numerical Methods in Engineering*, vol. 66, no. 13, pp. 2064–2085, 2006. DOI: 10.1002/nme.1617.
- [132] T. Rabczuk, T. Belytschko, and S. Xiao, „Stable particle methods based on lagrangian kernels,” *Computer Methods in Applied Mechanics and Engineering*, vol. 193, no. 12, pp. 1035–1063, 2004, Meshfree Methods: Recent Advances and New Applications. DOI: <https://doi.org/10.1016/j.cma.2003.12.005>.
- [133] Y. N. Rabotnov, „On the equation of state of creep,” in *Proceedings of the Institution of Mechanical Engineers, Conference Proceedings*, SAGE Publications Sage UK: London, England, vol. 178, 1963, pp. 2–117.
- [134] A. Q. Raeini, M. J. Blunt, and B. Bijeljic, „Modelling two-phase flow in porous media at the pore scale using the volume-of-fluid method,” *Journal of Computational Physics*, vol. 231, no. 17, pp. 5653–5668, 2012. DOI: 10.1016/j.jcp.2012.04.011.

- [135] P. W. Randles and L. D. Libersky, „Normalized sph with stress points,“ *International Journal for Numerical Methods in Engineering*, vol. 48, no. 10, pp. 1445–1462, 2000. DOI: [https://doi.org/10.1002/1097-0207\(20000810\)48:10<1445::AID-NME831>3.0.CO;2-9](https://doi.org/10.1002/1097-0207(20000810)48:10<1445::AID-NME831>3.0.CO;2-9).
- [136] ———, „Smoothed particle hydrodynamics: Some recent improvements and applications,“ *Computer Methods in Applied Mechanics and Engineering*, vol. 139, no. 1, pp. 375–408, 1996. DOI: [10.1016/S0045-7825\(96\)01090-0](https://doi.org/10.1016/S0045-7825(96)01090-0).
- [137] G. Rastello, R. Bennacer, G. Nahas, and M. Bogdan, „Effective permeability and transfer properties in fractured porous media,“ *Defect and Diffusion Forum*, vol. 362, pp. 172–189, 2015. DOI: [10.4028/www.scientific.net/DDF.362.172](https://doi.org/10.4028/www.scientific.net/DDF.362.172).
- [138] K. Ravi-Chandar, „Dynamic Fracture of Nominally Brittle Materials,“ *International Journal of Fracture*, vol. 90, no. 1, pp. 83–102, 1998. DOI: [10.1023/A:1007432017290](https://doi.org/10.1023/A:1007432017290).
- [139] K. Ravi-Chandar and W. G. Knauss, „An experimental investigation into dynamic fracture: III. On steady-state crack propagation and crack branching,“ *International Journal of Fracture*, vol. 26, no. 2, pp. 141–154, 1984. DOI: [10.1007/BF01157550](https://doi.org/10.1007/BF01157550).
- [140] J. Renner, T. Hettkamp, and F. Rummel, „Rock mechanical characterization of an argillaceous host rock of a potential radioactive waste repository,“ *Rock Mechanics and Rock Engineering*, vol. 33, no. 3, pp. 153–178, 2000. DOI: [10.1007/s006030070005](https://doi.org/10.1007/s006030070005).
- [141] J. R. Reveles, „Development of a total lagrangian sph code for the simulation of solids under dynamic loading,“ Cranfield University, 2007.
- [142] J. R. Rice, „A Path Independent Integral and the Approximate Analysis of Strain Concentration by Notches and Cracks,“ *Journal of Applied Mechanics*, vol. 35, no. 2, pp. 379–386, 1968. DOI: [10.1115/1.3601206](https://doi.org/10.1115/1.3601206).
- [143] J.-C. Robinet, „Minéralogie, porosité et diffusion des solutés dans l’argilite du callovo-oxfordien de bure (meuse, haute-marne, france) de l’échelle centimétrique à micrométrique,“ French, Ph.D. dissertation, Poitiers, 2008.
- [144] A. Y. Rozhko, „Two-phase fluid-flow modeling in a dilatant crack-like pathway,“ *Journal of Petroleum Science and Engineering*, vol. 146, pp. 1158–1172, 2016. DOI: [10.1016/j.petrol.2016.08.018](https://doi.org/10.1016/j.petrol.2016.08.018).
- [145] J. Salençon, *Handbook of continuum mechanics: General concepts thermoelasticity*. Springer Science & Business Media, 2012.
- [146] G. Sciarra, „Formulation of a phase field model of multiphase flow in deformable porous media,“ *E3S Web Conf.*, vol. 9, p. 16 006, 2016. DOI: [10.1051/e3sconf/20160916006](https://doi.org/10.1051/e3sconf/20160916006).

- [147] X. Shan and H. Chen, „Lattice Boltzmann model for simulating flows with multiple phases and components,“ *Physical Review E*, vol. 47, no. 3, pp. 1815–1819, 1993, Publisher: American Physical Society. DOI: 10.1103/PhysRevE.47.1815.
- [148] X. Shao, Z. Zhou, N. Magnenat-Thalmann, and W. Wu, „Stable and fast fluid–solid coupling for incompressible sph,“ *Computer Graphics Forum*, vol. 34, no. 1, pp. 191–204, 2015. DOI: <https://doi.org/10.1111/cgf.12467>.
- [149] L. D. G. Sigalotti, J. Klapp, O. Rendón, C. A. Vargas, and F. Peña-Polo, „On the kernel and particle consistency in smoothed particle hydrodynamics,“ *Applied Numerical Mathematics*, vol. 108, pp. 242–255, 2016. DOI: 10.1016/j.apnum.2016.05.007.
- [150] J. A. da Silva, P. K. Kang, Z. Yang, L. Cueto-Felgueroso, and R. Juanes, „Impact of confining stress on capillary pressure behavior during drainage through rough fractures,“ *Geophysical Research Letters*, vol. 46, no. 13, pp. 7424–7436, 2019. DOI: 10.1029/2019GL082744.
- [151] R. Sivanapillai, N. Falkner, A. Hartmaier, and H. Steeb, „A csf-sph method for simulating drainage and imbibition at pore-scale resolution while tracking interfacial areas,“ *Advances in Water Resources*, vol. 95, pp. 212–234, 2016, Pore scale modeling and experiments. DOI: 10.1016/j.advwatres.2015.08.012.
- [152] J.-H. Song, H. Wang, and T. Belytschko, „A comparative study on finite element methods for dynamic fracture,“ *Computational Mechanics*, vol. 42, no. 2, pp. 239–250, 2008. DOI: 10.1007/s00466-007-0210-x.
- [153] Y. Song, C. Davy, D. Troadec, *et al.*, „Multi-scale pore structure of CO_x claystone: Towards the prediction of fluid transport,“ en, *Marine and Petroleum Geology*, vol. 65, pp. 63–82, 2015. DOI: 10.1016/j.marpetgeo.2015.04.004.
- [154] Song, Yang, Davy, Catherine A., and Troadec, David, „Gas breakthrough pressure (gbp) through claystones: Correlation with fib/sem imaging of the pore volume,“ *Oil Gas Sci. Technol. - Rev. IFP Energies nouvelles*, vol. 71, no. 4, p. 51, 2016. DOI: 10.2516/ogst/2016001.
- [155] C. Tang, L. Tham, P. Lee, T. Yang, and L. Li, „Coupled analysis of flow, stress and damage (fsd) in rock failure,“ *International Journal of Rock Mechanics and Mining Sciences*, vol. 39, no. 4, pp. 477–489, 2002.
- [156] E. Tanné, T. Li, B. Bourdin, J.-J. Marigo, and C. Maurini, „Crack nucleation in variational phase-field models of brittle fracture,“ *Journal of the Mechanics and Physics of Solids*, vol. 110, pp. 80–99, 2018. DOI: <https://doi.org/10.1016/j.jmps.2017.09.006>.

- [157] A. Tartakovsky, N. Trask, K. Pan, *et al.*, „Smoothed particle hydrodynamics and its applications for multiphase flow and reactive transport in porous media,“ *Computational Geosciences*, vol. 20, no. 4, pp. 807–834, 2016, cited By 47. DOI: 10.1007/s10596-015-9468-9.
- [158] R. Vignjevic, N. Djordjevic, S. Gemkow, T. De Vuyst, and J. Campbell, „Sph as a nonlocal regularisation method: Solution for instabilities due to strain-softening,“ *Computer Methods in Applied Mechanics and Engineering*, vol. 277, pp. 281–304, 2014.
- [159] R. Vignjevic, J. Campbell, and L. Libersky, „A treatment of zero-energy modes in the smoothed particle hydrodynamics method,“ *Computer Methods in Applied Mechanics and Engineering*, vol. 184, no. 1, pp. 67–85, 2000. DOI: [https://doi.org/10.1016/S0045-7825\(99\)00441-7](https://doi.org/10.1016/S0045-7825(99)00441-7).
- [160] R. Vignjevic, J. R. Reveles, and J. Campbell, „Sph in a total lagrangian formalism,“ *CMC-Tech Science Press-*, vol. 4, no. 3, p. 181, 2006.
- [161] D. Violeau and R. Issa, *Numerical modelling of complex turbulent free-surface flows with the sph method: An overview*, 2007. DOI: <https://doi.org/10.1002/flid.1292>.
- [162] D. Violeau and A. Leroy, „On the maximum time step in weakly compressible SPH,“ *Journal of Computational Physics*, vol. 256, pp. 388–415, 2014. DOI: 10.1016/j.jcp.2013.09.001.
- [163] M. Wan, P. Delage, A. M. Tang, and J. Talandier, „Water retention properties of the callovo-oxfordian claystone,“ *International Journal of Rock Mechanics and Mining Sciences*, vol. 64, pp. 96–104, 2013. DOI: 10.1016/j.ijrmms.2013.08.020.
- [164] P. D. Washabaugh and W. G. Knauss, „A reconciliation of dynamic crack velocity and Rayleigh wave speed in isotropic brittle solids,“ *International Journal of Fracture*, vol. 65, no. 2, pp. 97–114, 1994. DOI: 10.1007/BF00032282.
- [165] A. C. Wiseall, R. J. Cuss, C. C. Graham, and J. F. Harrington, „The visualization of flow paths in experimental studies of clay-rich materials,“ *Mineralogical Magazine*, vol. 79, no. 6, pp. 1335–1342, 2015. DOI: 10.1180/minmag.2015.079.06.09.
- [166] K. Xu, J.-F. Daian, and D. Quenard, „Multiscale structures to describe porous media part ii: Transport properties and application to test materials,“ *Transport in Porous Media*, vol. 26, no. 3, pp. 319–338, 1997. DOI: 10.1023/A:1006519801173.
- [167] K. Xu, J.-f. Daian, and D. Quenard, „Multiscale structures to describe porous media part i: Theoretical background and invasion by fluids,“ *Transport in Porous Media*, vol. 26, no. 1, pp. 51–73, 1997. DOI: 10.1023/A:1006557915438.

- [168] W. Xu and J. Fish, „A multiscale modeling of permeability in a multi-porosity porous medium using smoothed particle hydrodynamics,“ *International Journal for Numerical Methods in Engineering*, vol. 111, no. 8, pp. 776–800, 2017. DOI: 10.1002/nme.5494.
- [169] J. Yang, M. Fall, and G. Guo, „A Three-Dimensional Hydro-mechanical Model for Simulation of Dilatancy Controlled Gas Flow in Anisotropic Claystone,“ *Rock Mechanics and Rock Engineering*, vol. 53, no. 9, pp. 4091–4116, 2020. DOI: 10.1007/s00603-020-02152-w.
- [170] Q. Yang, J. Yao, Z. Huang, *et al.*, „Pore-scale investigation of petro-physical fluid behaviours based on multiphase sph method,“ *Journal of Petroleum Science and Engineering*, vol. 192, 2020, cited By 1. DOI: 10.1016/j.petrol.2020.107238.
- [171] J. R. Young, „Modelling elastic dynamics and fracture with coupled mixed correction eulerian total lagrangian sph,“ The University of Edinburgh, 2018.
- [172] Y. Zaretskiy, S. Geiger, K. Sorbie, and M. Förster, „Efficient flow and transport simulations in reconstructed 3D pore geometries,“ *Advances in Water Resources*, vol. 33, no. 12, pp. 1508–1516, 2010. DOI: 10.1016/j.advwatres.2010.08.008.
- [173] C. Zhang and T. Rothfuchs, „Experimental study of the hydro-mechanical behaviour of the callovo-oxfordian argillite,“ *Applied Clay Science*, vol. 26, no. 1, pp. 325–336, 2004, Clays in Natural and Engineered Barriers for Radioactive Waste Confinement. DOI: 10.1016/j.clay.2003.12.025.
- [174] F. Zhang, S. Xie, D. Hu, J. Shao, and B. Gatmiri, „Effect of water content and structural anisotropy on mechanical property of claystone,“ *Applied Clay Science*, vol. 69, pp. 79–86, 2012. DOI: 10.1016/j.clay.2012.09.024.
- [175] B. Zhao, C. W. MacMinn, B. K. Primkulov, *et al.*, „Comprehensive comparison of pore-scale models for multiphase flow in porous media,“ *Proceedings of the National Academy of Sciences*, vol. 116, no. 28, pp. 13 799–13 806, 2019, Publisher: National Academy of Sciences. DOI: 10.1073/pnas.1901619116.